

UNIVERSITA' DEGLI STUDI DI NAPOLI "FEDERICO II"



FACOLTA' DI INGEGNERIA

TESI DI LAUREA IN INGEGNERIA AEROSPAZIALE

**PERFORMANCE EVALUATION
OF A RADAR DOPPLER/ALTIMETER
FOR MARS LANDING CONTROL**

RELATORE

Prof. Ing. Antonio Moccia

CORRELATORE

Ing. Giovanni Alberti

CANDIDATO

Giuseppe Cirillo

Matr. 347/878

ANNO ACCADEMICO 2008/2009

LIST OF CONTENTS

INTRODUCTION	9
1. EUROPEAN STRATEGY FOR SPACE	12
1.1. Aurora Program	14
1.2. ExoMars Mission	15
1.2.1. Mission Overview	16
1.2.2. Flight Segment	18
1.3. Radar Doppler / Altimeter	20
2. REQUIREMENTS	22
2.1. Operational Scenario	23
2.2. Performance Requirements	29
3. TECHNICAL SOLUTIONS	30
3.1. Historical Background	32
3.2. Radar Solutions for AVM	35
3.2.1. Frequency Modulated Continuous Wave Radar	36
3.2.2. Pulsed Continuous Wave Radar	38
3.3. Critical Requirements	41
3.3.1. Altitude Measurement	42
3.3.2. Altitude Measurement near Touchdown	43
3.4. Selected Radar Configuration	44
3.4.1. Sequentially Altitude and Velocity Measurement	46
4. MATHEMATICAL MODEL	49
4.1. Platform Attitude	50
4.2. Measurement Technique	56
4.2.1. Range Estimation	58
4.2.2. Noise Estimation	59
4.2.3. Velocity Estimation	60
4.2.4. Measurements Accuracies	61
4.2.5. Measurement Ambiguities	62
4.3. Range Integration Time Constraints	65
5. PERFORMANCE MODEL	67
5.1. Matlab® Codes Description	69
5.1.1. Scripts Description	72
5.1.2. Functions Description	74
5.2. Mars Backscattering Model	79
5.3. Signal to Noise Ratio Evaluation	82
5.4. Range Measurements Accuracy	86
5.4.1. Factors Affecting Range Measurements Accuracy	88
5.5. Velocity Measurements Accuracy	91
5.5.1. Factors Affecting Velocity Measurements Accuracy	95
6. PRELIMINARY SYSTEM DEFINITION	97

6.1.	Operating Frequency.....	98
6.2.	Sampling Frequency and IF Conversion	99
6.3.	Antenna Geometry.....	99
6.4.	Antenna Beamwidth and Gain	101
6.5.	Signal Bandwidth.....	101
6.6.	Receiver Noise Figure.....	102
6.7.	Antenna, Atmospheric & Vented Bags Losses.....	102
6.8.	Integration Time.....	103
6.9.	Pulse Repetition Frequency.....	106
6.10.	Transmitted Pulse Duration	108
6.11.	Signal Peak Power, Link Budget and Receiver Dynamics	108
6.12.	Detection Probability for Range Measurements.....	111
7.	PERFORMANCE OPTIMIZATIONS	114
7.1.	Analytic Investigation	115
7.2.	Numerical Investigation	117
7.2.1.	Range Investigation	117
7.2.2.	Velocity Investigation	119
7.3.	Preliminary Parameters Laws.....	126
7.3.1.	Integration Time Laws	128
7.3.2.	Pulse Repetition Frequency Laws	129
7.3.3.	Pulse Duration Laws	132
8.	PERFORMANCE EVALUATIONS	137
8.1.	Worst Case Descent	138
8.1.1.	Preliminary Inputs Setting	138
8.1.2.	Preliminary RDA Measurement Accuracy.....	140
8.1.3.	Time Measurements Improvements	144
8.1.4.	Geometric Improvement	149
8.1.5.	Final Worst Case RDA Configuration	162
8.2.	“Slow_Vert_Sim_Descent” Simulated Descent.....	164
8.2.1.	Descent Profile	164
8.2.2.	Inputs Setting.....	167
8.2.3.	RDA Measurement Accuracy	169
8.3.	“Fast_Vert_Sim_Descent” Simulated Descent.....	173
8.3.1.	Descent Profile	173
8.3.2.	Inputs Setting.....	176
8.3.3.	RDA Measurement Accuracy	178
	CONCLUSIONS	182
	DEFINITIONS	186
	ACRONYMS.....	192
	MATLAB® CODES	193
	REFERENCES	224
	ACKNOWLEDGEMENTS	225

LIST OF FIGURES

Figure 2-1 – EDL events for GNC (from EIP to first parachute opening). Radar Doppler/Altimeter is not operating.	23
Figure 2-2 – EDL events for GNC (from first parachute opening to final landing). Radar Doppler/Altimeter becomes functional after Front Shield Jettison.	24
Figure 2-3 – Free Fall Reference Frame before Touchdown	25
Figure 2-4 – Body and Ground Reference Frame for Descent phase	26
Figure 2-5 - Velocity components in defined Reference Frames for Descent phase	26
Figure 2-6 - Assumption for Mars surface backscattering.....	27
Figure 3-1 - Range Estimation Concept in space-borne altimeters from [Ref 4].....	39
Figure 3-2 – Pulsed limited configuration for illuminating the surface (from [Ref. 4] and www.aviso.oceanobs.com).....	40
Figure 3-3 Echo signals in pulse-limited and beam-limited conditions (from [Ref. 4] and www.aviso.oceanobs.com).....	41
Figure 3-4 – Range Measurement for RDA operations	42
Figure 3-5 – Surface observation strategy for RDA	45
Figure 3-6 – Measurement Timeline for the RDA.....	47
Figure 3-7 – High-Level RDA Timeline	48
Figure 4-1 – Range Measurement for RDA operations	50
Figure 4-2 – Off-nadir angles representation	51
Figure 4-3 – Frame references	51
Figure 4-4 – Coordinate frame for RDA equipment	52
Figure 4-5 – Surface observation strategy for each RDA unit	52
Figure 4-6 – Generic block diagram of (a) a coherent radar transmitter, and (b) Doppler radar receiver	56
Figure 4-7 – Range and velocity measurement block diagram	58
Figure 4-8 – Range Estimation Concept	59
Figure 4-9 – Noise Estimation Concept	59
Figure 4-10 – Velocity Estimation Concept	61
Figure 4-11 – Maximum PRF values for RDA non-ambiguous operations in Range	64
Figure 4-12 – Minimum PRF values for RDA non-ambiguous operations in Doppler	64
Figure 5-1 – Flow chart of performance model.....	68
Figure 5-2 – Experimental Cross Section per Unit Surface Area.....	79
Figure 5-3 – Modeled cross section per unit surface area	81
Figure 5-4 – Basic geometry involved in the evaluation of signal to noise ratio	83
Figure 5-5 – Received pulse shape for various radar altitudes.....	84
Figure 5-6 – Received pulse power taking into account actual transmitted pulse rising time and receiving bandwidth	85
Figure 5-7 – Achievable peak SNR as a function of radar altitude (integration factor included) for two values of transmitted pulse length	86
Figure 5-8 – Achievable range accuracy as a function of radar altitude	88
Figure 5-9 – The effect of terrain RMS slope as a function of radar altitude	90

Figure 5-10 – Example range accuracy as a function of radar altitude for various RMS slope values (the red curve is without slope).....	90
Figure 5-11 – Plot of K_x , K_y and K_z as a function of α	92
Figure 5-12 – Example SNR as a function of radar altitude for the velocity estimation as a function of radar altitude.....	93
Figure 5-13 – Velocity accuracy (pulse-pair technique) as a function of radar altitude and for various ρ^2 values	94
Figure 5-14 – Autocorrelation coefficient ρ^2 as a function of second moment of velocity power spectrum σ_v	94
Figure 5-15 – Autocorrelation coefficient ρ^2 as a function of antenna aperture	96
Figure 6-1 – Velocity accuracy conversion factor (from velocity beams to x, y and z axes). 100	
Figure 6-2 – Minimum integration time for single velocity measurement as a function of radar carrier frequency.....	104
Figure 6-3 – Received power	109
Figure 6-4 – Integrated SNR (range measurements) as a function of radar altitude for various off-nadir angle (0° , 15° and 35°)	111
Figure 6-5 – Detection probability as a function of SNR	113
Figure 7-1 – 3D plot Range measurement error δR as function of $T_{meas,R}$ and PRF_R	118
Figure 7-2 – Contour plot Range measurement error δR as function of $T_{meas,R}$ and PRF_R	118
Figure 7-3 – 3D plot Velocity measurement error δV as function of $T_{meas,V}$ and PRF_V	120
Figure 7-4 – Minimum values set as function of $T_{meas,V}$ and PRF_V	121
Figure 7-5 – Zoomed minimum values set as function of $T_{meas,V}$ and PRF_V	122
Figure 7-6 – Minimum values set as function of $T_{meas,V}$ and PRF_V	123
Figure 7-7 – Zoomed minimum values set as function of $T_{meas,V}$ and PRF_V	123
Figure 7-8 – Minimum values set as function of $T_{meas,V}$ and PRF_V	124
Figure 7-9 – Zoomed minimum values set as function of $T_{meas,V}$ and PRF_V	125
Figure 7-10 – Minimum values set as function of $T_{meas,V}$ and PRF_V	125
Figure 7-11 – Optimum integration time laws	128
Figure 7-12 – Optimum range PRF law.....	129
Figure 7-13 – Optimum velocity PRF law	130
Figure 7-14 – Zoomed optimum velocity PRF law	130
Figure 7-15 – Range pulsewidth bound.....	132
Figure 7-16 – Velocity pulsewidth bound.....	132
Figure 7-17 – Range pulsewidth law	133
Figure 7-18 – Range signal send-return time	133
Figure 7-19 – Velocity pulsewidth law $\alpha_{beam} = 15^\circ$	134
Figure 7-20 – Velocity signal send-return time with $\alpha_{beam} = 15^\circ$	135
Figure 7-21 – Velocity pulsewidth law $\alpha_{beam} = 20^\circ$	135
Figure 7-22 – Velocity signal send-return time with $\alpha_{beam} = 20^\circ$	136
Figure 8-1 – Range measurement accuracy	140
Figure 8-2 – Velocity measurement accuracies.....	141
Figure 8-3 – Zoomed velocity measurement accuracies	141
Figure 8-4 – Maximum achievable range measurement accuracy for null acceleration, Jerk and angular velocity.....	142

Figure 8-5 – Maximum achievable velocity measurement accuracies for null acceleration, Jerk and angular velocity	143
Figure 8-6 – Zoomed maximum achievable velocity measurement accuracies for null acceleration, Jerk and angular velocity	143
Figure 8-7 – Modified integration time law.....	144
Figure 8-8 – Modified integration time law.....	145
Figure 8-9 – Range measurement accuracy	145
Figure 8-10 – Range measurement accuracy loss	146
Figure 8-11 – Velocity measurement accuracies.....	147
Figure 8-12 – Velocity measurement accuracies.....	147
Figure 8-13 – V_x velocity measurement accuracy gain	148
Figure 8-14 – V_y & V_z velocity measurement accuracies gain	148
Figure 8-15 – Received velocity power.....	150
Figure 8-16 – Nominal case received power loss	150
Figure 8-17 – Worst case received power loss	151
Figure 8-18 – Velocity accuracy projection coefficients	151
Figure 8-19 – Velocity measurement accuracies.....	152
Figure 8-20 – Zoomed velocity measurement accuracies	152
Figure 8-21 – V_x velocity measurement accuracy loss.....	153
Figure 8-22 – V_y & V_z velocity measurement accuracies gain	153
Figure 8-23 – Total range measurement accuracy variation	154
Figure 8-24 – Total V_x velocity measurement accuracy variation	155
Figure 8-25 – Total V_y & V_z velocity measurement accuracies variation	155
Figure 8-26 – Range measurement accuracy excess	156
Figure 8-27 – V_x velocity measurement accuracy excess	157
Figure 8-28 – V_y & V_z measurement velocity accuracies excess.....	157
Figure 8-29 – Maximum achievable range measurement accuracy for null acceleration, Jerk and angular velocity.....	158
Figure 8-30 – Maximum achievable velocity measurement accuracies for null acceleration, Jerk and angular velocity	159
Figure 8-31 – Zoomed maximum achievable velocity measurement accuracies for null acceleration, Jerk and angular velocity.....	159
Figure 8-32 – Range measurement accuracy excess	160
Figure 8-33 – V_x velocity measurement accuracy excess	160
Figure 8-34 – V_y & V_z velocity measurement accuracies excess.....	161
Figure 8-35 – Law motion.....	164
Figure 8-36 – Velocity.....	164
Figure 8-37 – Acceleration.....	165
Figure 8-38 – Jerk	165
Figure 8-39 – Range sidelook angles	166
Figure 8-40 – Velocity sidelook angles	166
Figure 8-41 – Angular velocity.....	167
Figure 8-42 – Range backscattering	169
Figure 8-43 – Velocity backscattering	169

Figure 8-44 – Range SNR	170
Figure 8-45 – Velocity SNR	170
Figure 8-46 – Range measurement accuracy	171
Figure 8-47 – Velocity measurement accuracies.....	171
Figure 8-48 – Zoomed velocity measurement accuracies	172
Figure 8-49 – Law motion.....	173
Figure 8-50 – Velocity.....	173
Figure 8-51 – Acceleration.....	174
Figure 8-52 – Jerk	174
Figure 8-53 – Range sidelook angles	175
Figure 8-54 – Velocity sidelook angles	175
Figure 8-55 – Angular velocity.....	176
Figure 8-56 – Range backscattering	178
Figure 8-57 – Velocity backscattering	178
Figure 8-58 – Range SNR	179
Figure 8-59 – Velocity SNR	179
Figure 8-60 – Range measurement accuracy	180
Figure 8-61 – Velocity measurement accuracies.....	180
Figure 8-62 – Zoomed velocity measurement accuracies	181

LIST OF TABLES

Table 2-1 – Operational Scenario	28
Table 2-2 – Performance Requirements.....	29
Table 6-1 – Link budget for the two extreme case for the received power	110
Table 7-1 – RDA Parameters and Constraints	127
Table 8-1 – System parameter driven by worst-case requirements. All specified constant parameters are maintained constant from 10 m up to 3000 m, where the performance will be evaluated.....	139
Table 8-2 – Preliminary RDA definition driven by requirements observation. All specified constant parameters are maintained constant from 10 m up to 3000 m, where the performance will be evaluated.....	163
Table 8-3 – Simulated descent inputs for “Slow_Vert_Sim_Descent”	168
Table 8-4 – Simulated descent inputs for “Fast_Vert_Sim_Descent”	177

“Man will not always stay on Earth; the pursuit of light and space will lead him to penetrate the bounds of the atmosphere, timidly at first, but in the end to conquer the whole of solar space.”

Konstantin Eduardovich Tsiolkovsky

INTRODUCTION

For many years the European Space Agency (ESA) has been supporting the development of Landing Guidance and Navigation Control (GNC) technologies with potential applications to landing missions to the Moon, to Mercury, and to Mars.

As regards Mars, past landing missions have been accomplished through the use of robust landing systems, including the use of landing gears on the Viking I & II landers, or airbags on the Pathfinder and Spirit & Opportunity twin exploration rovers.

Future missions, however, are likely to employ heavier and complex payloads, so airbag-assisted landing concept reaches its limit. Therefore it is necessary to study in detail Landing Guidance and Navigation Control (GNC) concepts based on a final powered phase for a safe and accurate landing approach. This means that it will be possible to land in a region of high scientific interest; moreover, final powered phase implies less robust landing systems, because of touchdown more delicate in comparison to the airbags-assisted landing concept, so this will allow delivery of more massive scientific payloads for long term roving and sample returns.

Less robust, safe, accurate landing in difficult planetary terrain, including areas that are rocky, heavily sloped, or both, requires remote sensing of the surface in

order to choose an appropriate approach to the ground. This requirements lead to improved capabilities in the sensing of navigation data, including altitude and three dimensional velocities in real time along the final descent. All these requirements are relatively new and it is foreseeable that they will be applied consistently to future landing missions of the planetary exploration program.

While active or passive optical sensors might seem appropriate for this new concept of landing, an alternate approach based on a millimeter-wave electrically scanned phased array radar has been envisaged.

The present work will focus the attention on the Radar Doppler / Altimeter (RDA) on board of the Descent Module of ExoMars mission.

Following the technical proposal done in response to ESA Invitation to Tender, Thales Alenia Space Italy in Rome (TAS-I Rome) will be in charge for the overall development of RDA units.

Consortium for Research on Advanced Remote Sensing Systems (CoRiSTA) will participate to the activities being responsible of the RDA Performance Model for the optimization of the radar measurements accuracy.

Measurements accuracies are investigated in "Worst Case" descent conditions to obtain optimum laws for RDA key parameters. Investigation goals are to satisfy the assigned requirements for range and 3-axis velocity measurement. Subsequently, two simulated descent profiles are analyzed to validate RDA Performance Model.

The satisfaction of required measurements accuracy will lead to the Preliminary System Definition that is fundamental for following development, production and verification phase that will begin in 2010.

A summary of the treated matters is proposed in the following.

Chapter 1 deals with the European strategy for space, it describes Aurora program and the flagship ExoMars mission. Radar Doppler / Altimeter is introduced as key sensor to detect motion during the critical final descent phase.

Chapter 2 reports RDA requirements that are the baselines for next preliminary definition of instrument.

Chapter 3 analyzes RDA critical requirements and provides a technical solution.

Chapter 4 provides mathematical model for RDA analysis and development, such as platform attitude and measurement technique.

Chapter 5 introduces the RDA performance model that allows the analysis of RDA measurement accuracy during the final descent.

Chapter 6 introduces the preliminary RDA system definition on the basis of requirements and today's technological know-how.

Chapter 7 deals with the RDA performance optimizations to get the best laws for RDA key parameters during the final descent.

Chapter 8 shows the results of RDA performance in worst case and in some simulated descent.

1. EUROPEAN STRATEGY FOR SPACE

In November 16th 2000, Ministers representing the 15 Member States of the European Space Agency (ESA), gathered in Brussels at a meeting of the ESA Council, adopted a resolution that accompanies a joint ESA/EC document on a European Strategy for Space. A parallel resolution, based on the same document, has been endorsed by the European Research Council, also meeting in Brussels.

This was the very first time that the Councils of ESA and the EU had met on the same date and in the same place to adopt resolutions that would have constituted a common framework within which all European players, involved in space activities, would have developed their respective plans of action.

“Through these resolutions, European space policy takes a first step into a new phase in which space systems become an integral part of the overall political and economic efforts of European states – whether members of ESA or the EU – to promote the interests of European citizens”,

said ESA’s Director General, Antonio Rodotà [[Ref. 1](#)].

The European Strategy for Space identifies three lines of action:

1. Strengthening the foundations for space activities
2. Enhancing scientific knowledge
3. Reaping the benefits for society and markets

The first line encompasses broadening space technology and guaranteeing access to space through a family of launch vehicles. The second sees Europe continuing to pursue cutting-edge themes of space science and space contributions to the understanding of our planet's climate. It includes human spaceflight and optimization of the use of the International Space Station as an infrastructure for European research in all disciplines of space science. The third line of action has the objectives of seizing market opportunities and meeting the new demands of our society. It bears on satellite communications and the information technology sector, satellite navigation and positioning (Galileo), and systems monitoring the Earth for environment and security. This is where close cooperation between ESA and the EC will be most instrumental in putting space systems at the service of European policies responding to citizen's expectations.

The European Space Strategy also covers industrial aspects and pays specific attention to small and medium-size enterprises (SMEs). Public/Private partnerships are seen as a model for committing the public sector along with the complete industrial chain to an operational project.

The two adopted resolutions endorse the setting up of a cooperative structure that have brought together the ESA Executive and the European Commission. An interim high-level joint Task Force is has been set up to make proposals for the continuing development of the European Space Strategy and its implementation. In addition to being a partner in the setting up of joint programs responding to political initiatives of the European Union, ESA acts as the implementing organisation for the development and procurement of the space and ground segments associated with such initiatives.

1.1. Aurora Program

Aurora is part of Europe's strategy for space, endorsed by the European Union Council of Research and the ESA Council in 2001 [Ref. 2]. This strategy calls for Europe to:

1. Explore the solar system and the Universe
2. Stimulate new technology
3. Inspire the young people of Europe to take a greater interest in science and technology

As a result of this challenge, in 2001 ESA set up the Aurora Program. The primary objective of Aurora is to create, and then implement, a European long-term plan for the robotic and human exploration of the solar system, with Mars, the Moon and the asteroids as the most likely targets.

Curiosity about our world, and the Universe that surrounds us, has been the driving force behind human progress since prehistoric times. Today, the exploration of space remains one of the most stimulating and exciting areas of scientific research.

A second objective is to search for life beyond the Earth. Future missions under the program will carry sophisticated exobiology payloads to investigate the possibility of life forms existing on other worlds within the solar system. The Program will also provide for the missions and technology necessary to complement those planned in the existing ESA and national programs, in order to bring about a coherent European framework for exploration and to progressively develop a unified European approach.

It is clear from these objectives that the interdependence of exploration and technology is the basis of the Aurora Program. On the one hand the desire to explore provides the stimulus to develop new technology while on the other, it is the introduction of innovative technology that will make exploration possible.

Each phase of exploration on the way to the human exploration of Mars will require increasingly complex technology. In some cases existing technology can be further developed or adapted, but in many cases European industry will be asked to come up with new innovative technology to make future exploration missions possible. The technological studies to be carried out under the Aurora Program will enable Europe to select which of the many technologies on offer should be given

priority for development within Europe, as well as the value of the technologies offered by possible partners. Among the technology needed to make a human mission to Mars possible are: aerobraking, precision navigation and landing, propulsion systems that offer cheaper, faster travel; and life-support systems to enable humans to live in hostile space environments.

Aurora's approach is step-by-step. It means that missions will increase in complexity over time, culminating - if all goes well - in a human expedition to Mars by the year 2030. Steps on the way to Mars will probably include exploration of the Moon as well as:

1. Remote sensing of the Martian environment
2. Robotic exploration and surface analysis
3. Mars sample return missions
4. A robotic outpost

1.2. ExoMars Mission

ExoMars is the first mission in ESA's Aurora Exploration Program [Ref. 3]. ExoMars will pursue important science and technology objectives aimed at extending Europe's capabilities in planetary exploration.

It will demonstrate flight and in-situ qualification of key exploration enabling technologies to support the European ambitions for future robotic and human exploration missions.

The main technology demonstration objectives are:

1. Entry, Descent and Landing (EDL) of a large payload on the surface of Mars.
2. Surface mobility via a Rover having several kilometers of mobility range.
3. Access to sub-surface via a Drill to acquire samples down to 2 meters.
4. Automatic sample preparation and distribution for analyses of scientific experiments.

In parallel important scientific objectives will be accomplished through a state-of-the art scientific payload. In order of priority the ExoMars scientific objectives are:

1. To search for signs of past and present life on Mars.
2. To characterize the water/geochemical environment as a function of depth in the shallow subsurface.
3. To study the surface environment and identify hazards to future human missions.
4. To investigate the planet's subsurface and deep interior to better understand the evolution and habitability of Mars.

1.2.1. Mission Overview

The mission scenario includes the use of a dedicated Ariane 5 launch (from CSG, Kourou) in 2013, of a Spacecraft Composite, consisting of the Carrier Module (CM) and the Descent Module Composite (DMC). The backup launch service solution includes the use of Proton from Baikonur in Kazakhstan. The Spacecraft Composite will be compatible with both launchers and the mission design shall be compatible also for an alternative launch in 2016.

After a cruise phase on the order of 10 months the Spacecraft Composite will enter orbit around Mars where it will stay until the Global Dust Storm season has subsided.

After the Spacecraft Composite arrives in Mars orbit, it is checked out periodically while observations of the Mars environment are made in cooperation with NASA satellites to determine if any dust storms are expected to affect the landed mission. Once the decision to land is made, the Spacecraft Composite will perform a maneuver in orbit to put the entire vehicle on a collision course with Mars.

The Descent Module Composite will be ejected a few hours before entering the atmosphere at which time the Spacecraft Composite will separate into the Carrier Module and the Descent Module Composite. The Descent Module Composite will enter the atmosphere to begin its mission of entry, descent and landing in order to deliver a Lander to the surface of Mars. The Carrier Module

follows the Descent Module Composite after some delay and burns up in the atmosphere shortly after.

The Descent Module Composite will enter the atmosphere at a pre-determined angle to match the heat shield performance capabilities in order to slow it down from the planetary approach velocity to a speed at which parachutes may deploy (albeit still at supersonic speeds) in the Martian atmosphere. Once the parachutes are deployed the protective heat shield is jettisoned. The remaining part of the Descent Module Composite then further decelerates with the parachutes until it approaches the surface.

At the right moment control rockets are fired to brake and to stabilize the Lander for the final fall to the surface just prior to separation from the parachutes. The final fall to the surface is cushioned by vented bags which are inflated to protect the lander when it impacts the surface. The vented bags will deflate on impact, thereby absorbing the energy of the final descent. Once the Lander has safely landed on the Martian surface, it will open its structural walls to expose its cargo, the high-mobility Rover, which carries the Pasteur Payload and the sub-surface Drill. Also inside the Lander is a stationary payload called the Humbolt Payload (Geophysics and Environment Instruments). It will be activated after the Rover performs its egress maneuver. The overall surface operations duration is 180 sols (6 months). Rover surface operations begin after Rover egress and checkout.

At this time the scientific portion of the mission begins consisting of a mobile exploration of the Mars surface as well as exploration of the sub-surface using a drill and automatic sampling system on-board the Rover. The Rover and the Humbolt Payload will require Radioisotope Heater Units (RHU) to provide a robust surface mission.

During the cruise phase the Spacecraft Composite operations are controlled by the ESA Deep Space antennas and the Mission Control Centre located in ESOC, Darmstadt Germany. During the surface phase of the mission, communications from the Rover Operations Control Centre (ROCC) will be routed via the ESA ground system through to the NASA Deep Space Network to a NASA Orbiter at Mars. This communications path is used for commanding and telemetry during the surface mission at Mars.

All Rover operations are planned and executed from the Rover Operations Control Centre (ROCC) located in Turin, Italy. Mission data coming from the Rover will be split into engineering data and scientific data for assessments needed by the operations teams for planning future operations and monitoring the general health

of the Rover. The Experiment data is sent to the experiment teams for detailed scientific analysis and the final data sets are archived in the ESA science operations centre, ESAC, in Madrid, Spain.

The Lander operations will be coordinated by ESA in cooperation with a Humboldt science team who will perform the planning and data analysis within the context of a Lander Operations Control Centre (LOCC). The interfaces of the Lander for communications with Earth are through the same Orbiter as for the Rover based on an agreed data sharing approach. Experiment data are provided to the Humboldt experiment teams for detailed scientific analysis and the final data sets are archived in the ESA Astronomy Centre ESAC in Madrid, Spain.

1.2.2. Flight Segment

The ExoMars Flight Segment is made of the following System Elements:

1. The Spacecraft Composite (SC), which consists of:
 - 1.1. A Carrier Module (CM).
 - 1.2. A Descent Module Composite (DMC) consisting of the Descent Module (DM) and Rover Module (RM), transported to the Mars surface inside the DM.
2. The NASA Relay Orbiter (NRO).

The Carrier Module (CM) is the element that carries the Descent Module Composite (DMC) from Earth to Mars orbit. It allows to wait in orbit for favorable conditions before releasing the DMC into the correct trajectory for its entry, descent and landing.

The CM provides the services (that is launcher vehicle interface, propulsion, guidance, navigation, attitude control, telemetry and power, etc.) necessary for the cruise and Mars orbiting phases. After releasing the DMC, the CM continues in a collision course to Mars, breaking-up and burning as it enters the Martian atmosphere. During entry it experiences very high temperatures that are assumed to be sufficient to destroy all bacterial spores it would carry. A detailed analysis has to be provided to show this. Otherwise, bioburden control on CM will apply. The

Carrier complete break-up/burn-up is actually requested by the Exomars Planetary Protection policy.

The Descent Module Composite (DMC) is the element of the mission that performs the ballistic entry, descent and landing onto the Martian surface.

The DMC is a blunt-shape entry capsule mounted on the upper side of the Carrier Module. To achieve a safe entry, descent and landing onto the Martian surface, its design includes a heatshield, parachute system, descent thrusters, reaction control system and the Lander.

The Lander features the vented airbags and the required support and egress system in order to allow the egress of the Rover and the deployment of the GEP instruments.

The Composite (Carrier + DMC) is launched on Ariane 5 (backup Proton-M) and injected into the transfer trajectory to Mars directly by the upper stage of the launch vehicle. In such a way the SC does not need to use its own propulsion system for these highly propellant demanding maneuvers. Mid way on its cruise to Mars the Composite performs propulsive maneuvers (called deep Space Maneuvers) to correct the trajectory. On arrival at Mars the Composite activates its propulsion system to insert itself into an elliptic orbit around the Red Planet.

As the arrival coincides with the onset of the Global Dust Storm the Composite waits on that orbit until May 2015, right after the foreseen Earth-Mars superior conjunction, during which communications are not allowed by the presence of the Sun between the two planets.

Close to the periapsis of its orbit the Composite decelerates by means of the propulsion system and enters a collision-trajectory with the planet. Approximately 2 hours before reaching the altitude of 120 Km over the Mars surface (conventionally the Entry Interface Point), the Composite separates the DMC from the Carrier.

The linear separation rate is such that after separation the two Modules are actually flying on two different trajectories departing one from the other and pointing towards the Mars surface.

The Carrier is burned out and destroyed by the friction and the thermal loads during atmospheric entry. The DMC continues its flight to safely enter the Mars atmosphere with a flight path angle of 12° (TBC).

Once on the surface, the DMC deploys the Lander, which accommodates the Rover Module (RM) and the Geophysical and Environmental Payload (GEP) instruments.

The DMC includes the following Payload elements:

1. The Pasteur Payload (PPL), accommodated on the Rover Module
2. The Humboldt Payload (HPL), accommodated on the DM Lander

Both the PPL and the HPL are developed by Science Teams and provided by the national agencies in accordance with the corresponding Interface Requirements Document/Interface Control Documents issued by TAS-I in agreement with ESA and the Instrument Teams.

1.3. Radar Doppler / Altimeter

While the airbag-assisted landing concept reaches its limit as the payload becomes heavier and complex, it was necessary to study in detail the Landing Guidance and Navigation Control (GNC) based on a final powered phase for a safe landing approach. Such a controlled landing in a region of high scientific interest (and consequently possibly with relief) requires to have a GNC that guarantee accurate safe landing.

Past Mars landing missions have been accomplished through the use of robust landing systems, including the use of landing gear on the Viking I & II landers, or airbags on the Pathfinder and twin Spirit & Opportunity Exploration rovers. Future missions, however, are likely to employ less robust landing systems, as they allow the delivery of more massive scientific payloads for long term roving and sample returns.

Less robust, safe, accurate landing in difficult planetary terrain, including areas that are rocky, heavily sloped, or both, requires remote sensing of the surface in order to choose an appropriate approach to the ground. This requirements lead to improved capabilities in the sensing of navigation data, including altitude and three dimensional velocities in real time along the final descent.

While active or passive optical sensors might seem appropriate for this application, an alternate approach based on a millimeter-wave electrically scanned phased array radar is developed.

The measures are submitted to a couple of redundant Radar Doppler / Altimeters (RDA). They are lodged on the trust of the Descent Module (DM) and they are used during the final descent phase to support the DM landing GNC.

Radar Doppler / Altimeter offers several advantages over present optical sensors due to its ability to:

1. Operate at larger range of altitudes
2. Detect coherent measurement of the platform velocity in real time
3. Operate at any time of day
4. Operate with any weather
5. Operate through dust and engine plumes with a substantial reduction susceptibility

2. REQUIREMENTS

Preliminary Radar Doppler / Altimeter (RDA) definition is possible when mission overview and requirements are established.

In the following Chapter the requirements, related to the functions to be implemented by the RDA, will be reported.

Typically on Landers, two or more RDA unit are installed for redundancy motives, this choice ensures a single or more failure tolerant unit, meaning that any internal failure shall not preclude the correct provision of required measurement set. So, the requirements are intended applicable to single equipment. For ExoMars Lander, the current system design foresees the accommodation of 2 separate units which shall work at the same time.

2.1. Operational Scenario

Although in preliminary way, for a typical Mars descent, it is possible establish an operational scenario from which to elaborate preliminary RDA system definition.

The following Figure 2-1 illustrates the typical sequence of EDL events for the nominal trajectory at high altitude.

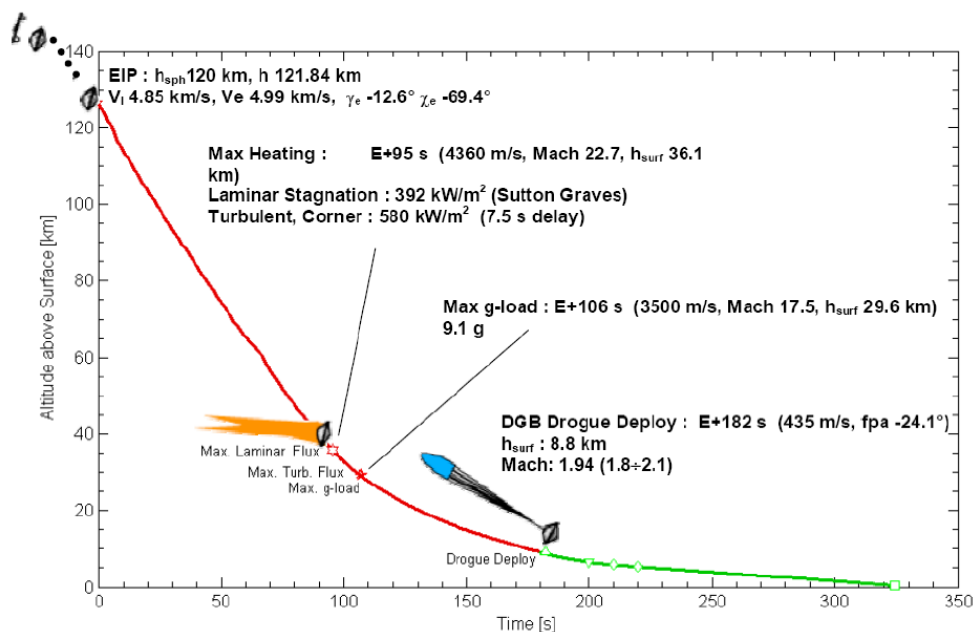


Figure 2-1 – EDL events for GNC (from EIP to first parachute opening). Radar Doppler/Altimeter is not operating.

Since Mars has an atmosphere, first entry phase is characterized by aerodynamic brake due to the shock wave generated by the stumpy body of Lander configuration around 35 km of altitude.

A second phase is characterized by aerodynamic brake due to the hypersonic parachutes around 9 km.

The following Figure 2-2 illustrates instead the typical sequence of EDL events for the nominal trajectory at low altitude.

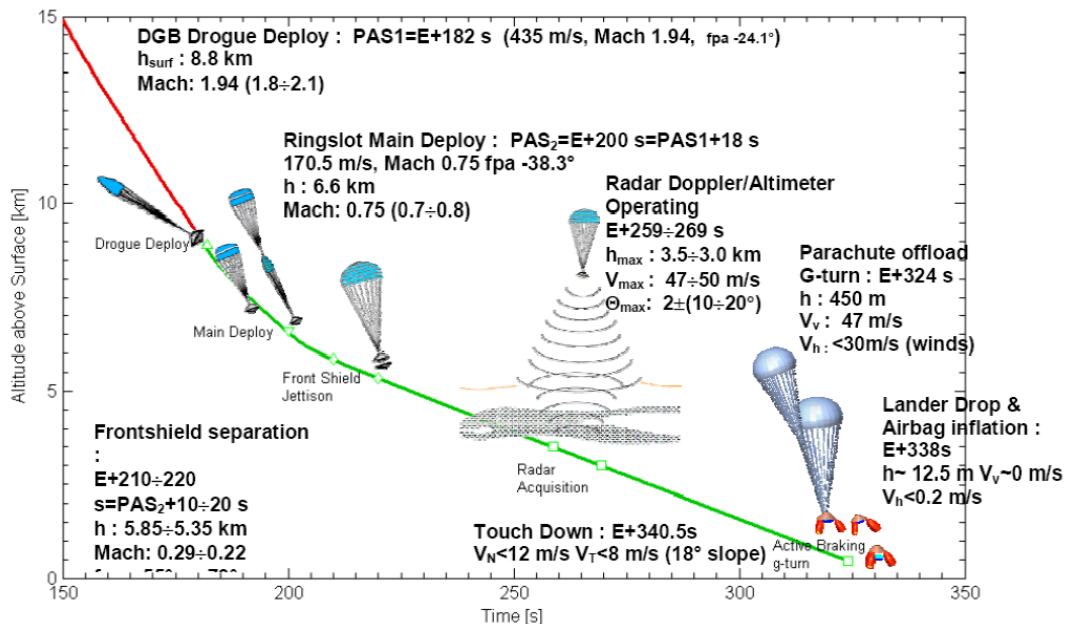


Figure 2-2 – EDL events for GNC (from first parachute opening to final landing). Radar Doppler/Altimeter becomes functional after Front Shield Jettison.

After the separation of the first set of parachutes, a third phase is characterized by aerodynamic brake due to a second set of subsonic parachutes around 6 km.

At an altitude of around 5 km, there is a front shield jettisoning, so RDA can work from an altitude of around 3 km.

At an altitude of around 450 m, the second set of subsonic parachutes goes in off-load G-turn, so there is a parachutes separation and final brake is due to retro rockets.

At an altitude of around 10 m, a few seconds before touchdown, with null vertical and horizontal velocity, there is a vented bags inflection and the end of RDA mission.

From around 10 m to touchdown there is a free fall of the descent module with constant acceleration equal to 3.69 m/s^2 .

Touchdown velocity can be evaluated considering the reference frame:

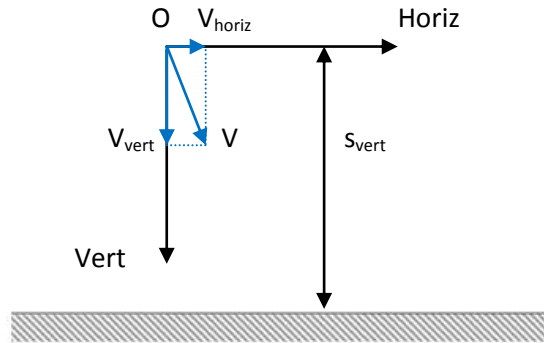


Figure 2-3 – Free Fall Reference Frame before Touchdown

So, the equations for free fall motion are:

$$\begin{cases} s_{vert} = \frac{1}{2} a_{0,vert} t^2 + V_{0,vert} t + s_{0,vert} \\ s_{horiz} = \frac{1}{2} a_{0,horiz} t^2 + V_{0,horiz} t + s_{0,horiz} \end{cases} \quad (2-1)$$

where s_{vert} , s_{horiz} are vertical and horizontal spatial motion respectively

$a_{0,vert}$, $a_{0,horiz}$ are vertical and horizontal initial acceleration

$V_{0,vert}$, $V_{0,horiz}$ are vertical and horizontal initial velocity

$s_{0,vert}$, $s_{0,horiz}$ are vertical and horizontal initial position respect to the Mars surface

t is the time

In this case, it is had:

$$a_{0,vert} = 3.69 \text{ m/s}^2 \quad , \quad a_{0,horiz} = 0 \text{ m/s}^2 \quad , \quad V_{0,vert} = 0 \text{ m/s} \quad , \quad V_{0,horiz} = 0 \text{ m/s}$$

$$s_{0,vert} = 0 \text{ m} \quad , \quad s_{0,horiz} = 0 \text{ m}$$

So, the equations for velocity can be written as:

$$\begin{cases} V_{vert}^2 = 2 a_{0,vert} s_{vert} \\ V_{horiz}^2 = 2 a_{0,horiz} s_{horiz} \end{cases} \quad (2-2)$$

That for a vertical free fall of about 10 m ($s_{vert} = 10 \text{ m}$, $s_{horiz} = 0 \text{ m}$) , they give:

$$\begin{cases} V_{vert} = \sqrt{2 \cdot 3.69 \cdot 10} = 8.59 \text{ m/s} \\ V_{horiz} = \sqrt{2 \cdot 0 \cdot 0} = 0 \text{ m/s} \end{cases} \quad (2-3)$$

Note: Numbers reported in figures are only indicative and the figures should be understood as typical Mars EDL only.

It is worth noting that altitude is intended as the distance to Martian surface along local vertical passing through DM Center of Mass and all the values reported in this Paragraph are intended to be in DM Body Reference Frame, indicated in Figure 2-4.

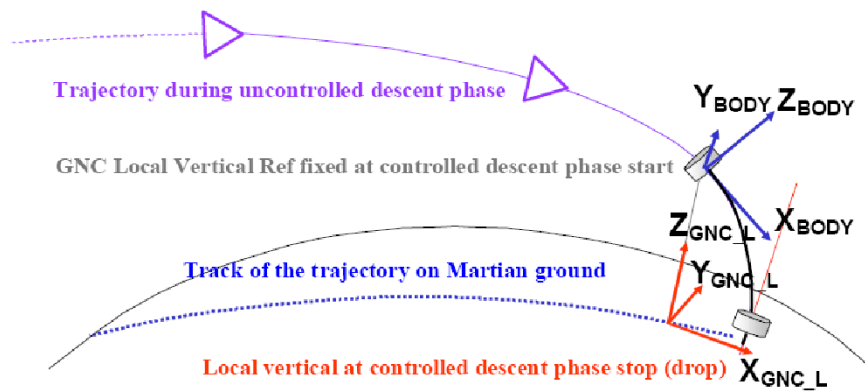


Figure 2-4 – Body and Ground Reference Frame for Descent phase

In the following Figure 2-5, detailed Body Reference Frame (BRF) is shown.

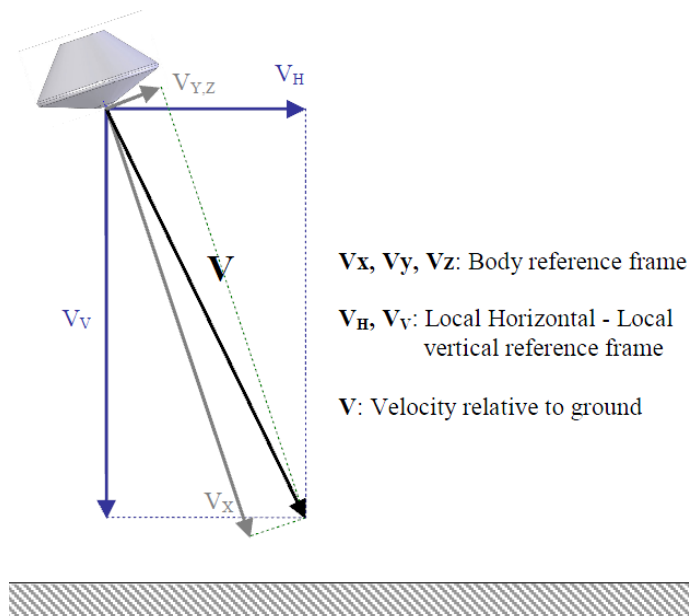


Figure 2-5 - Velocity components in defined Reference Frames for Descent phase

So, on the basis of the above reported sequence, the following table summarizes the baseline operational scenario used for preliminary RDA system definition. As a whole, they represent the mission baseline that is proposed for the preliminary RDA system definition. These satisfy typical descent needs on Mars.

Requirement	Comment	Value(s)
Unambiguous measurements interval for altitude		$H_{unamb} = 3000 \div 10 \text{ m}$
Unambiguous measurements interval for off-nadir angle	Generic beam off of nadir	$\theta_{unamb} = \pm 55^\circ$
Unambiguous measurements interval for velocity	$V_{xb,unamb}$, $V_{yb,unamb}$, $V_{zb,unamb}$ are intended as velocity components calculated in body reference frame defined in Figure 2-5	$V_{xb,unamb} = 0 \div 160 \text{ m/s}$ $V_{yb,unamb} = \pm 45 \text{ m/s}$ $V_{zb,unamb} = \pm 45 \text{ m/s}$
Typical velocity profile	<p>Velocity profile data are available from many planetary landing missions. The profile reported in Figure 2-6 is derived from linear interpolation of the following set of cardinal values:</p> <p>(H = 3000 m, V = 172 m/s)</p> <p>(H = 2000 m, V = 90 m/s)</p> <p>(H = 450 m, V = 55 m/s)</p> <p>(H = 12 m, V = 0.2 m/s)</p> <p>(H = 0 m, V = 0 m/s)</p>	<p>Figure 2-6 - Assumption for Mars surface backscattering</p>

Requirement	Comment	Value(s)
Accurate measurements interval for altitude		$H_{acc} = 2000 \div 10 \text{ m}$
Off-nadir angle	Spacecraft X_b -axis (body reference frame) off of nadir	$\theta_{X_axis} = \pm 35^\circ$
Velocity	V_{xb}, V_{yb}, V_{zb} are intended as velocity components calculated in body reference frame defined in Figure 2-5	$V_{xb} = 0 \div 64 \text{ m/s}$ $V_{yb} = \pm 45 \text{ m/s}$ $V_{zb} = \pm 45 \text{ m/s}$
Attitude changing rate		$\dot{\theta} = \pm 60^\circ/\text{s}$
Acceleration	a_{xb}, a_{yb}, a_{zb} are intended as acceleration components calculated in body reference frame defined in Figure 2-5	$a_{xb} = \pm 2.65 \text{ m/s}^2$ $a_{yb} = \pm 9.3 \text{ m/s}^2$ $a_{zb} = \pm 9.3 \text{ m/s}^2$
Jerk	J_{xb}, J_{yb}, J_{zb} are intended as Jerk components calculated in body reference frame defined in Figure 2-5	$J_{xb} = \pm 26.5 \text{ m/s}^3$ $J_{yb} = \pm 93 \text{ m/s}^3$ $J_{zb} = \pm 93 \text{ m/s}^3$
Slope	Root Mean Square value measured on a 100 m horizontal baseline	$s = 10^\circ$
Measurements Update Frequency		$f_{update} = 20 \text{ Hz}$

Table 2-1 – Operational Scenario

2.2. Performance Requirements

The required performance for the RDA equipment is specified in terms of RMS measurement errors for both altitude and velocity components estimation. The specified values of accuracy have to be achieved within the specific range of altitude as reported in Table 2-1.

The RDA performance must be always referred to Body Reference Frame (BRF).

The following table summarizes the baseline requirements used for preliminary RDA system definition. As a whole, they represent the requirements baseline that is proposed for the preliminary RDA system definition.

Requirement	Comment	Value(s)
Altitude measurement error	Root Mean Square value (1- σ)	$\delta H = 0.33\%$ of H \pm 0.8 m (scale factor + noise)
Velocity measurement error	Root Mean Square value (1- σ)	$\delta V_{xb} = 0.6\%$ of $V_{total} + 0.1$ m/s (scale factor + noise) $\delta V_{yb} = 0.6\%$ of $V_{total} + 0.1$ m/s (scale factor + noise) $\delta V_{zb} = 0.6\%$ of $V_{total} + 0.1$ m/s (scale factor + noise) $V_{total} = (V_{xb}^2 + V_{yb}^2 + V_{zb}^2)^{0.5}$

Table 2-2 – Performance Requirements

3. TECHNICAL SOLUTIONS

This Chapter is intended to provide general description of how the reported requirements (see [Chapter 2](#)) shall be duly taken into account during the development of the preliminary RDA system definition.

The proposed Chapter will be completed with problem areas, solutions and trade-offs analysis.

For ExoMars Lander, the considered equipment consists of two separate Radar Doppler / Altimeter (RDA) units in charge of supporting the Guidance, Navigation & Control (GNC) component of the Descent Module (DM) during the descent and landing phases.

The preliminary definition of the Radar Doppler Altimeter (RDA) is aimed at fully satisfying the requirements via a coherent and structured approach.

The RDA equipment is conceived to support the Descent Module GNC, which is in charge of (i) triggering autonomously the precise instants for every event related to the EDL phases, and (ii) during the landing, reduce the vertical and horizontal velocity components to the level compatible with a landing based on the vented bags technology.

In fact, the descent step for ExoMars DM, after the conclusion of the entry step, is based on the fact that the fall of the DM is slowed down by parachutes and finally controlled with the use of thrusters.

The necessity of extracting altitude and velocity information in support to GNC operations leads to RDA requirements for (i) high degree of accuracy of any measurement and (ii) real time response. This is made further challenging by the expected behavior of the DM during the descent phase in terms of changing attitude, acceleration and jerk.

As shown in Figure 2-2, RDA starts to operate at altitude of 3500-3000 meters, immediately later heat shield ejection. After this event, parachute brakes lander until its offload G-turn around an altitude of 450 meters. Therefore retrorockets burn so vertical velocity goes to zero under the sensing of Radar Doppler / Altimeter.

3.1. Historical Background

The European Space Agency (ESA) has supported for many years the development of Landing GNC technologies with potential applications to landing missions to the Moon, to Mercury and to Mars.

Within the frame of the Aurora Program, planetary landing is one of the most ambitious challenges. The requirement of “precision landing” is relatively new and it is foreseeable that it will be applied consistently to future landing missions of the planetary exploration program. Precision planetary landing is very attractive from a scientific point of view, as it allows performing in-situ experiments on a pre-determined exact location, enable sample return and eventually pave the way for human missions.

Soft landing considers an actively piloted landing that ensures safe and soft conditions at the contact with the planetary surface. The recent Mars exploration missions have highlighted the importance of having on-board the capacity to measure and compensate, partially or in totality the residual velocity of the lander in its final phases of descent because of the increasing mass of its payload. This prevent the utilization of the airbag landing concepts, that safely landed NASA's Mars Pathfinder and Mars Exploration Rovers, therefore for future Martian missions with more heavy payloads, a powered phase appears as the most promising solution in order to cancel the residual velocity following the descent and breaking phase under parachute, and to guarantee the kinematics conditions for a safe landing. This means that the baseline scenario for the ExoMars and Mars Sample Return Mission from ESA's Aurora Program will include such a powered descent, which will call for the design of the Guidance Navigation and Control (GNC) system for this active phase.

The on-going predefinition of the European missions to Mars, ExoMars and Mars Sample Return calls for the identification of the critical technologies and the preparation of European solutions for soft landing. Therefore, systems and technological solutions for safe planetary landing have been largely investigated.

First studies are conducted since earliest missions to the Moon and in the last two decades the research was fostered by planned and on-going missions to Mars, which all include the deployment and the operation of several instruments on the planet surface for ground-based information retrieval. This implies the design and

development of ad hoc solutions for the Entry, Descent and accurate Landing (EDL) process, including the Guidance, Navigation & Control (GNC) sub-system.

Among the required components, the GNC sub-system has to rely on ad hoc equipment for Altitude and Velocity Measurement (AVM), which plays a key role in the guidance of the module down to zero-meter level. The necessity of accurate guidance of the Composite Descent Module, accurate control of the descent onto Mars and timely triggering the subsequent events (parachute, airbags, etc) poses serious needs on the availability of the information on vertical and horizontal velocity (including acceleration) and altitude. These measurements should be provided by the AVM component at high refresh rate, with minimum latency, and in an accurate and verified manner.

Planetary landing is theoretically supported by a number of terminal descent sensors: radar, lidar, mechanical sensors, and gamma ray altimetry. In recent years, all these sensors have been investigated in order to understand their capability in meeting the requirements for planetary landing, which would reduce the inherent risks associated with a landing mission and at the same time allow soft and precision landing, fundamental for proper scientific return.

The various used sensors are:

Mechanical sensors: (or contact sensors) have heritage from the Gemini and Apollo capsule landing studies and related experimentation. Even though tests were successful, they do not provide the required position and velocity profile.

Radioactive sensors: The use of reflected radioactive particles off the surface is a technology used currently by the Russian space agency on the Soyuz vehicle. The on-board altimeter – Kaktus – contains a radioactive source that is used to determine the vehicle's distance above the ground, while velocity is deduced via integration of range measurements.

Lidar sensor: The Navigation for Planetary Approach and Landing (NPAL) study, an ESA TRP initiated in 2001, gives the foundation for a generic development and demonstration test bench for soft landing capacity, and develops a vision-based navigation solution. The NPAL navigation generalizes the DIMES system of the MER landers. An elegant breadboard demonstrates the concept at both architecture and performance levels. The NPAL test bench offers generic features for modelling and validating the complete GNC loop of a planetary lander, including a versatile adaptive guidance scheme compatible with hazard avoidance capacity, soft 6 DoF

robust control, and a virtual terrain emulation. LiGNC is a technological study part of ESA's AURORA Program, which evaluates the interest of Lidar technology for supporting soft landing. The LiGNC study builds a complete GNC solution making the most out of the LIDAR capacity. A specification of the LIDAR sensor permits to assess the challenges at both technology and space-qualification levels. LiGNC shares and extend the NPAL test bench to validate the performance of the Lidar sensor in a realistic environment. EADS Astrium SAS has led most studies from the Lunar Landing (LULA) study in the mid 90's to the recent studies NPAL (Navigation for Planetary Approach and Landing), focused on Vision-based Navigation, and LiGNC (LIDAR-Based GN&C for Automatic Rendezvous and Safe Landing).

Radar sensors: Radar techniques have been successfully used on all the Mars Landers and among them the Frequency Modulated Continuous Wave (FM-CW) and the Pulsed Doppler Radar configurations offer a high enough level of technology readiness for inclusion in the ExoMars mission. Past Lunar and Martian landing missions have actively sensed the landing surface during the terminal descent phase, but have uniformly done so with respect to obtaining altitude and/or velocity information. Nearly all recent missions, including the Mars Viking Mission, Mars Pathfinder, Mars Polar Lander and the twin Mars Exploration Rover made use of radar altimetry; Viking and Mars Polar Lander were further distinguished by the use of radar for sensing of the landing module velocity vector. The Mars Science Laboratory (MSL) mission, planned for fall 2009, led to further analyses concerning the optimal radar design in order to achieve the required AVM performance. Results reported in literature lead to the selection of radar configurations with high RF carriers (35-94 GHz), large signal bandwidth (1 GHz) and correspondingly very short pulses (down to 1 ns), being these latter parameters varied as a function of height. The proposed configurations represent a challenge for current technologies and real-time space-based digital processing, since they represent the evolution of currently operational space-borne pulsed radar payloads (e.g. space altimeters). Going back to the Lunar Landing expertise, different radar concepts were used in 60-70ies. Specifically, the issue for accurate velocity and altitude measurement in a wide operational envelope was solved by the adoption of enhanced FM-CW techniques. Specifically, Bessel Sideband FM-CW solution was implemented in order to guarantee performance at lower altitudes, while Interrupted Continuous Wave (ICW) was selected for higher altitudes. This dual-mode option closely resembles the design approach for airborne radar equipment.

After having described the various sensors, it is worth noting that typical landing accuracy of the order of 50 km are achievable with classical inertial and radar altimeter based GNC. This level of performance imposes constraints on the type of landing area selected, restricting the choice to roughly flat zones, in general less interesting from a scientific point of view. With more advanced GNC techniques, such as new lidar and radar sensors, the goal of reaching a landing accuracy of tens of meters is possible, opening the doors to unprecedented possibilities of landing in areas of high scientific interest.

The ExoMars mission includes a Descent Module (DM) that will face soft and precision landing within the EDL process. In this perspective, the Radar Doppler Altimeter has been selected for supporting the GNC of the Descent Module, as the suitable, available technology for meeting the system requirements. In fact, even if lidar technologies have a low mass and volume when compared to microwave components, the technology readiness level clearly favors radar solutions. In addition, the effect of the local Martian environment (dust) on lidar technologies could be significant enough at low altitudes.

3.2. Radar Solutions for AVM

The known radar devices for AVM in planetary landing applications are historically derived from:

1. operational space-borne payloads for planetary observation
2. airborne instruments for navigation support

Specifically, in the airborne scenario, a number of instruments are currently operated for the accurate, confident retrieval of the platform altitude and velocity. These estimates allow safer take-off and landing operations in adverse weather conditions and low visibility. The re-use of such operational devices in the space scenario has been often proposed and investigated, even though the more stringent requirements in planetary landing have revealed limits and drawbacks of such techniques. The engineering process for turning available airborne solutions into space equipment can be considered as a viable approach if specific drawbacks are overcome.

On the other hand, space-borne altimeters for range estimation have flown on a number of platforms and exhibited accurate performance in distance estimation. A number of examples are available and offer the chance of exploiting such heritage in designing a dedicated space-borne Doppler Altimeter. Current devices are unavoidably limited in velocity retrieval, but they are expected to evolve into fully integrated altimeter / velocimeters. The migration to higher transmitting frequencies ($f > 30$ GHz) and the availability of a number of off-nadir observation beams are key radar design features to achieve the desired AVM performance, if coupled with the required technological innovation in short pulses synthesis and nanosecond controlled devices.

Analyses have been carried out about the two-mentioned approaches. Standing the following considerations, the second approach is favored:

1. Inner limits of the airborne-derived radar techniques can be overcome only at the expense of a dramatic increase in system complexity both at RF and digital level.
2. Airborne navigation radar techniques rely on analogic components, which are hardly reproducible in a space scenario.
3. The technology readiness of RF and digital components for the space-derived systems has increased rapidly and the achievement of the required performance is at hand.

This turns into the trade-off performed between Frequency Modulated Continuous Wave (FM-CW) radar and Pulsed Continuous Wave (Pulsed CW) radar solutions.

3.2.1. Frequency Modulated Continuous Wave Radar

The type of radar that employs a time-continuous transmission, either modulated or un-modulated, has had wide applications since the 40ies [Ref. 4]. One of the earliest applications is the FM-CW (Frequency-Modulated Continuous Wave) altimeter: the first practical model was developed by the Western Electric Company in 1938, although the principle of altitude determination using radio-wave reflections was known ten years earlier, in 1928.

The CW radar exhibits great capabilities in sensing the target Doppler frequency, since the transmitted wave impinges on the target continually and is reflected towards the receive antenna. The reflected sinusoidal wave will be shifted in frequency from the transmitted frequency f_0 by an amount $\pm f_d$ which is proportional to the radial velocity v_r of the target relative to the radar. The received echo signal is heterodyned in the detector with a portion of the transmitter signal f_0 to produce a Doppler beat note of frequency f_d . This can be easily processed in order to extract the target radial velocity. One of the greatest shortcomings of the simple CW radar is its inability to obtain a measurement of range. This limitation can be overcome by modulating the CW carrier, as in the frequency-modulated continuous wave radar (FM-CW). The spectrum of a CW transmission can be broadened by the application of modulation, either in amplitude, frequency, or phase. A widely used technique for range measuring is to frequency-modulate the carrier in CW radars: the two-way travelling time (from the transmitting antenna to the target and then back to the receive antenna) is proportional to the difference in frequency between the echo signal and the transmitter signal. The greater the transmitter frequency deviation in a given time interval, the more accurate the measurement of the transit time and the greater will be the transmitted signal spectrum.

In the FM-CW radar the transmitter frequency is changed as a function of time in a known manner. If it is linearly varied within a given time interval (the "sweep" time), and if there is a reflecting object at distance R , an echo signal will exhibit a delay of $2R/c$ (where c is the speed of light). If the echo signal is combined with a portion of the transmitter signal, a beat note f_b is produced: the beat note (i.e., the difference frequency) is a measure of the target range, if there is no Doppler frequency shift. In most FM-CW radars periodicity of the modulation is implemented and triangular or saw-tooth frequency-modulation waveforms are used. In this case, the Doppler frequency shift – in case of moving targets – can be recovered. On one portion of the frequency modulation cycle the beat frequency is increased by the Doppler shift, while on the other portion, it is decreased.

If the FM-CW radar is used for single targets only, such as in the radio altimeter, it is not necessary to employ a linear modulation waveform. This is certainly advantageous since a sinusoidal or almost sinusoidal frequency modulation is easier to be obtained. The average beat frequency measured over a modulation cycle yields the correct value of target range. This leads to FM-CW solutions with sinusoidal modulation, which are widely used for airborne altimeters and early space instruments.

Similarly, the velocity measurement is carried out via estimation of the displacement of the signal sideband with reference to the expected ($f_d=0$) centroid in Doppler, which is given by the system intermediate frequency and the modulation frequency. Velocity along each beam is thus estimated via a Doppler centroid search technique. It is to be stressed that the estimation of the velocity can be compared to the problem for mean Doppler estimation in noisy background with spectrum width and amplitude. A number of approaches are available in literature and made operational in Weather Doppler radars and Synthetic Aperture Radars, herein exhibiting adequate performance.

3.2.2. Pulsed Continuous Wave Radar

The other solution for AVM measurement is the pulsed radar, which originates from the design approach used for space-borne altimeters. The main objective of such a system is to measure the distance between the radar and the surface: the most common application is determination of the local sea level relative to the Earth's geoid. The achieved accuracies are in the order of few centimeters, since changes on the order of centimeters in the mean surface height may correspond to substantial differences in the corresponding geophysical parameters. It is evident that range measurement accuracy and precision are the driving requirements for these radars.

The accuracy of an altimeter's height measurement depends on a number of parameters, including the Signal to Noise Ratio of the terrain backscattered echo and the implemented correction of the propagation delay suffered by the radar's round trip waveform. The precision is proportional to the radar's range resolution and inversely proportional to the square root of the number of statistically independent measurements (looks) combined for each data point. In general, SNR values are large and consequently bandwidth and looks become the driving requirements on system design.

The used pulsed waveforms allow accurate ranging for each transmitted signal by means of round-trip time delay measurement. This measurement can be performed within each PRI (Pulse Repetition Interval) and then averaged over multiple intervals (looks) in order to mitigate noise influence. Specifically, an optimal solution for altitude measurement is implemented in pulsed radar altimeters, which extract the echo wave delay by identifying the leading edge of the returned echo. This can be detected in correspondence of the time instant in which

the echo signal exceeds an adequate amplitude threshold. A number of well known techniques are currently operated in space-borne altimeter systems.

It is to be stressed that at the accuracy required for such space-borne instruments, the deceptively simple proportionality of range to delay-time must take into account the small but significant retardation of the radar microwaves as they propagate (both in the atmosphere and in the radar). The recorded precision of Earth Observation altimeters is provided in [Ref. 4], and it can be summarized as follows: GEOS-3 greater than 100 cm; Seasat around 100 cm; Geosat below 10 cm; ERS-1 below 10 cm; ERS-2 below 10 cm; TOPEX and JASON-1 around 2-3 centimeters. Small precision values can therefore be obtained. On the other hand, centimeter-scale range accuracy achievement is supported by averaging over the range response of many returns. In oceanographic applications, sea surface height is derived from the mid-point of the waveform's leading edge rise, after accumulating and averaging waveforms on a pulse-to-pulse basis. The following figure illustrates the concept (extracted from [Ref. 4]).

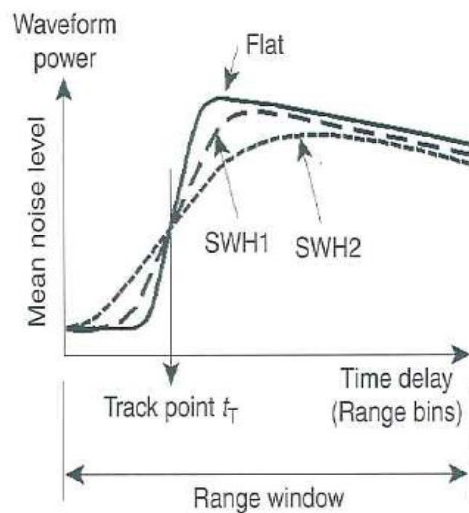


Figure 3-1 - Range Estimation Concept in space-borne altimeters from [Ref 4]

It is also to be stressed that for pulsed radars, the illumination geometry depends on the mutual relationship of pulse width and antenna beam width for the considered operational conditions. Considering a quasi-flat surface, the impinging radar pulse identifies on the surface annular circles whose spatial “thickness” corresponds to the projection of the pulse spatial duration. Each circle corresponds to a resolution cell contributing simultaneously and coherently the instantaneous

amplitude of the received echo. As time passes, the pulse impinges the surface and “activates” sequentially the annular rings reported in Figure 3-2.

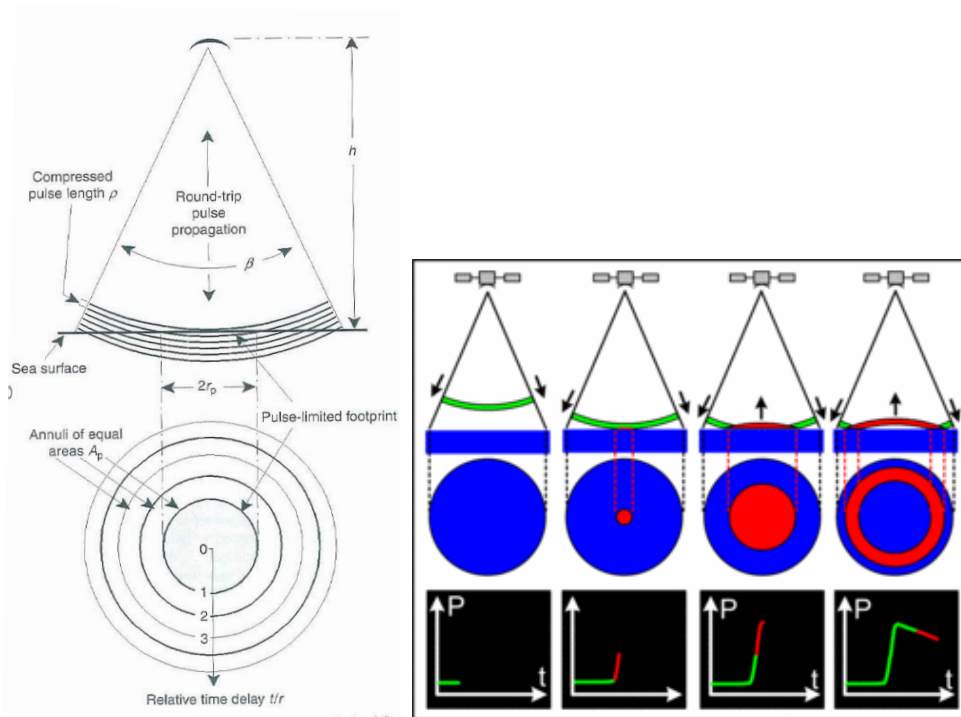


Figure 3-2 – Pulsed limited configuration for illuminating the surface (from [Ref. 4] and www.avisio.oceanobs.com)

This process determines the envelope of the received echo (including shape and instantaneous amplitude). In case of off-nadir beam pointing, the principle is identical with the exception of the shape of the project resolution cell, which becomes a circular sector. This illumination configuration is named “pulse-limited”.

It might happen that the pulse width in space exceeds the area illuminated by the antenna instantaneously, i.e., the surface intercepted by the 3dB antenna beam. This means that the echo instantaneous amplitude of the received echo will be mainly dictated by the latter terrain area, whose dimensions are dictated in this case by the antenna design. This illumination configuration is named “beam-limited”.

The shape of the received echo largely varies from pulse-limited to beam-limited configuration. Figure 3-3 reports sample echo signals for qualitatively illustrating the concept. In pulse limited conditions, it is known that the echo of the quasi-flat surface can be described by the Brown Model, whose typical shape is

reported in Figure 3-3. In oceanographic observations, the slope of the rising edge and the amplitude of the echo depend respectively on the wave height and the wind velocity.

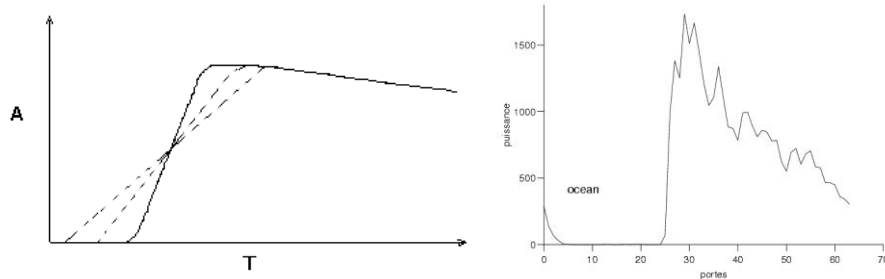


Figure 3-3 Echo signals in pulse-limited and beam-limited conditions (from [Ref. 4] and www.aviso.oceanobs.com)

On the other hand, platform velocity estimation can be efficiently performed by observing the returned echo over a sufficient time interval. The echo phase evolution from pulse to pulse is a direct indicator of the signal-superimposed Doppler frequencies, and basic frequency analysis (e.g., Fourier Transform or time correlation based techniques) is capable of extracting this information with a given precision and accuracy.

As radar signal bandwidth is concerned, pulsed radar configurations might be characterized by pulse modulation techniques, which allow pulse compression on receive and consequently enhanced spatial resolution. Chirp modulation of the transmitted pulse is the widely used technique for achieving best trade-off between transmitted energy and spatial resolution. Un-modulated techniques (namely, pulsed CW radars) are used in short range applications when power budget is not an issue.

3.3. Critical Requirements

The requirements, reported in [Chapter 2](#), drive the RDA system definition. The preliminary analysis of the requirements highlighted the criticality of a number of aspects that are to be carefully considered in the system design phase. The following sub-paragraphs address the key critical issues identified in the analysis. Special attention is paid to the aspects that introduce high risks, potential cost increase and schedule impact. In order to mitigate the influence of such factors, the

use of already developed and qualified hardware or technologies, and heritage from past experiences is maximized.

3.3.1. Altitude Measurement

The requirements identify the altitude to be measured as the distance from the surface along the local vertical passing through the centre of mass of the Descent Module. The estimation of such value requires the knowledge of the platform attitude with high precision in order to eliminate the effects of the squinted line-of-sight. The transformation of slant range distances along squinted beams into vertical altitude implies the knowledge of the instantaneous pitch, yaw and roll angles.

Figure 3-4 shows the pointing misalignment due to attitude angles.

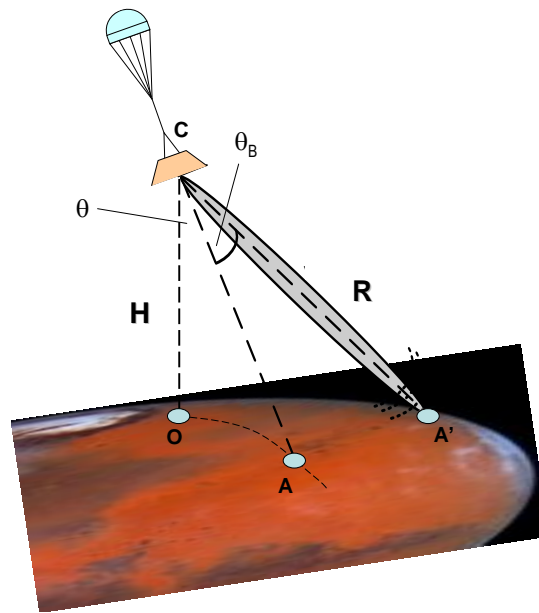


Figure 3-4 – Range Measurement for RDA operations

It is evident that the received signal allows estimating the slant range R , i.e., the distance CA' . The distance CO , i.e. the altitude of the platform, can be deduced only if the attitude angles are known, and specifically the off-nadir angle corresponding to the arc OA' .

These values can be extracted from the Inertial Measurement Unit (IMU) instrument, but no data exchange between RDA and IMU is foreseen. On the other hand, the estimation of the attitude angles directly from RDA measurements is feasible even though it largely increases the complexity of the measurements and requires numerical inversion of a 4-degree system of equations in 4 unknowns. This is judged out of scope of the RDA equipment and might interfere with the GNC module, which is specifically devoted to perform inversion and parameter tracking functions. In this perspective, the ranging functionality of the RDA equipment is intended as the capability of extracting slant range distances, which will be passed to the GNC component.

3.3.2. Altitude Measurement near Touchdown

Ranging functionalities near the touchdown can be achieved by means of proper radar waveforms. While pulsed radars always exhibit a blind range gap in the proximity of the system – due to the overlapping of the echo with the transmitted pulse trailing edge – continuous wave radars overcome this drawback by simultaneously activating TX and RX paths.

As discussed in the [Paragraph 2.1](#), the operational scenario for the RDA equipment extends down to 10 meters altitude. It corresponds to the zero-velocity altitude and initiates the Lander drop and vented bags inflation event. This event is reasonably expected to terminate the use of the RDA outputs. This implies that RDA equipment must be able to measure a minimum range of 10 meters.

3.4. Selected Radar Configuration

In [Paragraph 3.2](#), FM-CW and Pulsed CW radars have been introduced, now only one solution will be analyzed.

There are three considerations that lead to the selection of the Pulsed CW radar for the guidance of a Mars Lander:

1. Monostatic configuration is easily to implement, so it is possible reduce RDA mass and space covered on board of the lander.
2. The digital processing chain for the Pulsed CW radar is much less complex than the FM-CW radar; as an example, the latter necessarily relies on the Doppler frequency estimation via DFT, while the former can easily operate in the time domain for estimating the frequency (see [Chapter 4](#)).
3. There are large benefits from heritage on past space payloads design and development, which specifically focused on pulsed radar systems for a number of operational applications (SAR, altimetry, scatterometry, etc).

The selected RDA encompasses a pulsed CW radar configuration, which is based on the transmission of a narrow un-modulated pulse and the reception of the corresponding echo scattered from the terrain. As explained above, the temporal characteristics of the received echo (time delay and shape) are exploited in order to retrieve slant range distance, while the complex correlation of subsequent echoes – generated from successive pulses – is used in order to infer Doppler component. Mathematical relationships allow transforming these measurements into platform altitude and velocity vector.

So, RDA implements the altimeter function to measure range distance, not altitude, and doppler function to measure velocity in the BRF, as specified in the requirements. Because of the estimate of the DM speed is required over the three body reference axes, at least three independent measurements of Doppler components are required. These values will then be combined in order to retrieve the projections of the velocity vectors onto the selected axes, so at least three beams will be used to perform all measurements. When RDA works as altimeter, it can use the three beams to obtain range measurement, when RDA works as velocimeters, it can use the three beams to obtain three radial components of velocity and then velocity in body reference axes.

However, as shown in Figure 3-5, selected beams configuration have four beams to reduce altitude measurement error.

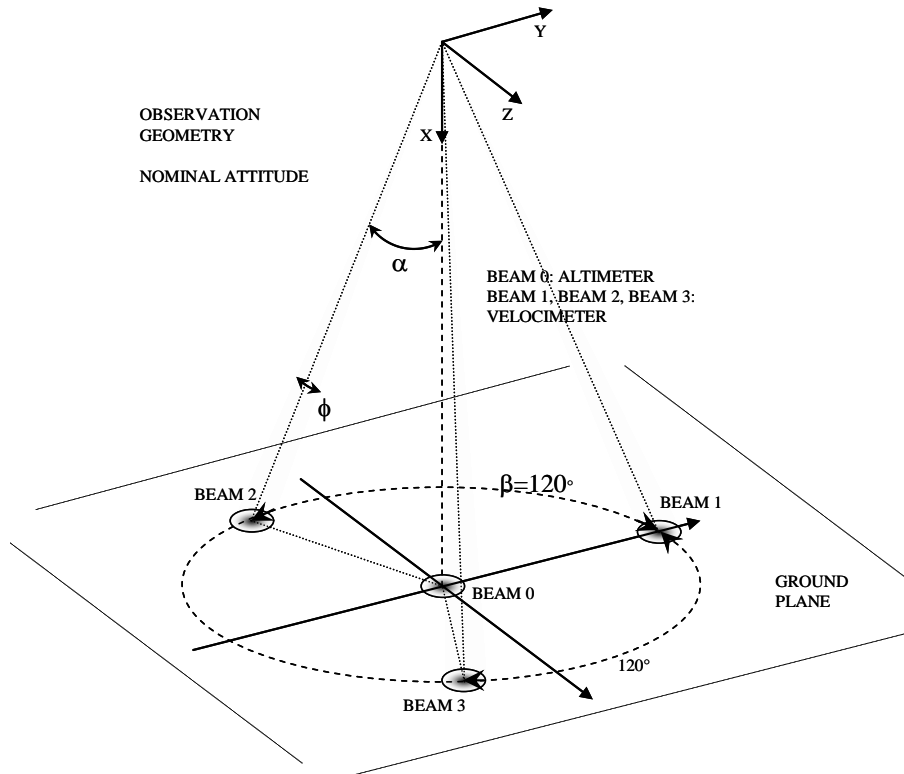


Figure 3-5 – Surface observation strategy for RDA

This is due to the fact that also in nominal attitude for platform (0-attitude):

1. The configuration that guarantees direct altitude measurement is characterized by altimeter beam along nadir direction.
2. Velocity measurements need three measures along three independent directions, each characterized for symmetric configuration by an off-nadir angle.
3. Slant range projection along nadir direction leads to an altitude measurement that is affected by a surplus angular coefficient error.

So configuration shown in Figure 3-5 is selected, where one beam (Beam 0) is dedicated to range measurement, while the other three beams (Beam 1, 2 and 3) are used to perform 3-axis velocity measurements.

Moreover, the four independent narrow beams, illuminating the Mars surface, are steered in proper angular directions that:

1. maximize the performance in velocity speed retrieval in the expected operational envelope
2. minimize the impact of measurement errors
3. minimize the errors induced by surface slope

3.4.1. Sequentially Altitude and Velocity Measurement

This Paragraph focuses on the selection of the strategy for providing sequentially altitude and velocity measurements, this has an impact on a number of system parameters.

The following technological and performance constraints apply:

1. Simultaneous estimation of range and Doppler components requires the design of a four-receiver system with increased complexity and costs, while a sequential measurement approach is feasible.
2. The minimum integration time is dictated by the accuracy required for velocity estimation (see [Paragraph 6.8](#)).
3. The requirement for AVM refresh rate ($f_{\text{update}} = 20$ Hz) dictates the maximum integration time to be traded off with the velocity accuracy performance (see [Paragraph 6.8](#)).
4. No use of the estimated value for the velocity vector, $\hat{\mathbf{V}} = [\hat{V}_x, \hat{V}_y, \hat{V}_z]$, is expected in the generation of the altitude estimation, \hat{h} .
5. The estimated value for the velocity vector, $\hat{\mathbf{V}} = [\hat{V}_x, \hat{V}_y, \hat{V}_z]$, is potentially based on the knowledge of the current altitude.
6. Signal decorrelation effects limit the improvement due to pulse-to-pulse integration basis, i.e. the integration time for each measurement.
7. Noise estimation is to be performed in order to adjust detection threshold, and signal-free intervals of the receiving window are to be ensured.

On the basis of the above considerations, the following strategy is selected:

1. Doppler and range measurements are performed sequentially in time within the maximum time interval $1/f_{\text{update}}$, and then combined.
2. The measurement intervals are selected in order to get as close as possible to the minimum integration time dictated by the required velocity accuracy.
3. The measurement intervals are potentially varied as a function of the altitude in order to meet the varying operational conditions.
4. The Doppler measurement processing chain is fed with the most recent estimate of altitude (i.e., from previous observation).

The above reported considerations lead to the selection of the sequential measurement technique reported in Figure 3-6. This allows proper radar parameters configuration independently for each beam.

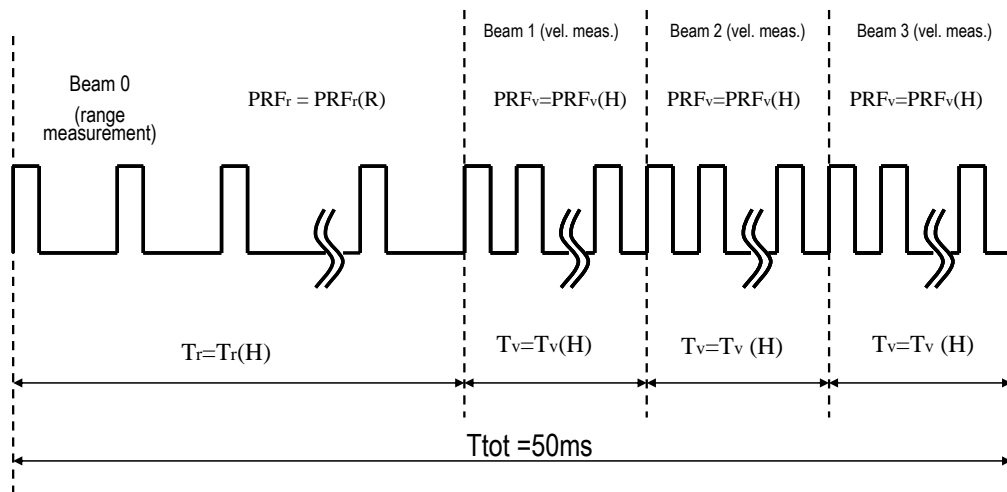


Figure 3-6 – Measurement Timeline for the RDA

With this configuration, even if four beams are used for all measurements, only one antenna is necessary. This is possible because RDA is a Pulsed CW radar, so it can work in monostatic configuration and it is possible to use a unique transmitting chain and a unique receiving chain that are connected through a switch matrix to the four antennas beams, this allows the RDA to be the simplest and compact possible.

So, the access to each single antenna beam (in TX and RX) is performed in time-division iteratively. If the measurement refresh rate is set at 20 Hz, a new measurement of range and three new velocity values are provided each $T_{\text{tot}} = 50$ ms. This time interval is divided into four time slots, each dedicated to transmitting, receiving and processing signal to/from a single antenna beam.

The high-level timeline foresees to operate the four different antenna beams available in a Time Domain Multiple Access approach. A part of the time-slot for Beam 0 will be dedicated to the noise power estimation needed to extract correctly the required measure.

A sketch of the high-level timeline of the instrument is presented in Figure 3-7.

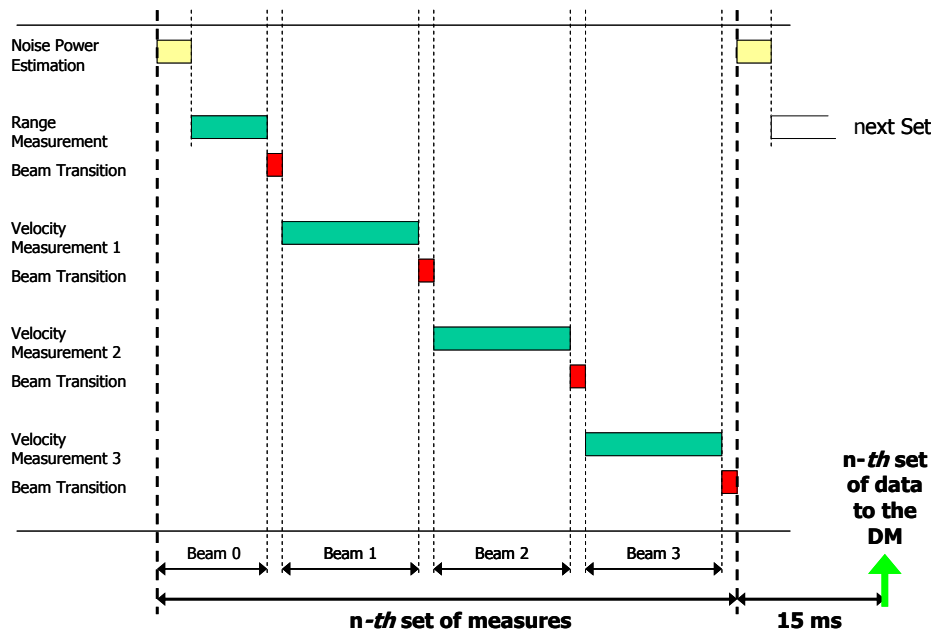


Figure 3-7 – High-Level RDA Timeline

Specifically, the PRF for the range beam will be selected in order to avoid ambiguities in range, while its value for the Doppler beams will be designed in order to guarantee non-ambiguous operations in Doppler. In this latter case, the radar might operate in the n^{th} ($n > 1$) ambiguity interval by tuning the PRF value from observation to observation in order to keep the received echo well inside the “listening” interval.

4. MATHEMATICAL MODEL

Radar is an object detection system that uses electromagnetic waves to identify the range, altitude, direction, or speed of both moving and fixed objects such as aircraft, ships, motor vehicles, weather formations, and terrain. In particular, radar systems are usually used for detecting target in noisy environment and for characterizing their main parameter such as range and velocity.

Both range and velocity can be determined by means of either time or frequency measurements. For example, a Pulsed CW radar is able to determine target's range by measuring the round-trip time of the transmitted pulse and its radial velocity by means of Doppler effect. A FM-CW radar instead can use also phase difference between transmitted and received signal for evaluating range.

This Chapter briefly illustrates the mathematical concepts for platform attitude, measurement technique for Pulsed CW radar, on which the algorithms for information extraction will rely on, and range integration time constraints.

4.1. Platform Attitude

The analysis of range and velocity measurement accuracies implies the knowledge of the platform attitude (instantaneous pitch, yaw and roll angles) because many factors are influenced by beams off-nadir angles such as backscattering and Signal to Noise Ratio.

Fixing nadir direction as the direction along the local vertical direction passing through the centre of mass of the Descent Module and θ angle (off-nadir angle) as the angle between a beam direction and nadir direction, a generic attitude leads to specific off-nadir angle for selected beam, as shown in Figure 4-1.

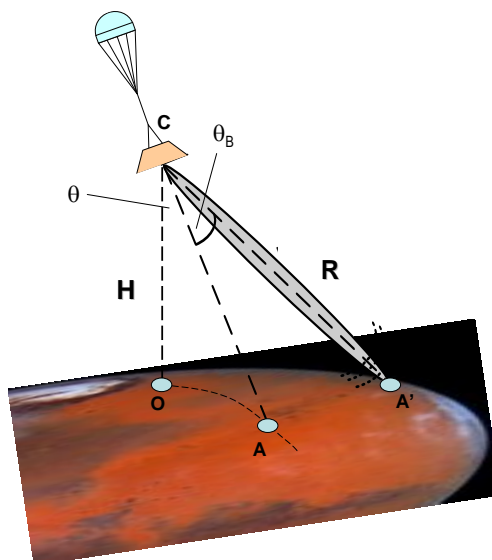


Figure 4-1 – Range Measurement for RDA operations

As regards range beam, off-nadir angle is due to direction of X_b -axis, but for each velocity beam, geometry is quite different because off-nadir is the sum of attitude angle and antenna beam steering.

In particular, for velocity beam the θ value is dictated by all yaw, pitch and roll angles of the DM, which originate the off-nadir observation conditions of X_b -axis, θ , reported in Figure 4-2. This value is to be superimposed to any intentional off-nadir antenna beam steering angles, θ_b .

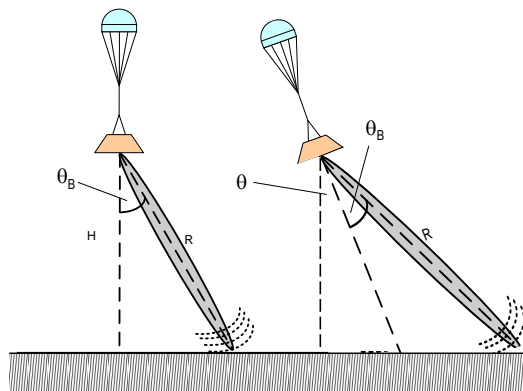


Figure 4-2 – Off-nadir angles representation

So, for each beam (B_0, B_1, B_2, B_3) there is a different θ that influences backscattering from mars surface, then Signal to Noise Ratio evaluation for range and velocity. For this reason, it is necessary to know $\theta = \theta(t)$ or attitude for the performance analysis.

For attitude analysis, two reference frames are introduced: Ground Reference Frame (GRF), $OXYZ$, and Body Reference Frame (BRF), $O_bX_bY_bZ_b$.

These two references are depicted below:

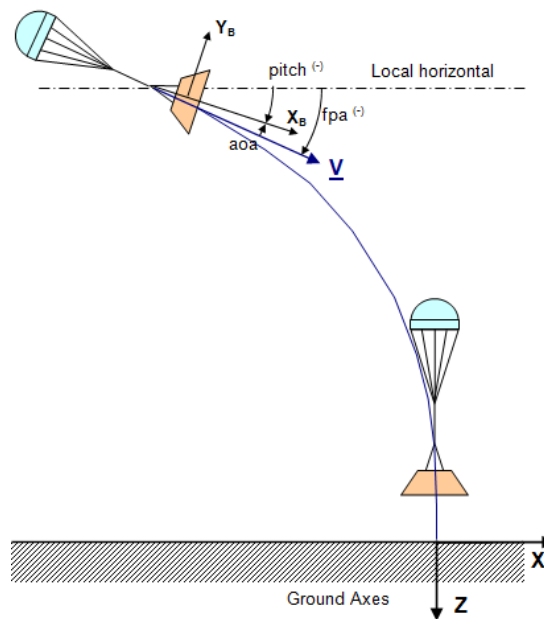


Figure 4-3 – Frame references

The coordinate reference frame – i.e. a body-referenced frame – which is used hereafter, is depicted in the Figure 4-4.

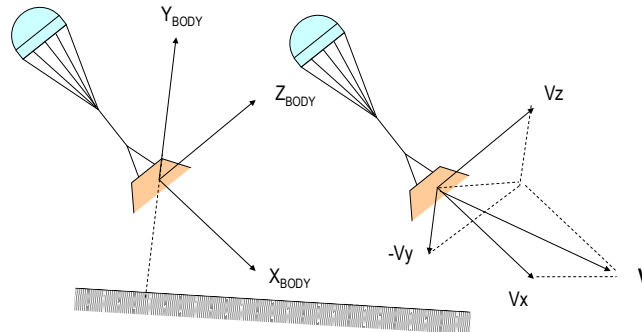


Figure 4-4 – Coordinate frame for RDA equipment

There is a third reference frame or Beams Reference Frame (BeRF) $O_{be}B_1B_2B_3$, where the axes are the three beam directions:

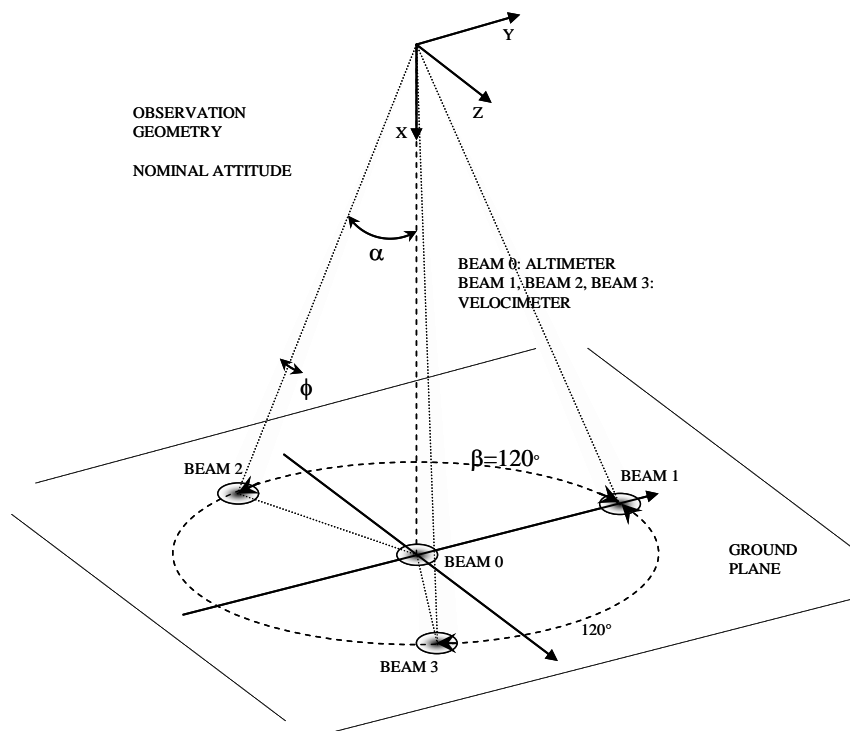


Figure 4-5 – Surface observation strategy for each RDA unit

It is to be stressed that BRF and BeRF are fixed each other, while BRF can be determinate respect to GRF by considering yaw, pitch and roll attitude angles.

There are transformation matrixes B (and its inverse C) that combines BeRF and BRF, and rotation matrix $M_{GRF2BRF}$ (and its inverse $M_{BRF2GRF}$) that combines BRF and GRF:

$$BeRF \xrightarrow{C} BRF \xrightarrow{M_{BRF2GRF}} GRF \quad (4-1)$$

$$GRF \xrightarrow{M_{GRF2BRF}} BRF \xrightarrow{B} BeRF \quad (4-2)$$

As regards B and C matrixes, being the three independent measures along the three beams, it is possible to express the velocity vector in any other basis of the 3D space. In particular, indicating with the subscripts B_1 , B_2 and B_3 the velocity component along the direction of the three beams and with X_b , Y_b and Z_b the direction of the three axes of the DM frame, the following matrix allows to convert velocity from basis BRF to basis BeRF:

$$B = \begin{bmatrix} b_{1x} & b_{2x} & b_{3x} \\ b_{1y} & b_{2y} & b_{3y} \\ b_{1z} & b_{2z} & b_{3z} \end{bmatrix} \quad (4-3)$$

where the n -th column contains the component of the n -th beam direction in the BRF basis.

Thus, the required three velocity components along the DM frame will be computed as:

$$\begin{bmatrix} V_x \\ V_y \\ V_z \end{bmatrix} = C \begin{bmatrix} V_1 \\ V_2 \\ V_3 \end{bmatrix} \quad (4-4)$$

where V_1 , V_2 and V_3 are the velocity measured along each beam and $C = B^{-1}$.

In order to design the geometry of the three beams, the following considerations apply:

1. The DM is supposed to have its X_b -axis pointing to the Mars surface and normal to it in nominal condition.
2. A cylindrical symmetry around DM X_b -axis is present.
3. The measure of velocity shall be guaranteed with an off-nadir pointing of the DM X_b -axis up to 55° .

Accounting for the considerations above and with reference to Figure 4-5, the parameters to be optimized are the off-nadir angle α and the beam aperture ϕ (beam 0 will be dedicated to range measure and now will not be considered).

Then, the matrix C is:

$$C = \begin{bmatrix} -\frac{\cos \beta}{\cos \alpha} \frac{1}{1-\cos \beta} & \frac{1}{4} \frac{1}{\left(\sin \frac{\beta}{2}\right)^2} \frac{1}{\cos \alpha} & \frac{1}{4} \frac{1}{\left(\sin \frac{\beta}{2}\right)^2} \frac{1}{\cos \alpha} \\ \frac{1}{\sin \alpha} \frac{1}{1-\cos \beta} & -\frac{1}{2} \frac{1}{\sin \alpha} \frac{1}{1-\cos \beta} & -\frac{1}{2} \frac{1}{\sin \alpha} \frac{1}{1-\cos \beta} \\ 0 & \frac{1}{2} \frac{1}{\sin \alpha} \frac{1}{\sin \beta} & -\frac{1}{2} \frac{1}{\sin \alpha} \frac{1}{\sin \beta} \end{bmatrix} \quad (4-5)$$

As regards M_{GRF2BRF} and M_{BRF2GRF} matrixes, yaw, pitch, and roll are a specific sequence of Euler angles very often used in aerospace applications to define the relative orientation of a vehicle. The three angles specified in this formulation are defined as the roll, pitch and yaw angles.

Yaw, pitch, and roll rotations are used in aerospace to define a rotation between a reference axis system and a vehicle-fixed axis system. An aircraft-body coordinate (BRF) system is fixed to the vehicle (rotates and translates with the vehicle), the origin of the BRF system is located at the vehicle's center of gravity, the X -axis points forward along some convenient reference line along the body, the Y -axis points to the right of the vehicle along the wing, and the Z -axis points downward to form an orthogonal right-handed system. A local horizontal and local vertical reference frame (LHLV) that shares the same origin as the BRF system but is always aligned with X pointing in the direction of true north, Y -axis pointing to true east, and the z -axis pointing down towards the center of gravity of the planet forming GRF.

Given this definition, the rotation sequence from LHLV // GRF to BRF is defined as follows:

1. Right-handed rotation about the Z -axis by the yaw γ angle.
2. Right-handed rotation about the new (once-rotated) Y -axis by the pitch β angle.
3. Right-handed rotation about the new (twice-rotated) X -axis by the roll α angle.

This rotation sequence can be represented mathematically by the following equations:

$$M_{GRF2BRF} = M_x(\alpha) \cdot M_y(\beta) \cdot M_z(\gamma) \quad (4-6)$$

$$X_{BRF} = M_{GRF2BRF} \cdot X_{GRF} \quad (4-7)$$

where $M_x(a)$, $M_y(a)$, and $M_z(a)$, is shorthand notation for the planar rotation matrices of a positive rotation by angle α about X-, Y-, and Z-axes, respectively, and X is a column vector of Cartesian coordinates.

The inverse rotation, from BRF to GRF, is represented by the transpose of this matrix:

$$M_{BRF2GRF} = M_{GRF2BRF}^T \quad (4-8)$$

The composite rotation matrix, from the GRF system to the ABC system, is defined as follows:

$$M_{GRF2BRF} = \begin{bmatrix} \cos(\beta) \cos(\gamma) & \cos(\beta) \sin(\gamma) & -\sin(\beta) \\ -\cos(\alpha) \sin(\gamma) + \sin(\alpha) \sin(\beta) \cos(\gamma) & \cos(\alpha) \cos(\gamma) + \sin(\alpha) \sin(\beta) \sin(\gamma) & \sin(\alpha) \cos(\beta) \\ \sin(\alpha) \sin(\gamma) + \cos(\alpha) \sin(\beta) \cos(\gamma) & -\sin(\alpha) \cos(\gamma) + \cos(\alpha) \sin(\beta) \sin(\gamma) & \cos(\alpha) \cos(\beta) \end{bmatrix} \quad (4-9)$$

As shown above, it is possible to compute all Cartesian vectors in all reference frames indicated. In particular, it is possible refer beam directions (BeRF axes) in GRF. Then, through a vectorial projection on vertical axe (Z-axis of GRF), it is possible obtain the wanted θ angle for each beam.

The knowledge of this angle allows the following computation of radiometric quantity for every beam, such as the backscattering and the Signal to Noise Ratio.

4.2. Measurement Technique

A simple block diagram of pulsed doppler radar is given in Figure 4-6, where the transmitting and receiving sub-systems are shown separately for convenience.

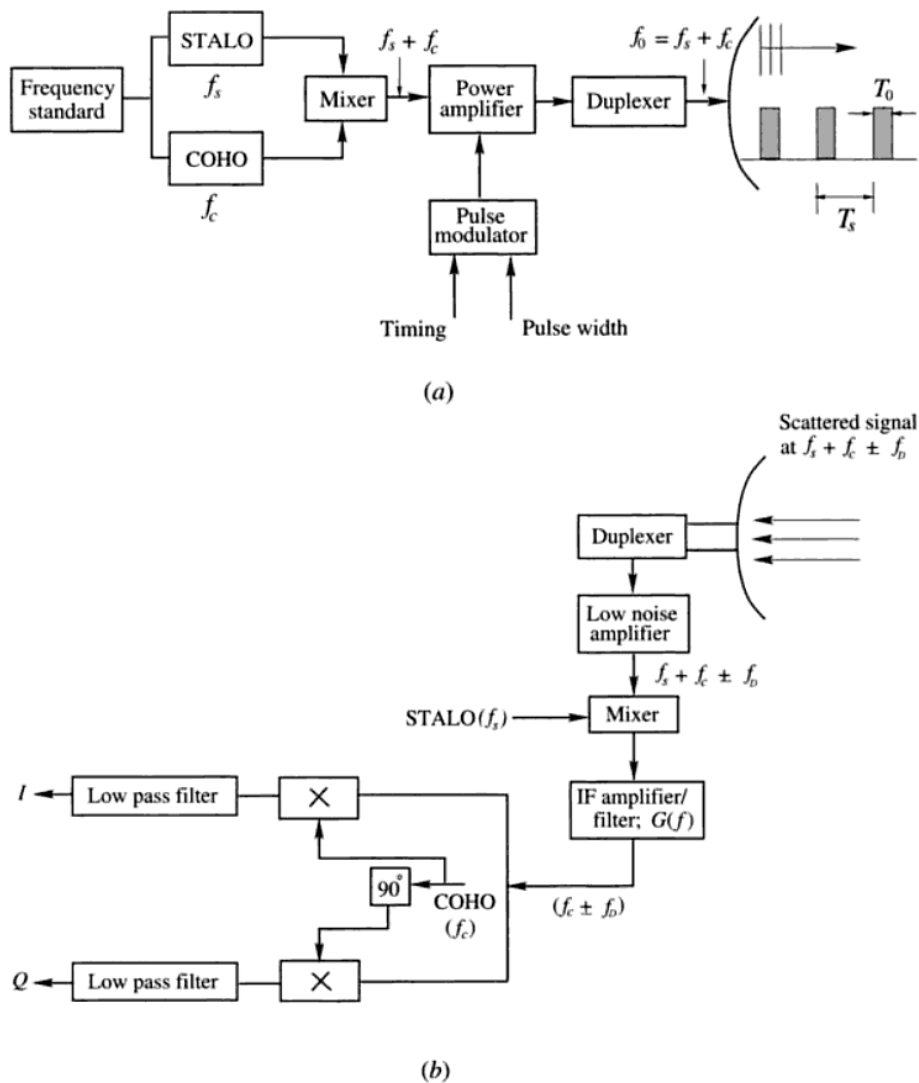


Figure 4-6 – Generic block diagram of (a) a coherent radar transmitter, and (b) Doppler radar receiver

While a wide variety of modulation types are used in radars, the simplest is the train of rectangular pulses whose pulsewidth, PT , and pulse repetition interval, PRI , are typically a few microseconds.

In coherent systems, the phase of transmitted signal is extremely stable from pulse to pulse (this property is known as phase coherency). Typically, two oscillators, a stable local oscillator (STALO) and a coherent oscillator (COHO), are used as very pure continuous wave (CW) signal sources.

The modulator controls the transmitter in pulsed system, enabling the generation of a train of pulses of specified pulsewidth and pulse repetition interval PRI. The final power amplifier brings the transmitted power to its desired level (pulse powers are typically in the range of watts. The final power amplifier in coherent systems is, generally, in the class of linear beam-microwave amplifying tubes, such as Klystrons or Traveling Wave Tubes (TWT).

Figure 4-6a is adapted from Skolnik (1980) [Ref. 4] and shows a generic radar transmitter block diagram. The final carrier frequency (f_0) is usually the sum of the STALO (f_s) and COHO (f_c) frequencies.

Another class of coherent-on-receive systems is built around transmitters which are power oscillators (e.g. magnetrons), whose phase is unpredictable (or random) and must be measured and tracked from pulse-to-pulse. Thus, the phase of the latest transmitted pulse sets the system phase reference (against which the scattered signal phase is compared).

A simplified block diagram of doppler radar receiver is shown in Figure 4-6b. The scattered signal from surface is essentially a scaled replica of the transmitted signal except for a range time delay (t_0) and doppler frequency shift (f_d).

In the receiver, the STALO frequency functions as the local oscillator, and the COHO frequency, which is at the intermediate frequency (IF) of the receiver, forms the reference for the phase detector (or in-phase/quadrature phase (I/Q) demodulation reference).

The received signal $s_r(t)$ is first amplified by the low noise amplifier (LNA), and then mixed with the STALO frequency to produce the IF signal just as in conventional superheterodyne receiver. Recall that the carrier frequency $f_0 = f_s + f_c$. The main amplification and filtering of the received signal is done in the IF portion of the receiver. The frequency response function of the IF part of receiver is denoted by $G(f)$, which is generally matched to the Fourier transform of the complex envelope of $s_r(t)$. A useful approximation for pulsed radars is that the IF receiver bandwidth is equal to the reciprocal of the transmitted pulsewidth (PT^{-1}) [Ref. 4]. For example, a typical pulsewidth of 1 μ s will correspond to an IF bandwidth of 1 MHz. If the IF bandwidth is much larger than PT^{-1} , then additional noise is introduced which lowers the output Signal to Noise Ratio (SNR). If the IF bandwidth is much narrower than PT^{-1} , then the noise is reduced along with a considerable part of the signal energy. Thus, there is an optimum IF bandwidth for which the output SNR is maximum [Ref. 4].

The output of the IF amplifier is fed into the I/Q demodulator whose function is to produce the in-phase (I) and the quadrature phase (Q) components of the envelope of received signal. As illustrated in Figure 4-6b, the COHO reference to the I/Q is shifted by 90°, and the original and phase-shifted references are compared with $s_r(t)$ and low-pass filtered to form the I and Q output.

As shown in Figure 4-7, after I/Q extraction, range and velocity measurements can be evaluated.

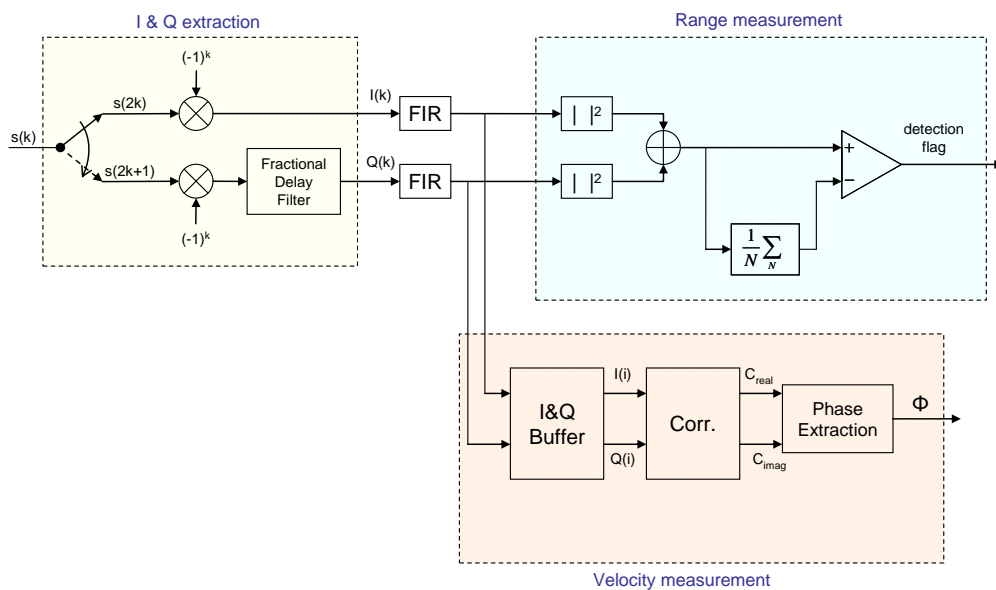


Figure 4-7 – Range and velocity measurement block diagram

4.2.1. Range Estimation

The range estimation is based on computation of the time elapsed from the transmission of a pulse of the signal to the reception of the corresponding echo. In fact, the range measurement is performed by means of a counter which starts synchronously when the transmitting pulse is generated and stops when the instantaneous echo power crosses the threshold, being the pulse width not infinitesimal. This time-information (number of clock cycles) is converted into the range information according current parameters and stored in the memory. This measurement is performed at each PRI within the range time-slot and all these data are averaged.

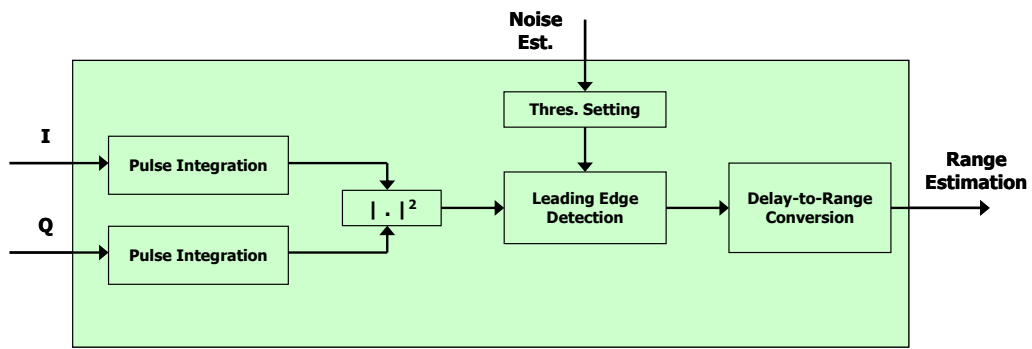


Figure 4-8 – Range Estimation Concept

The range estimation process (see Figure 4-8) starts with the integration of the received echo components along the time-slot dedicated to range. Then, the square of the modulus will be extracted and its value will be compared with a threshold to detect the crossing time. This time will be converted to a delay in respect of the start of transmission and eventually to range estimation.

The threshold setting is done calculating the average noise power on the first N samples at each PRI.

4.2.2. Noise Estimation

The noise estimation is needed to provide a guide to set the threshold for the leading-edge detection in the estimation of range.

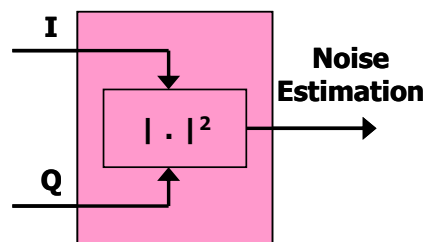


Figure 4-9 – Noise Estimation Concept

Basically it consists in a modulus extraction starting from the I and Q component of the received signal. In order to ensure an appropriate estimation of noise, a dedicated time-subslot will be used within the time-slot assigned to range measure.

4.2.3. Velocity Estimation

Velocity estimation relies on the well-known Doppler effect that relate the radial velocity between radar and target with the frequency-shift experienced by the signal travelling from radar to target and back.

Methods for estimating velocity work in the frequency domain and, essentially, they deal with the estimation of first moment of Doppler spectrum. Therefore a fast computation of a DFT of received signal is needed, with a great amount of real-time effort.

Other algorithms work in time domain [Ref. 5], such as the so called "Pulse-Pair", that can have significant advantages mainly from a computational point of view [Ref. 6].

The algorithm chosen to extract the Doppler frequency is the Pulse-Pair algorithm that is time-domain-based. In this way the computational effort needed to get the frequency-domain information is avoided.

Basically the Pulse-Pair algorithm consists in the computation of the phase of the autocorrelation function of the input signal. This phase is proportional to the velocity to be estimated.

In fact, the argument of the autocorrelation of the received signal can be expressed as:

$$q = \text{arg} \left(\frac{1}{M} \sum_{n=0}^{M-1} Z(nT_{\text{samp}}) Z^*((n+1)T_{\text{samp}}) \right) \quad (4-10)$$

where T_{samp} is the sampling interval

M is the number of available sample that depends on PRF and integration time T_{meas} :

$$M = T_{\text{meas}} \text{PRF} \quad (4-11)$$

The estimated velocity can be expressed as:

$$\hat{V} = \frac{V_a}{2\pi} q \quad (4-12)$$

where V_a is the velocity ambiguity interval, given by:

$$V_a = \frac{\lambda}{2 T_{\text{samp}}} \quad (4-13)$$

The block diagram of the velocity estimation is shown in Figure 4-9.

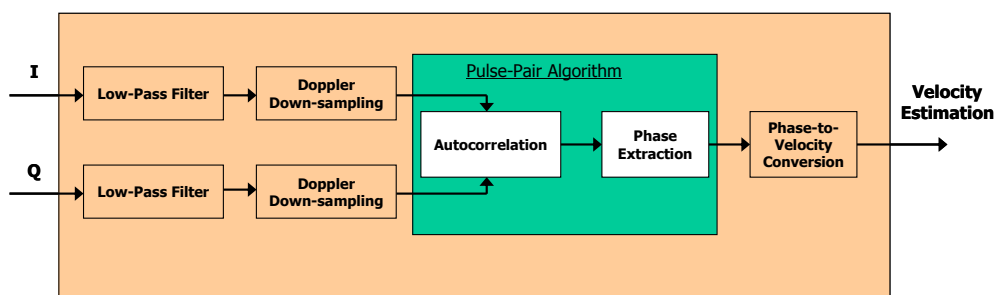


Figure 4-10 – Velocity Estimation Concept

The first step is to store one sample for each PRI and to perform the correlation.

Then the phase extraction is performed. This phase information is converted into the velocity information according current parameters. Once processing of all the three velocity beams is completed, this information is converted in the velocities along the three body axis (V_x , V_y and V_z) by means of a matrix multiplication.

Since this process does not require a high computational rate, it can be performed by the microprocessor, allowing more flexibility in terms of reconfiguration.

All the parameters involved in this process are programmable: length of buffer (L), phase to velocity conversion parameter, matrix for the velocities components extraction.

4.2.4. Measurements Accuracies

The accuracies of range and velocity measurements are essentially limited by noise so that it can be shown that the RMS error, $\delta Meas$, of a radar measurement, $Meas$, can be generally expressed as [Ref. 4]:

$$\delta Meas = \frac{k}{\sqrt{2 E/N_0}} \quad (4-14)$$

where E is the received signal energy

N_0 is the noise power per unit bandwidth

k is a constant

For time measurements k depends on the signal energy spectrum, while for a Doppler frequency measurements k depends on the second moment of velocity power spectra.

4.2.5. Measurement Ambiguities

Key requirements for the design of the RDA derive from the measurement ambiguities.

It is well known that sensing devices that attempt at extracting parameters from the reflected echo can be characterized by the ambiguity function in the frequency-time domain [Ref. 4]. If there were no theoretical restrictions, the ideal ambiguity diagram would consist of a single peak of infinitesimal thickness in the origin and be zero everywhere else. The single spike eliminates any ambiguities, and its infinitesimal thickness permits the frequency and the echo delay time to be determined simultaneously to as high degree of accuracy as desired. Estimation of time delay and frequency allows estimating range and velocity (via the Doppler frequency). In real conditions, the volume under the surface is finite. Therefore, the peak might be too broad to satisfy the requirements in accuracy and resolution. The peak shape is dictated by the transmitted waveform. The peak might be narrowed, but in order to conserve the volume under its surface, the function must be raised elsewhere. This might cause peaks to form at regions of the ambiguity diagram other than the origin and give rise to ambiguities. In general, the requirements for accuracy and ambiguity may not always be possible to satisfy simultaneously.

For the ExoMars RDA equipment, the non-ambiguous interval to be ensured is clearly specified, i.e. the distance between peaks in the ambiguity diagram for time and frequency measurement. This turns to a non-ambiguous envelope for RDA velocity and altitude measurements, which is dictated by the following parameters: V_x up to 160 m/s; V_y, V_z up to 45 m/s; H up to 3000 m; off-nadir angle θ up to $\pm 55^\circ$ (see Paragraph 2.1).

These values have to be carefully considered in the design of the radar waveform and the strategy for sensing the Mars scenario (e.g., the integration time, the transmitted pulse duration and shape, etc).

A sort of uncertainty relation exists for range and velocity ambiguities. On the basis of the following relations that allow to transform time delay to range and Doppler frequency to velocity:

$$\begin{cases} T_R = \frac{2R}{c} \\ f_D = \frac{2v}{\lambda} \sin\theta \end{cases} \quad (4-15)$$

the maximum non ambiguous range is:

$$R_{max} \leq \frac{c}{2PRF} \quad (4-16)$$

while the maximum velocity value is given by:

$$V_{max} = \frac{\lambda}{4} PRF \quad (4-17)$$

in case both negative and positive velocity have to be estimated.

Therefore the following relation can be written:

$$V_{max} R_{max} \leq \frac{c}{8\lambda} \quad (4-18)$$

Moreover, thanks to the relations (4-16) and (4-17), it is possible to establish PRFs range and velocity bounds along the descent:

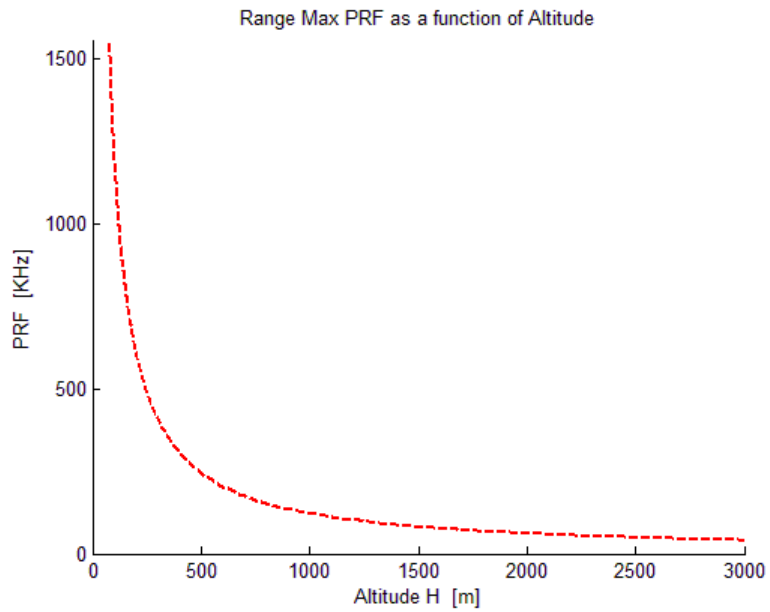


Figure 4-11 – Maximum PRF values for RDA non-ambiguous operations in Range

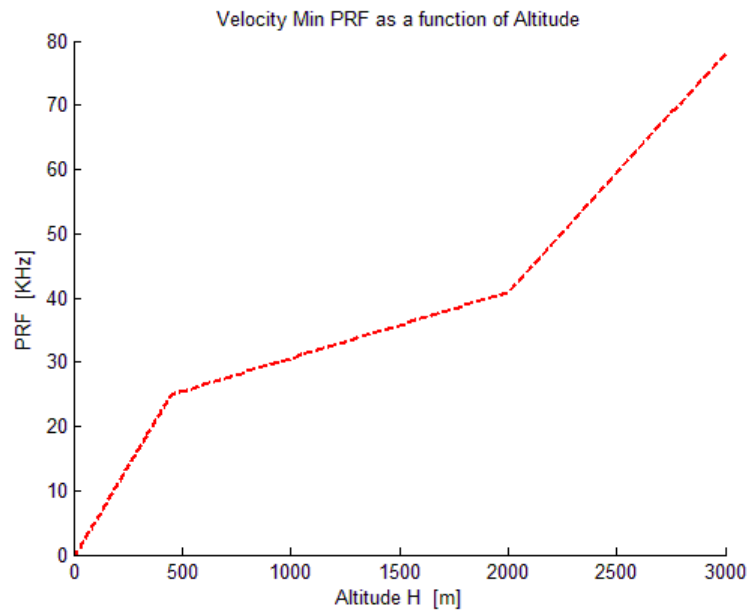


Figure 4-12 – Minimum PRF values for RDA non-ambiguous operations in Doppler

4.3. Range Integration Time Constraints

Two are the constraints that influence range integration time T_{meas} . First one is related to radial velocity, acceleration and jerk, second one is related to the perpendicular component to beam direction of angular velocity.

These constraints can be analyzed considering slant range variations. In particular, the maximum variation of slant range should be a fraction of the pixel spacing, such as:

$$\Delta R \leq \frac{1}{4} \frac{c}{2 f_c} \quad (4-19)$$

Considering that the variation of slant range due to radial velocity, acceleration and jerk can be written as:

$$\Delta R = V_{rad} T_{meas} + \frac{1}{2} a_{rad} T_{meas}^2 + \frac{1}{3} J_{rad} T_{meas}^3 \quad (4-20)$$

This gives first bound on the range integration time:

$$V_{rad} T_{meas} + \frac{1}{2} a_{rad} T_{meas}^2 + \frac{1}{3} J_{rad} T_{meas}^3 \leq \frac{c}{8 f_c} \quad (4-21)$$

Now considering that the variation of slant range due to angular velocity can be written as:

$$\Delta R = \frac{H \sin \vartheta}{\cos^2 \theta} \dot{\theta}_{\perp} T_{meas} \quad (4-22)$$

This gives second bound on the range integration time:

$$T_{meas} \leq \frac{\cos^2 \theta}{H \dot{\theta}_{\perp} \sin \theta} \frac{c}{8 f_c} \quad (4-23)$$

This relation gives undetermined results for null off-nadir angle, since it is based on the assumption that:

$$\frac{\dot{\theta}_{\perp} T_{meas}}{\theta} = 1 \quad (4-24)$$

So relation (4-23) can be replaced, around null off-nadir angle, with the following:

$$T_{meas} \leq \frac{1}{\theta_{\perp}} \arccos\left(\frac{H}{H + \frac{c}{8f_c}}\right) \quad (4-25)$$

where the most stringent relation is the first one.

Therefore, range integration time to be considered is the least value between conditions (4-21) and (4-25).

5. PERFORMANCE MODEL

The required performance for the RDA equipment is specified in terms of RMS measurement errors for both velocity components and altitude estimation. The specified values have to be achieved within the entire operational scenario, specified in Paragraph 2.1.

The specified performance (see Paragraph 2.2) is to be achieved in presence of vented bags in the FoV of the radars and plume impingement after thrusters activation. The preliminary system definition of the RDA must take into account such effects and performance degradation minimized in order to meet the goal values.

This Chapter will analyze RDA Performance Model. At first, Matlab® codes are described, and then the basic relations, on the basis of which the radar performance can be evaluated, will be described in the following Paragraphs.

The radar performance are evaluated by means of performance model. The general architecture of such model is presented in the flow chart of the Figure 5-1:

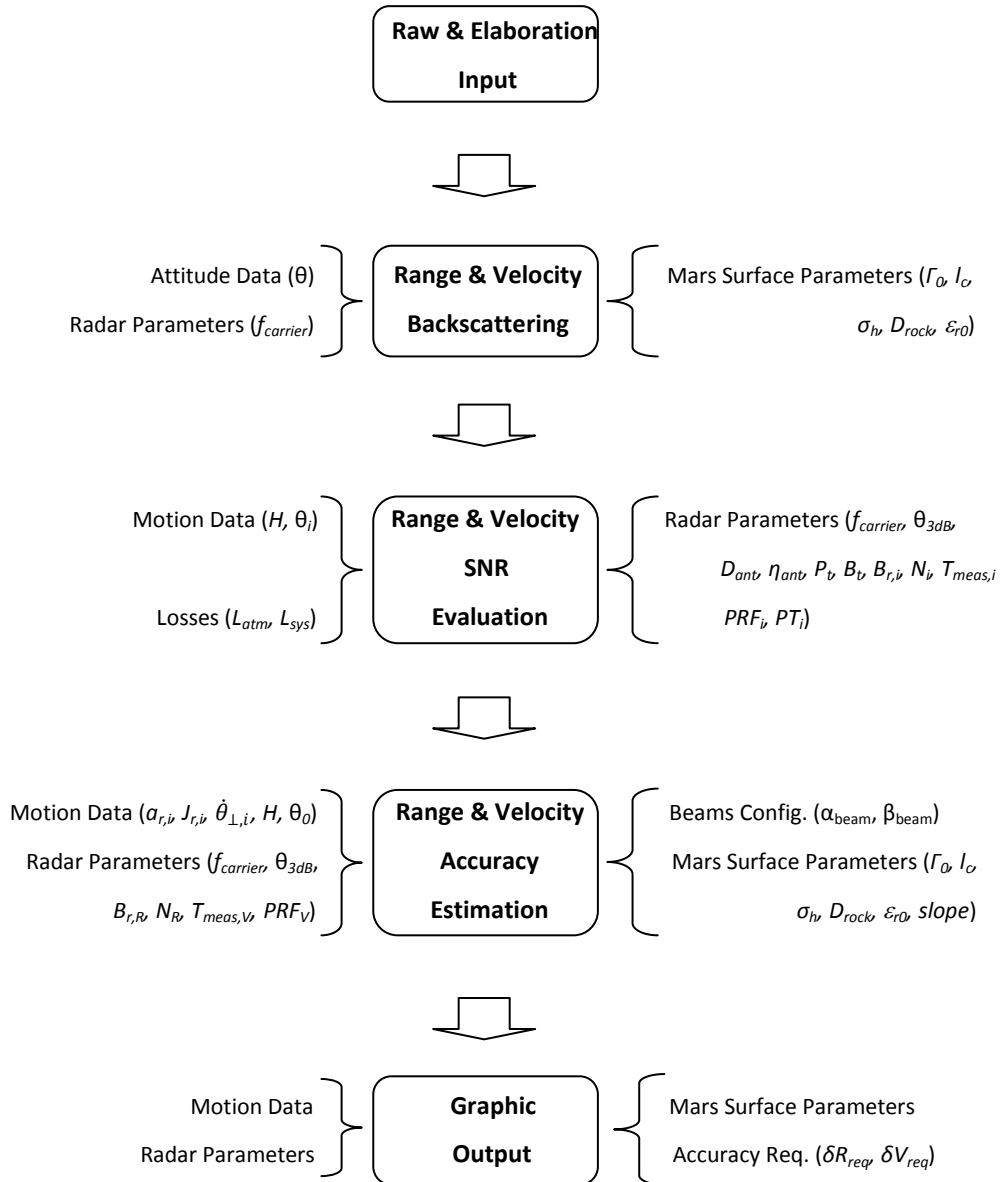


Figure 5-1 – Flow chart of performance model

Performance model uses mathematical closed form for expressing all errors involved in radar and processing. In this way, the model accepts input by user which basically provides radar trajectory (position, acceleration, jerk, attitude and angular velocity) as well as surface statistical parameters. Also the electromagnetic scattering is evaluated by means of statistical model in closed form.

5.1. Matlab® Codes Description

For the evaluation of RDA Performance, various Matlab® codes (M-files) have been implemented. M-files are a list of commands written in Matlab® language, two kinds of M-files are considered: scripts and functions.

Scripts do not accept input arguments or return output arguments. They operate on data in the workspace, previously loaded or initialized during script run.

Functions can accept input arguments and return output arguments. Internal variables are local to the function. They are utilized when some commands must be executed in various part of a generic script or when some commands can be utilized in different scripts.

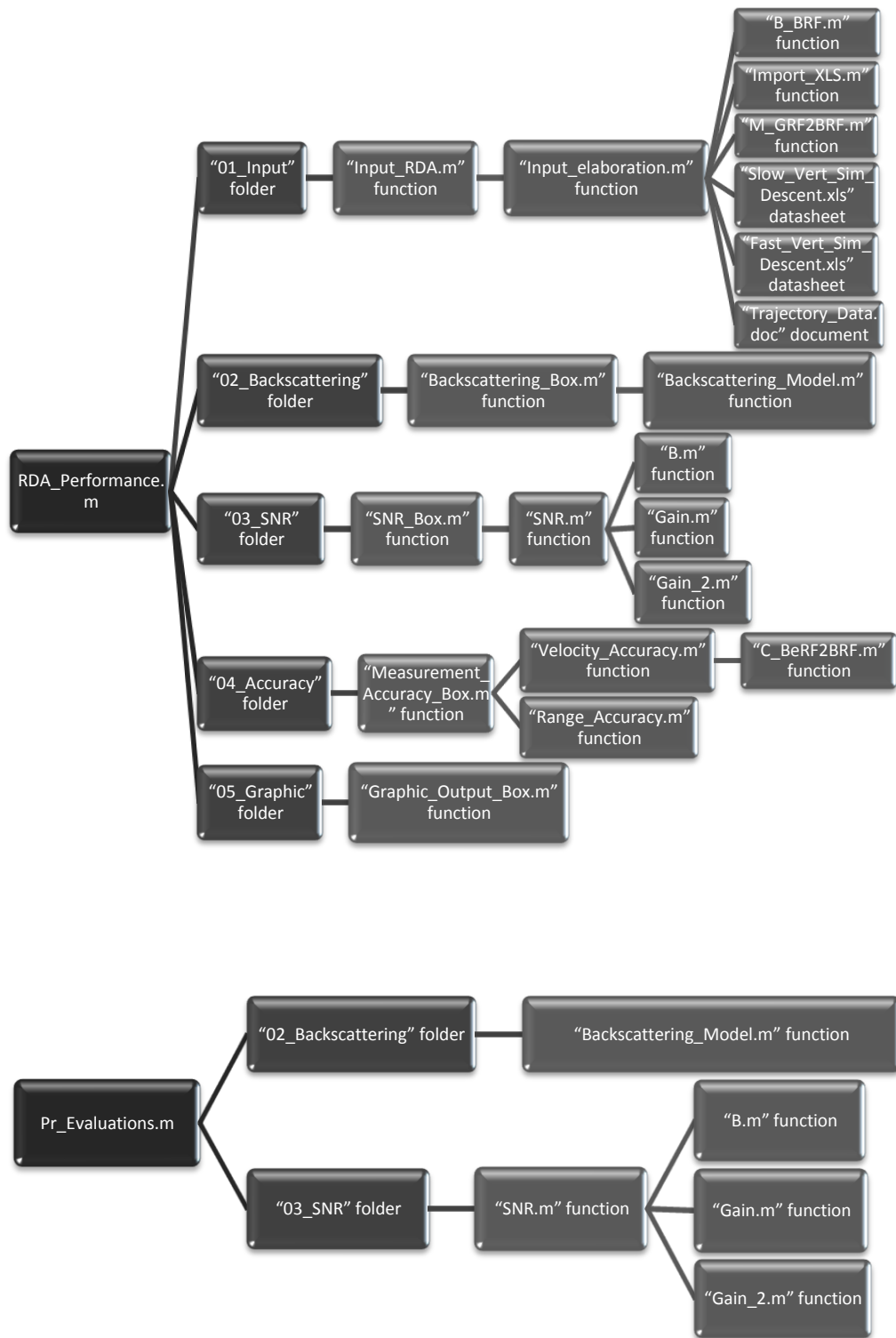
All implemented Matlab® scripts and functions are situated in the “RDA_Analysis_v1_4_3” main folder.

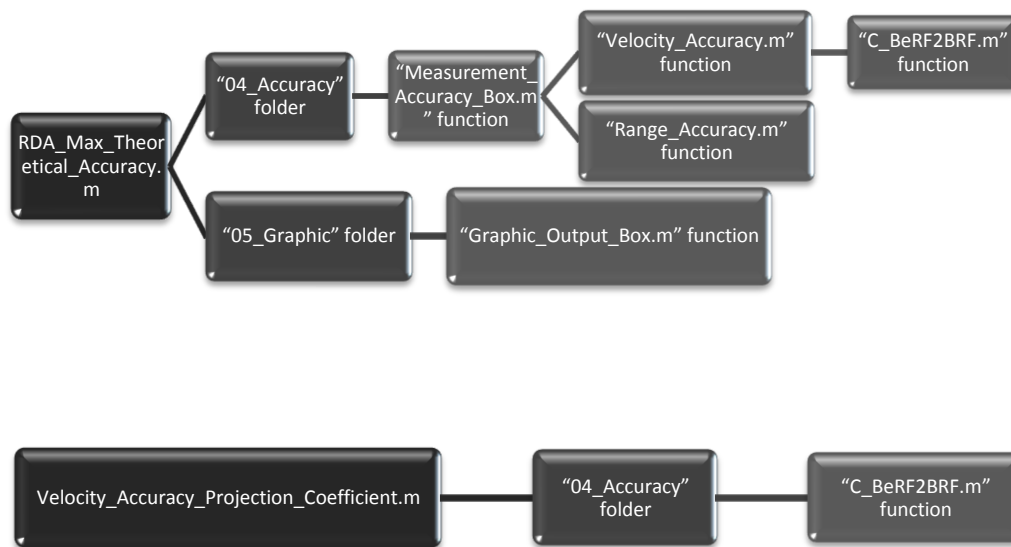
Its structure is characterized by the following elements:

1. “01_Input” folder:
 - “B_BRF.m” function
 - “Import_XLS.m” function
 - “Input_elaboration.m” function
 - “Input_RDA.m” function
 - “M_GRF2BRF.m” function
 - “Slow_Vert_Sim_Descent.xls” datasheet
 - “Fast_Vert_Sim_Descent.xls” datasheet
 - “Trajectory_Data.doc” document
2. “02_Backscattering” folder
 - “Backscattering_Box.m” function
 - “Backscattering_Model.m” function

3. "03_SNR" folder:
 - "B.m" function
 - "Gain.m" function
 - "Gain_2.m" function
 - "SNR.m" function
 - "SNR_Box.m" function
4. "04_Accuracy" folder:
 - "C_BeRF2BRF.m" function
 - "Measurement_Accuracy_Box.m" function
 - "Range_Accuracy.m" function
 - "Velocity_Accuracy.m" function
5. "05_Graphic" folder:
 - "Graphic_Output_Box.m" function
6. "Accuracy_Compact_Formulas.m" stand-alone script
7. "Accuracy_Improvements.m" stand-alone script
8. "Numerical_Range_Investigation.m" stand-alone script
9. "Numerical_Velocity_Investigation.m" stand-alone script
10. "Pr_Evaluations.m" script
11. "RDA_Max_Theoretical_Accuracy.m" script
12. "RDA_Performance.m" main script
13. "Velocity_Accuracy_Projection_Coefficient.m" script

Relationship between scripts and functions are:





Note: Stand-alone scripts don't have subfolder and they are fully autonomous.

5.1.1. Scripts Description

In this Paragraph, scripts for preliminary system definition and performance evaluations are described.

"Accuracy_Compact_Formulas.m" stand-alone script: Due to complex relationship among various radar parameters, for an analytic investigation, it is necessary to elaborate a symbolic compact formulation of range and velocity measurement accuracies. So *"Accuracy_Compact_Formulas.m"* has been elaborate. It is characterized firstly by a cleanness of workspace and command window, by figures closing, then by the assignation of the elements that define the accuracy formulas.

"Accuracy_Improvements.m" stand-alone script: During the optimization phase, it is useful to establish the range and velocity accuracy improvements step-by-step. So *"Accuracy_Improvements.m"* has been elaborate. It is characterized firstly by the loading of two different workspace to compare, by a cleanness of command window, by figures closing, and then the improvements of accuracy are elaborated and plotted.

“Numerical_Range_Investigation.m” stand-alone script: For range parameters optimization, it appears necessary to take a numerical investigation because of the difficulty of the analytical investigation. So “Numerical_Range_Investigation.m” has been elaborate. It is characterized firstly by a cleanness of workspace and command window, by figures closing, then by the assignation of the key radar parameters for the next numerical range investigation that finishes with various plot.

“Numerical_Velocity_Investigation.m” stand-alone script: For velocity parameters optimization, it appears necessary to take a numerical investigation because of the difficulty of the analytical investigation. So “Numerical_Velocity_Investigation.m” has been elaborate. It is characterized firstly by a cleanness of workspace and command window, by figures closing, then by the assignation of various set of key radar parameters for the next numerical velocity investigation that finishes with various plots.

“Pr_Evaluations.m” script: For link budget of received power, detection probability for range measurements and radar parameters optimization, it appears necessary to evaluate received power for various attitude values. So “Pr_Evaluations.m” has been elaborate. It is characterized firstly by a cleanness of workspace and command window, by figures closing, then by the assignation of attitude angles interval and by the evaluation of received power that finishes with various plot. This script calls the function: “Backscattering_Model.m” and “SNR.m” described in the follow Paragraph 5.1.2.

“RDA_Max_Theoretical_Accuracy.m” script: During the evaluation of radar performance, it is useful to establish the maximum theoretical measurement accuracies of RDA that can be obtained considering null all factors, this leads to the accuracies improvement. So “RDA_Max_Theoretical_Accuracy.m” has been elaborate. It is characterized firstly by the loading of the workspace of a normal performance evaluation, by a cleanness of command window, by figures closing, then all factors that lead to an error improvement are set equal to zero, so range and velocity accuracy are elaborated and plotted. This script calls two functions: “Measurement_Accuracy_Box.m” and “Graphic_Output_Box.m” described in the follow Paragraph 5.1.2.

“RDA_Performance.m” main script: It is the main script of RDA Performance Model. Through it, performance evaluations of worst case or simulated descent can be done. It is characterized firstly by a cleanness of workspace and command window, by figures closing, then by the assignation of all radar parameters and by next accuracy elaborations that finish with various plots. This script calls six function: “Input_RDA.m”, “Input_elaboration.m”, “Backscattering_Box.m”, “SNR_Box.m”, “Measurement_Accuracy_Box.m” and “Graphic_Output_Box.m” described in the follow [Paragraph 5.1.2](#).

“Velocity_Accuracy_Projection_Coefficient.m” script: During the optimization phase, it is useful to analyze velocity projection coefficients as function of beam off-nadir angle due to selected beams geometry. So “Velocity_Accuracy_Projection_Coefficient.m” has been elaborate. It is characterized firstly by a cleanness of workspace and command window, by figures closing, then by the assignation of beam angles interval, and by the evaluation of velocity accuracy projection coefficients. This script calls the “C_BeRF2BRF.m” function described in the follow [Paragraph 5.1.2](#).

5.1.2. Functions Description

In this Paragraph, functions for preliminary system definition and performance evaluations are described (in alphabetical order).

“B.m” function (“03_SNR” folder): This function elaborates the value of relation (5-10). Its syntax is:

```
function b = B(T,h,c,teta_off)
```

where T is the convolution time interval

h is actual altitude

c is light velocity

teta_off is the actual off-nadir beam angle.

"B_BRF.m" function ("01_Input" folder): This function implements transformation matrix from BeRF to BRF. Its syntax is:

```
function B = B_BRF(alpha, beta)
```

where alpha and beta are beam angles and are expressed in radians.

"Backscattering_Box.m" function ("02_Backscattering" folder): This function is a box function type, i.e., contains all functions for beams backscattering evaluations.

"Backscattering_Model.m" function ("02_Backscattering" folder): This function elaborates backscattering for specific beam direction. Its syntax is:

```
function sigma_0 = Backscattering_Model(teta,Epsilon,D,lambda)
```

where teta is beam off-nadir angle

Epsilon is surface dielectric constant

D is diameter of rock

lambda is carrier wavelength.

"C_BeRF2BRF.m" function ("04_Accuracy" folder): This function provides the coefficients for projection of velocity measurement accuracy along BRF axis. Its syntax is:

```
function C = C_BeRF2BRF(alpha, beta)
```

where alpha and beta are beam angles and are expressed in radians.

"Gain.m" function ("03_SNR" folder): This function provides antenna gain. Its syntax is:

```
function G = Gain(teta)
```

where teta is the -3dB antenna aperture.

“Gain_2.m” function (“03_SNR” folder): This function provides the quadratic value of antenna gain.

“Graphic_Output_Box.m” function (“05_Graphic” folder): This function is a box function type, i.e., contains all output necessary for performance evaluations.

“Import_XLS.m” function (“01_Input” folder): This function imports simulated descent data from Microsoft® Excel datasheet (*.xls type) for simulated descent performance evaluations. Its syntax is:

```
function Import_XLS(XLS)
```

where XLS is the full path of datasheet folder.

“Input_elaboration.m” function (“01_Input” folder): This function elaborates input data for next performance evaluations. It establishes all derived RDA parameters and set all laws that are previously selected by the user.

“Input_RDA.m” function (“01_Input” folder): This function allocates input basic data for next elaboration. The call of this function allows the user to choose the type of motion data (two simulated descent profile or worst case profile), beam off-nadir angle (15° or 20°), the type of range integration time law, the type of range and velocity Pulse Repetition Frequency laws and the type of range and velocity pulse duration laws.

“M_GRF2BRF.m” function (“01_Input” folder): This function implements flight angle matrix rotation from GRF to BRF (the matrix allows to write a generic vector of GRF in the BRF). Its syntax is:

```
function M = M_GRF2BRF(alpha,beta,gamma)
```

where alpha is roll angle

beta is pitch angle

gamma is yaw angle

“Measurement_Accuracy_Box.m” function (“04_Accuracy” folder): This function is a box function type, i.e., contains all functions for range and velocity measurement accuracy evaluations.

“Range_Accuracy.m” function (“04_Accuracy” folder): This function elaborates range measurement accuracy. Its syntax is:

```
function delta_R = Range_Accuracy(teta,E,beta_2_old,M,Br,N,fc,sigma_h,  
                                slope,c,H,teta_3_dB)
```

where teta is beam 0 off-nadir

E is range received energy

beta_2_old is normalized second central moment of range signal energy spectrum without correction terms

M is number of pulse

Br is the receiver bandwidth

N is noise

fc is sampling frequency

sigma_h is the surface roughness

slope is surface RMS slope

c is light velocity

H is altitude

teta_3_dB is -3dB antenna aperture

“SNR.m” function (“03_SNR” folder): This function elaborates Signal to Noise Ratio (SNR). Its syntax is:

```
function [Pr,SNR,E,beta_2] = SNR(teta,sigma_0,P_T,M,Br,N,H,Pt,Bt,  
                                teta_3_dB,c,lambda,D_ant,eta_ant, fc,  
                                n_over,L_atm,L_sys,Filter_flag)
```

where teta is beam off-nadir

sigma_0 is along beam backscattering

P_T is pulse duration
 M is pulse number
 B_r is receiver bandwidth
 N is noise
 H is altitude
 P_t is transmitted peak power
 B_t is transmitted bandwidth
 teta_3_db is -3dB antenna aperture
 c is light velocity
 lambda is carrier wavelength
 D_ant is antenna diameter
 eta_ant is antenna efficiency
 f_c is sampling frequency
 n_over is number of oversampling
 L_atm is atmospheric losses
 L_sys is system losses
 Filter_flag is flag for use or not of the filter

“SNR_Box.m” function (“03_SNR” folder): This function is a box function type, i.e., contains all functions for Signal to Noise Ratio (SNR) evaluations. It foresees worst case and simulated descent mode for fast computation in worst case mode (because SNR for velocity beam are identical).

“Velocity_Accuracy.m” function (“04_Accuracy” folder): This function elaborates velocity measurement accuracy. Its syntax is:

```

function [delta_V_X,delta_V_Y,delta_V_Z] = Velocity_Accuracy(
    SNR_V_B(ies),a_rad_B(ies),J_rad_B(ies),teta_rate_per_B(ies),
    PRF_V,T_meas_V,M_V,lambda,teta_3_dB,alpha_beam,beta_beam)
  
```

where SNR_V_B(ies) are the SNRs along n-ies beam

a_rad_B(ies) are the radial accelerations along n-ies beam

$J_{rad_B(ies)}$ are the radial Jerks along n-ies beam
 $teta_rate_per_B(ies)$ are perpendicular to n-ies beam angular rates
 PRF_V is velocity Pulse Repetition Frequency
 T_meas_V is velocity integration time
 M_V is velocity pulse number
 $lambda$ is carrier wavelength
 $teta_3_dB$ is -3dB antenna aperture
 $alpha$ beam, $beta$ beam are beam angles

5.2. Mars Backscattering Model

Mars terrain scattering characteristics foresees a Golombek & Rapp Surface Rock Distribution with the values for the Viking-1 landing site, i.e. :

- Number of rocks per m^2 of diameter D and higher:

$$N(D) = L e^{-sD} \quad (5-1)$$

with $L_{VL1} = 5.61$ and $s_{VL1} = 12.05$

- Fractional area covered by of rocks of diameter D and higher:

$$F_k(D) = k e^{-q(k)D} \quad (5-2)$$

with $k_{VL1} = 0.069$ and $q(k) = 1.79 + 0.152/k$

In the following Figure Mars terrain backscattering is reported at different frequencies.

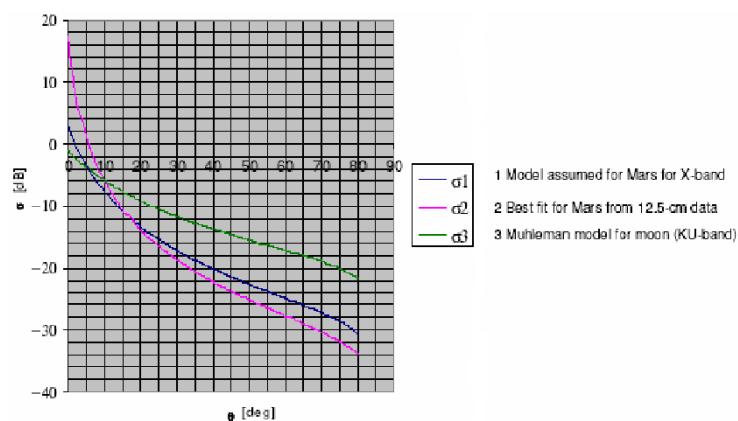


Figure 5-2 – Experimental Cross Section per Unit Surface Area

The above figure represents the estimation of Mars surface backscattering values evaluated at 3 different frequencies:

1. X-Band (8-12 GHz)
2. S-Band (2-4 GHz)
3. Ku-Band (12-18 GHz)

Specifically, on the basis of the current knowledge of Mars, the scattering behavior of the Mars surface is reported in Figure 5-2. The reported values are valid for X-band, S-band and Ku-band observation, and exhibit a decreasing behavior of the radar cross section $\sigma_0(f)$ per unit area as the incidence angle, θ_{inc} , increases. The σ_0 (X-band) value ranges from 18 to -34 dB as θ_{inc} passes from 0° to 80°. This model has been considered and validated in past missions to Mars. The behavior at S-band is instead derived from best fitting techniques, while the behavior at Ku band is extrapolated from the *Muhleman Model*, which is valid for Moon surface scattering. No scattering models or measurement data are available for higher frequencies. It is evident the flatness of the curve increases at higher frequencies.

Now, the derivation of the scattering behavior at RDA operating frequencies is discussed.

The Mars surface backscattering can be characterized using the Hagfors-Model (developed for the Lunar surface) and summarized as:

$$\sigma_0(\theta) = \frac{\Gamma_s}{2} \left(\frac{l_c \lambda}{4\pi\sigma_h^2} \right)^2 \left[\cos^4(\theta) + \left(\frac{l_c \lambda}{4\pi\sigma_h^2} \right)^2 \sin^2(\theta) \right]^{\frac{3}{2}} \quad (5-3)$$

where θ is the off-nadir angle

Γ_s is the surface reflectivity

λ is the wavelength

σ_h is the surface roughness

l_c is the surface correlation length

The surface reflectivity is calculated, assuming a fixed surface dielectric constant ϵ_{r0} , as:

$$\Gamma_s = \left| \frac{1 - \sqrt{\epsilon_{r0}}}{1 + \sqrt{\epsilon_{r0}}} \right|^2 \quad (5-4)$$

The surface statistical parameters can be related to surface rock distribution $N(D)$, where D is the diameter of the rock, by the following relations:

$$\begin{cases} \sigma_h = \frac{D}{3} \\ l_c = \sqrt{\frac{2}{N(D)}} \end{cases} \quad (5-5)$$

Assuming a rock distribution of Golombek & Rapp for the surface slope results:

$$\begin{cases} N(D) = L e^{-sD} = 5.61 e^{-12.05 D} \\ m_s = \frac{\sigma_h}{l_c} = \sqrt{2} \frac{D}{L} e^{sD} \end{cases} \quad (5-6)$$

Here the parameters of the rock distribution are fixed according to the results obtained by the Viking-I data analysis.

Using the results obtained by the recent missions, assuming a basalt or volcanic sediment material, the Mars surface dielectric constant can be fixed to $\epsilon_{r0} = 3$, while the diameter of the rock can be fixed to $D = 0.04$ m.

For these values, Mars backscattering model provides:

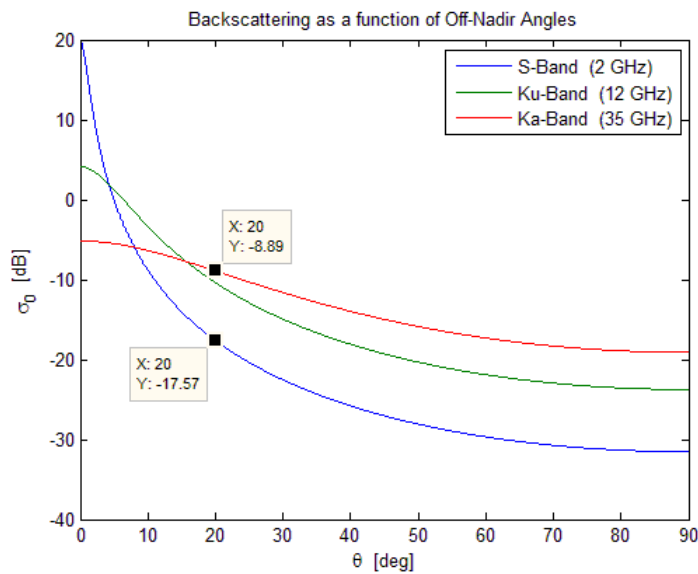


Figure 5-3 – Modeled cross section per unit surface area

Figure 5-3 shows that, increasing carrier frequency, the backscattering decreases for null off-nadir angles while increases for high off-nadir angles.

As shown also in Figure 5-2, from S-Band to Ka-Band the backscattering tends to be flat. This means that, also for high off-nadir angles, the echoes from Mars surface are more energetic. For example, from S-band to Ka-Band the backscattering increases from -17.57 dB to -8.89 dB for an off-nadir angle of 20°.

5.3. Signal to Noise Ratio Evaluation

The evaluation of Signal to Noise Ratio implies the assessment of received power by means of the well known radar equation.

In case of short-range radar, with narrow beams and short transmitted pulses, the interaction between the areas illuminated by the antenna beamwidth and transmitted power should be taken into account. This allows the evaluation of the variation of the received power with time that is mandatory for a correct evaluation of accuracy of possible time and frequency measurements.

In other words, the received power $P_r(t)$ can be evaluated by numerically solving the following integral [Ref. 7]:

$$P_r(t) = \frac{\lambda^2}{(4\pi)^3} \iint \frac{P_t(t-T) G^2(\theta-\theta_0, \varphi) \sigma_0(\theta, \varphi)}{R^4} dA \quad (5-7)$$

where (θ, φ) are respectively the across-track and along track angles

$P_t(t)$ is the transmitted pulse power

$G(\theta-\theta_0, \varphi)$ is the radar antenna gain supposed pointed with an off-nadir angle of θ_0

$\sigma_0(\theta, \varphi)$ is the terrain backscattering coefficient

$R = \frac{c T}{2}$ is the slant-range

The reference geometry in the across-track plane is shown below:

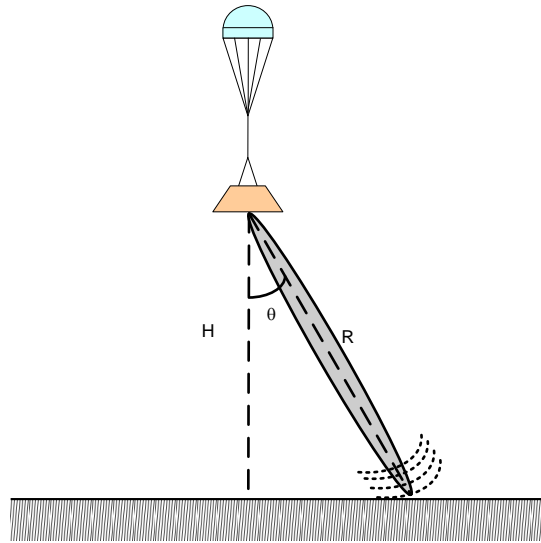


Figure 5-4 – Basic geometry involved in the evaluation of signal to noise ratio

The previous integral can be rearranged in the following way, in order to identify an equivalent area as in the classical radar equation form:

$$P_r(t) = \frac{\lambda^2 P_{t,p} G_0^2}{(4\pi)^3 H^4 L_{atm} L_{sys}} \sigma_{0,p} A_{eq}(t) \quad (5-8)$$

where $P_{t,p}$ is the transmitted peak power and, therefore, $P_t(t) = P_{tp} p(t)$

G_0 is the antenna maximum gain and the antenna gain is supposed to be separable $G(\theta, \varphi) = G_0 g_\theta(\theta - \theta_0) g_\varphi(\varphi)$

$\sigma_0(\theta, \varphi) = \sigma_{0,p} \gamma(\theta)$ is the scattering that is supposed to be dependent only on incidence angle

H is the spacecraft altitude

L_{atm} are the general atmospheric losses, including for example the effects of superficial dust and thrusters plumes

L_{sys} are the general system losses, including for example antenna front-end insertion losses

The equivalent area can be view as a convolution integral between the transmitted pulse and a function $b(T)$ that essentially takes into account the antenna gain, such as [Ref. 7]:

$$A_{eq}(t) = \int p(t - T) b(T) dT \quad (5-9)$$

$$\text{where } b(T) = \frac{2^4 H^6}{c^4} \int \frac{g_\theta^2(\theta - \theta_0) \gamma(\theta)}{T^5} d\theta \int g_\phi^2(\phi) d\phi \quad (5-10)$$

$$\cos(\theta) = \frac{2H}{cT} \quad (5-11)$$

The combined effects of radar geometry, antenna gain and transmitted pulse determine the actual shape of the received pulse and its power.

Some examples are reported in Figure 5-5 for various radar altitudes. In this case the transmitted pulse is supposed to be ideal (rectangular pulse) as well as the receiving channel to have infinite bandwidth.

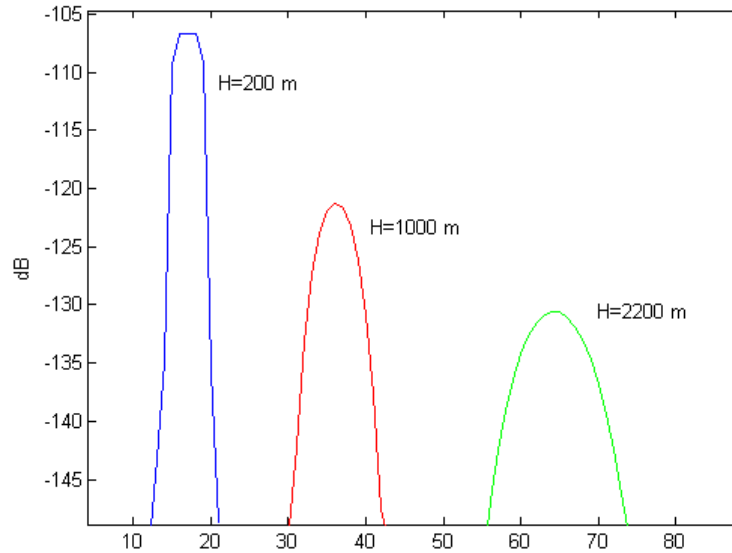


Figure 5-5 – Received pulse shape for various radar altitudes

If a realistic situation is considered, such as by considering 5 ns of rising time for the transmitted bandwidth and 15 MHz for the receiving bandwidth (B_r), at an altitude of 200 m, the received pulses tend to broaden as shown in Figure 5-6.

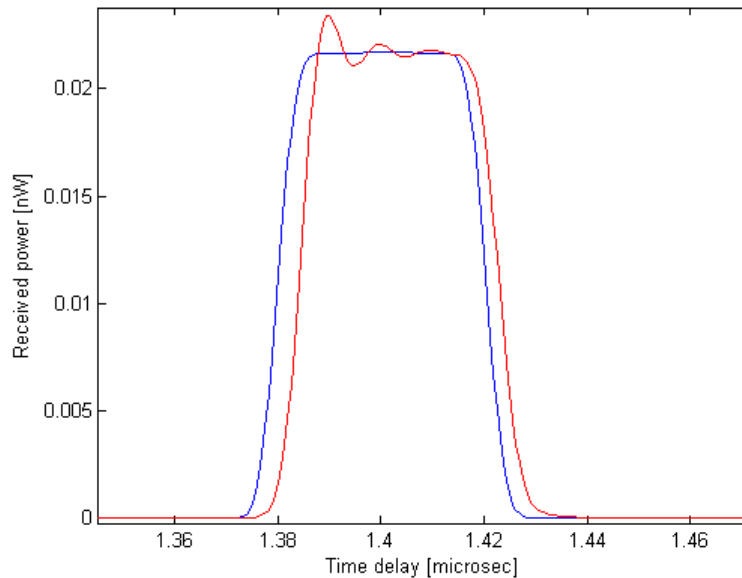


Figure 5-6 – Received pulse power taking into account actual transmitted pulse rising time and receiving bandwidth

In Figure 5-6 the received pulse is plotted in blue for an ideal rectangular transmitted pulse, while the received pulse is plotted in red for a real transmitted pulse. The differences among two received pulse are due to the complex interactions between the shape of transmitted pulse and Mars surface (see Paragraph 3.2.2).

Now, by considering the maximum value of received pulses S_r , it is possible to evaluate the peak signal to noise ratio, also including the improvement factor of M integrated pulses:

$$SNR = \frac{S_r}{K B_N T_0 F} M \quad (5-12)$$

where K is the Boltzmann constant

$B_N \approx B_r$ is the noise equivalent bandwidth

F is the receiver noise figure

T_0 is the receiver temperature

The achievable peak SNR as a function of radar altitude is shown in Figure 5-7.

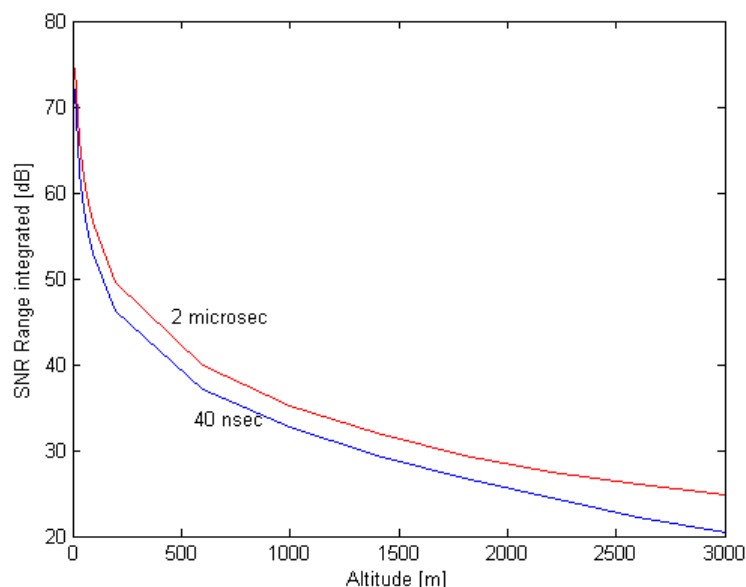


Figure 5-7 – Achievable peak SNR as a function of radar altitude (integration factor included) for two values of transmitted pulse length

Since the SNR depends by the equivalent area (relation (5-9)), that is the convolution integral of transmitted pulse and the quantity B (relation (5-10)), the Figure 5-7 shows that, among the other parameters, the SNR can be increased by increasing the duration of the pulse to be transmitted.

5.4. Range Measurements Accuracy

A Pulsed CW radar is able to determine target's range by measuring the round-trip time of the transmitted pulse. If a time estimation error is verified, this involves an error in the range measure.

The simplest method for performing time-delay measurements is to determine the time at which the leading edge of the received pulse crosses some threshold.

Taking into account the shape of the received pulse, the time-delay error can be expressed as [Ref. 4]:

$$\delta T_R = \frac{1}{\beta \sqrt{2 E/N_0}} \quad (5-13)$$

where β^2 is the normalized second central moment of the signal energy spectrum $|S(f)|^2$ and it is defined as:

$$\beta^2 = \frac{(2\pi)^2 \int_{-\infty}^{+\infty} f^2 |S(f)|^2 df}{\int_{-\infty}^{+\infty} |S(f)|^2 df} \quad (5-14)$$

Its square, β , is called effective bandwidth or RMS bandwidth.

For example for a Gaussian pulse shape, the time-delay error can be analytically expressed as:

$$\delta T_R = \frac{1.18}{\pi B \sqrt{2 E/N_0}} \quad (5-15)$$

where B is the 3-dB bandwidth of the signal.

Of course, if M are coherently integrated before the leading edge detection, the accuracy improves such as:

$$\delta T_R = \frac{1}{\beta \sqrt{2 M E/N_0}} \quad (5-16)$$

The time spread of received pulses causes a decrease of β factor of relations (5-13&16) and, therefore, a worse accuracy of possible time delay measurements.

In addition, the effect of sampling frequency (f_{samp}) in the receiving channel should be considered. It means that even for high values of SNR, the measurement is limited by the discrete time induced by the sampling frequency used in the receiver.

By supposing the range to be estimated uniformly distributed within a sampling interval, corresponding standard deviation of time error is:

$$\delta T_q = \frac{1}{f_{\text{samp}} \sqrt{12}} \quad (5-17)$$

which, being independent on radar altitude, acts as a minimum achievable error ($\text{SNR} \rightarrow \infty$).

By considering the two error components independent, the final range measurement accuracy (δR) can be written as:

$$\delta R = \frac{c}{2} \sqrt{\delta T_R^2 + \delta T_q^2} \quad (5-18)$$

An example of the achievable accuracy is plotted in Figure 5-8.

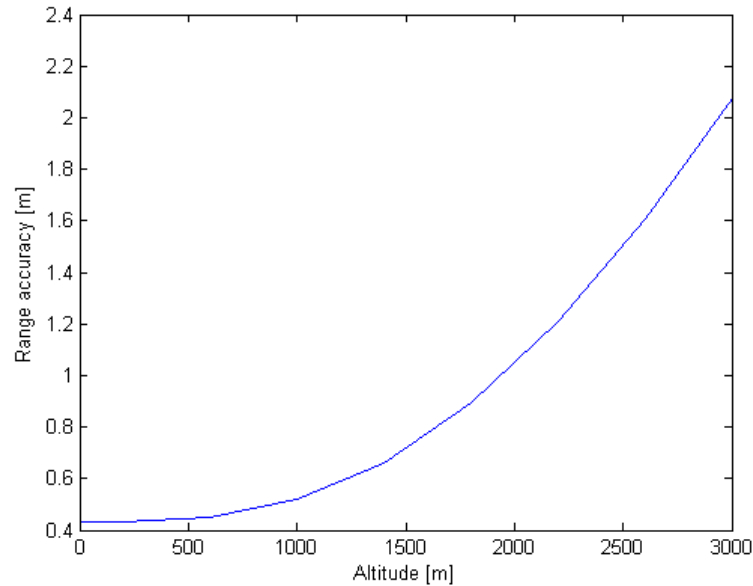


Figure 5-8 – Achievable range accuracy as a function of radar altitude

5.4.1. Factors Affecting Range Measurements Accuracy

The time spread of received pulses causes a decrease of β factor and, therefore, a worse accuracy of possible time delay measurements. All factors that contribute to time spread of received signal and, therefore modify the β factor of relations (5-13&16), can affect the final range accuracy.

For evaluating such impact, each factor should be included in the simulation and the β factor should be calculated by means of a Fourier transform.

An easy approximation can be done by considering Gaussian the receiving echo with standard deviation σ_t . Its Fourier transform is still a Gaussian with standard deviation σ_f given by:

$$\sigma_f = \frac{1}{2\pi \sigma_t} \quad (5-19)$$

In this case it is:

$$\beta = \sigma_f \quad (5-20)$$

In other words, by increasing the spread of the signal Doppler spectrum, the corresponding autocorrelation coefficient decreases causing a worse velocity accuracy.

For β factor correction, the main factors that will be taken into account in the following analysis are:

1. The effect of the surface roughness which is supposed to be Gaussian with standard deviation σ_h . The corresponding time spread of the received signal can be expressed as:

$$\sigma_{t1} = \frac{2\sigma_h}{c} \quad (5-21)$$

2. The effect of the surface RMS slope, s , which acts as a variation of the off-nadir angle. By some degree of approximation (validity of beam-limited condition) this effect can be evaluated by considering the equivalent variation of slant range swath (SW) within the antenna footprint due to a variation of the off-nadir angle $\Delta\theta$.

Since it is:

$$SW = H \left(\frac{1}{\cos(\theta + \theta_{3dB})} - \frac{1}{\cos(\theta - \theta_{3dB})} \right) \quad (5-22)$$

the effect of the RMS slope can be obtained by:

$$\sigma_{t2} = \frac{2\Delta SW}{c} = \frac{2}{c} (SW_{\theta+\Delta\theta} - SW_{\theta}) \quad (5-23)$$

$$\text{when } \Delta\theta = s \quad (5-24)$$

As example, Figure 5-9 shows the σ_{t2} term as a function of radar altitude. The σ_{t1} term can be considered negligible up to surface roughness of the order of few meters.

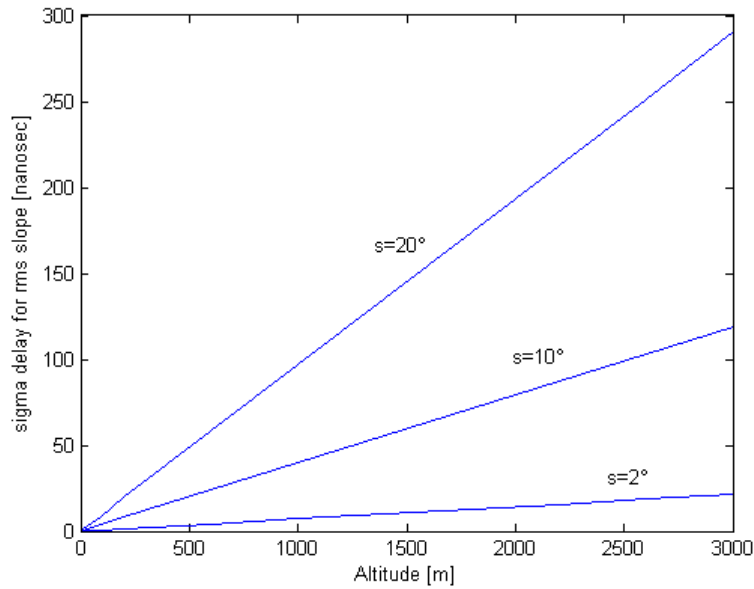


Figure 5-9 – The effect of terrain RMS slope as a function of radar altitude

The final achievable range accuracy is plotted in Figure 5-10 for various values of RMS slope.

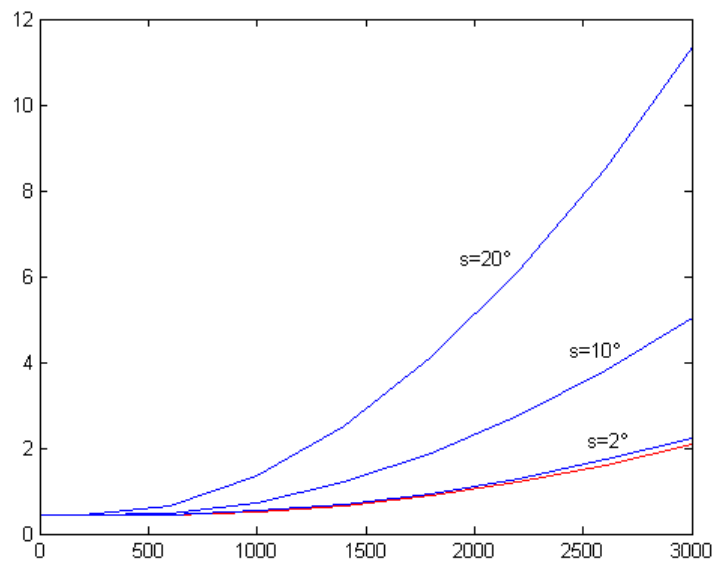


Figure 5-10 – Example range accuracy as a function of radar altitude for various RMS slope values (the red curve is without slope)

Therefore, considering β , it will be modified considering σ_{t1} and σ_{t2} . So, considering that σ , without correctional quantities, is equal to:

$$\sigma_t = \frac{1}{2\pi\beta} \quad (5-25)$$

By considering the original σ_t and the two correctional quantities, the final second moment of range power spectrum can be written as:

$$\sigma_{t,new} = \sqrt{\sigma_t^2 + \sigma_{t1}^2 + \sigma_{t2}^2} \quad (5-26)$$

A new β factor can be found:

$$\beta_{new} = \frac{1}{2\pi\sigma_{t,new}} \quad (5-27)$$

Correct δT_R must be written as:

$$\delta T_R = \frac{1}{\beta_{new} \sqrt{2N_p E/N_0}} \quad (5-28)$$

5.5. Velocity Measurements Accuracy

The algorithm chosen to extract the Doppler frequency is the Pulse-Pair algorithm that is time-domain-based. In this way the computational effort needed to get the frequency-domain information is avoided.

Basically the Pulse-Pair algorithm consists in the computation of the phase of the autocorrelation function of the input signal. This phase is proportional to the velocity to be estimated.

The standard deviation of such estimator is [Ref. 8]:

$$\delta V_{pp} = \left\{ \frac{V_a^2}{8\pi^2 M} \left[\frac{1}{\rho^2} (1 + SNR^{-1}) - 1 \right] \right\}^{1/2} \quad (5-29)$$

where ρ^2 is the autocorrelation coefficient, which in case of Gaussian power spectra can be expressed as a function of actual second moment σ_v of velocity power spectra, as [Ref. 8]:

$$\rho^2 = \exp\left(-4\pi^2 \frac{\sigma_v^2}{V_a^2}\right) \quad (5-30)$$

In this case the computational effort is of the order of M, instead of M·log₂M in case of DFT calculation.

The requirements for the Exomars RDA provide a maximum error that can be tolerated in the measurement of the velocity component in the DM frame (BRF). These errors will be a linear combination of the errors present in each beam.

Using a composition of errors based on RMS values and assuming the same error on each beam in worst case, the accuracies are:

$$\begin{cases} \sigma_x = K_x \sigma_b \\ \sigma_y = K_y \sigma_b \\ \sigma_z = K_z \sigma_b \end{cases} \quad (5-31)$$

where:

$$\begin{cases} K_x = \sqrt{c_{11}^2 + c_{12}^2 + c_{13}^2} \\ K_y = \sqrt{c_{21}^2 + c_{22}^2 + c_{23}^2} \\ K_z = \sqrt{c_{31}^2 + c_{32}^2 + c_{33}^2} \end{cases} \quad (5-32)$$

A plot of K_x, K_y and K_z versus α is shown in Figure 5-11. Note that K_y = K_z for every angle α as expected by simple geometrical considerations.

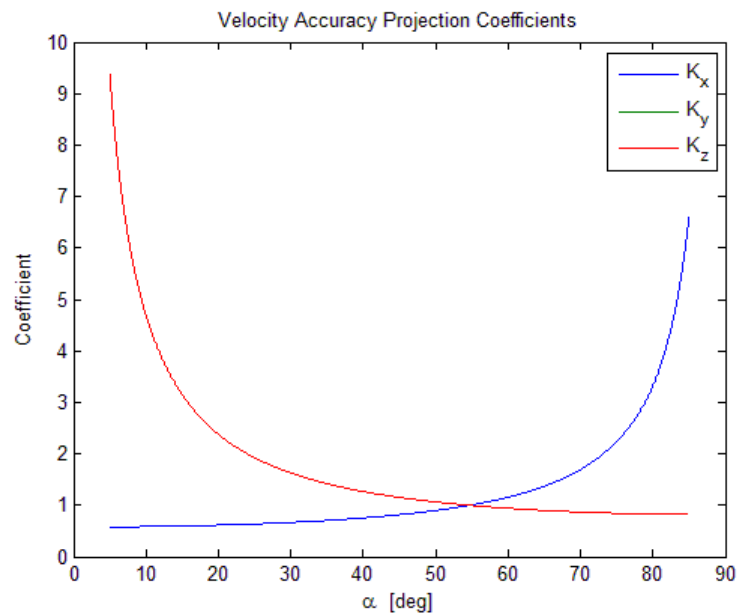


Figure 5-11 – Plot of K_x, K_y and K_z as a function of α

In nominal case, every velocity beam has an error σ_{bi} , so accuracies are:

$$\begin{cases} \sigma_x = [(C_{11} \sigma_{b1})^2 + (C_{12} \sigma_{b2})^2 + (C_{13} \sigma_{b3})^2]^{0.5} \\ \sigma_y = [(C_{21} \sigma_{b1})^2 + (C_{22} \sigma_{b2})^2 + (C_{23} \sigma_{b3})^2]^{0.5} \\ \sigma_z = [(C_{31} \sigma_{b1})^2 + (C_{32} \sigma_{b2})^2 + (C_{33} \sigma_{b3})^2]^{0.5} \end{cases} \quad (5-33)$$

Also in this case, as done for the range accuracy, the actual sampling frequency, induced by the finite integration time, should be considered. It is possible to write:

$$\delta V_q = \frac{V_a}{M \sqrt{12}} \quad (5-34)$$

Therefore, the total uncertainty of the velocity estimate is:

$$\delta V = \sqrt{\delta V_{pp}^2 + \delta V_q^2} \quad (5-35)$$

It is worth noting that, in the evaluation of noise power, the bandwidth to be considered (B_N) is related to twice (in case of measure of both positive and negative velocities) the maximum Doppler frequency expected:

$$B_N = 2 \max(f_D) = \frac{4 V_{max}}{\lambda} \quad (5-36)$$

For example, by considering a maximum velocity of 160 m/s, an integration time of 8.3 ms and a PRF of 100 KHz, the achievable SNR is reported in Figure 5-12.

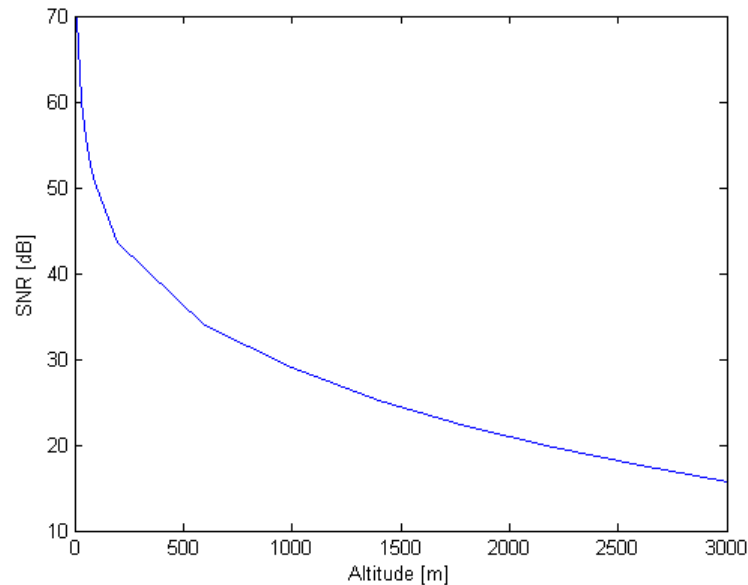


Figure 5-12 – Example SNR as a function of radar altitude for the velocity estimation as a function of radar altitude

The corresponding velocity accuracy is shown in Figure 5-13, for various ρ^2 values.

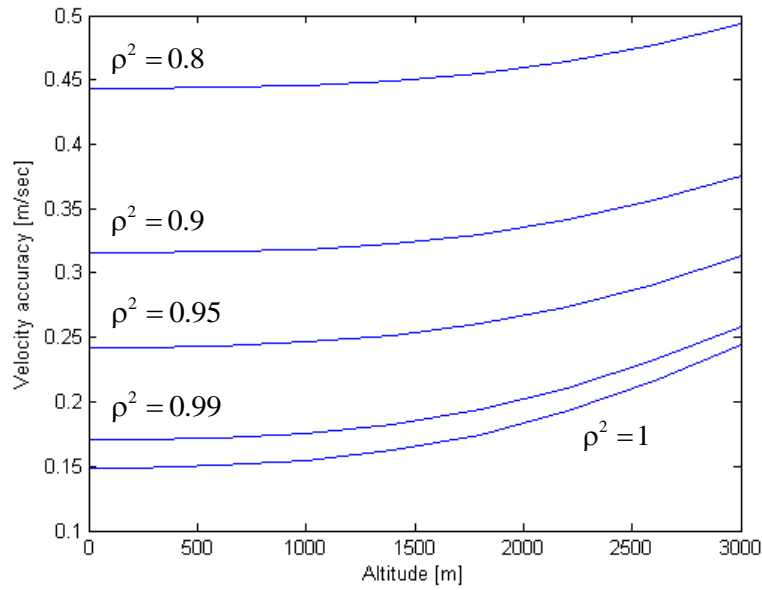


Figure 5-13 – Velocity accuracy (pulse-pair technique) as a function of radar altitude and for various ρ^2 values

As expected the final accuracy is limited, for high values of SNR and for $\rho^2 = 1$, by δV_q which in the present case is about 0.14 m/s.

Figure 5-14 shows the autocorrelation coefficient ρ^2 as a function of second moment of velocity power spectrum σ_v .

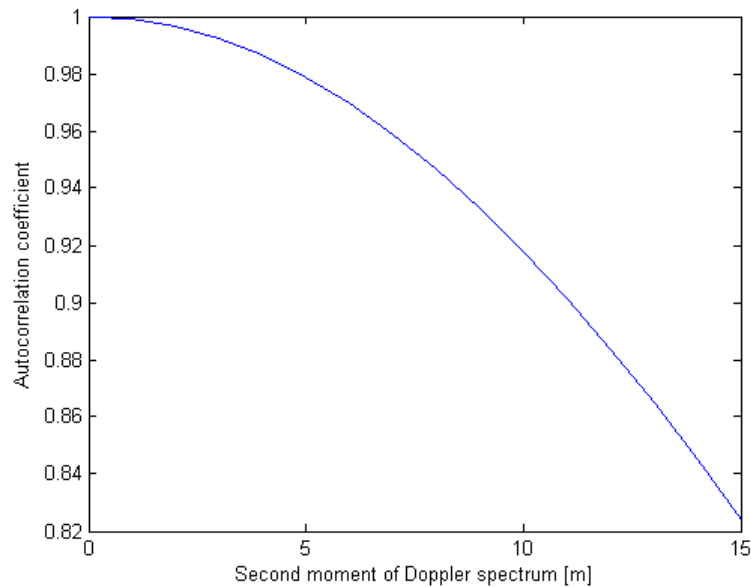


Figure 5-14 – Autocorrelation coefficient ρ^2 as a function of second moment of velocity power spectrum σ_v

5.5.1. Factors Affecting Velocity Measurements Accuracy

In general, all factors that contribute to second moment of signal Doppler spectrum (σ_v) can affect the final velocity accuracy. In other words, by increasing the spread of the signal Doppler spectrum, the corresponding autocorrelation coefficient decreases causing a worse velocity accuracy.

The main factors that will be taken into account in the following analysis are:

1. The effect of the finite integration time, that contributes to the final second moment of the velocity spectrum as:

$$\sigma_{V1} = \frac{\lambda}{2 T_{meas}} \quad (5-37)$$

As example, this term can be of the order of 0.5 m.

2. The effect of acceleration (a) and Jerk (J), since they cause, along each beam, a variation of the velocity within the integration time. By supposing these effects to be constant over the integration time, their contribution to the second moment of the Doppler spectrum can be written as:

$$\sigma_{V2} = a_r T_{meas} + \frac{1}{2} J_r T_{meas}^2 \quad (5-38)$$

By considering a radial acceleration of 3 m/s² and a radial jerk of 30 m/s³, this term is on the order of 0.03 m.

3. The effect of -3dB antenna aperture, θ_{3dB} , that causes a spread of possible off-nadir angles. In other words, considering a generic Doppler frequency f_D :

$$f_D = \frac{2V}{\lambda} \sin \theta \approx \frac{2V}{\lambda} \theta \quad (5-39)$$

$$\text{where } |\theta| \leq \frac{\theta_{3dB}}{2}$$

the corresponding spread in the velocity domain σ_v is:

$$\sigma_{V3} \approx 2 V \Delta \theta \quad (5-40)$$

which can be maximized such as:

$$\sigma_{V3} \leq \frac{\lambda PRF}{4} \theta_{3dB} \quad (5-41)$$

As example this term can be of the order 5 m.

4. The effect of antenna rotation with angular velocity, $\dot{\theta}$, since it causes, for rotations along a perpendicular directions to each beam, an additional spread of the off-nadir angle values. By supposing the perpendicular component of angular velocity to each beam to be constant over the integration time, this terms can be maximized as done before:

$$\sigma_{V4} \leq \frac{\lambda PRF}{2} \dot{\theta}_{\perp} T_{meas} \quad (5-42)$$

By considering an angular velocity of 60°/s, this term can be of the order of 4 m.

By considering all these terms independent, the final second moment of velocity power spectrum can be written as:

$$\sigma_V = \sqrt{\sigma_{V1}^2 + \sigma_{V2}^2 + \sigma_{V3}^2 + \sigma_{V4}^2} \quad (5-43)$$

In present examples, the final second moment of velocity power spectrum is equal to about 6.5 m, that implies a autocorrelation coefficient of about 0.96.

Examples done show that, among these effects, the most significant is that due to actual antenna aperture. By considering only this term and by recalling the expression of the autocorrelation coefficient, it is possible to write:

$$\rho^2 = e^{-4\pi^2 \theta_{3dB}^2} \quad (5-44)$$

which is plotted in Figure 5-15:

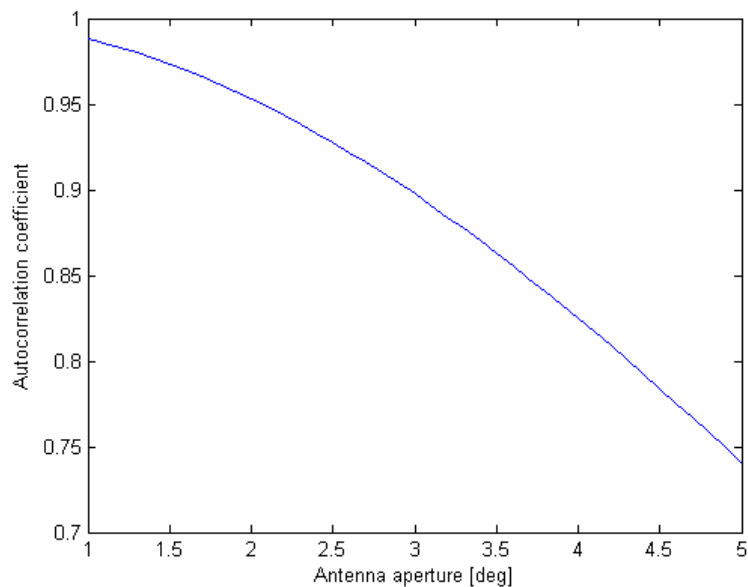


Figure 5-15 – Autocorrelation coefficient ρ^2 as a function of antenna aperture

6. PRELIMINARY SYSTEM DEFINITION

To achieve requirements, all radar parameters must be set in opportune way. Radar baselines are determined considering technological state of art, technological know-how, radar operative scenarios and reported requirements. In many cases, a compromise is necessary for optimum parameters choice.

This Chapter will analyze a preliminary system definition for first performance evaluation. After first evaluation, this system definition can be confirmed or modified to obtain specific performance improvements.

6.1. Operating Frequency

The selection of the carrier frequency is a major choice in the definition of the RDA. It impacts directly on size, mass as well as on performance. Size and mass considerations suggest use of high frequencies (i.e. short wavelengths) in order to use smaller microwave components and to limit the antenna size needed to get the desired beamwidth.

On the performance side, the main topics to be introduced are:

1. *The backscattering model of the terrain*: the minimum value for the terrain backscattering coefficient σ_0 and also its interval of variation are important parameter in the evaluation of the hardware requirements needed to meet the radar performance. Current models foresee a smaller range of variation for σ_0 as frequency increases and also a higher absolute level for large incidence angles.
2. *The need to have enough resolution in velocity measurement*: the selected approach to velocity measurement is to extract information by the Doppler-shift experienced by the radar signal as the DM is moving in respect to the martian surface. It is well-known that the amount of Doppler-shift for a fixed velocity is a linear function of the carrier frequencies and, therefore, using high frequencies helps velocity measurement resolution and accuracy.
3. *The beam aperture for a fixed antenna size*: beam aperture shall be narrow in order to increase antenna gain and to improve measurement accuracy (see Figure 5-15). In fact, beam aperture depends linearly by wavelength and therefore from the inverse one of the carrier frequency.

All the factors briefly recalled above, push for a carrier frequency as high as possible (within a reasonable range). At the same time, availability, reliability and cost and schedule risk mitigation for the hardware implementation, set an upper bound to frequencies usable for this specific mission.

Taking into account technological issues and heritage, an operating frequency in Ka band (35 GHz) has been selected.

6.2. Sampling Frequency and IF Conversion

In order to reduce size and power consumption of the Electronics Sub-system (ELS), it is implemented the final down-conversion to baseband and the I&Q components extraction in the digital domain. In this approach, the fundamental parameter to be selected is the sampling frequency of the A/D converter. The choice is driven by the necessity to avoid aliasing according to the Nyquist sampling theorem and the aim to simplify as much as possible the I&Q extraction process.

In addition, the value of sampling frequency determines the maximum quantization error accepted for range measurements, given by relation (5-17).

By assuming a minimum range error of 40 cm, the sampling frequency, after signal modulus extraction, should be equal to 100 MHz. This implies a sampling frequency on real signal, before modulus extraction, of 200 MHz.

A practical rule very useful to simplify the digital down-conversion and the I&Q extraction is to select a sampling frequency four times higher than the IF. The IF conversion frequency is selected to 50 MHz.

Of course, this conversion frequency is compatible with the expected receiving signal bandwidth (see [Paragraph 6.5](#)).

6.3. Antenna Geometry

The selected antenna geometry is that shown by Figure 3-5, with a central beam pointed at nadir for range measurements and three pointed at off-nadir dedicated to velocity measurements.

As explained in [Paragraph 3.4](#), the choice of the off-nadir angle shall take into account that small values would cause an increased error in velocity measure along y and z axes (high values for K_y and K_z) that would further tighten the required performance for the Doppler measure.

At the same time considerations about backscattering coefficient and received echo power impose to limit the value of such angle.

Considering that requirements describe an operational scenario where off-nadir angles up to 35° are foreseen, and that non-ambiguous measures are to be given for off-nadir angle up to 55°, values above 20° are not feasible.

For the velocity beams, a preliminary value of 15° seems to be a good compromise and has been selected for the following analysis.

With this value of off-nadir angle, Figure 6-1, shows a factor of 3 for converting velocity measurements to those required along y- and z-axes. The conversion factor for x-axis is around 0.6.

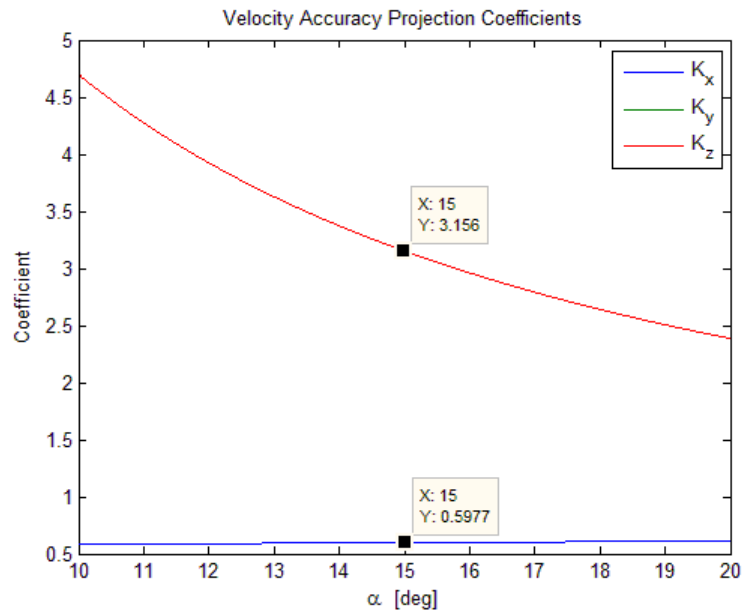


Figure 6-1 – Velocity accuracy conversion factor (from velocity beams to x, y and z axes)

Therefore a factor of 3 can be selected as worst-case condition. So, in the following analysis, the obtained velocity accuracies will be multiplied by a factor of 3 for taking into account the conversion for the velocity components along x, y and z axis.

6.4. Antenna Beamwidth and Gain

Analysis of Figure 5-15 shows that a sufficient correlation coefficient (about 0.9) can be obtained if the antenna aperture is less than about 3° . This explains easily the main reason to have narrow antenna beams. The -3dB antenna beamwidth is fixed to 3° .

This goal can be reached, at the working frequency, by considering a $15 \times 15 \text{ cm}^2$ antenna aperture. The size is compatible with the typical available size and weight of the whole RDA system.

For the following analysis, each beam will be considered as produced by a uniformly illuminated squared aperture. By supposing an efficiency of 0.7, the gain is equal to 34 dB.

6.5. Signal Bandwidth

At the minimum working altitude (10 m) the received signal is expected after 66.7 ns after the leading edge of the transmitted pulse. This implies very short time for switching off the signal before opening the sampling window.

Therefore, also considering technological issues, the rising time up of the transmitted pulses should be set to 5 ns. This implies a bandwidth of the transmitting chain of 200 MHz ($B_t \approx 1/t_{\text{rise}}$) [Ref. 4].

The received bandwidth, instead, is due to the duration of the received pulses, that is mainly due to the transmitted pulse length but it is also affected by scattering geometry.

By considering a minimum pulse length of 66.7 ns, it is expected a maximum received bandwidth of 15 MHz ($B_r \approx 1/t_{\text{pulse}}$). In fact, if the receiver passband is too wide compared with the spectral bandwidth of radar signal, extra noise is introduced (since noise power is proportional to bandwidth) and the signal to noise ratio is reduced. On the other hand, if the receiver bandwidth is too narrow, the noise is reduced but so is the signal energy. Consequently, too narrow a bandwidth relative to the signal spectral width reduced the signal to noise ratio, too wide a bandwidth also reduced the signal to noise ratio. Thus, there is an optimum value of bandwidth relative to signal spectral width that maximized the signal to noise ratio. With rectangular-like pulses and conventional filter design, experience

showed that the maximum signal to noise ratio occur when the receiver bandwidth B_r is approximately equal to the reciprocal of the pulsewidth t_{pulse} or when $B_r t_{\text{pulse}} \approx 1$ [Ref. 4].

6.6. Receiver Noise Figure

Driven by technological issues, a noise figure of 5 db is assumed for the receiving chain.

6.7. Antenna, Atmospheric & Vented Bags Losses

The insertion losses due to antenna front-end is assumed to be 4 dB, including transmission and receiving paths ($L_{\text{sys}} = 4$ dB).

The effects of either superficial dust and thrusters plumes have been included in the total atmospheric losses. The overall effect has been assumed to be 2 dB two-way ($L_{\text{atm}} = 2$ dB).

Another attenuation is induced by the vented bags that can be the most critical item in the whole link budget of the system. In fact the vented bags impact on the RDA performance is expected to be significant, and ad hoc countermeasures shall be adopted in order to minimize this effect. The preliminary analysis of vented bags induced performance degradation with vented bags layers of total 5 cm-thickness, showed two possible operational conditions:

- If perfect adherence is ensured between vented bags layers, the one-way insertion loss is in the 2-3 dB range.
- If void or gases are present between successive vented bags layers, the insertion loss rises up to 35 dB.

The effect of vented bags is assumed to be 2 dB two-way ($L_{\text{bags}} = 2$ dB).

Overall losses are set equal to 4 dB for system losses (L_{sys}) and 4 dB for atmospheric and vented bags losses ($L_{\text{atm}} + L_{\text{bags}}$).

6.8. Integration Time

The necessity of estimating the velocity components of the descent module with the required accuracy (see [Paragraph 2.2](#)) turns into the requirement for accurate Doppler velocity measurement. It is well known that the accuracy of velocity estimation dependent on the Signal to Noise Ratio (SNR) (see [Paragraph 5.3](#)), and can be theoretically minimized by achieving high SNR values. The accuracy for velocity component estimation along the Line of Sight (LoS) straightforwardly follows as a function of the accuracy in Doppler estimation via the radar wavelength. However, the accuracy of the estimate is limited by the quantization error that is introduced by the sampling frequency (see [Paragraph 5.5](#)). It is possible to write the accuracy of the velocity component as the sum of two terms, the former derived from doppler velocity measurement accuracy, δV_{pp} (see relation (5-29)), and the latter related to the quantization effect, δV_q (see relation (5-34)).

It is known [[Ref. 4](#)] that the velocity resolution is determined by the integration time, T_{meas} . In this case the integration time is the interval of persistence on a given antenna beam for collecting the relevant terrain echo/s. The resulting accuracy is equal to:

$$\delta V_q = \frac{\lambda}{2\sqrt{12} T_{meas}} \quad (6-1)$$

This means that in high-SNR conditions, the term δV_{pp} can be neglected, and the requirements should be met by the δV_q term only. From the above reported relationship, it is possible to obtain the minimum integration time values to achieve the required accuracy in high-SNR conditions.

For example, if the required accuracy in high-SNR conditions is equal to 0.1 m/s and the update frequency is selected among 20, 40 or 50 Hz, the minimum integration time is reported in Figure 6-2 as a function of radar carrier frequency.

In this Figure, maximum integration time is also reported for each selectable update frequency.

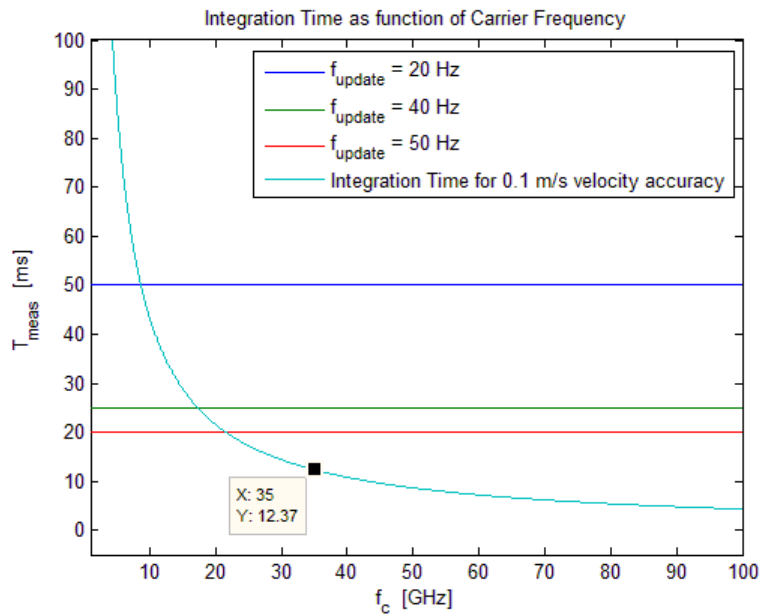


Figure 6-2 – Minimum integration time for single velocity measurement as a function of radar carrier frequency

Figure 6-2 shows that for each carrier frequency, there is a minimum integration time that allows to achieve the required accuracy in high-SNR conditions. If T_{meas} can be selected great than this value, δV_q is smaller; otherwise T_{meas} can be smaller but required accuracy in high-SNR conditions isn't verified.

Considering system constraints, it is worth noting that T_{meas} is only up-limited by selected update frequency, while minimum integration time is only an indication to obtain required accuracy in high-SNR conditions and can be violate.

It is evident that at lower frequencies, minimum integration time is very close or even exceeds the selected measurement refresh time, and therefore the two requirements (i.e., accuracy and refresh rate) cannot be satisfied simultaneously. In any case, it is to be stressed that the refresh time is intended as the time interval between two successive deliveries of the four measurements (V_x , V_y , V_z and H).

If these operations are operated sequentially, the time allocated for each velocity measurement is further diminished, so the integration time is a driving requirement and subject to critical trade-off for RDA definition.

So, Figure 6-2 leads to an important engineering considerations: to achieve a required or greater accuracy in high-SNR conditions, a precise values interval for the integration time must be considered. To obtain the amplest interval, high values of carrier frequency and low update frequency must be taken into account.

It is worth noting that preliminary system definition has led to $f_c = 35$ GHz and $f_{\text{update}} = 20$ Hz. So, for this example the values interval for the integration time is [12.37, 50] ms and, under the hypothesis of equal sequential integration times, each measurement had an integration time equal to 12.5 ms.

For range and velocity integration time, a preliminary value can be evaluated considering range integration time constraints (see [Paragraph 4.3](#)). The constraints up-limits range integration time through the relations (4-21) and (4-25)

As regards first expression, range integration time can be evaluated considering worst case values for radial velocity, acceleration and jerk expressed in terms of along x_b -, y_b - and z_b -axis components (see [Paragraph 2.1](#)). Worst case for range integration time is when the antenna boresight is aligned with the each vector quoted before.

Therefore it is assumed that radial components are equal to their module:

$$\begin{aligned} V_r &= 90.2 \text{ m/s} \\ a_r &= 13.4 \text{ m/s}^2 \\ J_r &= 134.2 \text{ m/s}^3 \end{aligned} \tag{6-2}$$

As regards second expression, range integration time can be evaluated considering worst case values for angular velocity vector (see [Paragraph 2.1](#)). Worst case for range integration time is when the antenna boresight is perpendicular with the angular velocity vector.

Therefore it is assumed that perpendicular component is equal to its module:

$$\dot{\theta}_{\perp} = 60^\circ/\text{s} \tag{6-3}$$

So, the integration time for range measurements is set to 4.154 ms.

For velocity measurements, the integration time affects the autocorrelation coefficient through equations (5-37), (5-38) and (5-42) and directly the final velocity accuracy expressed by (5-29).

Its value can be determined by taking into account the integration time for range measurements $T_{meas,R}$ and total update frequency, f_{update} , for measurements:

$$T_{meas,V} \leq \frac{1}{3} \left(\frac{1}{f_{update}} - T_{meas,R} \right) \quad (6-4)$$

Therefore, by considering a measurement update frequency of 20 Hz, the integration time for range measurements is set to 15.28 ms.

Of course this value corresponds to a minimum velocity measurable of about 0.3 m/s, since minimum a wavelength should be observed within the integration time.

Optimum range and velocity integration times will be analyzed in [Paragraph 7.1](#) and [7.2](#) and selected in [Paragraph 7.3.1](#) after optimization analysis.

6.9. Pulse Repetition Frequency

The PRF values are mainly influenced by the ambiguities. If the Pulsed CW radar configuration has high PRF values – usually implemented in order to sense high Doppler signals unambiguously and to improve SNR with a great number of pulses, M – this leads to ambiguities in range, given the range interval of interest for landing radars. This turns into the basic trade-off for Doppler altimeter radars: range versus Doppler ambiguity.

In fact, the requirement for range ambiguity is expressed in terms of maximum altitude and off-nadir angle:

$$\begin{cases} H_{max} = 3000 \text{ m} \\ \theta_{max} = \pm 55^\circ \end{cases} \quad (6-5)$$

This implies, in the worst case, a maximum slant range of about 5230 m and a preliminary PRF value less than about 28.7 KHz.

The requirement for velocity ambiguity, at an altitude of 3000 m, is expressed in terms of velocity component, such as:

$$\begin{cases} V_{x,max} = 160 \text{ m/s} \\ V_{y,max} = \pm 45 \text{ m/s} \\ V_{z,max} = \pm 45 \text{ m/s} \end{cases} \quad (6-6)$$

The worst case is when the antenna boresight is aligned with the vector of maximum velocity. Therefore we assume:

$$V_{max} = \sqrt{V_{x,max}^2 + V_{y,max}^2 + V_{z,max}^2} = 172.2 \text{ m/s} \quad (6-7)$$

This forces a preliminary PRF value greater than about 80 KHz.

From this analysis it is clear that a single value of PFR can't satisfy both the requirement for range and velocity ambiguities, so Pulsed CW radar configuration can't work in single-mode radar. This is the main reason to have separate beams for estimating velocity and range, by excluding possible complicate solutions (staggered PRF).

Therefore, beams dedicated to range and velocity measurements must work with different PRF values. In particular, the antenna beam dedicated to range measurement is identified as "Beam 0" and it is characterized by its own observation parameters (persistence time, PRF) and radar waveform parameters (pulse width). The other three beams are dedicated to velocity measurements and their relevant parameters generally differ from Beam 0 parameters, while identical one to the other.

Of course, the maximum value of PRF will condition the maximum transmitted pulse duration.

Optimum range and velocity pulse repetition frequencies will be analyzed in [Paragraph 7.1](#) and [7.2](#) and selected in [Paragraph 7.3.2](#) after optimization analysis.

6.10. Transmitted Pulse Duration

The increase of the transmitted pulse duration allows to have higher SNR and, therefore, better performance for both range and velocity measurements.

The maximum value is limited by the available time for reception given by the PRF value and the maximum expected range.

The minimum value is given by technological issues and it determines the minimum working range of the RDA system. In fact, a Pulsed CW radar can't work for time delay values less than the transmitted pulse duration.

Considering that the requirements impose a minimum operative altitude of 10 meters, the minimum transmitted pulse duration is set equal to 66.7 ns.

Optimum range and velocity transmitted pulse duration will be analyzed in Paragraph 7.1 and 7.2 and selected in Paragraph 7.3.3 after optimization analysis.

6.11. Signal Peak Power, Link Budget and Receiver Dynamics

The basic relations for evaluating the expected signal to noise ratio have been reported in Paragraph 5.3. On the basis of this formulation, in this Paragraph, in order to infer the expected signal dynamics, the system link budget for various attitude values will be evaluated.

To this end, the system parameters assessed up to here, will be used.

The value of the transmitted peak power is driven by technological issue, a level of 30 dBm (1 W) is assumed. PRF is a linear law between (3000 m , 100 KHz) and (10 m, 2 KHz), the transmitted pulse duration has been assumed equal to its max values compatibly with systems bounds.

In order to assess the dynamics of the receiver, the expected maximum and minimum values of received power will be determined.

To determine these two extreme cases is not easy, since there are the combined effects of altitude and integration area, that is, the system passes from beam to pulse limited conditions by changing off-nadir angle and altitude.

To this aim, Figure 6-3 shows the received power as a function of radar altitude for three values of off-nadir angle: the minimum (0°), the maximum (20° of antenna pointing + 35° of attitude) and a mean value (30°). The transmitted pulse duration has been assumed equal to its max values compatibly with systems bounds.

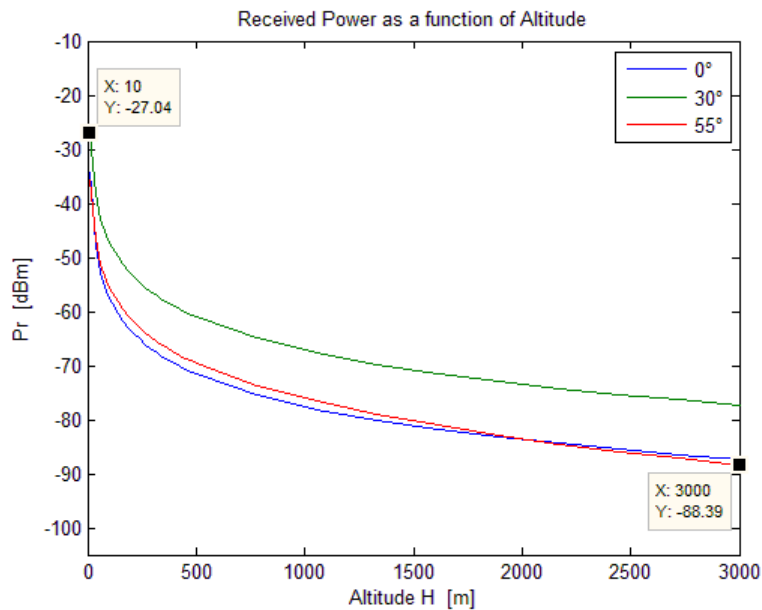


Figure 6-3 – Received power

The maximum received power happens at the minimum altitude (10 m) but for an off-nadir angle of 30° , since the wider antenna footprint tends to dominate with respect to the decrease of backscattering coefficient.

Instead, as expected, the minimum received power refers to the higher altitude (3000 m) and off-nadir angle (55°), even if for null off-nadir received power is quite close because of the combined effects of altitude and integration area.

As shown in Figure 6-3, at low altitude the higher received power is -27.04 dB for an off-nadir of 30° , while at high altitude the lower received power is -88.39 dB for an off-nadir of 55° .

So, two extreme cases are characterized by an off-nadir of 30° at 10 m of altitude for maximum received power and by an off-nadir of 55° at 3000 m of altitude for minimum received power. All this parameters are reported in the two columns of link budget performed in following Table 6-1:

	Maximum Received Power $\left\{ \begin{array}{l} H = 10 \text{ m} \\ \theta = 30^\circ \\ P_t = 66.7 \text{ ns} \end{array} \right.$	Minimum Received Power $\left\{ \begin{array}{l} H = 3000 \text{ m} \\ \theta = 55^\circ \\ P_t = 1 \mu\text{s} \end{array} \right.$
P_{tp}	30 dBm	
$\frac{\lambda^2}{(4\pi)^3}$	-74.3 dB	
G_0^2	68 dB	
$\frac{1}{H^4}$	-40 dB	-139.1 dB
$L_{atm} \cdot L_{sys}$	-8 dB	
A_{eq}	8.87 dB	51.62 dB
σ_0	-11.6 dB	-16.62 dB
P_r	-27.04 dBm	-88.39 dBm
$K \cdot B_N \cdot T_0 \cdot F$	-127.22 dBm	-139.38 dBm
	-125.23 dBm	

Table 6-1 – Link budget for the two extreme case for the received power

As indicated in Table 6-1, in preliminary analysis, the maximum expected signal dynamic that the receiver should deal with is 61.35 dB.

6.12. Detection Probability for Range Measurements

Signal to noise ratio is the key parameter affecting the performance of the system and its evaluation has been treated in [Paragraph 5.3](#). While the actual performance, in terms of range and velocity accuracies, will be assessed in [Chapter 8](#), the aim of the present Paragraph is to demonstrate that the system is always able to work with high level of detection probability, for range measurements.

For accomplishing this goal, the worst case for range measurements will be considered, so maximum off-nadir angle for X_b -axis is selected equal to 35° . For range measurements, PRF is selected equal to 25 KHz, the transmitted pulse duration has been assumed equal to its max values compatibly with systems bounds. The number of pulses to be integrated is equal to 103 (25 KHz x 4.154 ms).

Figure 6-4 shows the achievable SNR as a function of radar altitude for attitude equal to 0° , 15° and 35° .

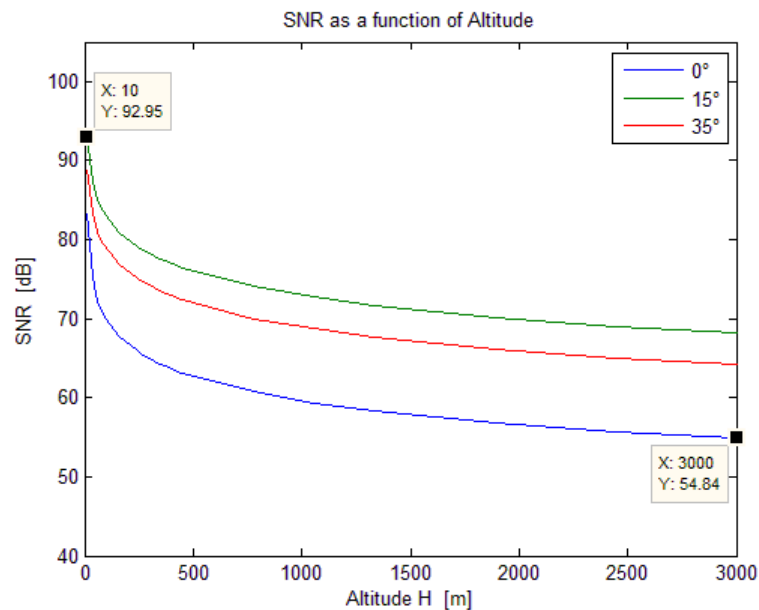


Figure 6-4 – Integrated SNR (range measurements) as a function of radar altitude for various off-nadir angle (0° , 15° and 35°)

Therefore, for range measurements, it is expected to have integrated SNR ranging from 54.84 dB up to 92.95 dB.

For radar system it always exists a trade-off between the probability of target detection when the target is present and the probability of false alarm when the target is not present. In the case of RDA system, it is preferable to work with low false alarm probability, since this means a wrong range measurements.

For this reason the design choice is to fix the probability of false alarm to a value that imposes no risk to the mission and then to infer the probability of detection as a function of this value and of the SNR value.

The value chosen for the probability of false alarm P_{fa} can be deduced from the acceptable mean time between two consecutive false alarms T_{fa} , by using the relation [Ref. 4]:

$$P_{fa} = \frac{1}{B_r T_{fa}} \quad (6-8)$$

Considering that the whole operative life of the RDA is of the order of 100 seconds, a T_{fa} one order of magnitude greater (1000 s) is acceptable; moreover, receiver bandwidth is 15 MHz at low altitude and 50 KHz at high altitude, so that gives a false alarm probability of 6.67×10^{-11} at low altitude and 2×10^{-8} at high altitude.

The probability of detection can be evaluated with the following simplified expression [Ref. 4]:

$$P_D = \frac{e^A}{1+e^A} \quad (6-9)$$

where:

$$\begin{cases} A = \frac{SNR-B}{0.12 B+1.7} \\ B = \log\left(\frac{0.62}{P_{fa}}\right) \end{cases} \quad (6-10)$$

The detection probability as a function of SNR is plotted in the following Figure 6-5.

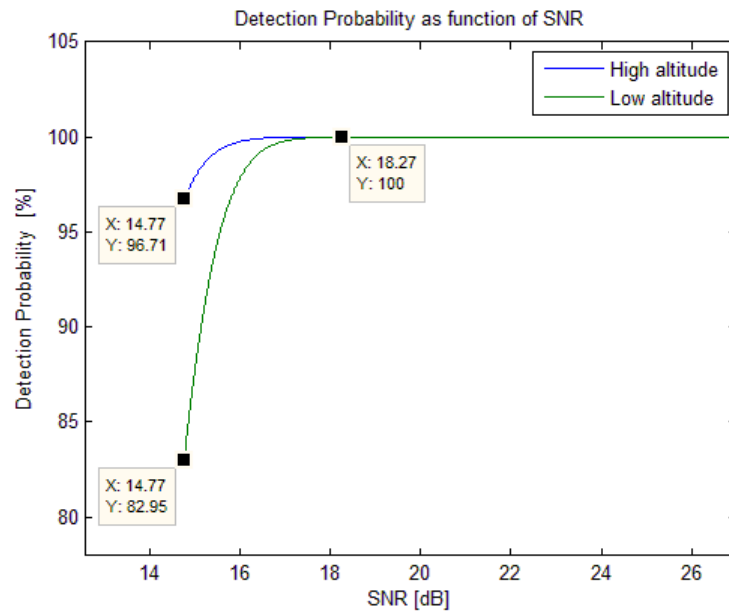


Figure 6-5 – Detection probability as a function of SNR

This Figure shows that detection probability reaches 100 % from SNR levels greater than 18.27 dB both at high and at low altitude, so considering that in worst case signal to noise ratio reaches the minimum value of 54.84 dB, RDA system detection probability is equal to 100 % along the entire descent.

Therefore, in the worst case along the entire descent, for range measurements the RDA system will be always able to work with a mean time between wrong measurements (false alarm) much greater (1000 s) that the operative life of the instrument itself with a probability of detection very close to 100 %.

So, the effect of both false alarm and detection probability will not be considered in the evaluation of system performance.

7. PERFORMANCE OPTIMIZATIONS

The primary goal of Performance Optimizations is to minimize, as far as possible, range and velocity measurement errors, i.e., increase range and velocity accuracies. This is done establishing optimum preliminary parameters values and laws.

This goal leads, as far as possible, to the respect of reported requirements (see Chapter 2).

For radar optimizations, a first analytical investigation will be done, but, due to complex relationship among all radar parameters, numerical investigation will be necessary for best radar optimizations.

The computer software used for this purpose is Matlab®.

7.1. Analytic Investigation

In this Paragraph, an analytical range and velocity measurement error optimization will be considered.

Thanks to Matlab® “Accuracy_Compact_Formulas.m” stand-alone script, range and velocity errors can be written as:

$$\delta R = \frac{1}{12} c \left(18 \frac{N}{\beta^2 PRF_R T_{meas,R} E_{r,R} B_r} + \frac{3}{f_{samp}^2} \right)^{1/2} \quad (7-1)$$

$$\delta V = \left[\frac{1}{24} \left(18 PRF_V K_{xyz}^2 \lambda^2 \left[\frac{\left(1 + \frac{N}{PRF_V T_{meas,V}} \right)^2}{\left\{ \frac{-\pi^2 \left[4 \frac{\lambda^2}{T_{meas,V}^2} + 16 \left(\alpha_r T_{meas,V} + \frac{1}{2} J_r T_{meas,V}^2 \right)^2 + PRF_V^2 \lambda^2 \theta_{3dB}^2 + 4 PRF_V^2 \lambda^2 \theta_1^2 T_{meas,V}^2 \right]} \right\}} \right] - 1 \right] + \frac{12 \frac{\lambda^2}{T_{meas,V}^2}}{\pi^2 T_{meas,V}} \right)^{1/2} \quad (7-2)$$

where c is light velocity

λ is radar wavelength

f_{samp} is sampling frequency

B_r is echo bandwidth

N is noise

$E_{r,R}$ is range received energy

Pr_V is velocity beam received power

β is the effective bandwidth

θ_{3dB} is -3dB antenna beam aperture

a_r is velocity beam radial acceleration

J_r is velocity beam radial jerk

$\dot{\theta}$ is attitude changing rate

$T_{meas,R}$, $T_{meas,V}$ are respectively range and velocity integration time

PRF_R , PRF_V are respectively range and velocity pulse repetition frequency

K_{xyz} is velocity projection coefficient.

Analytical dependences under investigation are PT_R , PT_V , $T_{meas,R}$, $T_{meas,V}$, PRF_R , PRF_V :

- As regards pulse duration PT_R and PT_V , it is hard to explicit this analytical dependences because of convolution integrals. However, the PT_R and PT_V increases lead to the $E_{r,R}$, β and Pr_V increases. This analytically leads to decrease of range and velocity measurement error, so the optimization is achieved when pulses duration is maximized compatibly with system constrains such as pulse repetition intervals (PRIs) and signals trip time.
- As regards range integration time $T_{meas,R}$, analytically, its increase leads to decrease range measurement error, so the optimization is achieved when range integration time is maximized compatibly with system bounds such as range integration time constraints (see [Paragraph 4.3](#)).
- As regards velocity integration time $T_{meas,V}$, analytically, it is hard to investigation this dependence for the attainment of the optimization, so it will be done a numerical investigation.
- As regards range pulse repetition frequency PRF_R , analytically, its increase leads to decrease range measurement error, so the optimization is achieved when range pulse repetition frequency is maximized compatibly with system constrains such as range ambiguity (see [Paragraph 4.2.5](#)).
- As regards velocity pulse repetition frequency PRF_V , analytically, it is hard to investigation this dependence for the attainment of the optimization, so it will be done a numerical investigation.

Note: The range received energy, $E_{r,R}$, and the effective bandwidth, β , are only function of range pulse duration PT_R : $E_{r,R} = f(PT_R)$ and $\beta = f(PT_R)$. Velocity received power, Pr_V , is only function of velocity pulse duration PT_V : $Pr_V = f(PT_V)$. So, integration times and pulse repetition frequencies don't influence $E_{r,R}$, β and Pr_V .

7.2. Numerical Investigation

Numerical dependences under investigation are $T_{meas,R}$, $T_{meas,V}$, PRF_R and PRF_V . As reported in the Preliminary Analysis, considering the typical values near touchdown for ExoMars mission, constant values are equal to:

$$f_c = 35 \text{ GHz} \quad ; \quad f_{samp} = 100 \text{ MHz} \quad ; \quad B_r = 15 \text{ MHz}$$

$$E_{r,R} = -120 \text{ dBm} \quad ; \quad \theta_{3dB} = 3^\circ \quad ; \quad \beta = 1 \text{ GHz}$$

7.2.1. Range Investigation

Thanks to Matlab® “Numerical_Range_Investigation.m” stand-alone script, a numerical range investigation is done. Considering the 3D plot of range measurement error δR as function of $T_{meas,R}$ and PRF_R :

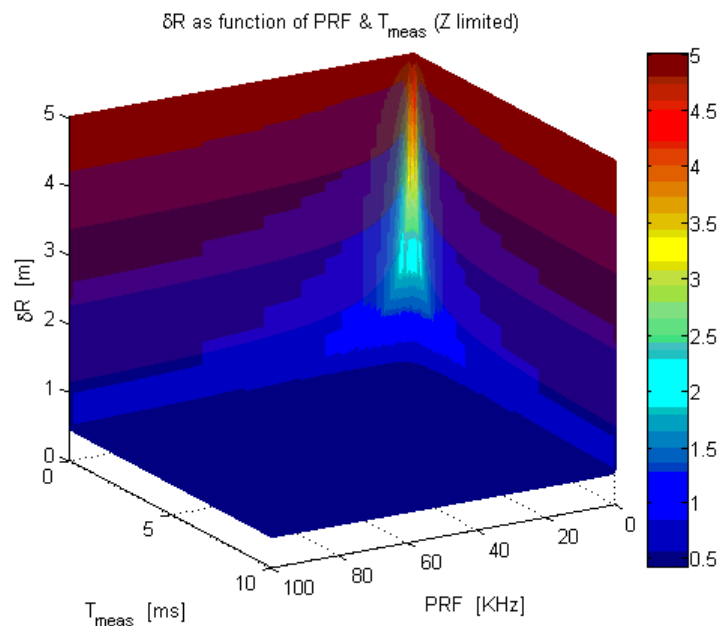


Figure 7-1 – 3D plot Range measurement error δR as function of $T_{meas,R}$ and PRF_R

Numerical investigation confirms that range measurement error decreases when $T_{\text{meas,R}}$ and PRF_R increase.

In particular, as explained in the preliminary analysis, $T_{\text{meas,R}}$ is up-limited because of range integration time constraints (see [Paragraph 4.3](#)). For ExoMars mission parameters, this limit is equal to 4.154 ms. So, considering this value as optimum value, increasing PRF_R leads to reported range measurement error:

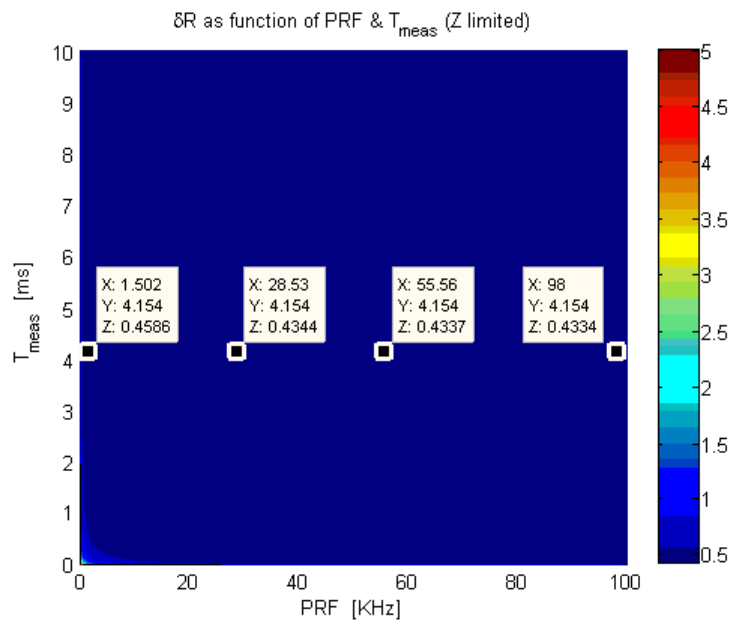


Figure 7-2 – Contour plot Range measurement error δR as function of $T_{\text{meas,R}}$ and PRF_R

Plot confirms that range measurement error decreases when PRF_R increases.

By increasing PRF_R , this error tends to minimum range measurement error achievable due to quantization effect (see [Paragraph 5.4](#)):

$$\delta R_{\min} = \frac{c}{2\sqrt{12}} \frac{1}{f_{\text{samp}}} = 0.4330 \text{ m} \quad (7-3)$$

So, it does not appear convenient to consider very high PRF_R .

7.2.2. Velocity Investigation

Thanks to Matlab® “Numerical_Velocity_Investigation.m” stand-alone script, a numerical velocity investigation is done.

As reported in the Preliminary Analysis, considering the typical values for ExoMars mission and half worst case means values:

$$\begin{aligned} P_{r,V} &= -50 \text{ dBm} & a_r &= 6.5 \text{ m/s}^2 \\ J_r &= 65 \text{ m/s}^3 & \dot{\theta}_{\perp} &= 0.5 \text{ rad/s} \end{aligned}$$

The 3D plot of velocity measurement error δR as function of $T_{\text{meas},V}$ and PRF_V is shown:

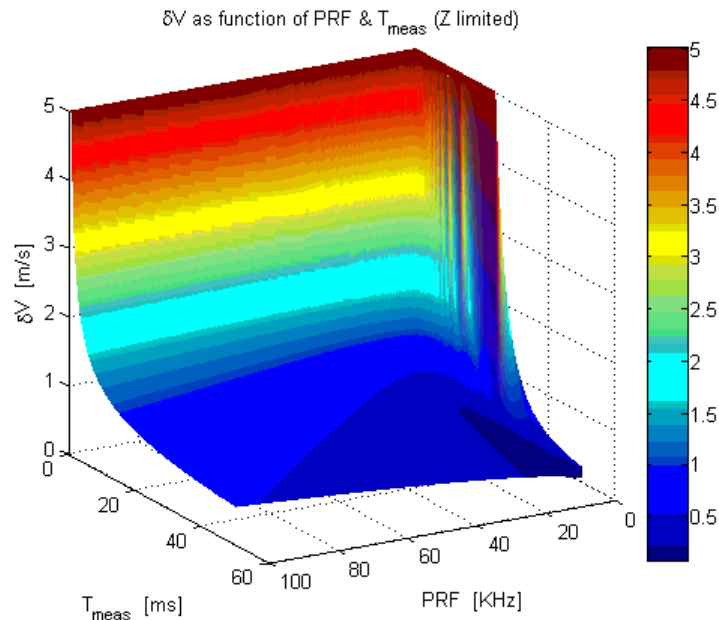


Figure 7-3 – 3D plot Velocity measurement error δV as function of $T_{\text{meas},V}$ and PRF_V

Numerical investigation shows that low PRF and time integration values lead to very high measurement errors.

By increasing $T_{\text{meas},V}$ values, measurement error decreases while increasing PRF value, measurement error decreases then before, for high PRF values, there is a little error increase.

So, minimum values set along PRF axes are determined with some parameterizations for velocity measurement error. These parameterizations are done respect to $Pr_V, a_r, J_r, \dot{\theta}$.

Two main parameterizations are investigated:

1. Respect to Pr_V with $a_r, J_r, \dot{\theta}$ half of worst case values
2. Respect to $a_r, J_r, \dot{\theta}$ with Pr_V half of worst case value

1. Analytically, the minimization of velocity measurement error is possible considering high values of Pr_V and good backscattering, it means that high values of pulse duration are preferred. For typical values of ExoMars mission, the Pr_V interval is:

$$P_{r,V} = [-100 \ -90 \ -80 \ -70 \ -60 \ -50 \ -40 \ -30 \ -20] \text{ dBm}$$

with half of worst case values:

$$a_r = 6.5 \text{ m/s}^2 \ ; \ J_r = 65 \text{ m/s}^3 \ ; \ \dot{\theta}_{\perp} = 0.5 \text{ rad/s}$$

So, the minimum values set of velocity measurement error, δR , as function of $T_{\text{meas},V}$ and PRF_V along PRF axes is shown:

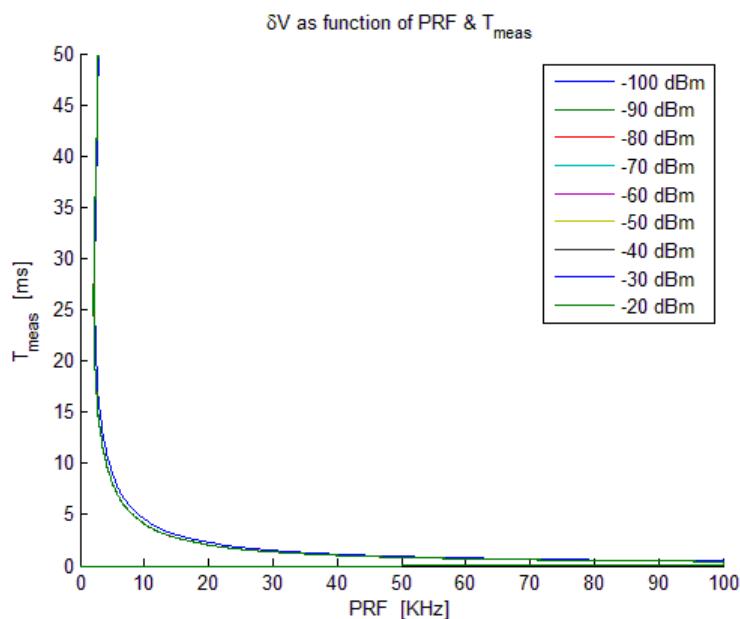


Figure 7-4 – Minimum values set as function of $T_{\text{meas},V}$ and PRF_V

In particular, considering system bound for velocity integration time $T_{meas,V} = \frac{1}{3} \left(\frac{1}{f_{update}} - T_{meas,R} \right)$, for ExoMars mission parameters, this limit is equal to 15.28 ms. So, set this value as optimum $T_{meas,V}$, optimum parameterized PRF_V values are:

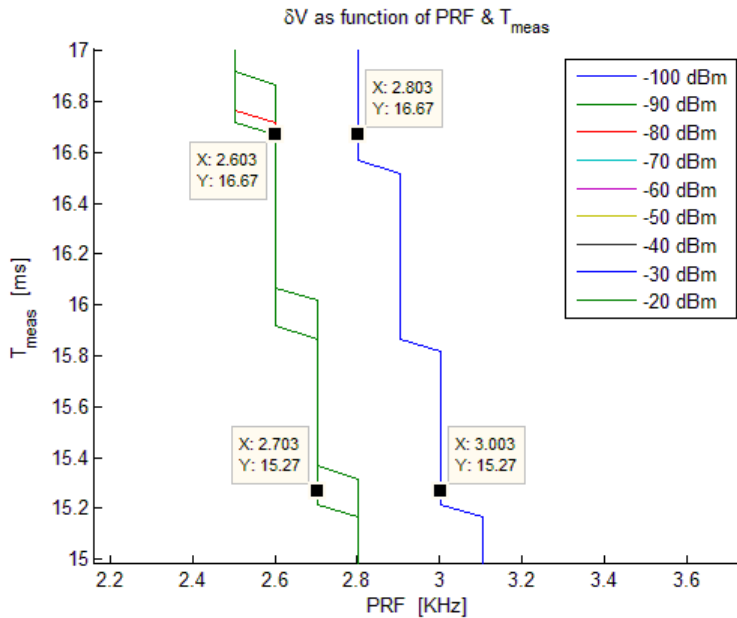


Figure 7-5 – Zoomed minimum values set as function of $T_{meas,V}$ and PRF_V

As shown in Figure, $T_{meas,V}$ set equal to 15.27 ms leads to optimum PRF_V that is about 2.7 KHz for high Pr_V , about 3.0 KHz for low Pr_V . $T_{meas,V}$ set equal to 16.67 ms leads to optimum PRF_V that is about 2.6 KHz for high Pr_V , about 2.8 KHz for low Pr_V .

So, optimum PRF_V is around 2.6 ÷ 2.7 KHz at low altitude where Pr_V is high and around 2.8 ÷ 3.0 KHz at high altitude where Pr_V is low.

- For typical values of ExoMars mission, motion a_r , $\dot{\theta}$ and Jerk J_r interval are:

$$a_r = [0 \div 13.4165] \text{ m/s}^2 ; \dot{\theta}_{\perp} = [0 \div 1.0472] \text{ rad/s} ; J_r = [0 \div 134.1650] \text{ m/s}^3$$

with mean value:

$$P_{r,V} = -50 \text{ dBm}$$

So, the minimum values set of velocity measurement error, δR , as function of $T_{meas,V}$ and PRF_V along PRF axes is shown:

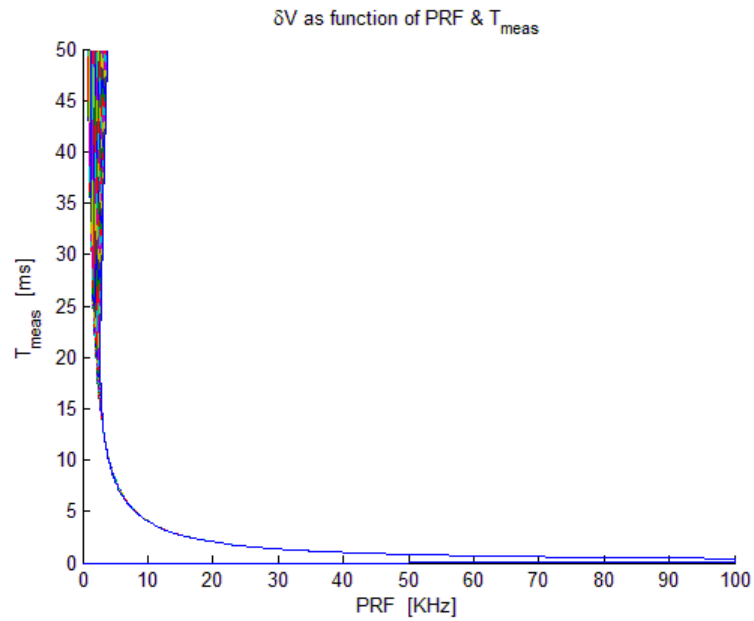


Figure 7-6 – Minimum values set as function of $T_{meas,V}$ and PRF_V

In particular, considering once more system bound for velocity integration time equal to 15.28 ms as optimum $T_{meas,V}$, optimum parameterized PRF_V values are:

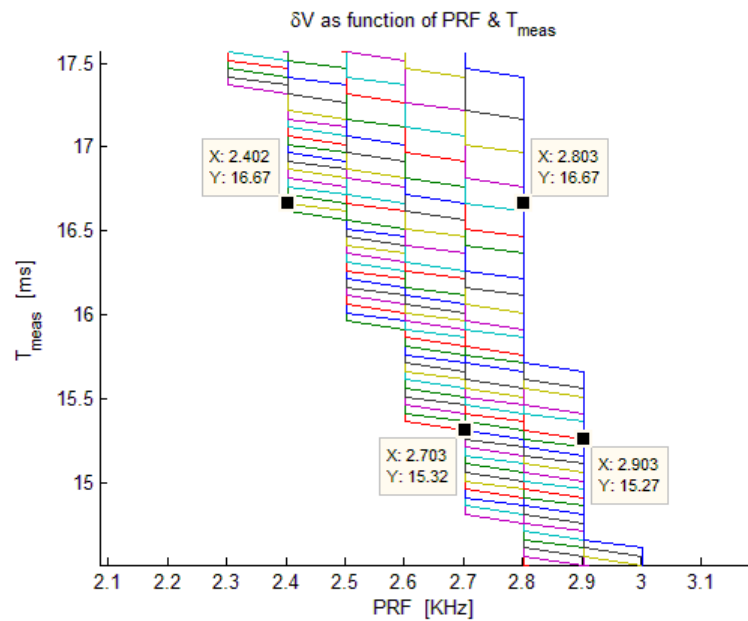


Figure 7-7 – Zoomed minimum values set as function of $T_{meas,V}$ and PRF_V

As shown in Figure, $T_{\text{meas},V}$ set equal to 15.27 ms leads to optimum PRF_V that is about 2.7 ÷ 2.9 KHz. $T_{\text{meas},V}$ set equal to 16.67 ms leads to optimum PRF_V that is about 2.4 ÷ 2.8 KHz.

So, optimum PRF_V is around 2.4 ÷ 2.9 KHz.

Now, three simulations are considered:

1. Half of worst case values
2. Simulated descent means values
3. Null dynamics and Jerk values

1. In half of worst case means values, parameters considered are:

$$P_{r,V} = -50 \text{ dBm} \quad ; \quad a_r = 6.5 \text{ m/s}^2 \quad ; \quad J_r = 65 \text{ m/s}^3 \quad ; \quad \dot{\theta}_{\perp} = 0.5 \text{ rad/s}$$

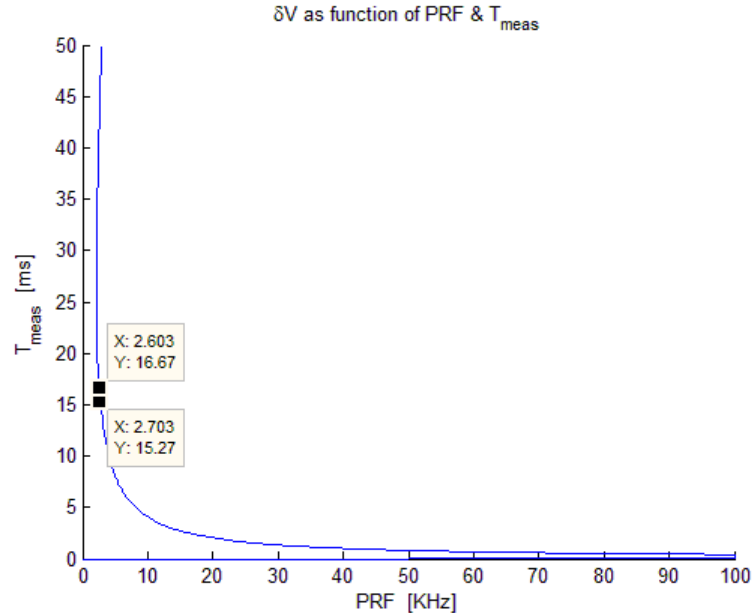


Figure 7-8 – Minimum values set as function of $T_{\text{meas},V}$ and PRF_V

2. In simulated descent means values, parameters considered are:

$$P_{r,v} = -50 \text{ dBm} \quad ; \quad a_r = 0.05 \text{ m/s}^2 \quad ; \quad J_r = 10 \text{ m/s}^3 \quad ; \quad \dot{\theta}_{\perp} = 0.08 \text{ rad/s}$$

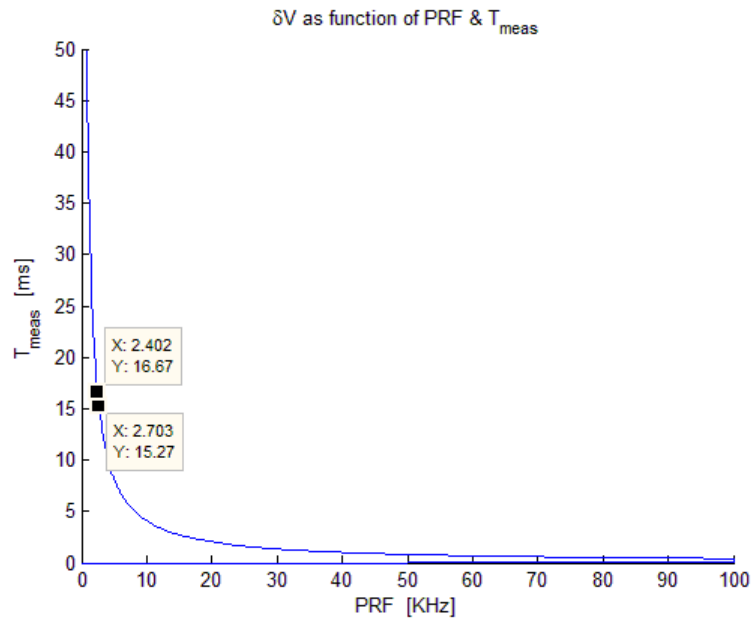


Figure 7-9 – Zoomed minimum values set as function of $T_{\text{meas},v}$ and PRF_v

3. In null dynamics and Jerk values, parameters considered are:

$$P_{r,v} = -50 \text{ dBm} \quad ; \quad a_r = 0 \text{ m/s}^2 \quad ; \quad J_r = 0 \text{ m/s}^3 \quad ; \quad \dot{\theta}_{\perp} = 0 \text{ rad/s}$$

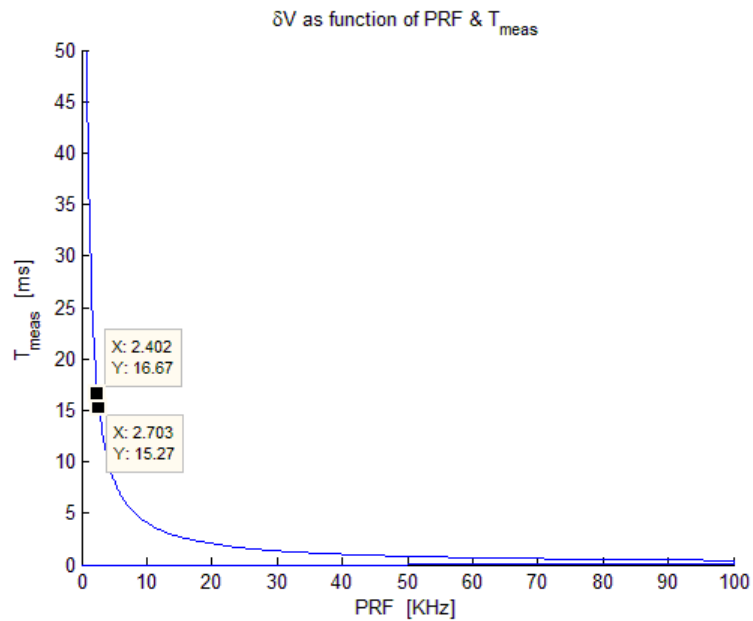


Figure 7-10 – Minimum values set as function of $T_{\text{meas},v}$ and PRF_v

So, Figure 7-8 shows that optimum PRF_V is about 2.7 KHz ($T_{meas,V} = 15.28$ ms) and about 2.6 KHz ($T_{meas,V} = 16.67$ ms).

Figure 7-9 and Figure 7-10 show that optimum PRF_V is about 2.7 KHz ($T_{meas,V} = 15.27$ ms) and about 2.4 KHz ($T_{meas,V} = 16.67$ ms).

Therefore reassuming, the investigation shows that optimal values that minimize measurements errors are:

- PT_R, PT_V as high as possible, compatibly with system bounds
- $T_{meas,R} = 4.154$ ms
- $T_{meas,V} = 15.28$ ms
- PRF_R as high as possible, compatibly with system bounds
- $PRF_V = 2.4 \div 2.9$ KHz (2.6 KHz preferred) at low altitude, $2.8 \div 3.0$ KHz at high altitude

7.3. Preliminary Parameters Laws

The definition of the Pulsed CW Radar solution focuses on the selection of the radar system parameters values, which ensure the satisfaction of the reported requirements. Analytic and numerical investigation investigate the necessary trade-offs on the basis of system constraints and performance metrics.

In case of contrasting requirements prioritization of system drivers will be conducted and overall definition finalized. It has furnished the indications to select radar principal parameters for the measurement errors minimization.

Key radar parameters are conditioned by system bounds and the indications of the optimization investigation, so along the descent, same radar parameters have a variation laws that must be a trade-off among them.

The key radar parameters to be identified for preliminary system definition are reported in the following Table 7-1, where constraints and metrics are:

Parameter	Acronym	Influencing factors & Notes
Range and Velocity beams Integration Time	$T_{meas,R}$ $T_{meas,V}$	<ul style="list-style-type: none"> - Range Integration Time Constraints - To ensure Doppler accuracy/resolution - Within total refresh interval
Range and Velocity Pulse Repetition Frequency	PRF_R PRF_V	<ul style="list-style-type: none"> - To ensure reception of the entire echo signal without overlapping with the transmitted pulse - To avoid range ambiguities up to the highest altitude in the operational envelope - To ensure “reading” of the maximum Doppler component
Pulse length	PT_R PT_V	<ul style="list-style-type: none"> - To ensure range estimation at low altitudes (avoiding overlapping with transmitted pulse) - Minimum Signal Trip Time - Function of PRF on the basis of achievable duty cycle

Table 7-1 – RDA Parameters and Constraints

The reported constraints and metrics have been largely discussed in the [Chapters 6](#), while mathematical relationships are reported in details in [Chapter 4](#) and [5](#). A graphical representation of the global trade-off rationale among the above reported relationships is quite complex due to the mutual dependence of several parameters.

For this reason, the rationale is explained in narrative in the following Paragraphs where, thanks to Matlab® “RDA_Performance.m” main script, all parameters laws are investigated.

The determination of laws is done sequentially, first setting range integration time because of its bound is independent from the other parameters. Set it, velocity integration time is set itself by considering cycle update frequency.

Range and velocity PRF are set by considering their extreme ambiguity values (PRF_R at low altitude is up-limited, while PRF_V is down-limited).

Range and velocity pulse repetition interval are conditioned by choice of range and velocity PRF and by send-return trip echo time.

7.3.1. Integration Time Laws

As indicated before, to obtain the measurement errors minimization, integration times must be as high as possible.

The optimum values are $T_{meas,R} = 4.154$ ms and $T_{meas,V} = 15.28$ ms, so a flat laws are selected during the descent:

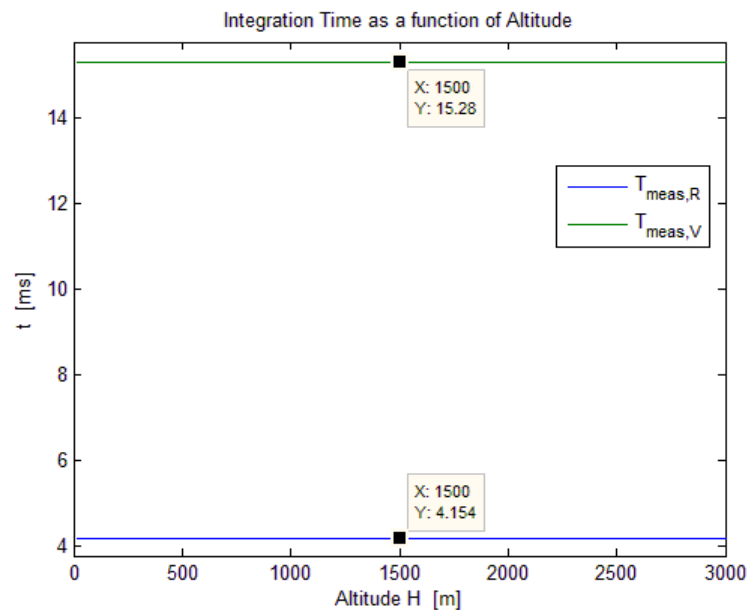


Figure 7-11 – Optimum integration time laws

Figure 7-11 shows that during the entire descent, integration times are always the same. For range this leads to a numbers of pulses equal to 103 if its PRF is set equal to 25 KHz. For velocity this leads to a numbers of pulses equal to 39 if its PRF is set equal to 2.6 KHz or 44 if its PRF is set equal to 2.9 KHz.

7.3.2. Pulse Repetition Frequency Laws

As indicated before, to obtain the measurement errors minimization, PRF_R must be as high as possible, while PRF_V must be equal to 2.6 KHz at low altitude, and 2.8 ÷ 3.0 KHz at high altitude.

Now considering system bounds, PRFs limits are discussed in [Paragraph 4.2.5](#), so optimum range PRF law is shown:

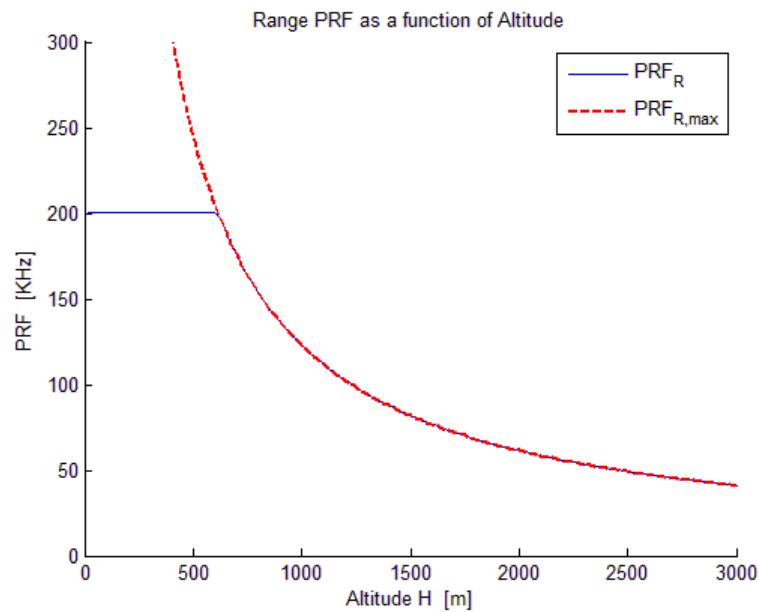


Figure 7-12 – Optimum range PRF law

Figure 7-12 shows that range PRF is set equal to its maximum ambiguous values of at high altitude, while at low altitude PRF is up limited around 200 KHz under 700 m of altitude.

In particular, even if in altitude range of 10 ÷ 700 m, PRF can be higher, because of technological limits and since higher values are useless for accuracy, an up-limit of about 200 KHz appears the best.

This law satisfies, as far as possible, range error minimization indications.

Here optimum velocity PRF law is shown:

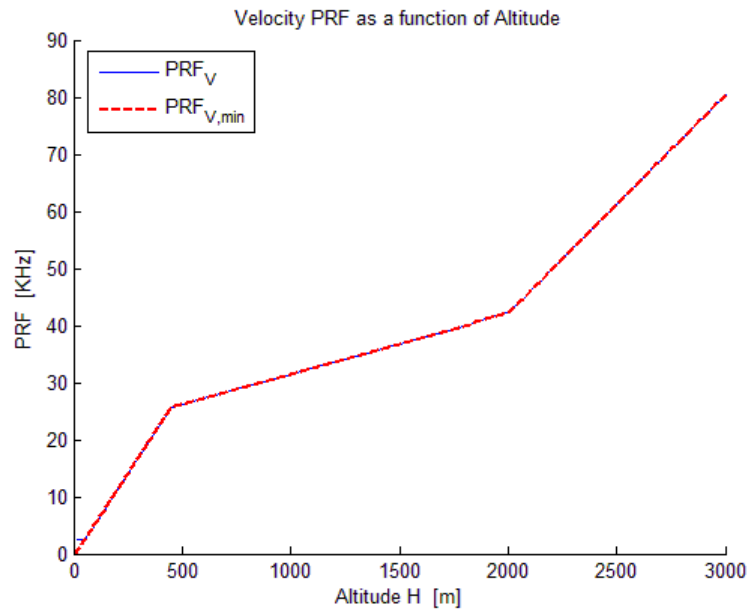


Figure 7-13 – Optimum velocity PRF law

In particular, zooming Velocity PRF at low altitude:

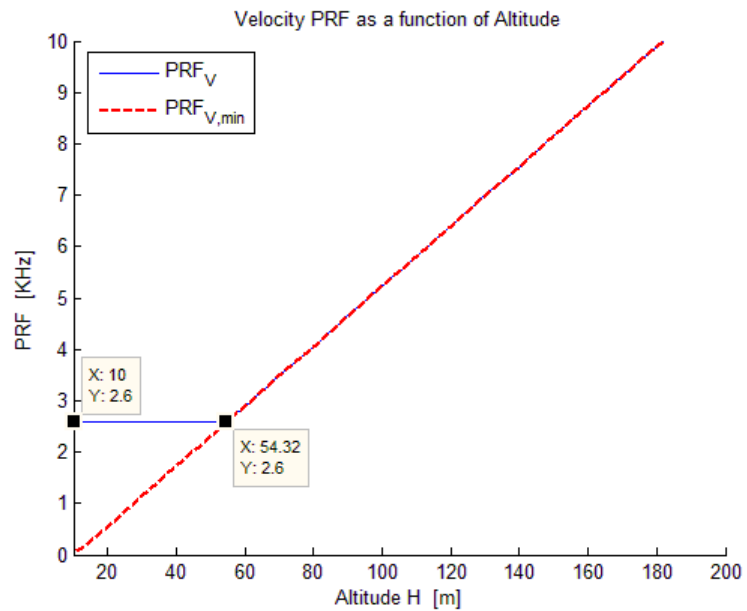


Figure 7-14 – Zoomed optimum velocity PRF law

Figure 7-13 shows that velocity PRF is set equal to its minimum ambiguous values at high altitude, while at low altitude PRF is down limited at 2.6 KHz under 60 m of altitude as shown in Figure 7-14.

This choice is driven by the consideration that system bounds allow the full satisfaction of velocity error minimization indications (2.6 KHz) at low altitude. At high altitude, minimum ambiguous values are greater than optimum values, so system bounds don't allow full satisfaction of velocity error minimization indications (2.8 ÷ 3.0 KHz), and selected PRF is the minimum possible (minimum ambiguous values).

7.3.3. Pulse Duration Laws

As indicated before, to obtain the measurement errors minimization, PT_R and PT_V must be as high as possible, compatibly with Pulse Repetition Interval (PRI) and minimum Signal Trip Time.

These limits depend on the chosen PRFs and they are shown to follow:

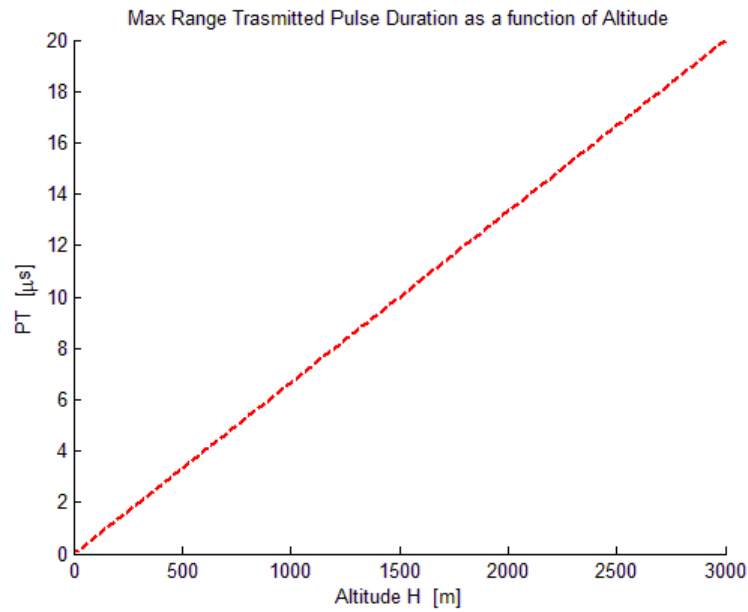


Figure 7-15 – Range pulsewidth bound

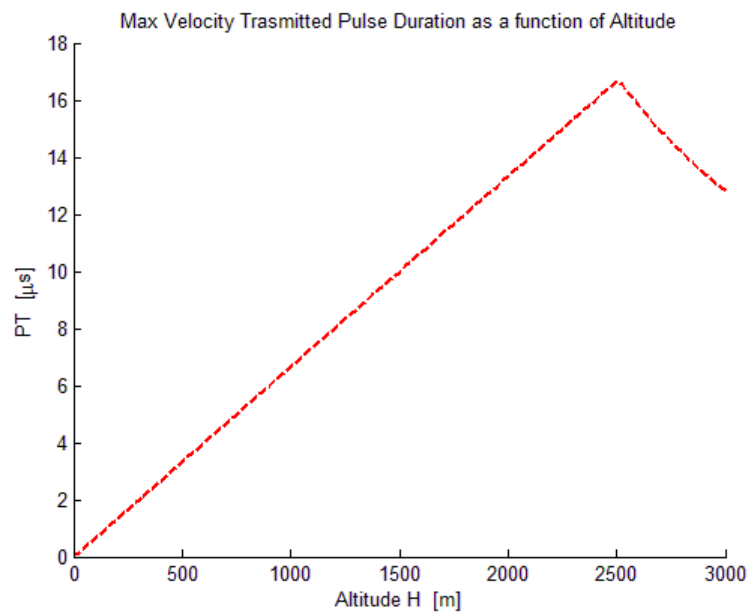


Figure 7-16 – Velocity pulsewidth bound

An optimum Range Pulse Duration law is shown:

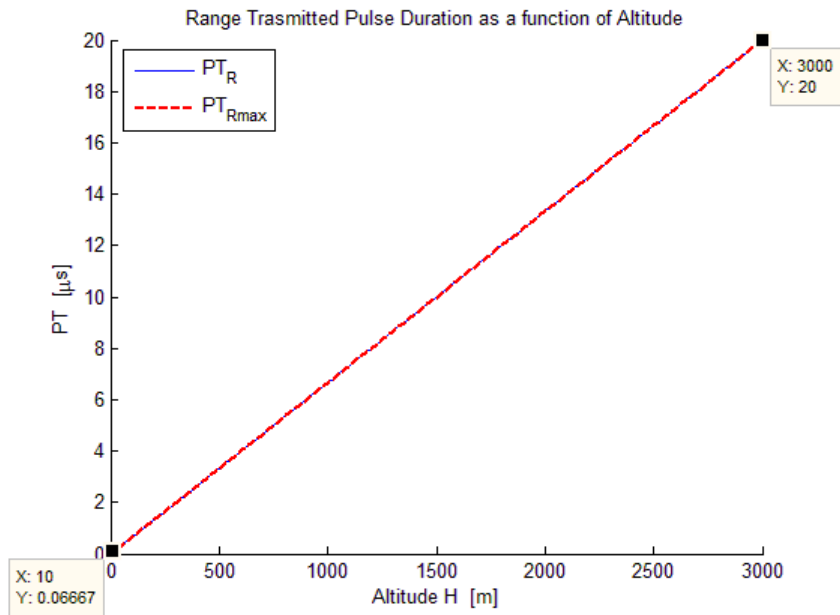


Figure 7-17 – Range pulsewidth law

This law is compatible with system bounds such as Range Signal Send/Return Time:

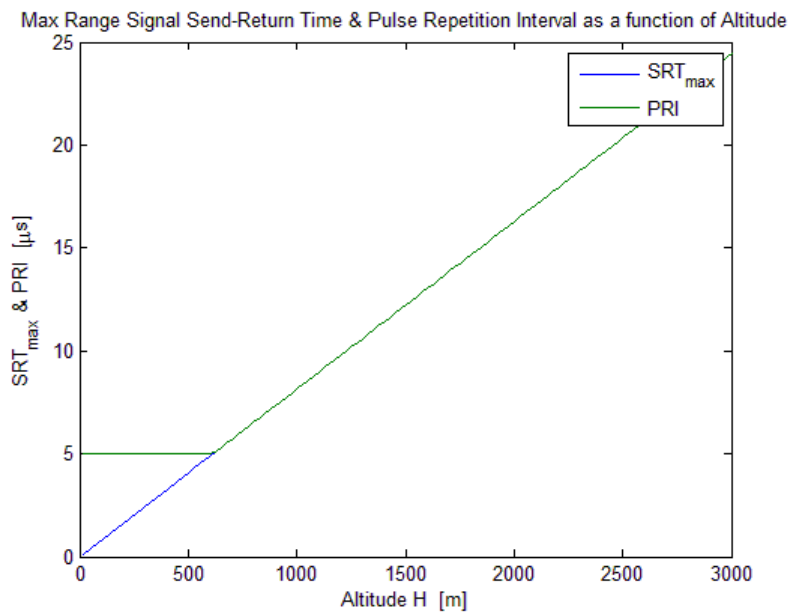


Figure 7-18 – Range signal send-return time

Figure 7-18 shows that echoes always return before sending next pulse.

For Optimum Velocity Pulse Duration laws, two cases are investigated:
 $\alpha_{\text{beam}} = 15^\circ$ and $\alpha_{\text{beam}} = 20^\circ$.

For $\alpha_{\text{beam}} = 15^\circ$, proposed optimum velocity Pulse Duration law is shown:

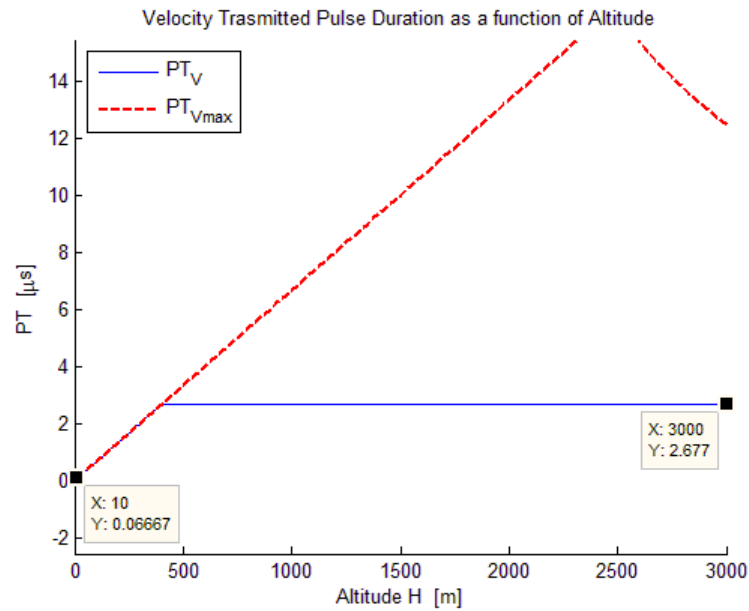


Figure 7-19 – Velocity pulsewidth law $\alpha_{\text{beam}} = 15^\circ$

PT_V is up-limited to guarantee a complete echo return before launching another under an altitude of 2000 m.

This implies that RDA architecture is simpler and RDA performance is guaranteed in altitude range in which measurements must satisfy requirements (0 ÷ 2000 m).

In fact, this law is compatible with system bounds such as Range Signal Send/Return Time:

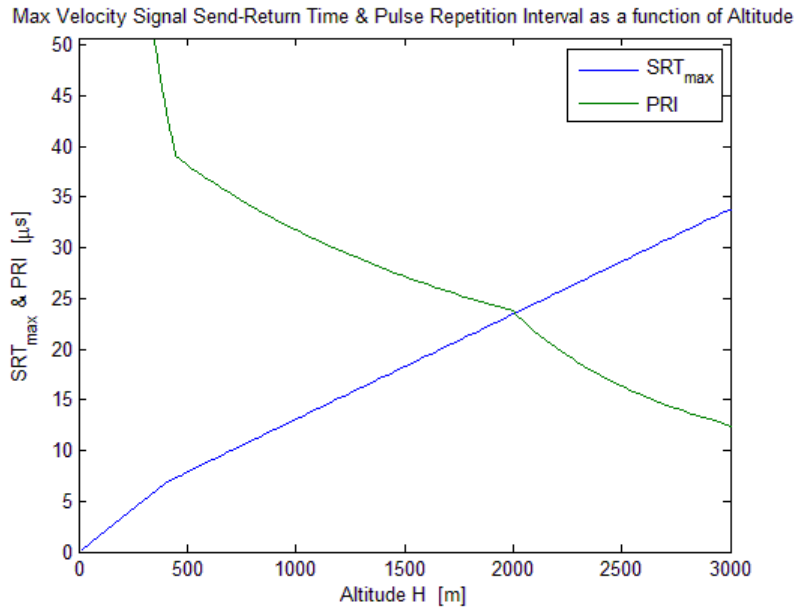


Figure 7-20 – Velocity signal send-return time with $\alpha_{\text{beam}} = 15^\circ$

For $\alpha_{\text{beam}} = 20^\circ$, proposed optimum Velocity Pulse Duration laws is shown:

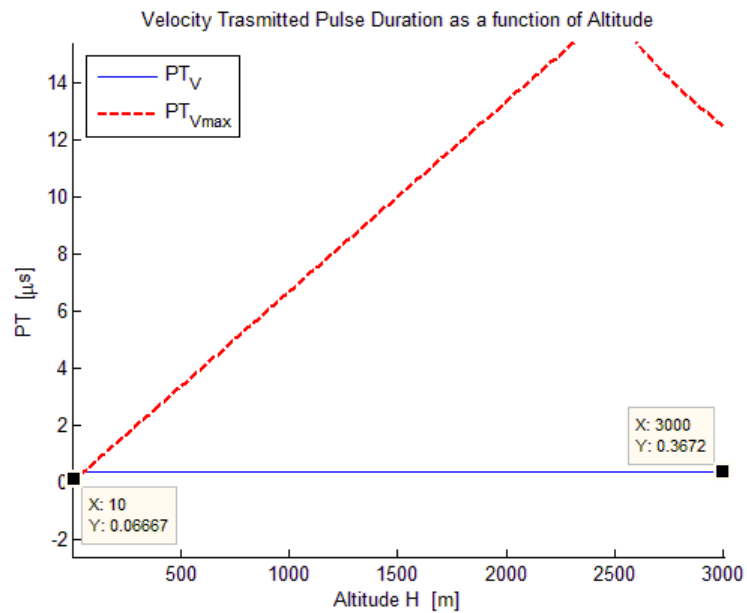


Figure 7-21 – Velocity pulsewidth law $\alpha_{\text{beam}} = 20^\circ$

PT_V is also up-limited to guarantee a complete echo return before launching another under an altitude of 2000 m, but now this limit is smaller for the Range Signal Send/Return Time limit.

This implies that RDA architecture is simpler and RDA performance is guaranteed in altitude range in which measurements must satisfy reported requirements (0 ÷ 2000 m).

This law is compatible with system bounds such as Range Signal Send/Return Time:

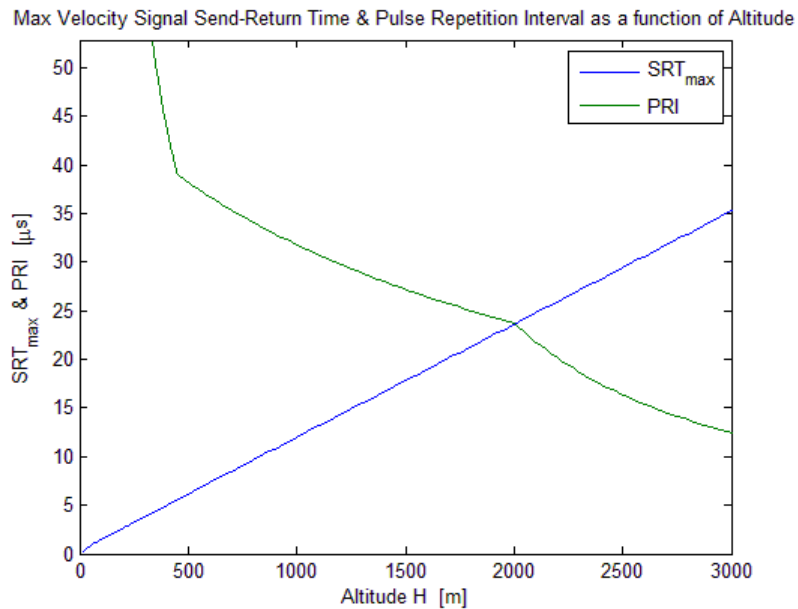


Figure 7-22 – Velocity signal send-return time with $\alpha_{\text{beam}} = 20^\circ$

Figure 7-20 and 7-22 show that over an altitude of 2000 m, echo return after sending next pulse.

This is not a problem because this choice doesn't compromise RDA accuracy at low altitude and measurement accuracies must to be guaranteed under an altitude of 2000 m. Over an altitude of 2000 m, measurement can be achieved with less accuracy and thanks to dedicated signal management.

8. PERFORMANCE EVALUATIONS

After having established full radar model and its preliminary optimum parameters, it is possible to elaborate radar performance.

This evaluations lead to performance analysis that can confirm the satisfaction of the reported requirements or not. In this case, a second investigation will be done modifying preliminary system definition to achieve the total verification of requirements or, if it is not possible, to obtain some improvement respect to first definition.

In this Chapter performance are elaborated for:

1. "Worst Case" descent
2. "Slow_Vert_Sim_Descent" simulated descent
3. "Fast_Vert_Sim_Descent" simulated descent

These evaluations are possible through the Matlab® "RDA_Performance.m" main script.

8.1. Worst Case Descent

8.1.1. Preliminary Inputs Setting

In this Paragraph, performance evaluation will be done by using the worst case input for all key parameters driven by requirements, i.e. acceleration, jerk, angular velocity and attitude as well as terrain slope and roughness.

Considerations, analysis and trade-off done in Chapters 2, 6 and 7 have allowed to define, even in a preliminary way, the main worst case parameters of RDA system.

These parameters are summarized in Table 8-1:

Operating Frequency	35 GHz
Measurements Update Frequency	20 Hz
Sampling Frequency (I&Q)	100 MHz
IF Frequency	50 MHz
Antenna Illumination	Uniform
Antenna -3dB Aperture	3°
Antenna Gain	33.75 dB
Transmitted Peak Power	30 dBm
Transmitted Pulse Rising Time	5 ns
Transmitting Bandwidth	200 MHz
Receiving Bandwidth	15 MHz (at low altitude)
Receiver Temperature	290 K
Receiver Noise Figure	5 dB
Antenna FE Losses (Tx & Rx)	4 dB
Atmospheric Losses	4 dB

Geometric Beam Angles	0° (range beam) 15° (velocity beams)
Local Terrain Slope (RMS value)	10°
Surface Roughness	0.1 m
Velocity	90.25 m/s
Acceleration	13.4 m/s ²
Jerk	134.2 m/s ³
Attitude Angles	35° (range beam) 50° (velocity beams)
Angular Velocity	60 °/s
Integration Times	4.2 ms (range beam) 15.2 ms (velocity beams)
PRFs	Variable (see Figures 7-12÷14)
Pulse Durations	Variable (see Figures 7-17&19)

Table 8-1 – System parameter driven by worst-case requirements. All specified constant parameters are maintained constant from 10 m up to 3000 m, where the performance will be evaluated.

8.1.2. Preliminary RDA Measurement Accuracy

In this section Matlab® “RDA_Performance.m” main script works with worst case input.

Following, range measurement accuracy result is shown:

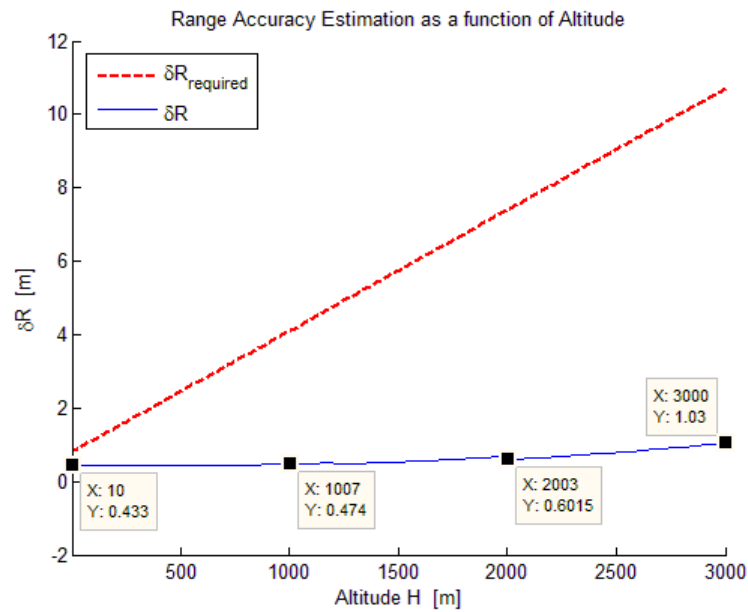


Figure 8-1 – Range measurement accuracy

Figure 8-1 shows that for range measurements, requirement is observed in worst case input along the entire descent. Therefore, as far as the range measurement is concerned, in any case the defined RDA system is able to meet the accuracy requirement within the entire range of altitude.

Now, velocity measurement accuracies are shown:

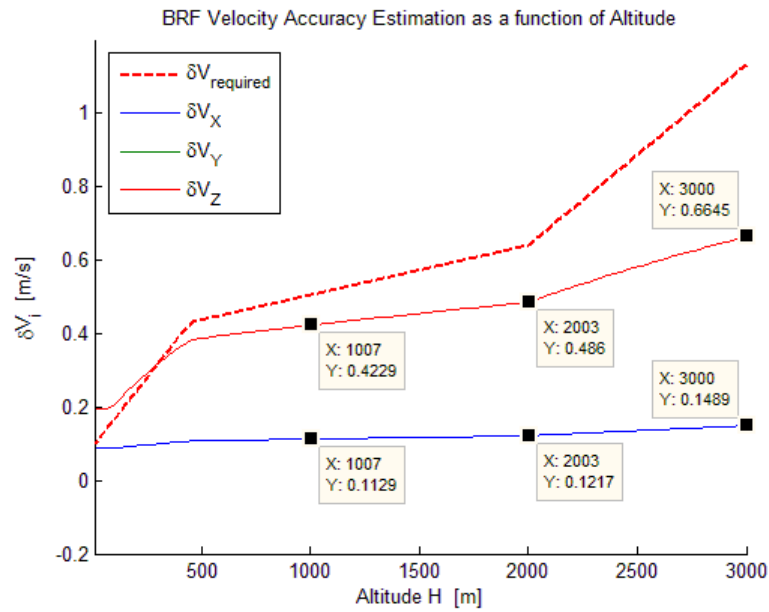


Figure 8-2 – Velocity measurement accuracies

In particular, around final descent:

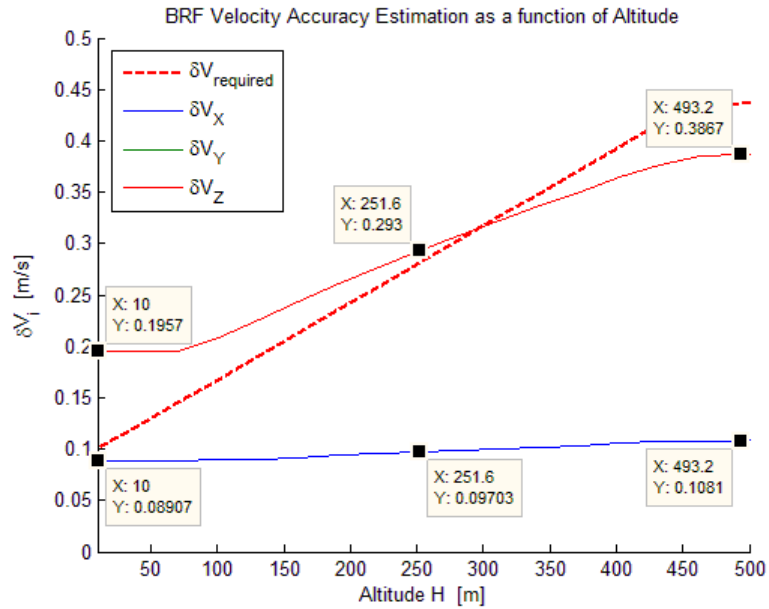


Figure 8-3 – Zoomed velocity measurement accuracies

Figure 8-2 and Figure 8-3 show that in any case for V_x measurements, requirement is observed in worst case input along the entire descent while for V_y and V_z , this is observed in worst case input only over 300 m of altitude.

The main difference between V_x and V_y & V_z accuracies is due to geometric velocity beam configuration. In fact, in worst case, along-beam accuracies are the same, but along body axes these are different because of off-nadir angle, α . Low α angles lead to high V_y & V_z errors because of geometric coefficients increases, but high α angles lead to low backscattering so along-beam errors increases. A good compromise for velocity beam angles will be investigated later.

It is worth noting that in worst case performance evaluation, since each velocity beam has the same off-nadir angle, considering the selected beams geometry, the velocity measurements accuracy along Y_b & Z_b axis is the same.

The whole situation can be improved if the requirement on off-nadir angle, acceleration, angular velocity, Jerk, slope and surface roughness can be relaxed. In particular, for null off-nadir angle, acceleration, angular velocity, Jerk, slope and surface roughness, achievable range and velocity accuracy can be considered the theoretical limit of the defined system.

So, accuracies re-computation can be done with the inputs:

$$\sigma_h = 0 \text{ m} \quad ; \quad \text{slope} = 0^\circ \quad ; \quad \theta_{B0} = 0^\circ$$

$$a_{r,Bi} = 0 \text{ m/s}^2 \quad ; \quad J_{r,Bi} = 0 \text{ m/s}^3 \quad ; \quad \dot{\theta}_{\perp,Bi} = 0 \text{ rad/s} \quad (i=1,2,3)$$

Therefore, theoretical limit of the range measurement accuracy is:

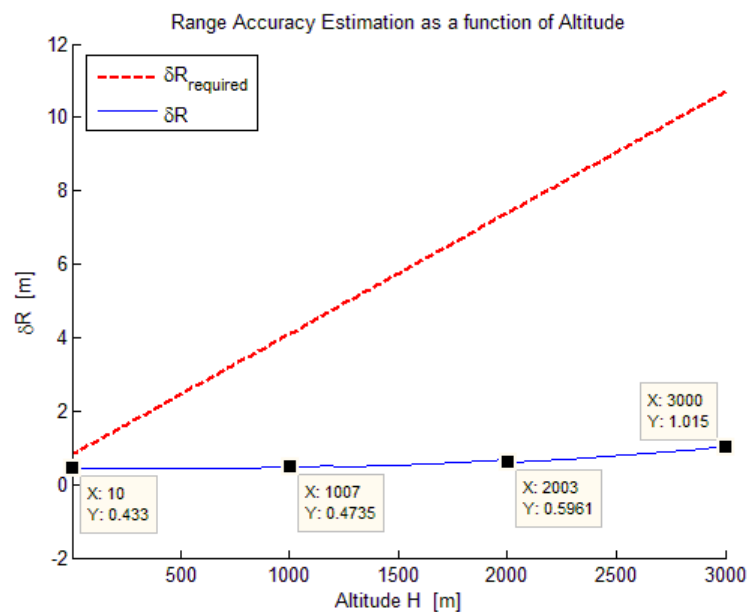


Figure 8-4 – Maximum achievable range measurement accuracy for null acceleration, Jerk and angular velocity

Figure 8-4 shows that for range measurements, as it was predictable, requirement is yet observed in worst case input along the entire descent.

While theoretical limit of the velocity measurement accuracies is:

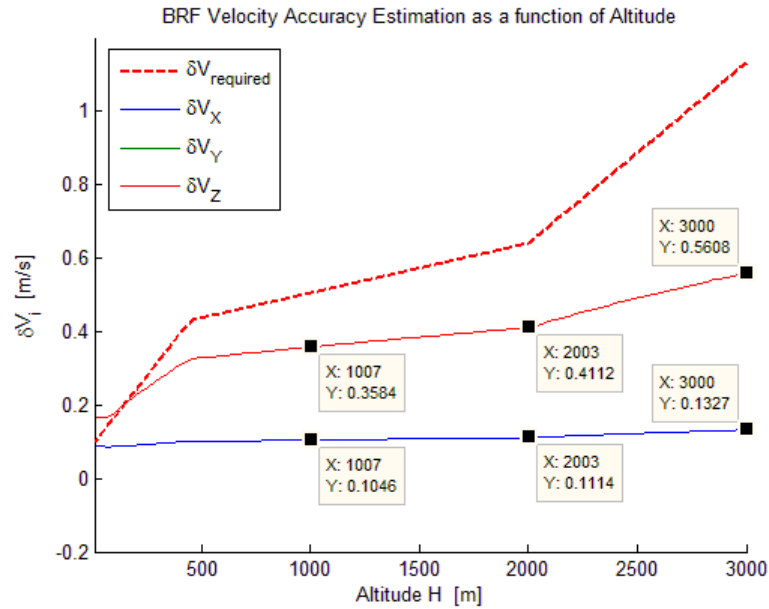


Figure 8-5 – Maximum achievable velocity measurement accuracies for null acceleration, Jerk and angular velocity

In particular, around final descent:

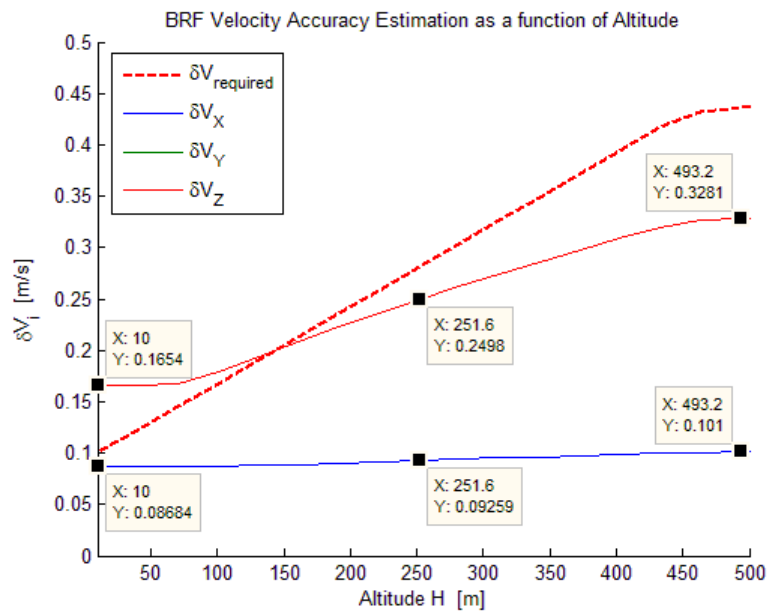


Figure 8-6 – Zoomed maximum achievable velocity measurement accuracies for null acceleration, Jerk and angular velocity

Figure 8-5 and Figure 8-6 show that in any case for V_x measurements, as it was predictable, requirement is observed in worst case input along the entire descent, while for V_y and V_z , this is observed in worst case input only over 150 m of altitude.

It is also worth noting that the requirement of 0.1 m/s at very low altitude comes from the assumption that the velocity of the DM is null at 10 m of altitude. If it is not the case, the requirement will increase and will approach or overcome the minimum achievable velocity accuracy by the RDA system.

8.1.3. Time Measurements Improvements

An improvement can be done considering that also in worst case, range measurement has great margin before exceed requirements in the crucial range of altitude of 10 ÷ 2000 m, as reported in the requirements (see [Paragraph 2.1](#)).

So, in this interval, decreasing range integration time, it is possible increase velocity integration time. This implies a greater range measurement error, but, verified that range requirement is still observed in the crucial range of altitude of 10 ÷ 2000 m, velocity measurement error is smaller.

Here, modified T_{meas} laws are shown:

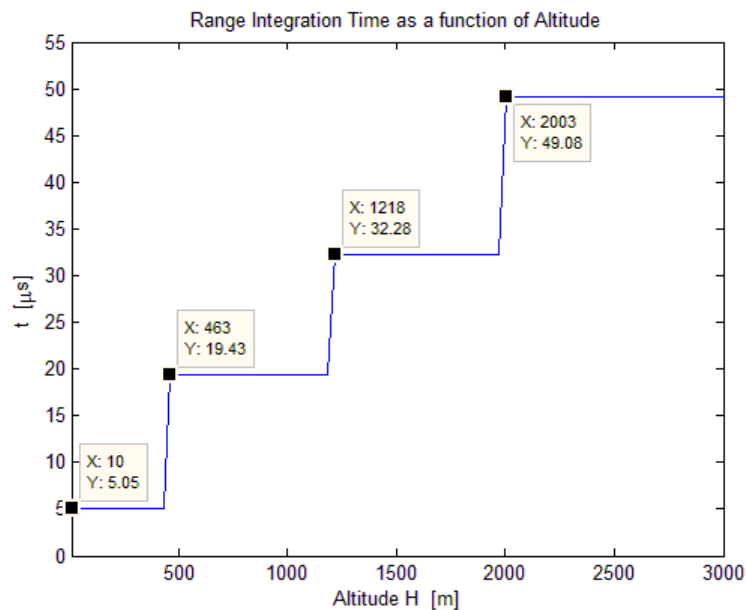


Figure 8-7 – Modified integration time law

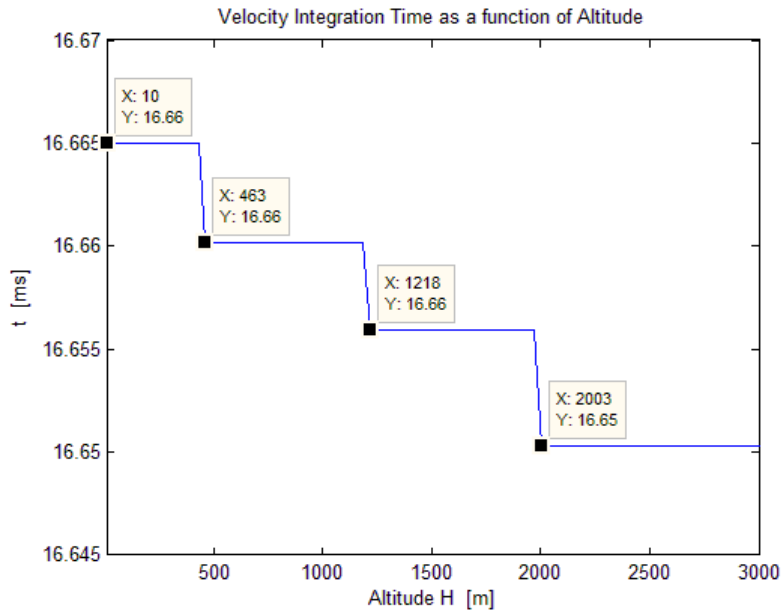


Figure 8-8 – Modified integration time law

The solution selected is step-type for easy hardware implementation. This laws lead to higher velocity integration time at low altitude where V_y & V_z velocity measurement accuracies exceed requirement for obtain best measures improvement.

With modified laws, Matlab® “RDA_Performance.m” main script provides new range measurement accuracy:

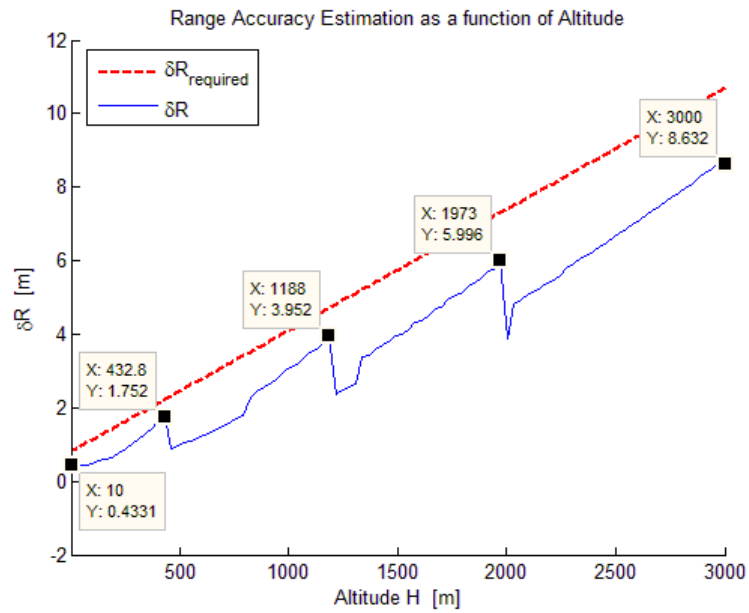


Figure 8-9 – Range measurement accuracy

Figure 8-9 shows that, even if requirements are satisfied, new laws imply a range accuracy loss that can be calculate with “Accuracy_Improvements.m” script.

The discontinuities present at an altitude of 450 m, 1200 m, 2000 m are due to step-type laws selected for range and velocity integration time.

Here, the range accuracy loss is shown:

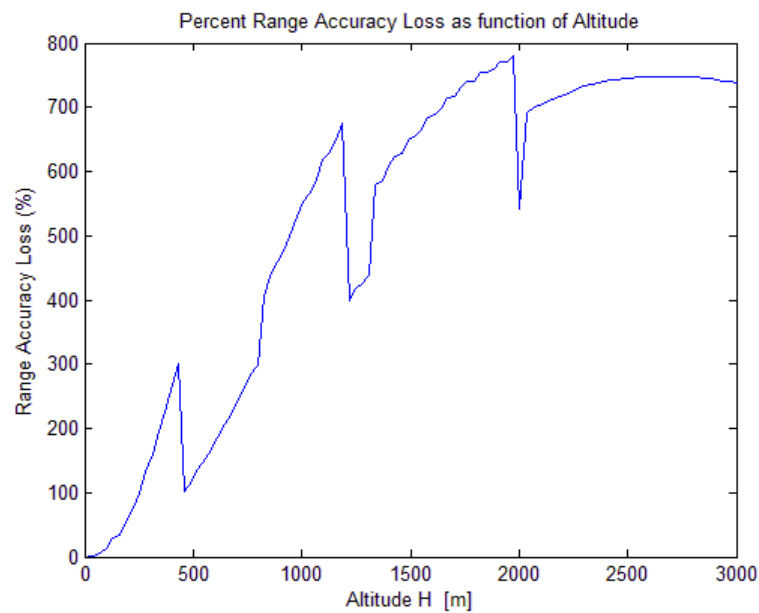


Figure 8-10 – Range measurement accuracy loss

Figure 8-10 shows during the descent, range loss is about 0 ÷ 780 % and around final descent phase, range loss is about 0 ÷ 13.9 % .

Here, new velocity measurement accuracies are shown:

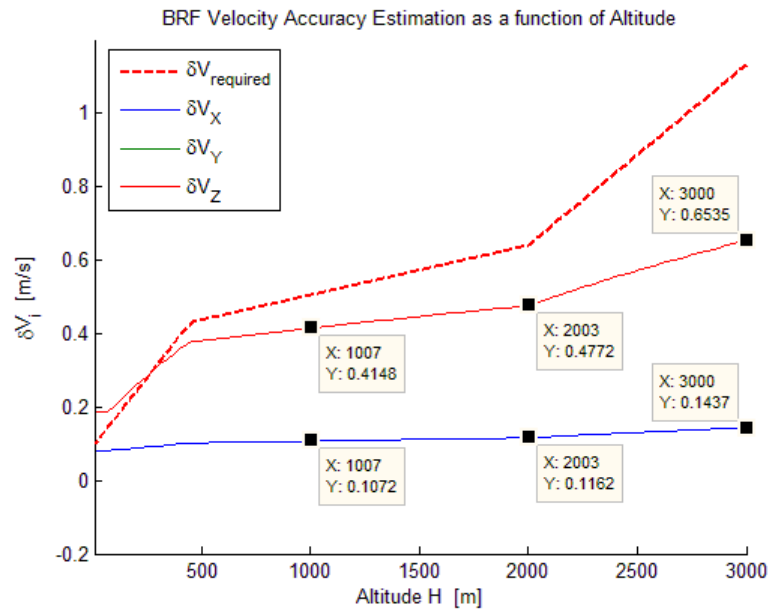


Figure 8-11 – Velocity measurement accuracies

In particular, around final descent:

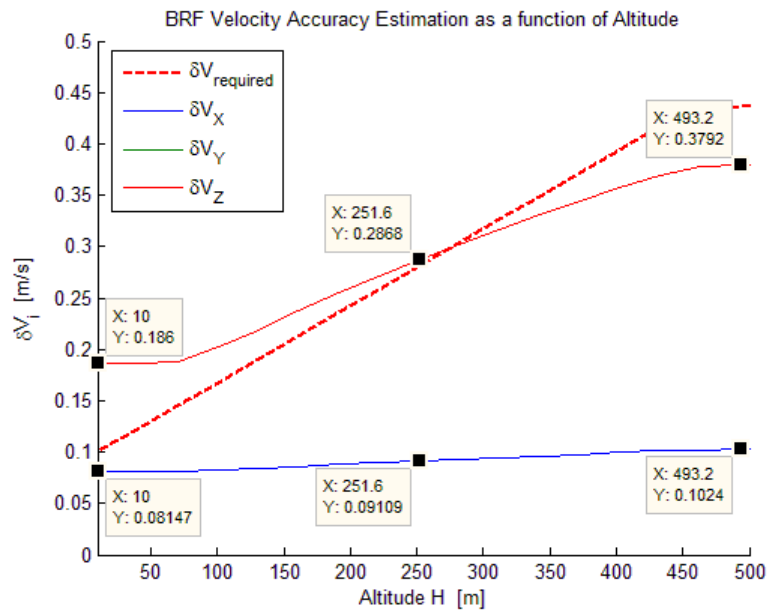


Figure 8-12 – Velocity measurement accuracies

Figure 8-11 and Figure 8-12 show that new law implies a V_x and V_y & V_z accuracies gain that can be calculate with “Accuracy_Improvements.m” script.

Here, the velocity measurement accuracy variations are shown:

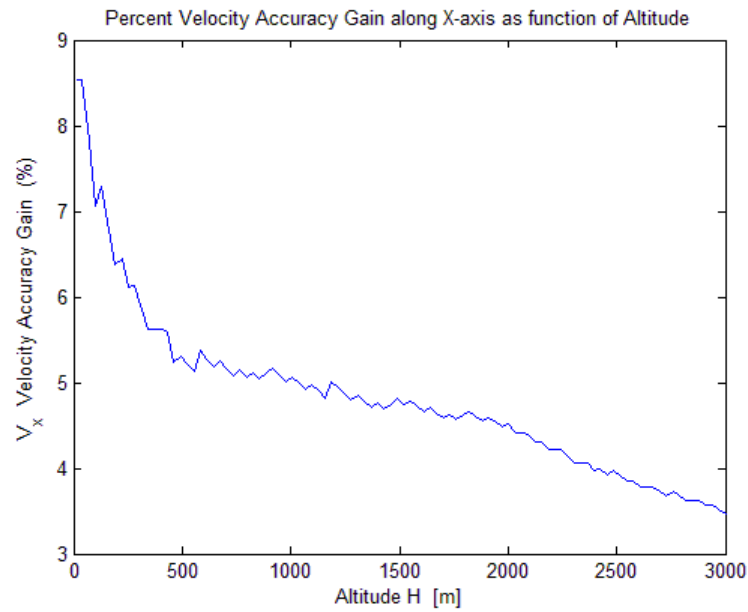


Figure 8-13 – V_x velocity measurement accuracy gain

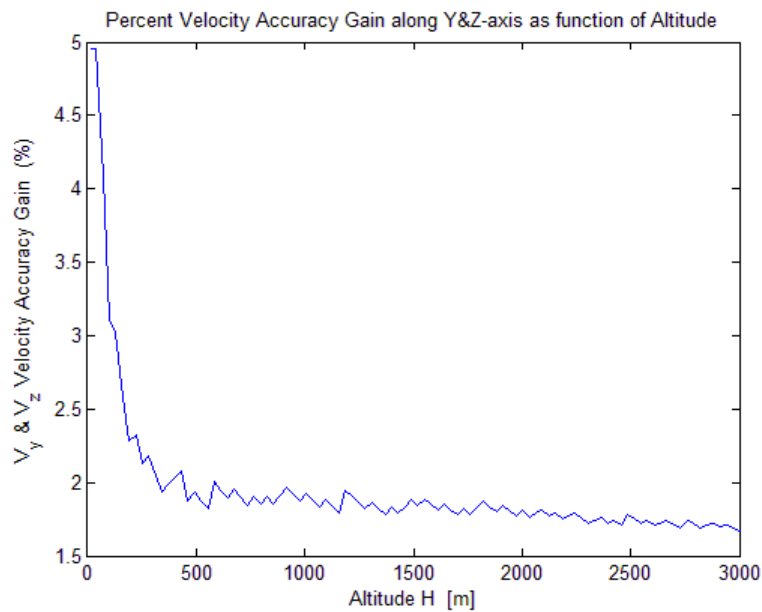


Figure 8-14 – V_y & V_z velocity measurement accuracies gain

Figure 8-13 shows that during the descent, V_x velocity gain is about 3.5 ÷ 8.5 % and around final descent phase, V_x velocity gain is about 7 ÷ 8.5 % .

Figure 8-14 shows that during the descent, V_y & V_z velocity gain is about 1.6 ÷ 5 % and around final descent phase, V_y & V_z velocity gain is about 3.1 ÷ 5 % .

8.1.4. Geometric Improvement

The selected antenna geometry is shown in Figure 3-5, with a central beam pointed at nadir for range measurements and three pointed at off-nadir dedicated to velocity measurements.

A meaningful improvement can be done if geometric beam angle increases. As reported previously, the main difference between V_x and V_y & V_z accuracies is due to geometric velocity beam configuration. In fact, in worst case, along-beam accuracies are the same, but along body axes these are different because of off-nadir α angle. Low α angles lead to high V_y & V_z errors because of geometric coefficients increases, but high α angles lead to low backscattering so along-beam errors increases.

A good compromise for velocity beam angles will be investigated here.

Considering that requirements describe an operational scenario where off-nadir angles up to 35° are foreseen, and that non-ambiguous measures are to be given for off-nadir angle up to 55° , values above 20° are not feasible.

Preliminary choice is 15° . Now, beam angle will be increased to 20° to analyze if the gain due to geometric configuration is greater than the loss due to lower backscattering.

This inquiring is done thanks to Matlab® “Pr_Evaluations.m”, “Accuracy_Improvements.m” and “Velocity_Accuracy_Projection_Coefficient.m” script respectively.

So, thanks to Matlab® “Pr_Evaluations.m” script, received power for beam angle equals to 15° and 20° are shown in nominal attitude ($\theta_{att} = 0^\circ$, $\theta = 15^\circ$, 20°) and in worst case attitude ($\theta_{att} = 35^\circ$, $\theta = 50^\circ$, 55°):

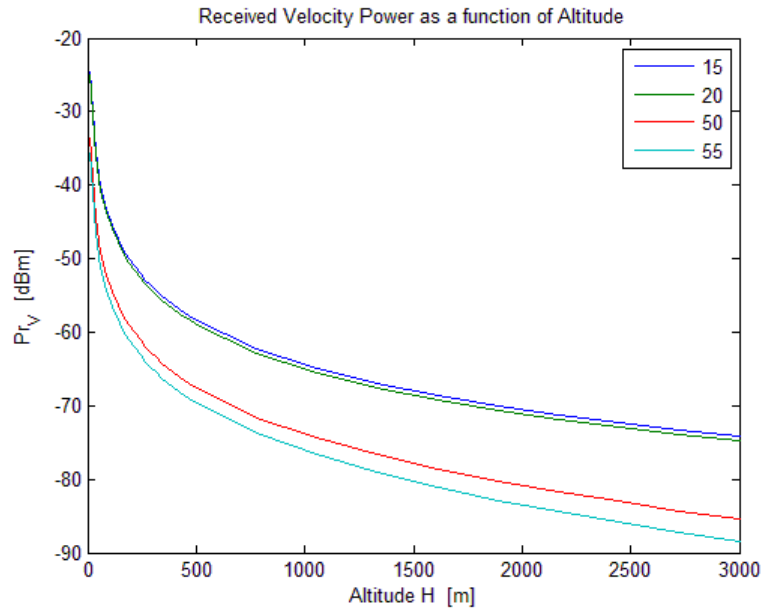


Figure 8-15 – Received velocity power

Here, loss due to low backscattering in nominal attitude and worst case attitude are shown:

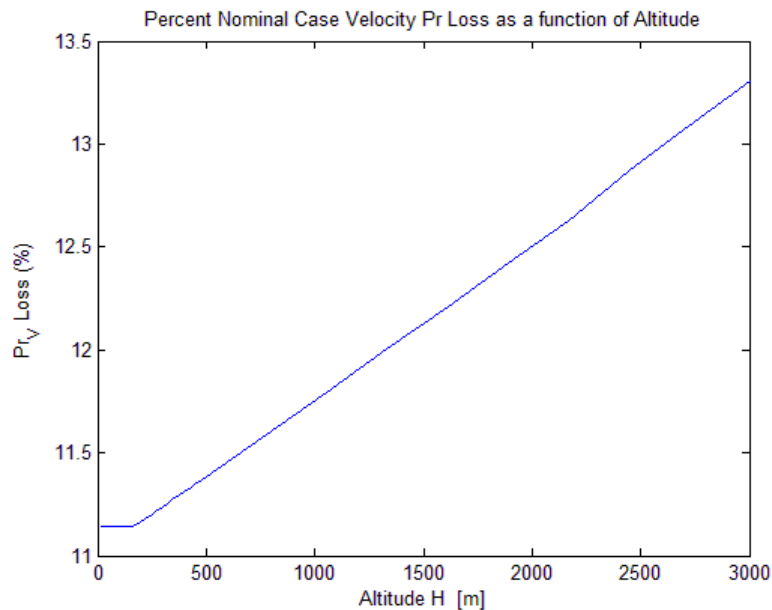


Figure 8-16 – Nominal case received power loss

Figure 8-16 shows that nominal loss is about 11.2 ÷ 13.3 % .

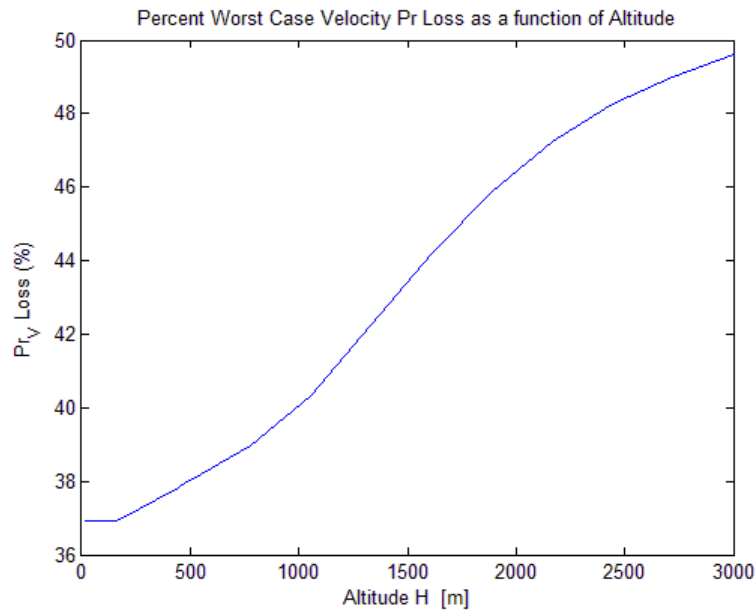


Figure 8-17 – Worst case received power loss

Figure 8-17 shows that worst case loss is about 37 ÷ 49.5%

As regards gain due to geometric configuration, thanks to Matlab® “Velocity_Accuracy_Projection_Coefficient.m” script, coefficients for beam angle equals to 15° and 20° are shown:

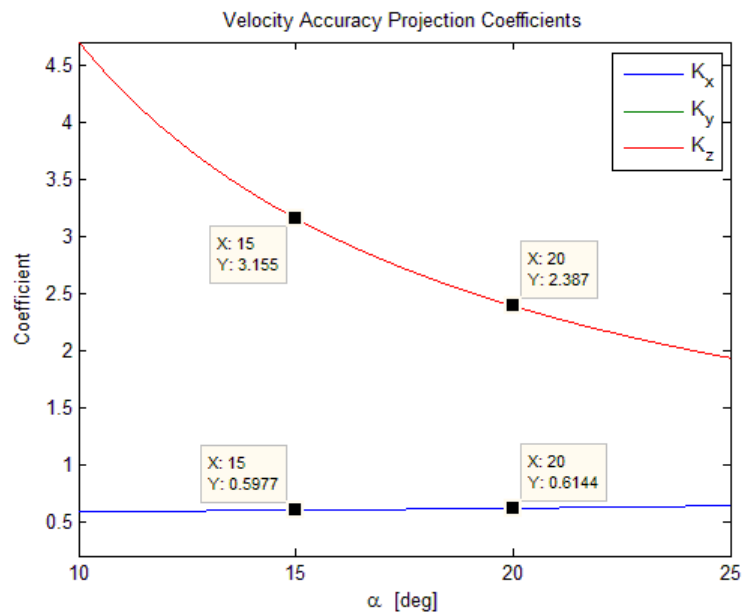


Figure 8-18 – Velocity accuracy projection coefficients

Therefore, with selected modified geometric configuration, Matlab® “RDA_Performance.m” main script provides the same range measurement accuracy as shown in Figure 8-9, because of beam angle doesn’t condition it, while new velocity measurement accuracies are quite different, as shown in the following Figure 8-19 and Figure 8-20.

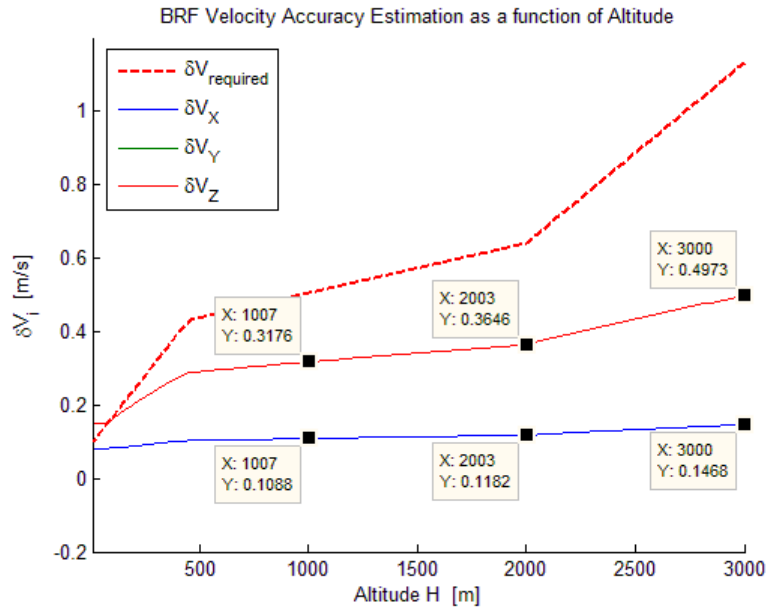


Figure 8-19 – Velocity measurement accuracies

In particular, around final descent:

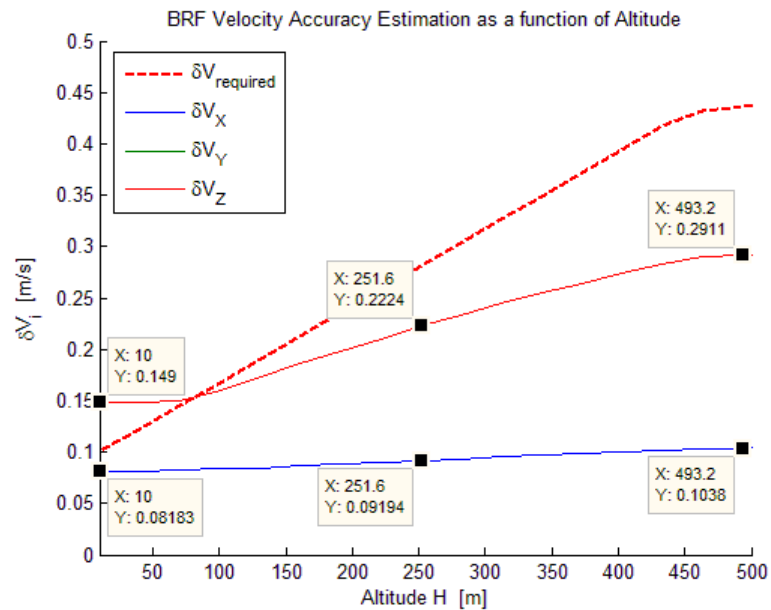


Figure 8-20 – Zoomed velocity measurement accuracies

Figure 8-19 and Figure 8-20 confirm what was theoretically predictable, i.e., measurement error of V_x velocity component increases, while measurement error of V_y and V_z velocity components decreases but at low altitude these components still exceed requirements.

Therefore, thanks to Matlab® “Accuracy_Improvements.m” script, velocity measurement accuracy variations are shown:

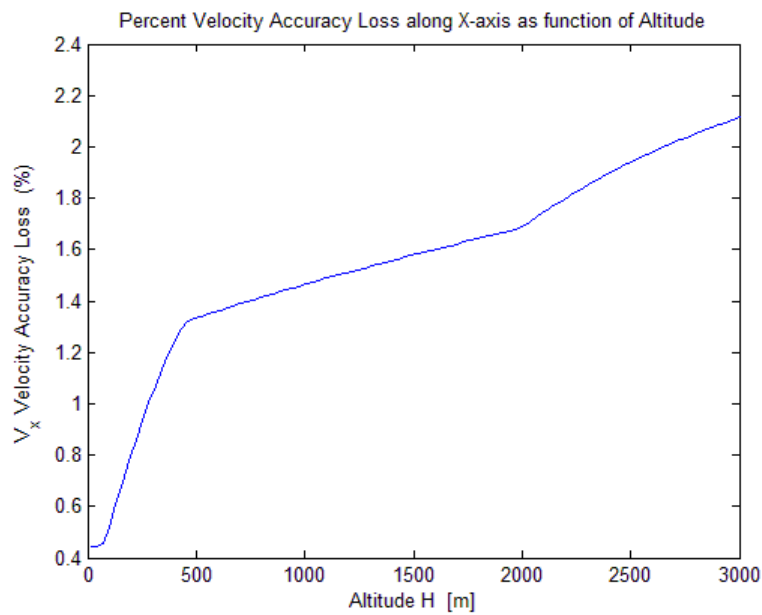


Figure 8-21 – V_x velocity measurement accuracy loss

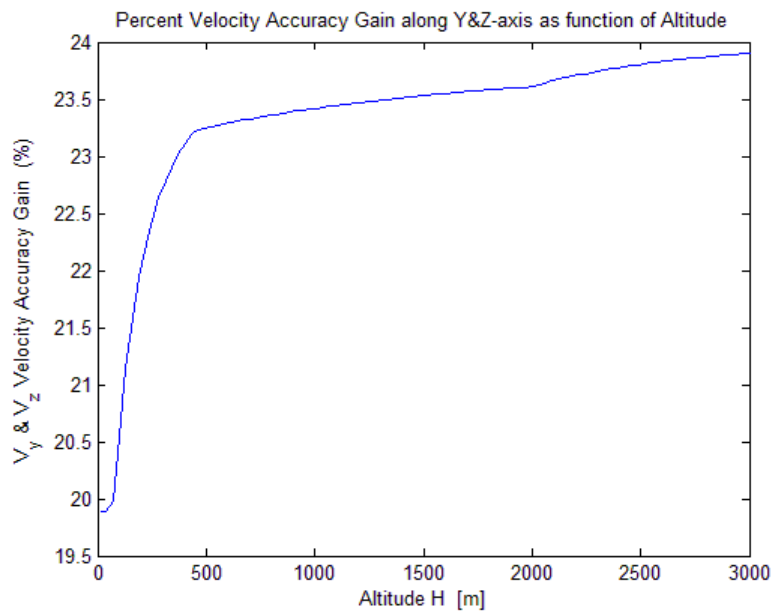


Figure 8-22 – V_y & V_z velocity measurement accuracies gain

Figure 8-21 shows that V_x measurement accuracy loss is about $0.44 \div 2.1 \%$.

Figure 8-22 shows that V_y & V_z measurement accuracies gain is about $19.9 \div 23.9 \%$

Note: At high altitude, accuracy loss increases and accuracy gain decreases because of pulse duration laws selected for beam angle equal to 20° (see Figure 7-22). This selection is driven by velocity Signal Send-Return Time that must be less than velocity PRI. This choice leads to less measurement accuracy at high altitude but at low altitude, near the touchdown, nothing changes.

Therefore, this geometric configuration leads to worsening in V_x measurement accuracy but to a considerable improvement in V_y & V_z measurement accuracies.

Being satisfied requirement of V_x velocity measurement error also for this configuration, even if in worse way, new beam configuration is confirmed because of V_y & V_z velocity measurement errors are more next to its limit.

Being confirmed all the changed parameters above presented, here a total improvements respect to the first preliminary system definition are elaborated thanks to Matlab® “Accuracy_Improvements.m” script.

Total range measurement accuracy variation respect to preliminary definition is shown:

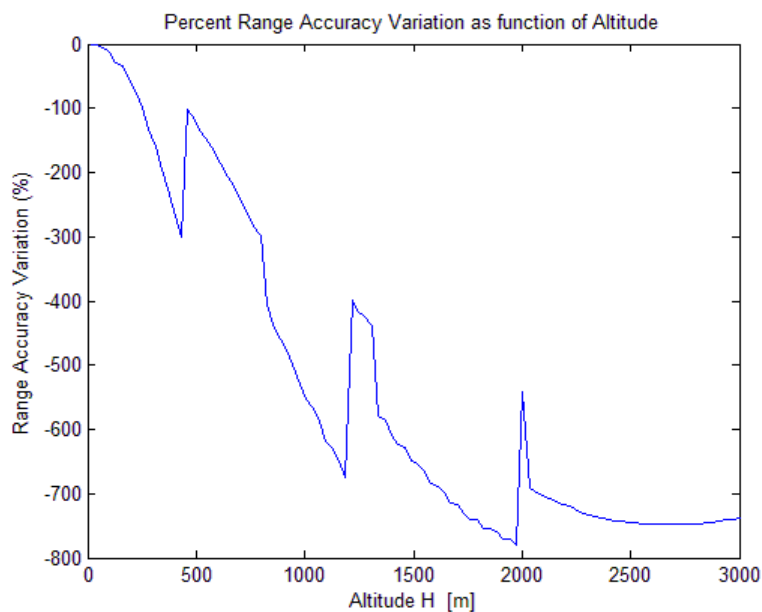


Figure 8-23 – Total range measurement accuracy variation

Figure 8-23 shows that along the entire descent range measurement accuracy variation is about $0 \div -780\%$ and around the final descent is about $0 \div -13.9\%$.

Respect to preliminary definition, the total velocity measurement accuracy variations are shown:

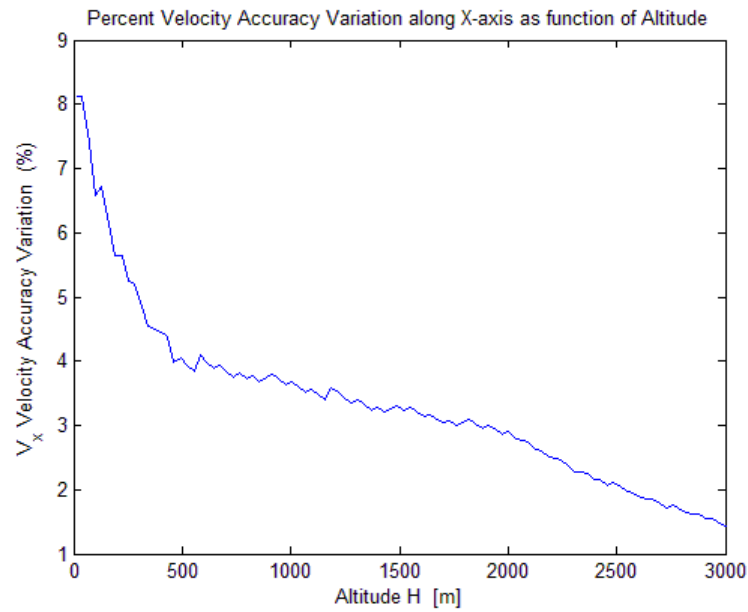


Figure 8-24 – Total V_x velocity measurement accuracy variation

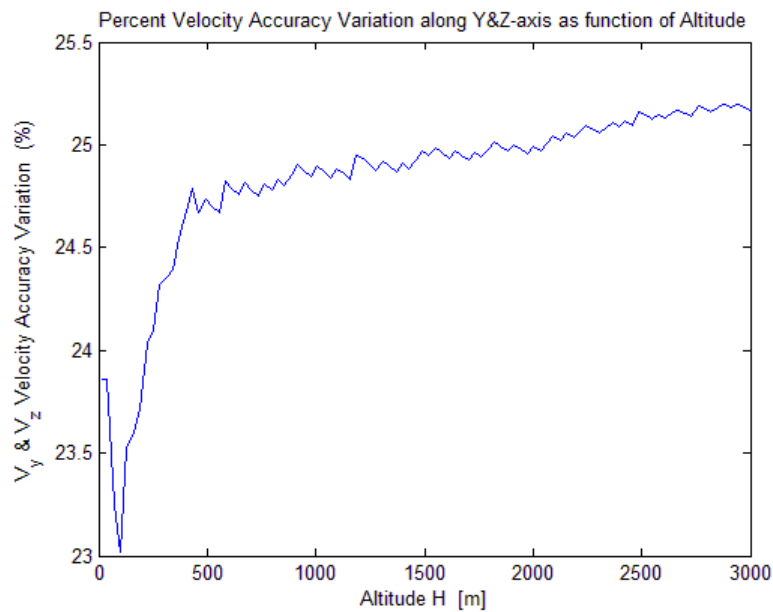


Figure 8-25 – Total V_y & V_z velocity measurement accuracies variation

Figure 8-24 shows that along the entire descent V_x velocity measurement accuracy variation is about $1.4 \div 8.1 \%$ and around the final descent is about $6.6 \div 8.1 \%$.

Figure 8-25 shows that along the entire descent V_y & V_z velocity measurement accuracy variation is about $23 \div 25.1 \%$ and around the final descent is about $23 \div 23.9 \%$.

Therefore, final modified laws lead to:

- Range accuracy impairment along the entire descent, but the requirement is observed in the crucial range of altitude of $0 \div 2000$ m.
- V_x velocity measurement accuracy is higher at low altitude because of time measurement increase and lower at high altitude because of velocity pulse duration decrease and beam angle increase.
- V_y & V_z velocity measurement accuracies are higher along the entire descent but it exceeds requirement at low altitude.

Now, for this configuration, it is possible analyze the differences between measurement errors done and its limit. In fact, the possible excesses of measurements accuracy respect to requirements are shown:

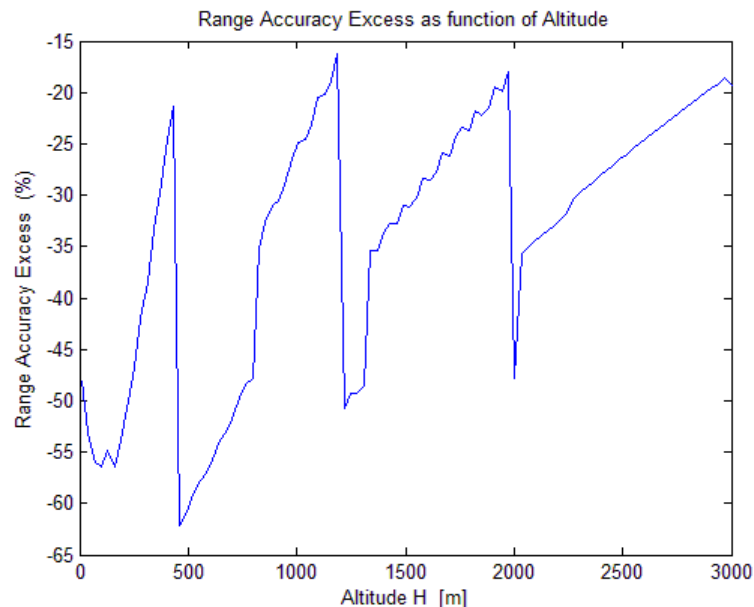


Figure 8-26 – Range measurement accuracy excess

Figure 8-26 shows that range measurement accuracy doesn't exceed requirements along all descent.

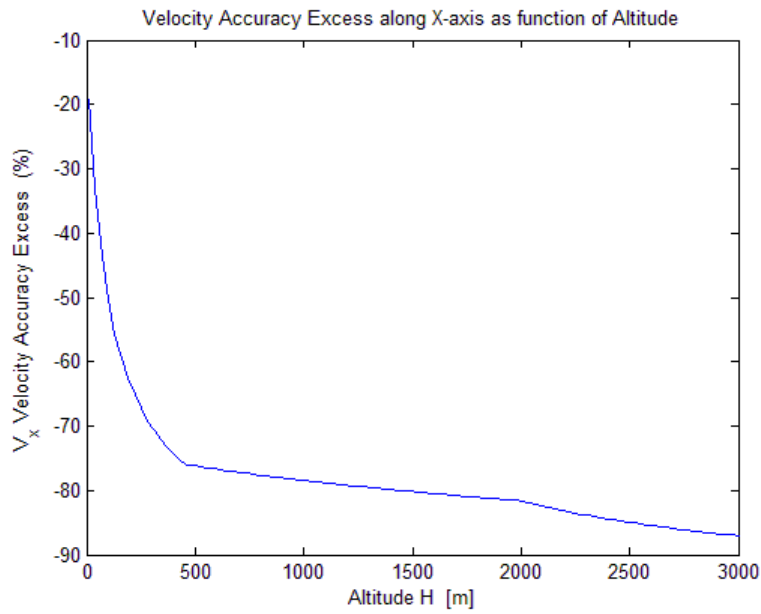


Figure 8-27 – V_x velocity measurement accuracy excess

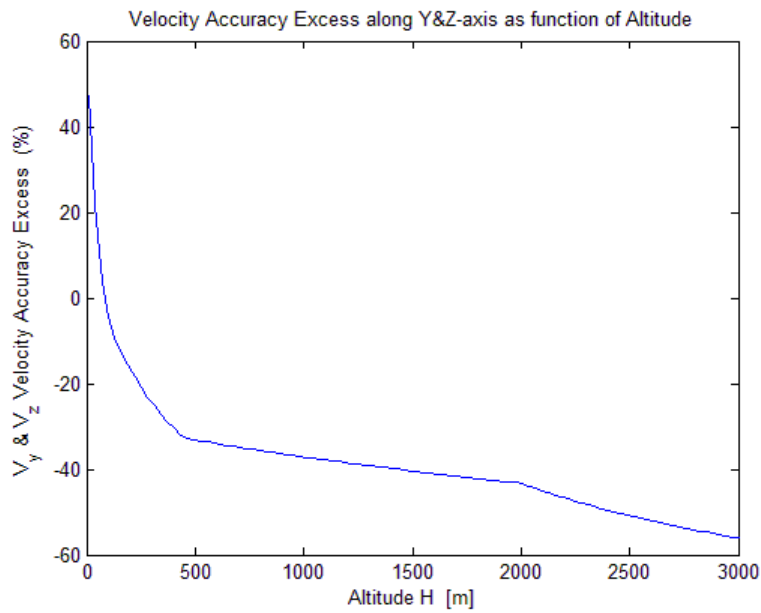


Figure 8-28 – V_y & V_z measurement velocity accuracies excess

Figure 8-27 shows that V_x velocity measurement accuracy doesn't exceed requirements along all descent.

Figure 8-28 shows that V_y & V_z velocity measurement accuracies exceed requirements around the final descent phase of 47.5 %.

The whole situation can also be improved if the requirement on off-nadir angle, acceleration, angular velocity, Jerk, slope and surface roughness can be relaxed. In particular, for null off-nadir angle, acceleration, angular velocity, Jerk, slope and surface roughness, achievable range and velocity accuracy can be considered the theoretical limit of the defined system.

So, accuracies re-computation can be done with the inputs:

$$\sigma_h = 0 \text{ m} \quad ; \quad \text{slope} = 0^\circ \quad ; \quad \theta_{B0} = 0^\circ$$

$$a_{r,Bi} = 0 \text{ m/s}^2 \quad ; \quad J_{r,Bi} = 0 \text{ m/s}^3 \quad ; \quad \dot{\theta}_{\perp,Bi} = 0 \text{ rad/s} \quad (i=1,2,3)$$

Therefore, new theoretical limit of the range measurement accuracy is:

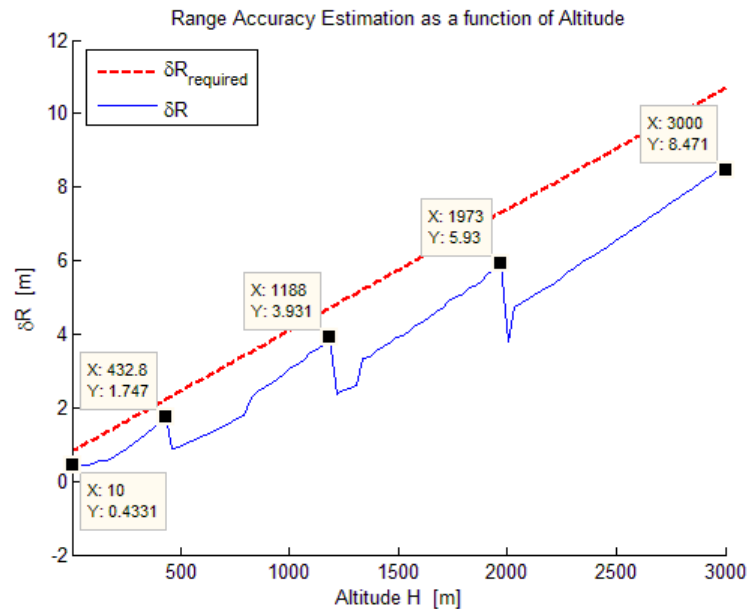


Figure 8-29 – Maximum achievable range measurement accuracy for null acceleration, Jerk and angular velocity

Figure 8-29 shows that for range measurements, as it was predictable, requirement is yet observed in worst case input along the entire descent.

The discontinuities present at an altitude of 450 m, 1200 m, 2000 m are yet due to step-type laws selected for range and velocity integration time.

While new theoretical limits of the velocity measurement accuracies are:

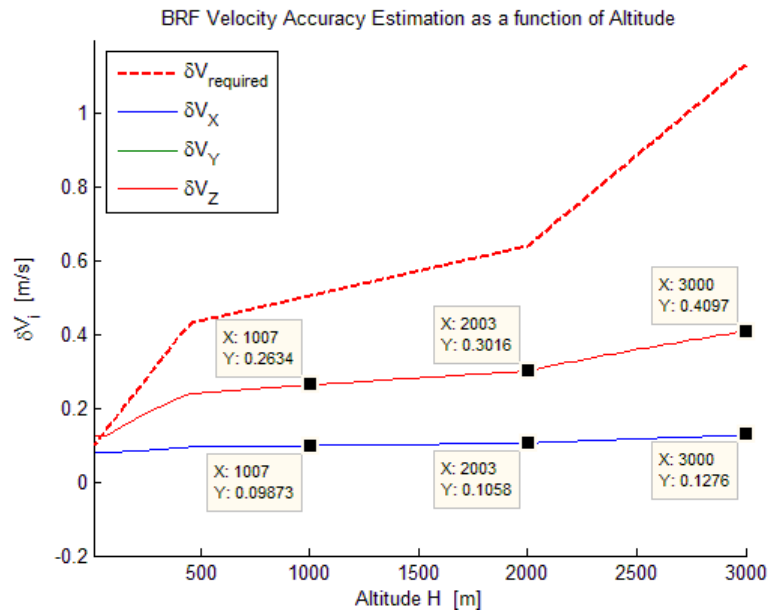


Figure 8-30 – Maximum achievable velocity measurement accuracies for null acceleration, Jerk and angular velocity

In particular, around final descent:

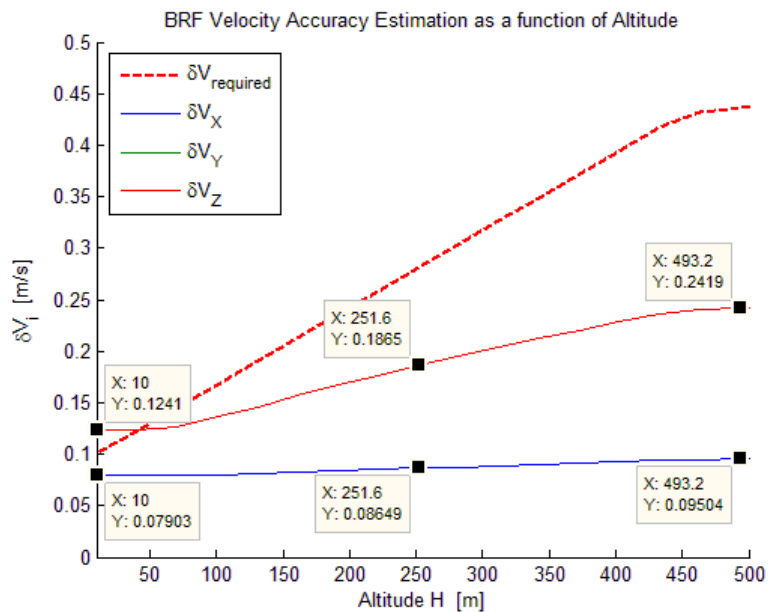


Figure 8-31 – Zoomed maximum achievable velocity measurement accuracies for null acceleration, Jerk and angular velocity

Figure 8-30 and Figure 8-31 show that in any case for V_x measurements, as it was predictable, requirement is observed in worst case input along the entire descent, while for V_y and V_z , this is observed in worst case input only over 50 m of altitude.

In particular, the possible excess of measurement accuracies respect to requirements are shown again:

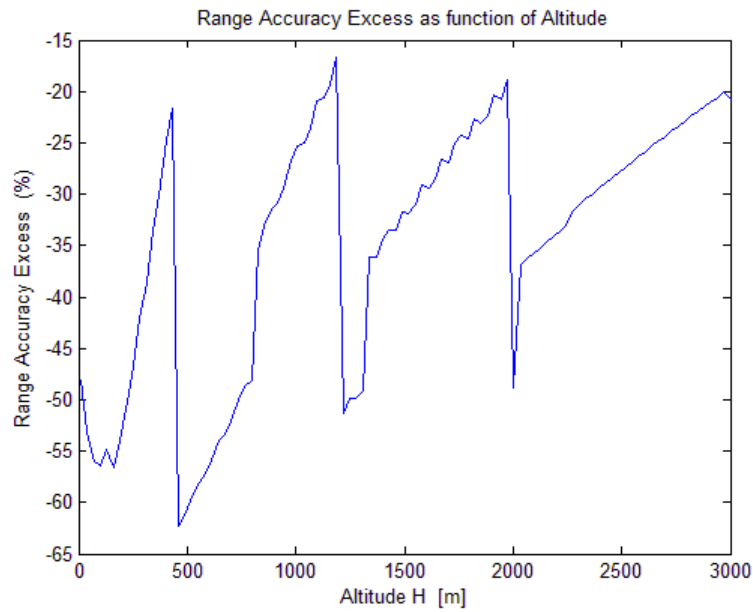


Figure 8-32 – Range measurement accuracy excess

Figure 8-32 shows that range measurement accuracy doesn't exceed requirements along the entire descent.

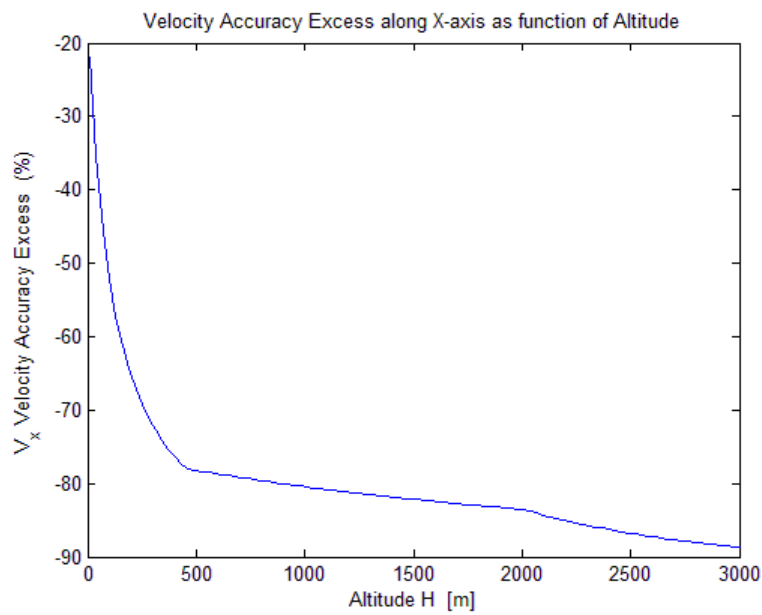


Figure 8-33 – V_x velocity measurement accuracy excess

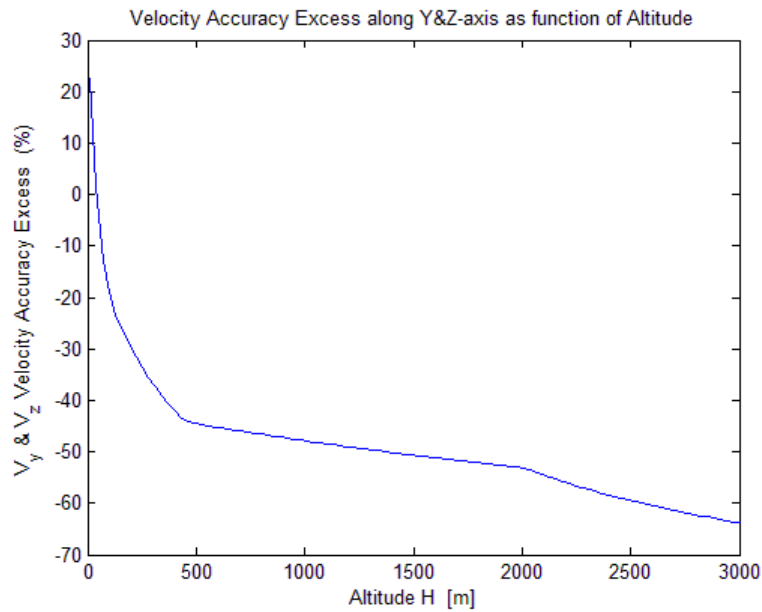


Figure 8-34 – V_y & V_z velocity measurement accuracies excess

Figure 8-33 shows that V_x velocity measurement accuracy doesn't exceed requirements along the entire descent.

Figure 8-34 shows that V_y & V_z velocity measurement accuracies exceed requirements around the final descent phase but the excess is smaller, in fact it is equal to 22.9 % in comparison to 47.5 % .

It is also worth noting that the requirement of 0.1 m/s at very low altitude comes from the assumption that the velocity of the DM is null at 10 m of altitude. If it is not the case, the requirement will increase and will approach or overcome the minimum achievable velocity accuracy by the RDA system.

8.1.5. Final Worst Case RDA Configuration

After the modification of key radar parameters, final RDA configuration for worst case analysis, characterized by a summary of chosen preliminary system definition and worst case input, is reported here:

Operating Frequency	35 GHz
Measurements Update Frequency	20 Hz
Sampling Frequency (I&Q)	100 MHz
IF Frequency	50 MHz
Antenna Illumination	Uniform
Antenna -3dB Aperture	3°
Antenna Gain	33.75 dB
Transmitted Peak Power	30 dBm
Transmitted Pulse Rising Time	5 ns
Transmitting Bandwidth	200 MHz
Receiving Bandwidth	15 MHz (at low altitude)
Receiver Temperature	290 K
Receiver Noise Figure	5 dB
Antenna FE Losses (Tx & Rx)	4 dB
Atmospheric Losses	4 dB
Geometric Beam Angles	0° (range beam) 20° (velocity beams)
Local Terrain Slope (RMS value)	10°
Surface Roughness	0.1 m
Velocity	90.25 m/s

Acceleration	13.4 m/s ²
Jerk	134.2 m/s ³
Attitude Angles	35° (range beam) 55° (velocity beams)
Angular Velocity	60 °/s
Integration Times	Variable (see Figures 8-7&8)
PRFs	Variable (see Figures 7-12÷14)
Pulse Durations	Variable (see Figures 7-17&21)

Table 8-2 – Preliminary RDA definition driven by requirements observation. All specified constant parameters are maintained constant from 10 m up to 3000 m, where the performance will be evaluated.

8.2. “Slow_Vert_Sim_Descent” Simulated Descent

8.2.1. Descent Profile

“Slow_Vert_Sim_Descent” simulated descent profile is characterized by:

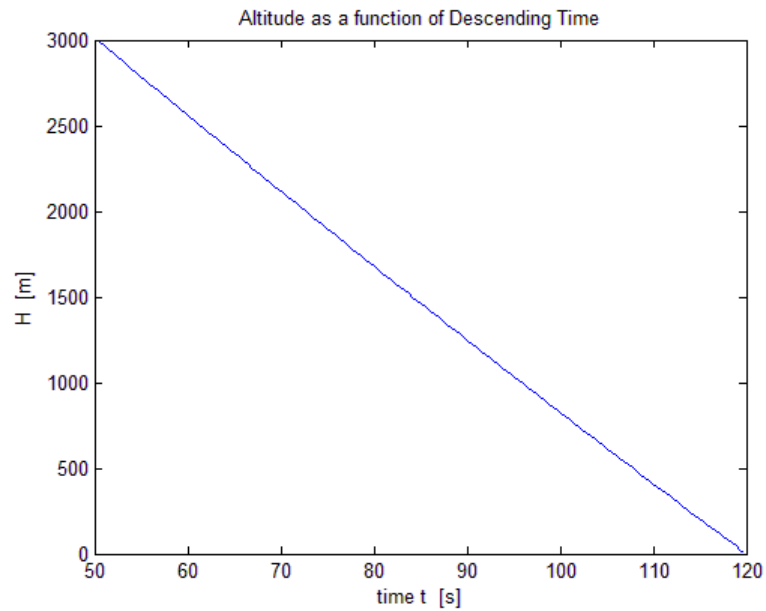


Figure 8-35 – Law motion

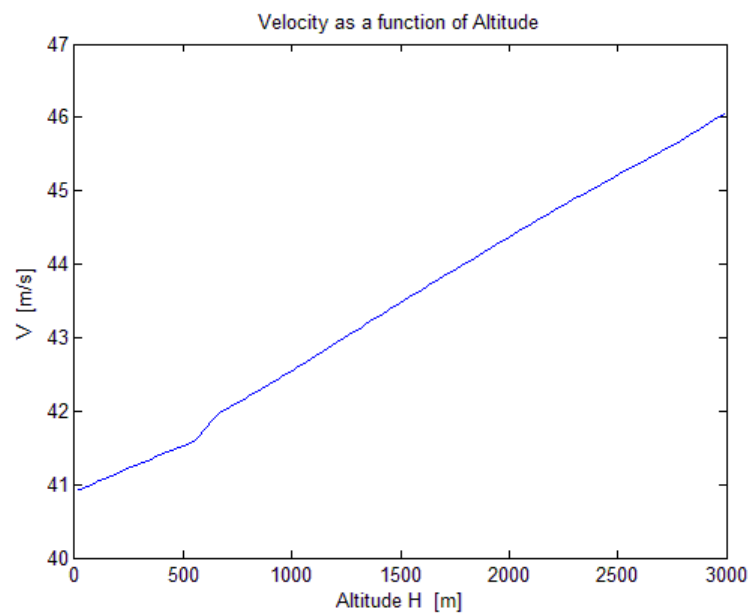


Figure 8-36 – Velocity

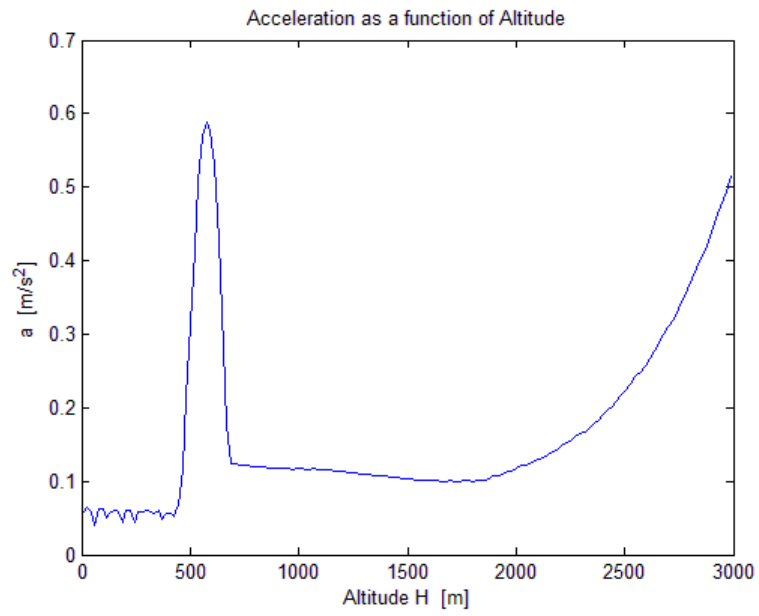


Figure 8-37 – Acceleration

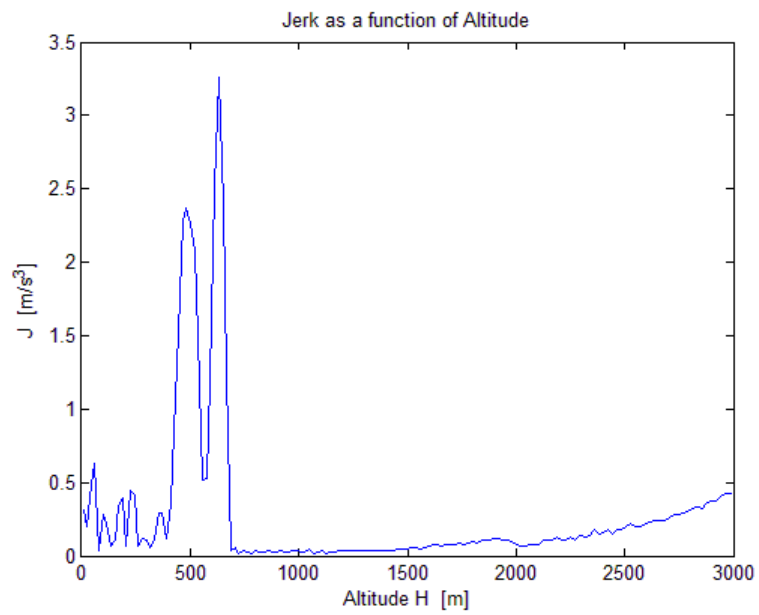


Figure 8-38 – Jerk

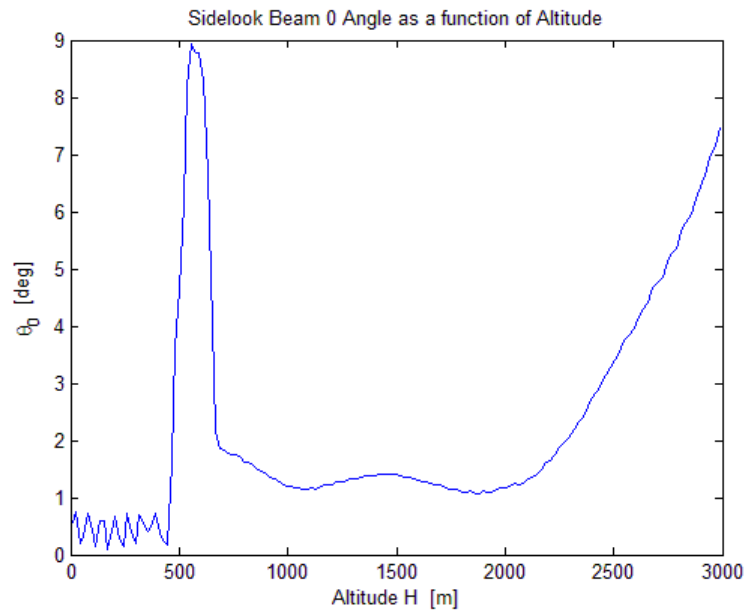


Figure 8-39 – Range sidelook angles

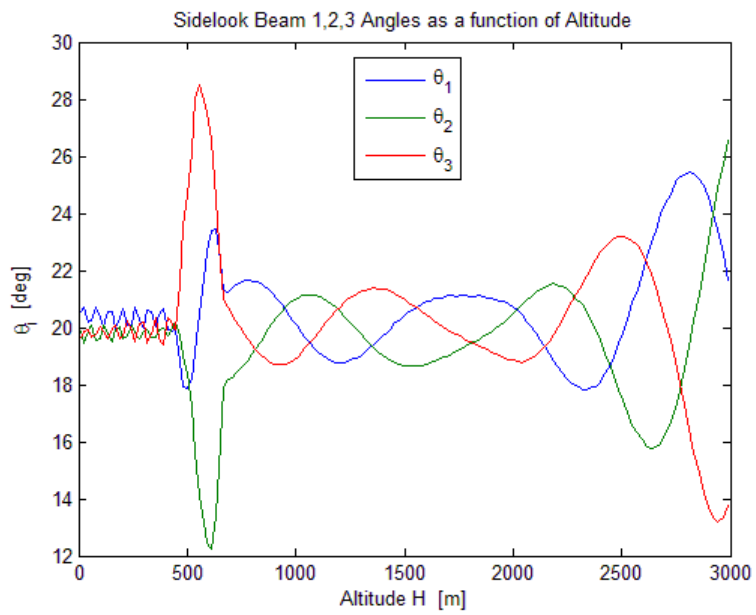


Figure 8-40 – Velocity sidelook angles

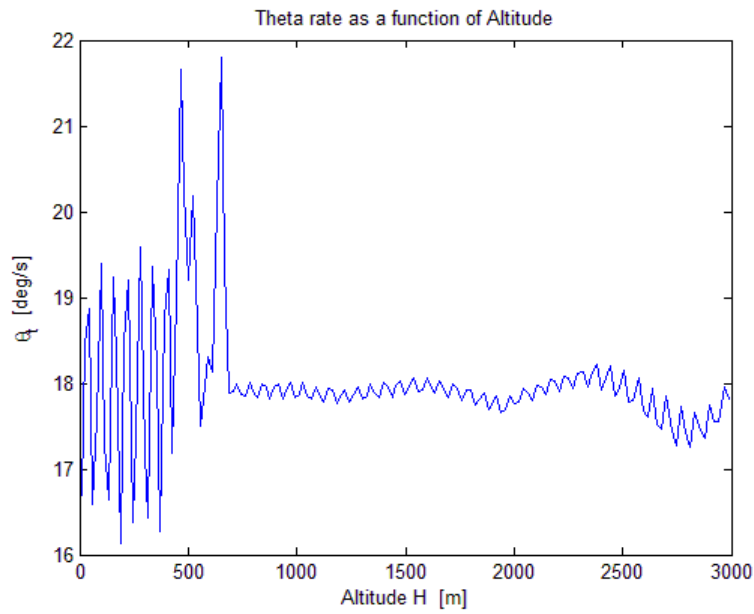


Figure 8-41 – Angular velocity

8.2.2. Inputs Setting

RDA configuration for “Slow_Vert_Sim_Descent” simulated descent analysis, characterized by a summary of chosen preliminary system definition and simulated descent input, is reported here:

Operating Frequency	35 GHz
Measurements Update Frequency	20 Hz
Sampling Frequency (I&Q)	100 MHz
IF Frequency	50 MHz
Antenna Illumination	Uniform
Antenna -3dB Aperture	3°
Antenna Gain	33.75 dB
Transmitted Peak Power	30 dBm

Transmitted Pulse Rising Time	5 ns
Transmitting Bandwidth	200 MHz
Receiving Bandwidth	15 MHz (at low altitude)
Receiver Temperature	290 K
Receiver Noise Figure	5 dB
Antenna FE Losses (Tx & Rx)	4 dB
Atmospheric Losses	4 dB
Geometric Beam Angles	0° (range beam) 20° (velocity beams)
Local Terrain Slope (RMS value)	10°
Surface Roughness	0.1 m
Velocity	Variable (see Figure 8-36)
Acceleration	Variable (see Figure 8-37)
Jerk	Variable (see Figure 8-38)
Attitude Angles	Variable (see Figures 8-39&40)
Angular Velocity	Variable (see Figure 8-41)
Integration Times	Variable (see Figures 8-7&8)
PRFs	Variable (see Figures 7-12÷14)
Pulse Durations	Variable (see Figures 7-17&21)

Table 8-3 – Simulated descent inputs for “Slow_Vert_Sim_Descent”

8.2.3. RDA Measurement Accuracy

In this Paragraph Matlab® “RDA_Performance.m” main script works with “Slow_Vert_Sim_Descent” simulated descent input.

Followings, range and velocity backscattering and SNR results are shown:

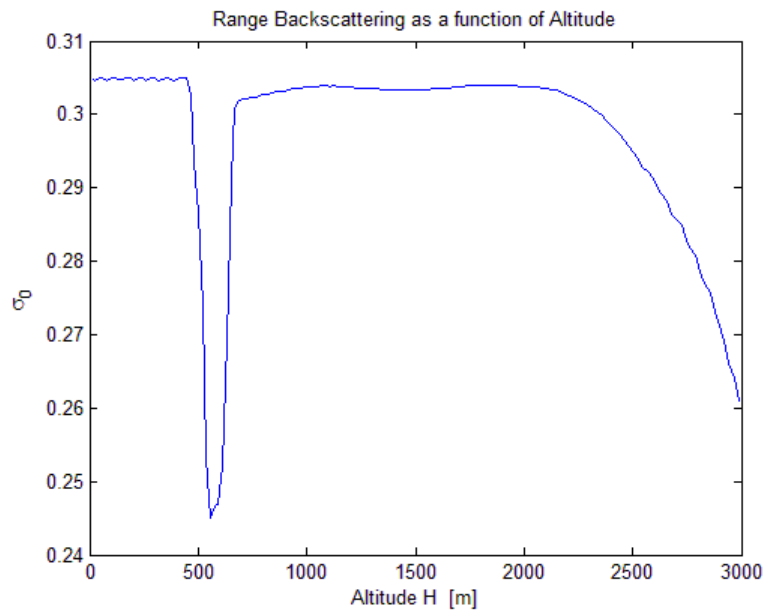


Figure 8-42 – Range backscattering

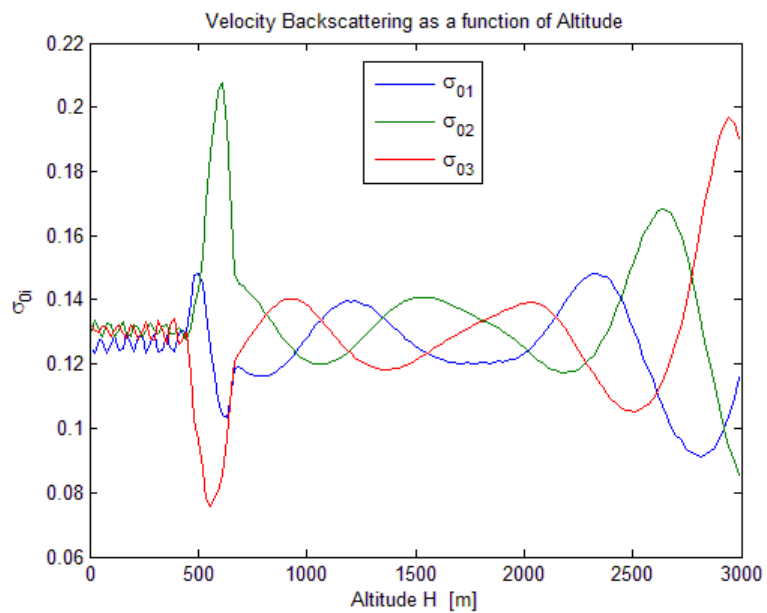


Figure 8-43 – Velocity backscattering

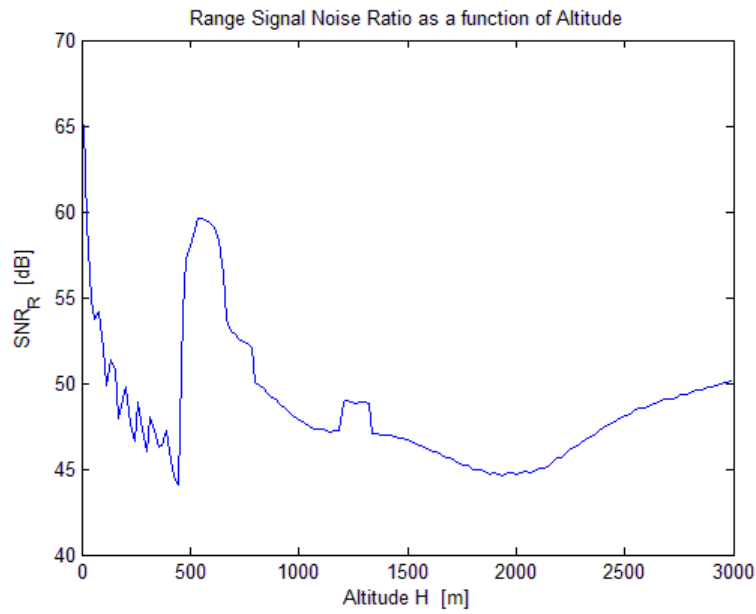


Figure 8-44 – Range SNR

In Figure 8-44 the discontinuities present at an altitude of 450 m, 1200 m, 2000 m are due to step-type laws selected for range and velocity integration time.

At low altitude, little discontinuities are due to the sudden changes of attitude of the descent module.

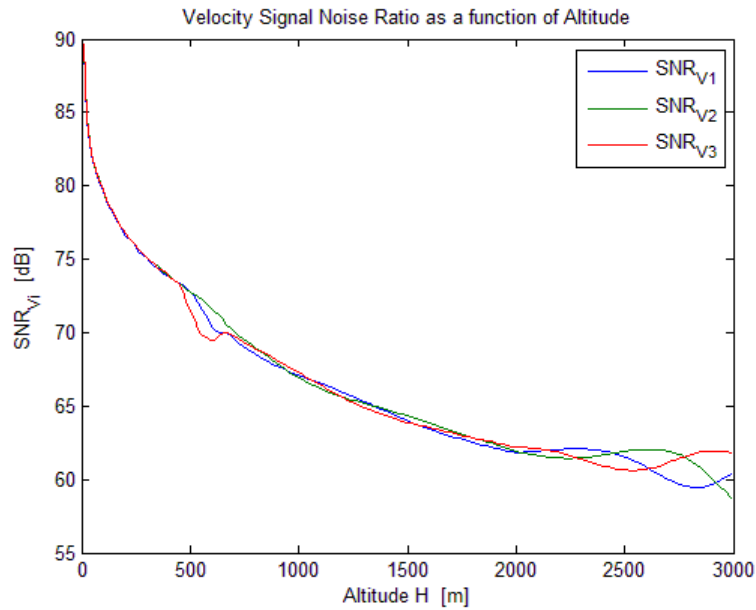


Figure 8-45 – Velocity SNR

Therefore, Matlab® “RDA_Performance.m” main script provides the measurement accuracies:

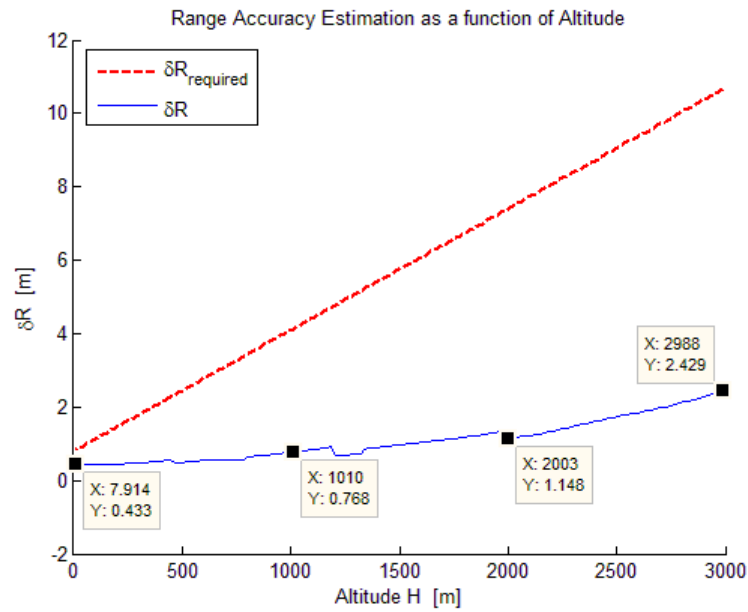


Figure 8-46 – Range measurement accuracy

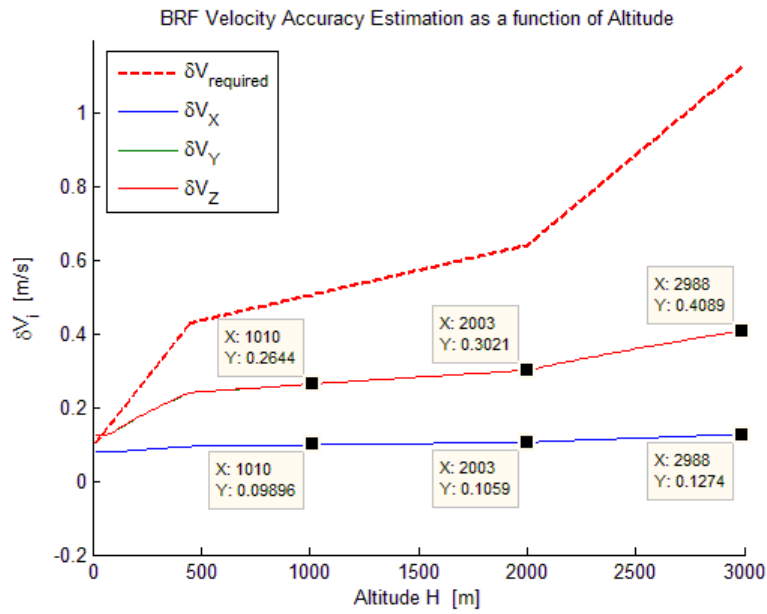


Figure 8-47 – Velocity measurement accuracies

In particular, around final descent:

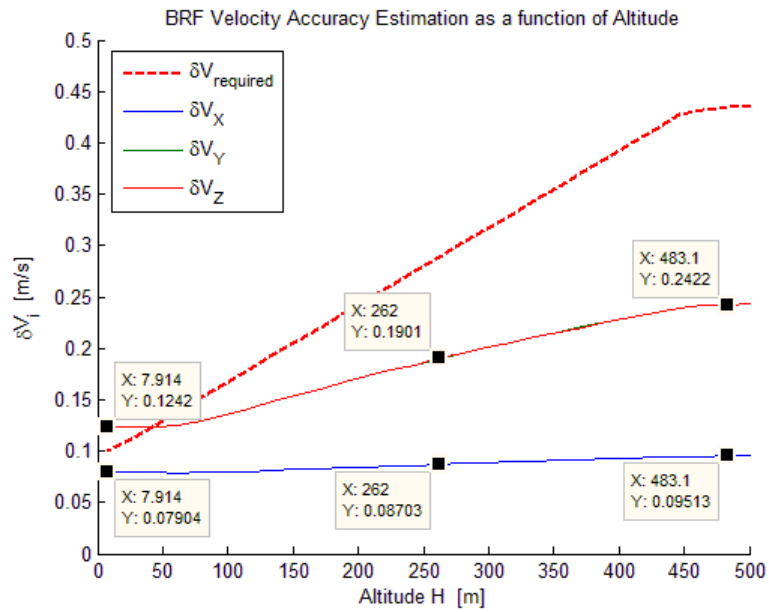


Figure 8-48 – Zoomed velocity measurement accuracies

Figures 8-46÷48 confirm that RDA satisfies range and V_x measurements accuracy along the entire descent, while V_y & V_z measurements accuracies aren't satisfied also in this case.

It is worth noting that in simulated descent performance evaluation, even if each velocity beam hasn't the same off-nadir angle, considering the selected beams geometry, the velocity measurements accuracy along Y_b & Z_b axis is almost the same.

8.3. “Fast_Vert_Sim_Descent” Simulated Descent

8.3.1. Descent Profile

“Fast_Vert_Sim_Descent” simulated descent profile is characterized by:

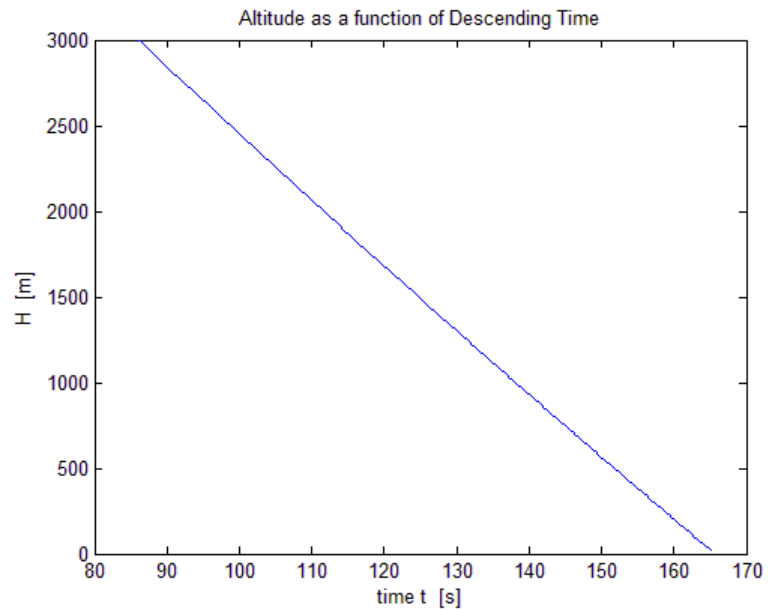


Figure 8-49 – Law motion

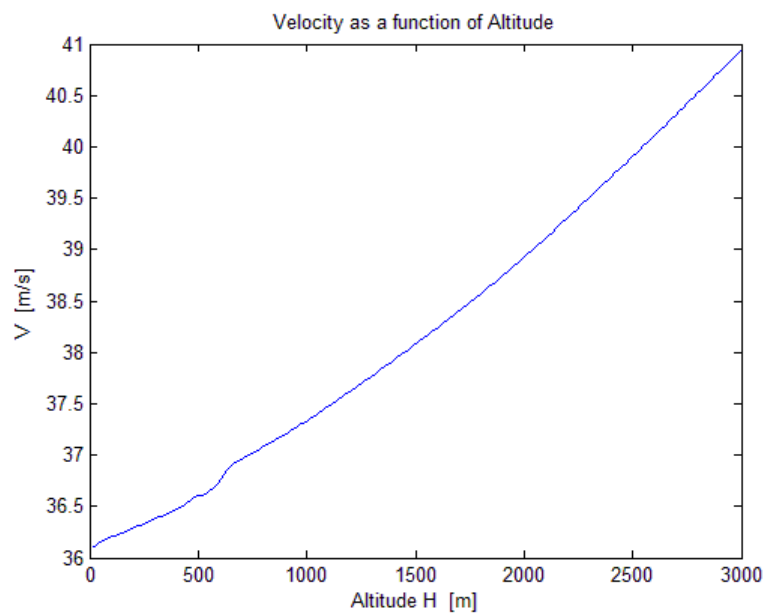


Figure 8-50 – Velocity

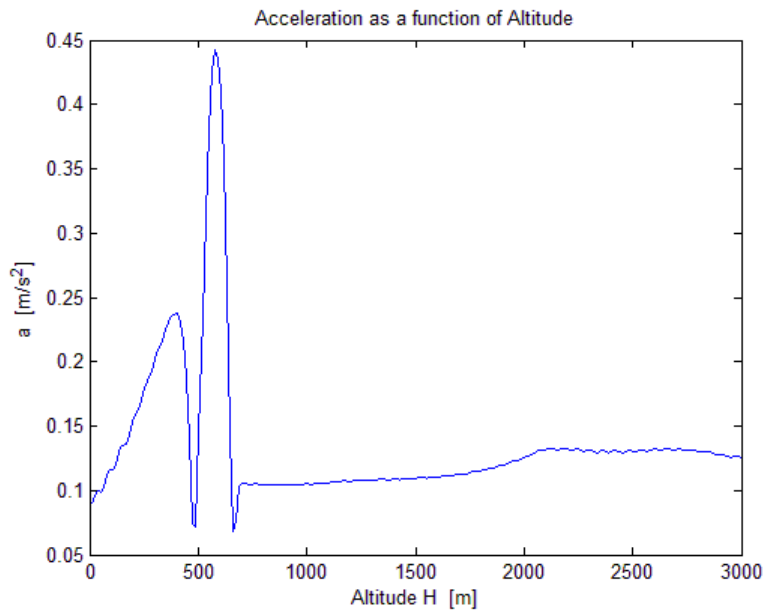


Figure 8-51 – Acceleration

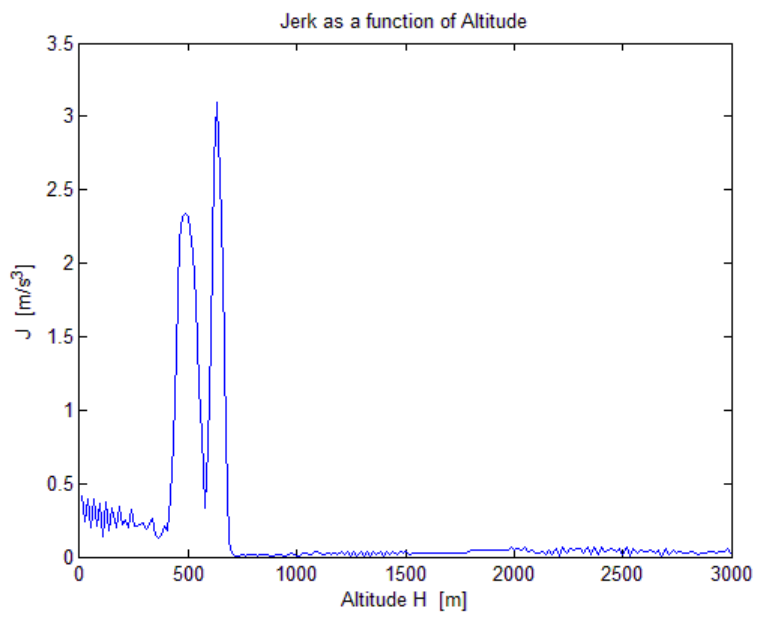


Figure 8-52 – Jerk

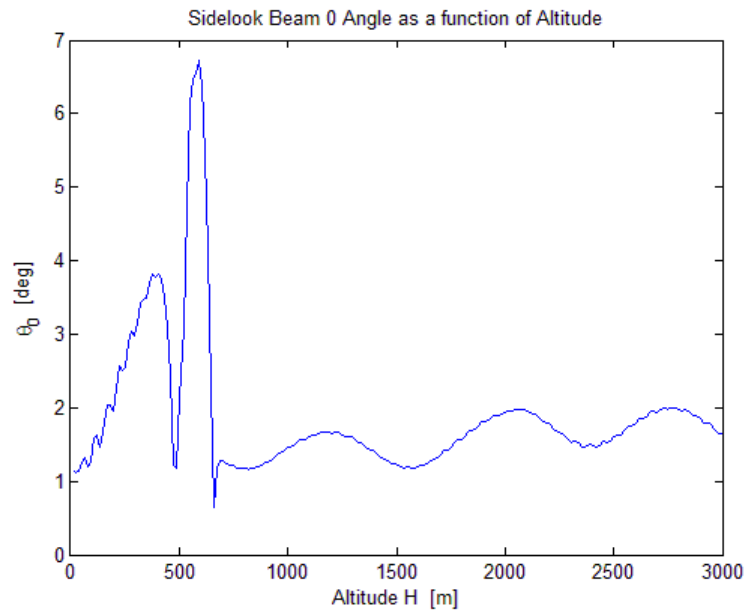


Figure 8-53 – Range sidelook angles

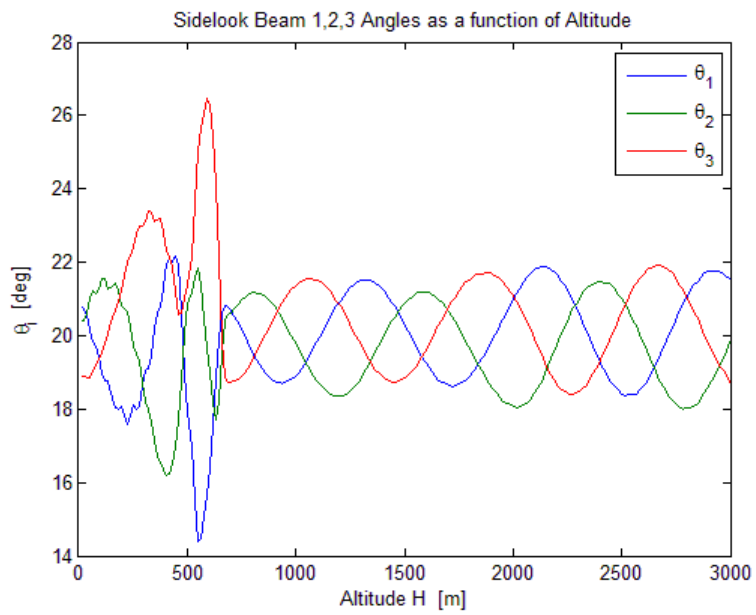


Figure 8-54 – Velocity sidelook angles

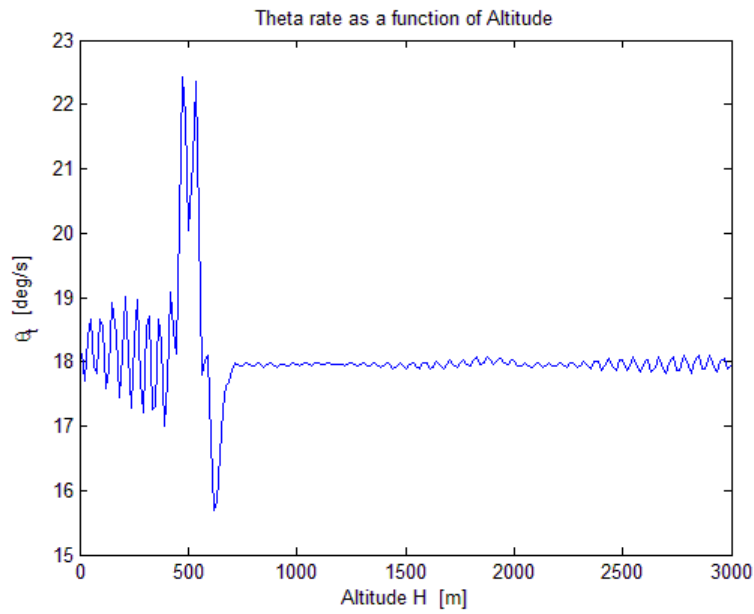


Figure 8-55 – Angular velocity

8.3.2. Inputs Setting

RDA configuration for “Fast_Vert_Sim_Descent” simulated descent analysis, characterized by a summary of chosen preliminary system definition and simulated descent input, is reported here:

Operating Frequency	35 GHz
Measurements Update Frequency	20 Hz
Sampling Frequency (I&Q)	100 MHz
IF Frequency	50 MHz
Antenna Illumination	Uniform
Antenna -3dB Aperture	3°
Antenna Gain	33.75 dB
Transmitted Peak Power	30 dBm

Transmitted Pulse Rising Time	5 ns
Transmitting Bandwidth	200 MHz
Receiving Bandwidth	15 MHz (at low altitude)
Receiver Temperature	290 K
Receiver Noise Figure	5 dB
Antenna FE Losses (Tx & Rx)	4 dB
Atmospheric Losses	4 dB
Geometric Beam Angles	0° (range beam) 20° (velocity beams)
Local Terrain Slope (RMS value)	10°
Surface Roughness	0.1 m
Velocity	Variable (see Figure 8-50)
Acceleration	Variable (see Figure 8-51)
Jerk	Variable (see Figure 8-52)
Attitude Angles	Variable (see Figures 8-53&54)
Angular Velocity	Variable (see Figure 8-55)
Integration Times	Variable (see Figures 8-7&8)
PRFs	Variable (see Figures 7-12÷14)
Pulse Durations	Variable (see Figures 7-17&21)

Table 8-4 – Simulated descent inputs for “Fast_Vert_Sim_Descent”

8.3.3. RDA Measurement Accuracy

In this Paragraph Matlab® “RDA_Performance.m” main script works with “Fast_Vert_Sim_Descent” simulated descent input.

Followings, range and velocity backscattering and SNR results are shown:

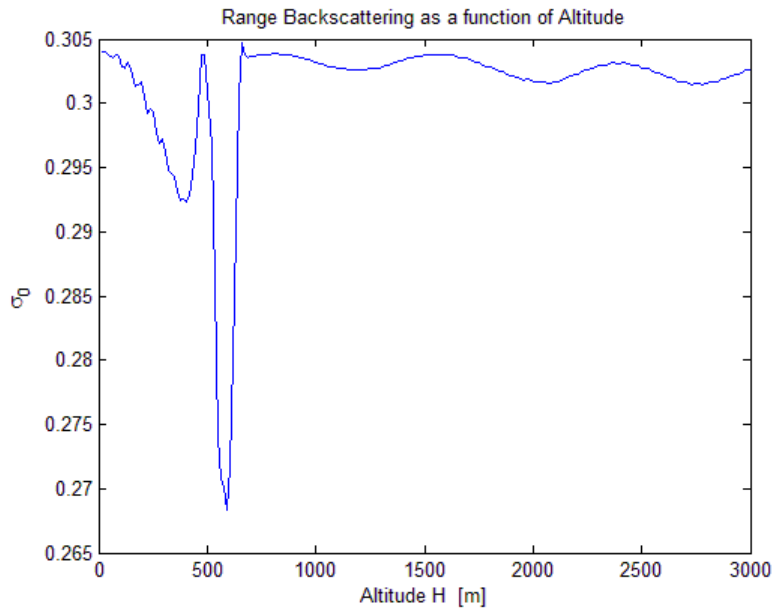


Figure 8-56 – Range backscattering

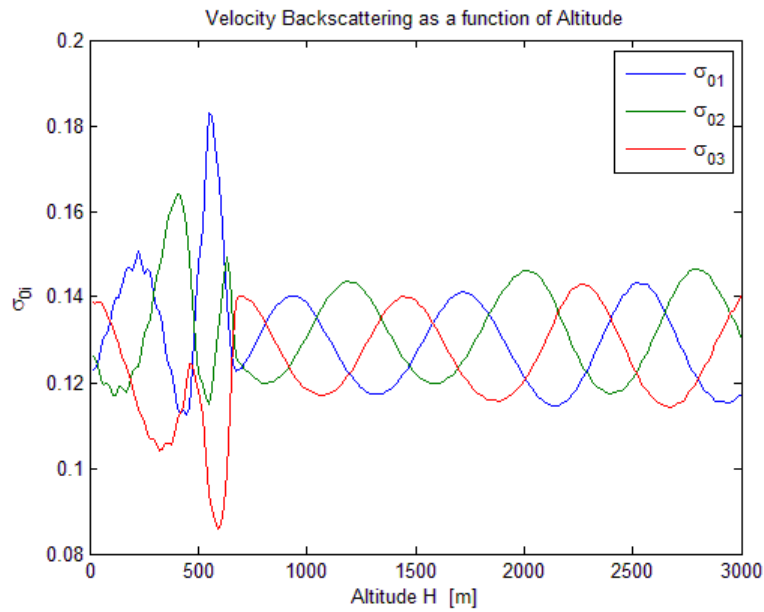


Figure 8-57 – Velocity backscattering

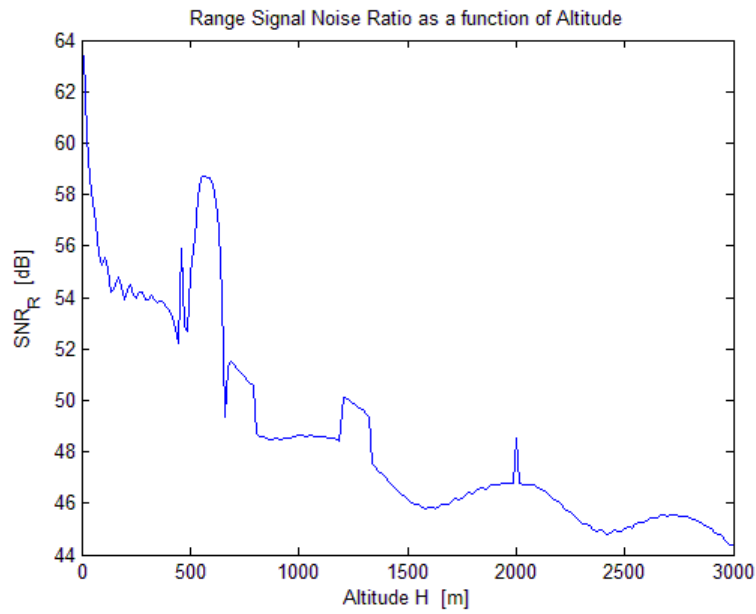


Figure 8-58 – Range SNR

In Figure 8-58 the discontinuities present at an altitude of 450 m, 1200 m, 2000 m are due to step-type laws selected for range and velocity integration time.

At low altitude, little discontinuities are due to the sudden changes of attitude of the descent module.

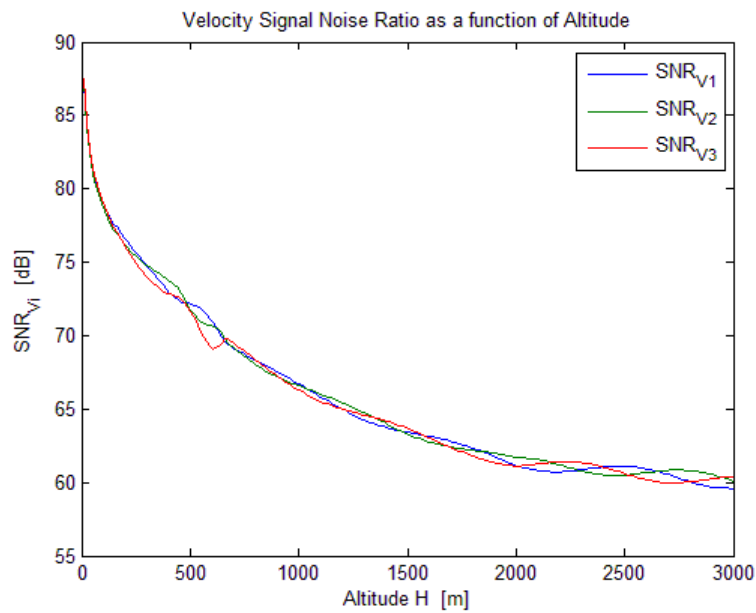


Figure 8-59 – Velocity SNR

Therefore, Matlab® “RDA_Performance.m” main script provides the measurement accuracies:

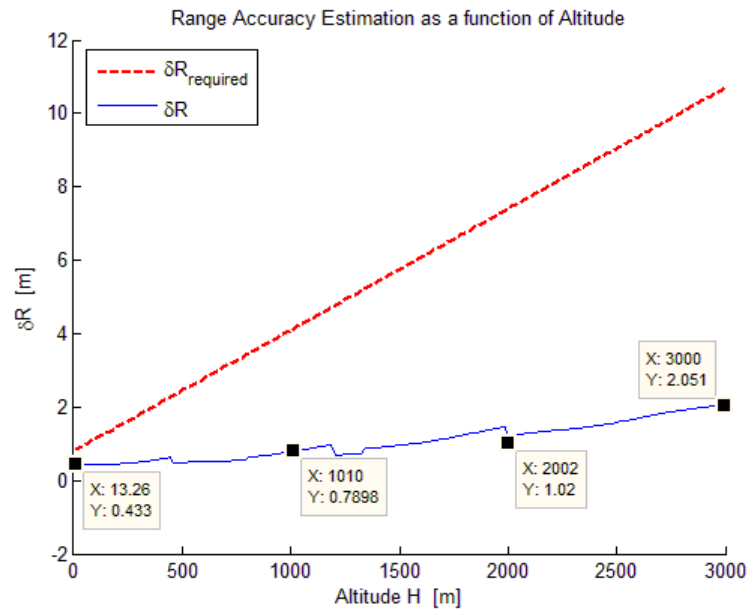


Figure 8-60 – Range measurement accuracy

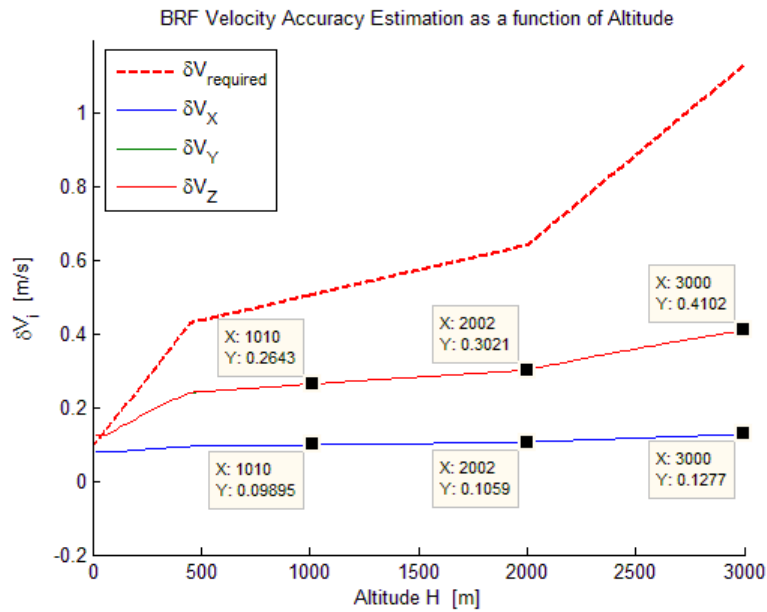


Figure 8-61 – Velocity measurement accuracies

In particular, around final descent:

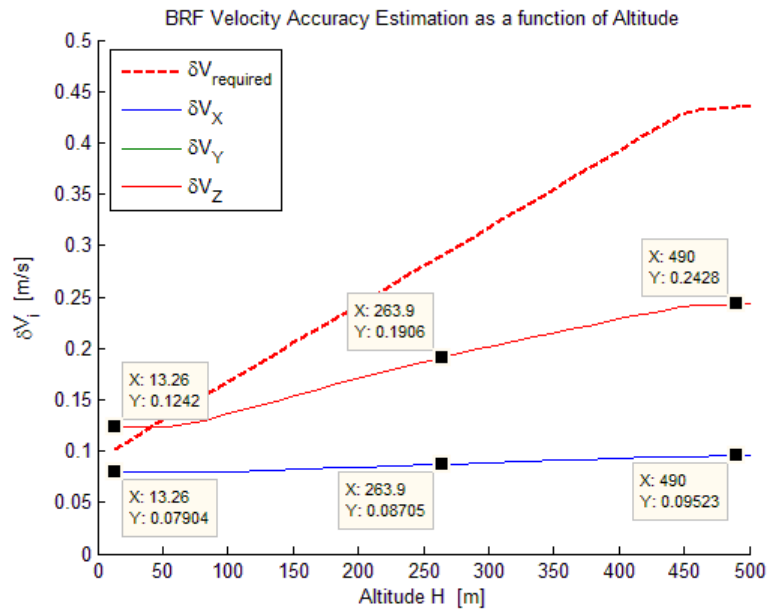


Figure 8-62 – Zoomed velocity measurement accuracies

Figures 8-60÷62 confirm that RDA satisfies range and V_x measurements accuracy along the entire descent, while V_y & V_z measurements accuracies aren't satisfied also in this case.

It is worth noting that in simulated descent performance evaluation, even if each velocity beam hasn't the same off-nadir angle, considering the selected beams geometry, the velocity measurements accuracy along Y_b & Z_b axis is almost the same.

CONCLUSIONS

The requirement of safe and accurate landing of heavier and complex payloads is relatively new and it is foreseeable that it will be applied consistently to future landing missions of the planetary exploration programs. On the base of the reported requirements and technological know-how, this work has studied a preliminary definition of the sensor onboard the Lander of ExoMars mission that will support Landing Guidance and Navigation Control (GNC) during the final descent phase on Mars.

The preliminary system definition leads to a Ka-band Radar Doppler/Altimeter in order to use smaller microwave components and to limit the antenna size needed to get the desired beamwidth.

Other key parameters have been selected thanks to the optimization analysis. This investigation has allowed us to select time integration laws, pulse repetition frequency laws and pulse duration laws both for range and velocity measurements.

Subsequently, the implementation of RDA Performance Model has been elaborated with Matlab® engineering software.

The Performance Model has allowed the analysis of sensor accuracy in different cases. Considering the optimum laws selected during the optimization analysis, the results for the worst case have shown that range measurement accuracy and velocity measurement accuracy along X_b -axis satisfy the reported requirements along the entire descent and, therefore, also in the key altitude range of $0 \div 2000$ m, while velocity measurement accuracies along Y_b & Z_b -axis at low altitude exceed maximum tolerable values approximately of 95.7 % before inflating vented bags.

To achieve the full satisfaction of the reported requirements at low altitude, two changes have been proposed: the selection of a step-type law for time integration both for range and velocity measurements and the increase of velocity beam angle.

The new preliminary system definition exhibits less accurate range measurements, however, they still respect the reported requirements along the entire descent. This leads to a considerable improvement for velocity measurements accuracy, in fact at low altitude velocity measurement error along X_b -axis decreases from 0.089 m/s to 0.082 m/s with a gain of about 8%, while along Y_b & Z_b -axis decreases from 0.2 m/s to 0.15 m/s with a gain of about 25%.

After the improvements, the results for the worst case have also shown that range measurement accuracy and velocity measurement accuracy along X_b -axis satisfy the reported requirements along the entire descent and, therefore, also in the key altitude range of $0 \div 2000$ m, while velocity measurement accuracies along Y_b & Z_b -axis at low altitude still exceed maximum tolerable values approximately of 47.5 % before inflating the vented bags.

In the hypothesis of null vertical and horizontal velocity before inflating the vented bags, an error of 0.082 m/s in the measurement of velocity component along X_b -axis and of 0.15 m/s in the measurement of velocity component along Y_b & Z_b -axis appears to be tolerable because touchdown occurs with maximum predictable vertical velocity of about $8.59 \text{ m/s} + 0.089 \text{ m/s}$ and horizontal velocity of about 0.15 m/s. This is possible thanks to vented bags that absorb the final touchdown velocity avoiding lander crash because of non-zero vertical velocity component and/or overturn because of non-zero horizontal velocity component.

So, in worst case this work shows that heavier and complex payloads can land on Mars with safe and accurate approach to surface thanks to Radar Doppler/Altimeter sensors.

Two simulated descent profile have been also analyzed, the results in this case have shown that range measurement accuracy and velocity measurement accuracy along X_b -axis satisfy the reported requirements along the entire descent and, therefore, also in the key altitude range of $0 \div 2000$ m, while velocity measurement accuracies along Y_b & Z_b -axis at low altitude exceed maximum tolerable values approximately of 24.1 % before inflating vented bags.

It is worth noting that the constant envelope of Radar Doppler/Altimeters appears of fundamental importance because not only ExoMars Lander will use these sensors, but all missions of Aurora Program will have the same necessity. So, obtaining know-how about these sensors is strategic for future European space activities.

It is also worth noting that technologies developed for Exomars mission and for Aurora Program can be utilized also in earthly applications such as Guidance and Navigation Control (GNC) for Unmanned Aerial Vehicles (UAVs).

In fact, as these vehicles acquire new strategic capabilities through advancements in technology, new sensing and control strategies will be required to enable these vehicles to perform robustly in a safe manner. This requires good estimates of the vehicle states.

Many strategies exist for vehicle state estimation for autonomous navigation and often several sensor types are utilized to take advantage of different measurement characteristics. Sensors measure specific parameters often making direct measurements of the complete set of state variables impossible. Instead these measurements are used to estimate the vehicle states and often also relevant environmental features. The challenge is to choose a set of sensors that yields enough information to generate accurate estimates. Among them, Radar Doppler/Altimeters can have a remarkable role.

*“...So never mind the darkness
We still can find a way
'Cause nothin' lasts forever
Even cold November Rain...”*

November Rain

Use Your Illusion I - Guns N' Roses

DEFINITIONS

Aliasing: The process by which frequencies too high to be analyzed with the given sampling interval appear at a frequency less than the Nyquist frequency.

Ambiguous Velocity: See Velocity Aliasing.

Amplitude: The maximum magnitude of a quantity.

Analog: Class of devices in which the output varies continuously as a function of the input.

Antenna Gain: The measure of effectiveness of a directional antenna as compared to an isotropic radiator; maximum value is called antenna gain by convention.

Antenna Pattern: (Also called radiation pattern, beam pattern, lobe pattern.) A graphical representation of the radiating properties of an antenna as a function of space coordinates.

Attenuation: Any process in which the flux density (power) of a beam of energy is dissipated.

Autocorrelation: A measure of similarity between displaced and undisplaced (in time, space, etc.) versions of the same function.

Azimuth: A direction in terms of the 360 degree compass.

Backscatter: That portion of power scattered back in the incident direction.

Bandpass Filter: A filter whose frequencies are between given upper and lower cutoff values, while substantially attenuating all frequencies outside these values (this band).

Bandwidth: The number of cycles per second between the limits of a frequency band.

Band Reject Filter: (or notch filters) are used to pass a large operating band of frequencies, while rejecting a narrow band of frequencies.

Beamwidth: Angular width of the antenna pattern. Usually the width where the power density is one-half that of the axis of the beam.

Bias: A systematic difference between an estimate of and the true value of the parameter.

Central Limit Theorem: Statistical theorem showing that averages approach a Gaussian distribution independent of the input distribution.

Coherence: The property of two or more waves that are in phase both temporally and spatially. Waves are coherent if they have the same wavelength and a fixed phase relationship with each other.

Coherent Radar: A radar that utilizes both signal phase and amplitude to determine target characteristics.

Complex Signal: A signal containing both amplitude and phase information.

Correlation: A measure of similarity between variables or functions.

Couplet: Adjacent maxima of radial velocities of opposite signs.

Covariance: A measure of the degree of association between two variables. In Doppler radars, the argument (or angle) of the covariance of the complex signal is a measure of the Doppler frequency.

Dealiasing: Process of correcting for aliases in the velocity measurement. See also Velocity Aliasing.

Decibel (dB): A logarithmic expression for ratio of two quantities. dBm is a decibel with respect to 1 milliwatt.

Mathematically: $dB = 10 \text{ Log } (P_1/P_2)$

$$dBm = 10 \text{ Log } (P/10^{-3})$$

Doppler Shift: The change in frequency at a receiver due to the relative motion of the receiver and the energy source.

Doppler Spectral Moments: Statistical moments of Doppler frequency or Doppler velocity, regarding these quantities as continuously distributed random variables with a probability density function equal to the normalized Doppler spectrum.

Dwell Time: Time over which a signal estimate is made. Usually, the time required for the antenna to transverse one degree.

Dynamic Range: The ratio, usually expressed in decibels, or the maximum to the minimum signal that a system can handle. Used to describe limits of receivers.

Echo: Energy backscattered from a target as seen on the radar display.

Estimate: A statement of the value of a quantity or function based on a finite number of samples.

Folding: See Range Folding.

Frequency: The number of recurrences of a periodic phenomenon per unit time. Electromagnetic energy is usually specified in Hertz (Hz), which is a unit of frequency equal to one cycle per second.

Frequency Carrier: It is the fundamental transmitted microwave frequency. It is modulated so that it exists for a few microseconds each pulse repetition time. This limit is called the transmitted pulse.

Gaussian: Refers to the Normal distribution; phenomena whose events are normally distributed are Gaussian distributed. This is the most common distribution encountered in physical processes.

Homodyning: The transfer of signal intelligence from one carrier to another by mixing of signals at different frequencies.

Incident Power Density: Energy per unit area incident on the radar target.

In-phase: The component of a complex signal along the real axis in the complex plane.

Iso-dop: Contour of constant Doppler velocity values.

Instability: A property of the steady state of a system such that certain disturbances or perturbations introduced into the steady state will increase in magnitude, the maximum perturbation amplitude always remaining larger than the initial amplitude.

Klystron: An electron tube used as a low-power oscillator or a high-power amplifier at ultrahigh frequencies. Noted for exceptional stability over long periods of transmission.

Mainlobe: The envelope of electromagnetic energy along the main axis of the beam.

Maximum Unambiguous Range: The maximum range to which transmitted pulse wave can travel and return to the radar before the next pulse is transmitted.

Maximum Unambiguous Velocity: The maximum range of radial velocity that can be observed without ambiguity by a Doppler radar. Velocities outside this interval are folded into the interval. *See* Velocity aliasing and Nyquist Frequency.

Mean Doppler Velocity: Reflectivity-weighted average velocity of targets in a given volume sample. Usually determined from a large number of successive pulses. Also called mean radial velocity. Doppler velocity usually refers to spectral density first moment; radial velocity to base data.

Microwave: Electromagnetic radiation having wavelengths between approximately 1 mm and 1 m (corresponding to 0.3- and 300-GHz frequency). Active systems operating at these wavelengths are called radar, although the definition of radar

requires a capability to measure distance that is not always included in active microwave systems.

Modulation: Variation of the amplitude, frequency, or phase of a wave due to the mixing of two signals.

Monostatic Radar: A radar that uses a common antenna for both transmitting and receiving.

Notchwidth: The 3 dB band width of a rejection filter.

Nyquist Interval: (Also Nyquist velocity). The maximum time interval between equally spaced samples of a signal that will enable the signal waveform to be completely determined. Also known as the (absolute value) of the maximum unambiguous velocity that can be measured by a Doppler radar, e.g., 50 m/s.

Nyquist Co-Interval: The full range of the Nyquist interval, e.g., +/- 50 m/s.

Nyquist Frequency: The highest frequency that can be determined in data that have been discretely sampled. For data sampled at frequency f_s , this frequency is $f_s/2$.

Nyquist Sampling Theorem: In order to unambiguously measure a frequency, a sampling rate of at least two times this frequency is required. Doppler radar sampling rate is equal to the pulse repetition frequency (PRF).

Oscillator: The general term for an electric device that generates alternating currents or voltage. The oscillator is classified according to frequency of the generated signal.

Phase: A particular angular stage or point of advancement in a cycle; the fractional part of the angular period through which the wave had advanced, measured from the phase reference.

Phase Shift: The angular difference of two periodic functions.

Platform: support platform on which the payload is mounted.

Polarization: With respect to a transverse electromagnetic wave, the correlation between two orthogonal components of its electric (or, equivalently, magnetic) field.

Propagation: Transmission of electromagnetic energy as waves through or along a medium.

Pulse: A single short duration transmission of electromagnetic energy.

Pulse Duration: Time occupied by a burst of transmitted radio energy. This may also be expressed in units of range (pulse length). Also called pulsewidth.

Pulse Pair Processing: Name for the technique of mean velocity estimation by calculation of the signal complex covariance argument. The calculation requires two consecutive pulses.

Pulse Radar or **Pulsed Radar:** A type of radar, designed to facilitate range measurement, in which the transmitted energy is emitted in periodic brief transmissions.

Pulse Repetition Frequency (PRF): The number of pulses transmitted per second.

Pulse Repetition Rate: See Pulse Repetition Frequency.

Pulse Repetition Time (PRT): The pulse interval from the beginning of one pulse to the beginning of the next succeeding pulse.

Pulsewidth: The time occupied by an individual broadcast from a radar.

Quadrature: The component of the complex signal that is 90 degrees out of phase with the in-phase component. This component lies along the imaginary axis in the complex plane.

Radar Cross Section: The area of a fictitious perfect reflector of electromagnetic waves that would reflect the same amount of energy back to the radar as the actual target.

Radar Velocity (v): The component of motion of the target toward or away from the radar.

Random Variable (Variate): A variable characterized by random behavior in assuming its different possible values. Mathematically, it is described by its probability distribution, which specifies the possible values of a random variable together with the probability associated (in an appropriate sense) with each value. A random variable is said to be "continuous" if its possible values extend over a continuum, "discrete" if its possible values are separated by finite intervals.

Range Folding: Apparent range placement of a multiple trip return. A multiple return appears at the difference of the true range and a multiple of the unambiguous range.

Range Unfolding: Process of removing range ambiguity in apparent range of a multitrip target.

Receiver: An instrument used to detect the presence of and to determine the information carried by electromagnetic radiation. A receiver includes circuits designed to detect, amplify, rectify, and shape the incoming radio-frequency signals received at the antenna.

Scatterer: Any object capable of reflecting the radar signal.

Sidelobe: Secondary radiated energy maximum other than the radar main beam. Typically contains a small percentage of energy compared to the mainlobe.

Signal Processor: A computer processor used to apply a series of algorithms to the output of the receiver in order to estimate the spectral moments contained in the received backscattered signal.

Signal to Noise Ratio: A ratio that measures the comprehensibility of data, usually expressed as the signal power divided by the noise power.

Slant Range: The line-of-sight distance between two objects.

Spectral Density: The distribution of power by frequency.

Spectrumwidth: A measure of dispersion of velocities within the radar sample volume. Standard deviation of the mean radial velocity spectrum.

Standard Deviation: The positive square root of the signal variance.

Synchronous Detection: Processing that retains the received amplitude and phase but that removes the intermediate carrier frequency.

Target: Objects that produce echoes.

Transmitter: The equipment used for generating and amplifying a radio frequency (RF) carrier signal, modulating the carrier signal with intelligence, and feeding the modulated carrier to an antenna for radiation into space as electromagnetic waves.

Unambiguous Range: The range to which a transmitted pulse wave can travel and return to the radar before the next pulse is transmitted.

Unimodal: A distribution having only one localized maximum, i.e., only one peak.

Variance: A measure of variability.

Velocity Aliasing: Ambiguous detection of radial velocities outside the Nyquist co-interval.

Watt: The unit of power in the meter-kilogram-second (MKS) system of units; equal to one joule per second.

Wavelength: The distance a wave will travel in the time required to generate one cycle.

ACRONYMS

A/D or ADC: Analog to Digital Converter

AM: Amplitude Modulation

AVM: Altitude and Velocity Measurements

CoRiSTA: Consorzio di Ricerca su Sistemi di Telesensori Avanzati or
Consortium for Research on Advanced Remote Sensing Systems

D/A or DAC: Digital to Analog Converter

DM: Descent Module

DSP: Digital Signal Processing

EDL: Entry, Descent & Landing

ESA: European Space Agency

FM-CW: Frequency Modulated-Continuous Wave

FoV: Field of View

GNC: Guidance, Navigation & Control

GPS: Global Positioning System

HW: Hardware

IMU: Inertial Measurement Unit

ITT: Invitation To Tender

LAPS: Lidar-based Autonomous Planetary Landing System

LBNAT: LIDAR-Based Navigation Analysis Tool

LEOP: Launch, Early Orbit Phase

LIDAR: Laser Imaging Detection and Ranging

MER: Mars Exploration Rovers (NASA Rover)

NPAL: Navigation for Planetary Approach and Landing

PRF: Pulse Repetition Frequency

PRI: Pulse Repetition Interval

RDA: Radio Doppler/Altimeter

SC: Spacecraft

SNR: Signal-to-Noise Ratio

TBC: To Be Confirmed

USO: Ultra-Stable Oscillator

w.r.t.: with respect to

MATLAB® CODES

```
% Script delegated to elaborate the expression of Range and Velocity Measurement Accuracy
```

```
clear all  
close all  
clc
```

```
% Expression of Range Measurement Accuracy
```

```
syms PRF_R T_meas_R N Br beta_2_new E_R fc c
```

```
M_R = PRF_R .* T_meas_R;  
N_0 = N ./ Br;
```

```
delta_T_R = 1./sqrt(beta_2_new * 2 .* M_R .* E_R ./ N_0);  
delta_T_q = 1/fc/sqrt(12);
```

```
delta_R = c/2 * sqrt(delta_T_R.^2 + delta_T_q.^2) %#ok<NOPTS>
```

```
% Expression of Velocity Measurement Accuracy
```

```
syms PRF_V T_meas_V Pr_V N lambda a_rad J_rad teta_3_dB pi teta_rate_per Kxyz
```

```
M_V = PRF_V .* T_meas_V;  
SNR_V = Pr_V ./ N .* M_V;
```

```
V_a = PRF_V .* lambda/2; % Unambiguous velocity da controllare
```

```
sigma_V_1 = lambda/2./T_meas_V;  
sigma_V_2 = a_rad .* T_meas_V + J_rad/2 .* T_meas_V.^2;  
sigma_V_3 = lambda * PRF_V/4 * teta_3_dB;  
sigma_V_4 = lambda * PRF_V/2 .* teta_rate_per .* T_meas_V;
```

```
sigma_V = sqrt(sigma_V_1.^2 + sigma_V_2.^2 + sigma_V_3.^2 + sigma_V_4.^2);
```

```
rho_2 = exp(- 4 * (pi .* sigma_V ./ V_a).^2);
```

```
delta_V_pp_Beam = sqrt(V_a.^2/8/pi^2./M_V .* (1./rho_2 .* (1 + 1./SNR_V).^2 - 1));  
delta_V_pp_BRF = delta_V_pp_Beam * Kxyz;
```

```
delta_V_q = V_a ./ M_V ./ sqrt(12);
```

```
delta_V = sqrt(delta_V_pp_BRF.^2 + delta_V_q.^2) %#ok<NOPTS>
```

```
% Script delegated to numerical Range Inquiry
```

```
clear all  
close all  
clc
```

```
% Parameters setting
```

```
c = 3e8;  
K_Boltzman = 1.38e-23;  
Temp = 290;
```

```
% Typical ExoMars values
```

```
fc = 100e6;  
Br = 15e6;  
F = 10^(5/10);  
E_R = 1e-15;  
beta_2_new = 1e12;
```

```
% Parameter elaboration
```

```
N = K_Boltzman * Temp * Br * F;
```

```
% Delta_R elaboration
```

```

fitt = 1000;
PRF_R_vett = linspace(0,100000,fitt);
T_meas_R_vett = linspace(0,10e-3,fitt);

[PRF_R,T_meas_R] = meshgrid(PRF_R_vett,T_meas_R_vett);
delta_R = 1./12.*c.*(18./beta_2_new./PRF_R./T_meas_R./E_R.*N./Br+3./fc.^2).^1/2);

figure(1)
Lim = 5;
delta_R_filt = delta_R;
for ii = 1 : length(PRF_R)
    j_nan = find(delta_R(ii,:) >= Lim);
    delta_R_filt(ii,j_nan) = Lim;
end
surf(PRF_R/1000,T_meas_R*1000,delta_R_filt,'FaceColor','interp','EdgeColor','none')
colorbar
title('\deltaR as function of PRF & T_m_e_a_s (Z limited)')
xlabel('PRF [KHz]')
ylabel('T_m_e_a_s [ms]')
zlabel('\deltaR [m]')

```

```

% Script delegated to numerical Velocity Inquiry

clear all
close all
clc

% Parameters setting
c = 3e8;
K_Boltzman = 1.38e-23;
Temp = 290;
Kxyz = 1.5;

% Typical ExoMars values
f0 = 35e9;
D_ant = 0.15;
Br = 15e6;
F = 10^(5/10);

% Parameter elaboration
lambda=c/f0;
teta_3_dB = 0.88 * lambda/D_ant;
N = K_Boltzman * Temp * Br * F;

% Delta_V elaboration
fitt = 1000;
PRF_V_vett = linspace(0,100e3,fitt);
T_meas_V_vett = linspace(0,50e-3,fitt);

[PRF_V, T_meas_V] = meshgrid(PRF_V_vett,T_meas_V_vett);

% Case A
Pr_V_vett = [1e-13 1e-12 1e-11 1e-10 1e-9 1e-8 1e-7 1e-6 1e-5];
a_rad = 6.5;
J_rad = 65;
teta_rate_per = 0.5;

PRF_V_min_1 = zeros(length(Pr_V_vett),fitt);
T_meas_V_min_1 = zeros(length(Pr_V_vett),fitt);

for ii = 1 : length(Pr_V_vett)

    Pr_V = Pr_V_vett(ii);
    delta_V_1 = 1./24.*(18./pi.^2.*PRF_V.*lambda.^2./T_meas_V.*(1./exp(-
pi.^2.*(4.*lambda.^2./T_meas_V.^2+16.*(a_rad.*T_meas_V+1./2.*J_rad.*T_meas_V.^2).^2+PRF_V.^2.*lambda.^2
.*teta_3_dB.^2+4.*PRF_V.^2.*lambda.^2.*teta_rate_per.^2.*T_meas_V.^2)/PRF_V.^2./lambda.^2).*(1+1./Pr_V.*

```

```

N./PRF_V./T_meas_V).^2-1).*Kxyz.^2+12.*lambda.^2./T_meas_V.^2).^^(1/2);

[Min_1,Col_1] = min(delta_V_1,[],2);
PRF_V_min_1(ii,:) = PRF_V_vett(Col_1');
T_meas_V_min_1(ii,:) = T_meas_V_vett;

end

figure(1)
Lim = 5;
delta_V_filt_1 = delta_V_1;
for ii = 1 : length(PRF_V)
    j_nan = find(delta_V_1(ii,:) >= Lim);
    delta_V_filt_1(ii,j_nan) = Lim;
end
surf(PRF_V/1000,T_meas_V*1000,delta_V_filt_1,'FaceColor','interp','EdgeColor','none')
title('\deltaV as function of PRF & T_m_e_a_s (Z limited)')
colorbar
xlabel('PRF [KHz]')
ylabel('T_m_e_a_s [ms]')
zlabel('\deltaV [m/s]')

figure(2)
hold on
plot(PRF_V_min_1'/1000,T_meas_V_min_1'*1000)
title('\deltaV as function of PRF & T_m_e_a_s')
xlabel('PRF [KHz]')
ylabel('T_m_e_a_s [ms]')
legend('-100 dBm', '-90 dBm', '-80 dBm', '-70 dBm', '-60 dBm', '-50 dBm', '-40 dBm', '-30 dBm', '-20 dBm')
hold off

% Case B
Pr_V = 1e-8;
fitt_d = 50;
a_rad_vett = linspace(0,13.4165,fitt_d);
J_rad_vett = linspace(0,134.1650,fitt_d);
teta_rate_per_vett = linspace(0,1.0472,fitt_d);

PRF_V_min_2 = zeros(fitt_d,fitt);
T_meas_V_min_2 = zeros(fitt_d,fitt);

for ii = 1 : fitt_d

    a_rad = a_rad_vett(ii);
    J_rad = J_rad_vett(ii);
    teta_rate_per = teta_rate_per_vett(ii);

    delta_V_2 = 1./24.*(18./pi.^2.*PRF_V.*lambda.^2./T_meas_V.*(1./exp(-
pi.^2.*(4.*lambda.^2./T_meas_V.^2+16.*(a_rad.*T_meas_V+1./2.*J_rad.*T_meas_V.^2).^2+PRF_V.^2.*lambda.^2.*
teta_3_dB.^2+4.*PRF_V.^2.*lambda.^2.*teta_rate_per.^2.*T_meas_V.^2)/PRF_V.^2./lambda.^2).*(1+1./Pr_V.*
N./PRF_V./T_meas_V).^2-1).*Kxyz.^2+12.*lambda.^2./T_meas_V.^2).^^(1/2);

    [Min_2,Col_2] = min(delta_V_2,[],2);
    PRF_V_min_2(ii,:) = PRF_V_vett(Col_2');
    T_meas_V_min_2(ii,:) = T_meas_V_vett;

end

figure(3)
Lim = 5;
delta_V_filt_2 = delta_V_2;
for ii = 1 : length(PRF_V)
    j_nan = find(delta_V_2(ii,:) >= Lim);
    delta_V_filt_2(ii,j_nan) = Lim;
end
surf(PRF_V/1000,T_meas_V*1000,delta_V_filt_2,'FaceColor','interp','EdgeColor','none')
title('\deltaV as function of PRF & T_m_e_a_s (Z limited)')

```

```

colorbar
xlabel('PRF [KHz]')
ylabel('T_m_e_a_s [ms]')
zlabel('\deltaV [m/s]')

figure(4)
hold on
plot(PRF_V_min_2'/1000,T_meas_V_min_2'*1000)
title('\deltaV as function of PRF & T_m_e_a_s')
xlabel('PRF [KHz]')
ylabel('T_m_e_a_s [ms]')
hold off

% Case C
Pr_V = 1e-8;
a_rad = 6.5;
J_rad = 65;
teta_rate_per = 0.5;

delta_V_3 = 1./24.*(18./pi.^2.*PRF_V.*lambda.^2./T_meas_V.*(1./exp(-
pi.^2.*(4.*lambda.^2./T_meas_V.^2+16.*(a_rad.*T_meas_V+1./2.*J_rad.*T_meas_V.^2).^2+PRF_V.^2.*lambda.^2
.*teta_rate_per.^2.*T_meas_V.^2)./PRF_V.^2./lambda.^2).*(1+1./Pr_V.*
N./PRF_V./T_meas_V).^2-1).*Kxyz.^2+12.*lambda.^2./T_meas_V.^2).^(1/2);

[Min_3,Col_3] = min(delta_V_3,[],2);
PRF_V_min_3 = PRF_V_vett(Col_3);
T_meas_V_min_3 = T_meas_V_vett;

figure(5)
Lim = 5;
delta_V_filt_3 = delta_V_3;
for ii = 1 : length(PRF_V)
    j_nan = find(delta_V_3(ii,:) >= Lim);
    delta_V_filt_3(ii,j_nan) = Lim;
end
surf(PRF_V/1000,T_meas_V*1000,delta_V_filt_3,'FaceColor','interp','EdgeColor','none')
title('\deltaV as function of PRF & T_m_e_a_s (Z limited)')
colorbar
xlabel('PRF [KHz]')
ylabel('T_m_e_a_s [ms]')
zlabel('\deltaV [m/s]')

figure(6)
hold on
plot(PRF_V_min_3'/1000,T_meas_V_min_3'*1000)
title('\deltaV as function of PRF & T_m_e_a_s')
xlabel('PRF [KHz]')
ylabel('T_m_e_a_s [ms]')
hold off

% Case D
fitt_d = 50;
Pr_V = 1e-8;
a_rad = 6.5;
J_rad = 65;
teta_rate_per = 0.5;

Kxyz_vett = linspace(0.1,5,fitt_d);

PRF_V_min_4 = zeros(fitt_d,fitt);
T_meas_V_min_4 = zeros(fitt_d,fitt);

for ii = 1 : fitt_d

    Kxyz = Kxyz_vett(ii);

    delta_V_4 = 1./24.*(18./pi.^2.*PRF_V.*lambda.^2./T_meas_V.*(1./exp(-

```

```

pi.^2.*(4.*lambda.^2./T_meas_V.^2+16.*(a_rad.*T_meas_V+1./2.*J_rad.*T_meas_V.^2).^2+PRF_V.^2.*lambda.^2
.*teta_3_dB.^2+4.*PRF_V.^2.*lambda.^2.*teta_rate_per.^2.*T_meas_V.^2)/PRF_V.^2./lambda.^2).*(1+1./Pr_V.*
N./PRF_V./T_meas_V).^2-1).*Kxyz.^2+12.*lambda.^2./T_meas_V.^2).^^(1/2);

[Min_4,Col_4] = min(delta_V_4,[],2);
PRF_V_min_4(ii,:) = PRF_V_vett(Col_4');
T_meas_V_min_4(ii,:) = T_meas_V_vett;

end

figure(7)
Lim = 5;
delta_V_filt_4 = delta_V_4;
for ii = 1 : length(PRF_V)
    j_nan = find(delta_V_4(ii,:) >= Lim);
    delta_V_filt_4(ii,j_nan) = Lim;
end
surf(PRF_V/1000,T_meas_V*1000,delta_V_filt_4,'FaceColor','interp','EdgeColor','none')
colorbar
title('\deltaV as function of PRF & T_m_e_a_s (Z limited)')
xlabel('PRF [KHz]')
ylabel('T_m_e_a_s [ms]')
zlabel('\deltaV [m/s]')

figure(8)
hold on
plot(PRF_V_min_4'/1000,T_meas_V_min_4'*1000)
title('\deltaV as function of PRF & T_m_e_a_s')
xlabel('PRF [KHz]')
ylabel('T_m_e_a_s [ms]')
hold off

% Case E
Pr_V = 1e-8;
a_rad = 0;
J_rad = 0;
teta_rate_per = 0;

delta_V_5 = 1./24.*(18./pi.^2.*PRF_V.*lambda.^2./T_meas_V.*(1./exp(-
pi.^2.*(4.*lambda.^2./T_meas_V.^2+16.*(a_rad.*T_meas_V+1./2.*J_rad.*T_meas_V.^2).^2+PRF_V.^2.*lambda.^2
.*teta_3_dB.^2+4.*PRF_V.^2.*lambda.^2.*teta_rate_per.^2.*T_meas_V.^2)/PRF_V.^2./lambda.^2).*(1+1./Pr_V.*
N./PRF_V./T_meas_V).^2-1).*Kxyz.^2+12.*lambda.^2./T_meas_V.^2).^^(1/2);

[Min_5,Col_5] = min(delta_V_5,[],2);
PRF_V_min_5 = PRF_V_vett(Col_5');
T_meas_V_min_5 = T_meas_V_vett;

figure(9)
Lim = 5;
delta_V_filt_5 = delta_V_5;
for ii = 1 : length(PRF_V)
    j_nan = find(delta_V_5(ii,:) >= Lim);
    delta_V_filt_5(ii,j_nan) = Lim;
end
surf(PRF_V/1000,T_meas_V*1000,delta_V_filt_5,'FaceColor','interp','EdgeColor','none')
colorbar
title('\deltaV as function of PRF & T_m_e_a_s (Z limited)')
xlabel('PRF [KHz]')
ylabel('T_m_e_a_s [ms]')
zlabel('\deltaV [m/s]')

figure(10)
hold on
plot(PRF_V_min_5'/1000,T_meas_V_min_5'*1000)
title('\deltaV as function of PRF & T_m_e_a_s')
xlabel('PRF [KHz]')
ylabel('T_m_e_a_s [ms]')

```

```

hold off

% Case F
Pr_V = 1e-8;
a_rad = 0.05;
J_rad = 10;
teta_rate_per = 0.1;

delta_V_6 = 1./24.*(18./pi.^2.*PRF_V.*lambda.^2./T_meas_V.*(1./exp(-
pi.^2.*(4.*lambda.^2./T_meas_V.^2+16.*(a_rad.*T_meas_V+1./2.*J_rad.*T_meas_V.^2).^2+PRF_V.^2.*lambda.^2
.*teta_3_dB.^2+4.*PRF_V.^2.*lambda.^2.*teta_rate_per.^2.*T_meas_V.^2)./PRF_V.^2./lambda.^2).*(1+1./Pr_V.*
N./PRF_V./T_meas_V).^2-1).*Kxyz.^2+12.*lambda.^2./T_meas_V.^2).^^(1/2);

[Min_6,Col_6] = min(delta_V_6,[],2);
PRF_V_min_6 = PRF_V_vett(Col_6');
T_meas_V_min_6 = T_meas_V_vett;

figure(11)
Lim = 5;
delta_V_filt_6 = delta_V_6;
for ii = 1 : length(PRF_V)
    j_nan = find(delta_V_6(ii,:) >= Lim);
    delta_V_filt_6(ii,j_nan) = Lim;
end
surf(PRF_V/1000,T_meas_V*1000,delta_V_filt_6,'FaceColor','interp','EdgeColor','none')
colorbar
title('\deltaV as function of PRF & T_m_e_a_s (Z limited)')
xlabel('PRF [KHz]')
ylabel('T_m_e_a_s [ms]')
zlabel('\deltaV [m/s]')

figure(12)
hold on
plot(PRF_V_min_6'/1000,T_meas_V_min_6'*1000)
title('\deltaV as function of PRF & T_m_e_a_s')
xlabel('PRF [KHz]')
ylabel('T_m_e_a_s [ms]')
hold off

```

% Script delegated to analyze Worst Case scenario for received power

```

clear all
close all
clc

addpath('02_Backscattering','03_SNR')

global teta_3_dB

% Case Selection
Choice = menu('Select Data Input','1','2');

if Choice == 1
    % Pr Budget & Range&Velocity Accuracy Investigation
    teta_R_grad_vett = [0 15 35];
    teta_V_grad_vett = [0 30 55];
elseif Choice == 2
    % Geometric Analysis
    teta_R_grad_vett = [0 35];
    teta_V_grad_vett = [15 20 50 55];
end

% Altitude
H_up = linspace(3000,500,10);
H_low = linspace(500,10,20);
H = [H_up(1:end-1) H_low];

```

```

% Worst Case Values in BRF
V_xb_worst = 64;
V_yb_worst = 45;
V_zb_worst = 45;

a_xb_worst = 2.65;
a_yb_worst = 9.3;
a_zb_worst = 9.3;

J_xb_worst = 26.5;
J_yb_worst = 93;
J_zb_worst = 93;

teta_rate_mod_worst_deg = 60; % degree

% Required & Non-Ambiguity Max Values Input in BRF
H_worst = 3000;
V_xb_worst_non_amb = 160;
V_yb_worst_non_amb = 45;
V_zb_worst_non_amb = 45;

% Radar Parameters
c = 3e8;
K_Boltzman = 1.38e-23;
f_update = 20;
f0 = 35e9;
f_IF = 50e6;
fc = 100e6;
Pt = 1; % Transmitted Peak Power
Bt = 200e6; % Peak Rise Time setted equal to 5 ns
D_ant = 0.15;
eta_ant = 0.653;
Temp = 290;
F = 10^(5/10); % Receiver Noise Figure
L_atm = 10^(4/10); % Atmospheric Losses
L_sys = 10^(4/10); % System Losses
Filter_flag = 2; % selected NO

% Mars Parameters
Epsilon = 3;
D = 0.04;
sigma_h = 0.1;
slope_deg = 10;

% Degree to Radiant Conversion
teta_rate_mod_worst = deg2rad(teta_rate_mod_worst_deg);
teta_R_vett = deg2rad(teta_R_grad_vett);
teta_V_vett = deg2rad(teta_V_grad_vett);
slope = deg2rad(slope_deg);

% "Worst Case" module elaboration
V_mod_worst = sqrt(V_xb_worst.^2 + V_yb_worst.^2 + V_zb_worst.^2);
V_mod_worst_non_amb = sqrt(V_xb_worst_non_amb.^2 + V_yb_worst_non_amb.^2 + V_zb_worst_non_amb.^2);
a_mod_worst = sqrt(a_xb_worst.^2 + a_yb_worst.^2 + a_zb_worst.^2);
J_mod_worst = sqrt(J_xb_worst.^2 + J_yb_worst.^2 + J_zb_worst.^2);

% Integrations Time Laws
TO_1 = acos(H_worst/(H_worst + c/8/fc))/teta_rate_mod_worst;
TO_2 = fzero(@(x)V_mod_worst * x + a_mod_worst/2 * x.^2 + J_mod_worst/3 * x.^3 - c/8/fc,0);

T_meas_R_worst = min(TO_1,TO_2);
T_meas_R = T_meas_R_worst * ones(1,length(H));

f_meas_R = 1./T_meas_R;
f_meas_V = 1./((1./f_update - 1./f_meas_R)/3);

T_meas_V = 1./f_meas_V;

```

```

% PRF laws
PRF_R = 25000 * ones(1,length(H));
PRF_V = (100e3-2e3) / (3000-10) * (H-10) + 2e3;
PRF_V = PRF_V(1:length(H));

% Pulse Duration Laws
PRI_R = 1./PRF_R;
PRI_V = 1./PRF_V;

P_T_R_max_1 = 2 * H / c;
P_T_R_max_2 = PRI_R;
P_T_R_max = min(P_T_R_max_1,P_T_R_max_2);

P_T_V_max_1 = 2 * H / c;
P_T_V_max_2 = PRI_V;
P_T_V_max = min(P_T_V_max_1,P_T_V_max_2);

P_T_R = P_T_R_max;
P_T_V = P_T_V_max;
ii = find(H>150);
P_T_V(ii) = min(P_T_V_max(ii));

% Pulses Number
M_R = floor(PRF_R .* T_meas_R);
M_V = floor(PRF_V .* T_meas_V);

% Range and Velocity Receiver Bandwidth
Br_R = 1./P_T_R;
Br_V = 1./P_T_V;

% Range and Velocity Received Noise
N_R = K_Boltzman * Temp * Br_R * F;
N_V = K_Boltzman * Temp * Br_V * F;

% Radar Parameters
lambda = c/f0;
teta_3_dB = 0.88 * lambda/D_ant;

n_over(H<=H_worst) = 30;
n_over(H<=2000) = 50;
n_over(H<=1200) = 100;
n_over(H<=450) = 200;
n_over(H<=450/3) = 300;

% Parameters initialization for measurement accuracy elaboration
sigma_R = zeros(length(teta_R_vett),length(H));
Pr_R = zeros(length(teta_R_vett),length(H));
SNR_R = zeros(length(teta_R_vett),length(H));
E_R = zeros(length(teta_R_vett),length(H));
beta_2_R_old = zeros(length(teta_R_vett),length(H));
delta_R = zeros(length(teta_R_vett),length(H));
sigma_V = zeros(length(teta_V_vett),length(H));
Pr_V = zeros(length(teta_V_vett),length(H));
SNR_V = zeros(length(teta_V_vett),length(H));

for ii = 1:length(teta_R_vett)

    ii %#ok<NOPTS>

    teta_B0_worst = teta_R_vett(ii) * ones(1,length(H));
    sigma_R(ii,:) = Backscattering_Model(teta_B0_worst,Epsilon,D,lambda);
    [Pr_R(ii,:),SNR_R(ii,:),E_R(ii,:),beta_2_R_old(ii,:)] =
    SNR(teta_B0_worst,sigma_R(ii,:),P_T_R,M_R,Br_R,N_R,H,Pt,Bt,teta_3_dB,c,lambda,D_ant,eta_ant,fc,n_over,L_atm
    ,L_sys,Filter_flag);

end

```

```

for ii = 1:length(teta_V_vett)

    ii %#ok<NOPTS>

    teta_B123_worst = teta_V_vett(ii) * ones(1,length(H));
    sigma_V(ii,:) = Backscattering_Model(teta_B123_worst,Epsilon,D,lambda);
    [Pr_V(ii,:),SNR_V(ii,:)] =
SNR(teta_B123_worst,sigma_V(ii,:),P_T_V,M_V,Br_V,N_V,H,Pt,Bt,teta_3_dB,c,lambda,D_ant,eta_ant,fc,n_over,L_a
tm,L_sys,Filter_flag);

end

% Graphic Output

if Choice == 1

    figure(1)
    plot(H,sigma_R)
    title('Range Backscattering as a function of Altitude')
    xlabel('Altitude H [m]')
    ylabel('\sigma_0')
    legend('0°','15°','35°')

    figure(2)
    plot(H,sigma_V)
    title('Velocity Backscattering as a function of Altitude')
    xlabel('Altitude H [m]')
    ylabel('\sigma_0')
    legend('0°','30°','55°')

    figure(3)
    plot(H,10*log10(Pr_R)+30)
    title('Received Range Power as a function of Altitude')
    xlabel('Altitude H [m]')
    ylabel('Pr_R [dBm]')
    legend('0°','15°','35°')

    figure(4)
    plot(H,10*log10(Pr_V)+30)
    title('Received Velocity Power as a function of Altitude')
    xlabel('Altitude H [m]')
    ylabel('Pr_V [dBm]')
    legend('0°','30°','55°')

    figure(5)
    plot(H,10*log10(SNR_R))
    title('Range SNR as a function of Altitude')
    xlabel('Altitude H [m]')
    ylabel('SNR_R [dB]')
    legend('0°','15°','35°')

    figure(6)
    plot(H,10*log10(SNR_V))
    title('Velocity SNR as a function of Altitude')
    xlabel('Altitude H [m]')
    ylabel('SNR_V [dB]')
    legend('0°','30°','55°')

elseif Choice == 2

    Delta_Pr_1 = 1 - Pr_V(2,:) ./ Pr_V(1,:);
    Delta_Pr_2 = 1 - Pr_V(4,:) ./ Pr_V(3,:);

    Delta_Pr_1_perc = Delta_Pr_1 * 100;
    Delta_Pr_2_perc = Delta_Pr_2 * 100;

    figure(7)

```

```

plot(H,10*log10(Pr_V)+30)
title('Received Velocity Power as a function of Altitude')
xlabel('Altitude H [m]')
ylabel('Pr_V [dBm]')
legend('15','20','50','55')

figure(8)
plot(H,Delta_Pr_1_perc)
title('Percent Nominal Case Velocity Pr Loss as a function of Altitude')
xlabel('Altitude H [m]')
ylabel('Pr_V Loss (%)')

figure(9)
plot(H,Delta_Pr_2_perc)
title('Percent Worst Case Velocity Pr Loss as a function of Altitude')
xlabel('Altitude H [m]')
ylabel('Pr_V Loss (%)')

end

```

```

% Radar Doppler/Altimeter Performance Analysis for ExoMars Mission

% Change Log.
%
% v1.0.0
% Preliminar Chart Flow implementation for "Warst Case" and Simulated inputs
%
% v1.0.1
% Same formula & output corrections
%
% v1.1.0
% T_meas_R improvement with same proposed laws
% V_radial, acc_radial, Jerk_radial & Teta_rate_perp corrections in delta_V computations present in 04_Accuracy
folder/BeRF_Velocity_Accuracy.m
% "Worst Case" input implemented
%
% v1.2.0
% Pulse Duration and PRF improvement with same proposed laws
% Input bounds due to RDA fisic models & operations scenario
% Output Choice report
%
% v1.2.1
% Pulse Durations and PRFs analysis
%
% v1.2.2
% Pulse Duration laws
%
% v1.2.3
% Optimum T_meas_R definition, Graphic improvement
%
% v1.3.0
% New management of "Warst Case" and Simulated inputs
%
% v1.4.0
% New scripts implemented in main folder for RDA Engineering Design
%
% v1.4.1
% Br corrections
%
% v1.4.2
% Br_R&Br_V implementation
%
% v1.4.3
% Correction of SNR formula

```

```

% Matlab initialization

clear all
close all
clc

addpath('01_Input','02_Backscattering','03_SNR','04_Accuracy','05_Graphic')

global teta_3_dB time position_z velocity_x velocity_y velocity_z yawAngle pitchAngle rollAngle acc_x acc_y acc_z
yawRate pitchRate rollRate %#ok<NUSED>

%% % Main Body
% Raw & Elaborated Input Box

[position_z_up,position_z_down,H_P_T_flat,H_worst,V_xb_worst,V_yb_worst,V_zb_worst,a_xb_worst,a_yb_worst
,a_zb_worst,J_xb_worst,J_yb_worst,J_zb_worst,teta_att_worst_deg,teta_rate_mod_worst_deg,H0,V0,H1,V1,H2,V
2,H3,H4,V_xb_worst_non_amb,V_yb_worst_non_amb,V_zb_worst_non_amb,alpha_beam_deg_vett,beta_beam_deg
eg,c,K_Boltzman,Temp,f_update,f0,f_IF,fc,Bt,Pt,P_T_down,P_T_up_R,P_T_up_V,D_ant,eta_ant,Epsilon,D,sigma_h,s
lope_deg,F,L_atm,L_sys,req_perc,Input_motion,alpha_beam_flag,T_meas_R_flag,PRF_R_flag,PRF_V_flag,P_T_R_fl
ag,P_T_V_flag,Filter_flag] = ...
    Input_RDA;

[alpha_beam,beta_beam,teta_att_worst,teta_rate_mod_worst,slope,t,H,V_mod,a_mod,J_mod,H_worst_req,V_m
od_worst_req,a_mod_worst_req,J_mod_worst_req,teta_rate_mod_worst_req,teta_B0,teta_B1,teta_B2,teta_B3,a
_rad_B1,a_rad_B2,a_rad_B3,J_rad_B1,J_rad_B2,J_rad_B3,teta_rate_mod,teta_rate_per_B1,teta_rate_per_B2,teta
_rate_per_B3,PRF_R,PRF_V,PRF_R_max,PRF_V_min,P_T_R,P_T_V,P_T_R_max,P_T_V_max,T_meas_R,T_meas_V,M
_R,M_V,Br_R,Br_V,N_R,N_V,lambda,teta_3_dB,n_over,delta_R_req,delta_V_req,Se_Re_max_R,Se_Re_max_V] = ...
Input_elaboration(position_z_up,position_z_down,H_P_T_flat,H_worst,V_xb_worst,V_yb_worst,V_zb_worst,a_xb
_worst,a_yb_worst,a_zb_worst,J_xb_worst,J_yb_worst,J_zb_worst,teta_att_worst_deg,teta_rate_mod_worst_deg
,H0,V0,H1,V1,H2,V2,H3,H4,V_xb_worst_non_amb,V_yb_worst_non_amb,V_zb_worst_non_amb,alpha_beam_deg
_vett,beta_beam_deg,c,K_Boltzman,Temp,f_update,f0,fc,P_T_down,P_T_up_R,P_T_up_V,D_ant,slope_deg,F,req_
perc,Input_motion,alpha_beam_flag,T_meas_R_flag,PRF_R_flag,PRF_V_flag,P_T_R_flag,P_T_V_flag);

tic % time counter

% Backscattering Box
[sigma_0_R,sigma_0_V_B1,sigma_0_V_B2,sigma_0_V_B3] =
Backscattering_Box(teta_B0,teta_B1,teta_B2,teta_B3,Epsilon,D,lambda);

% SNR Evaluation Box
[Pr_R,Pr_V_B1,Pr_V_B2,Pr_V_B3,SNR_R,SNR_V_B1,SNR_V_B2,SNR_V_B3,E_R,beta_2_R_old] = ...
SNR_Box(teta_B0,teta_B1,teta_B2,teta_B3,sigma_0_R,sigma_0_V_B1,sigma_0_V_B2,sigma_0_V_B3,P_T_R,P_T_V,
M_R,M_V,Br_R,Br_V,N_R,N_V,H,Pt,Bt,teta_3_dB,c,lambda,D_ant,eta_ant,fc,n_over,L_atm,L_sys,Input_motion,Filter
_flag);

% Estimation Accuracy Box
[delta_R,delta_V_X,delta_V_Y,delta_V_Z] = ...
Measurement_Accuracy_Box(teta_B0,E_R,beta_2_R_old,SNR_V_B1,SNR_V_B2,SNR_V_B3,a_rad_B1,a_rad_B2,a_ra
d_B3,J_rad_B1,J_rad_B2,J_rad_B3,teta_rate_per_B1,teta_rate_per_B2,teta_rate_per_B3,PRF_V,T_meas_V,M_R,M
_V,Br_R,N_R,fc,sigma_h,slope,c,H,lambda,teta_3_dB,alpha_beam,beta_beam);

t_estim = toc; % End Time Counter

% Graphic Output box

Graphic_Output_Box(t,H,V_mod,a_mod,J_mod,teta_B0,teta_B1,teta_B2,teta_B3,teta_rate_mod,PRF_R,PRF_V,PRF
_R_max,PRF_V_min,P_T_R,P_T_V,P_T_R_max,P_T_V_max,T_meas_R,T_meas_V,M_R,M_V,sigma_0_R,sigma_0_V
_B1,sigma_0_V_B2,sigma_0_V_B3,Pr_R,Pr_V_B1,Pr_V_B2,Pr_V_B3,SNR_R,SNR_V_B1,SNR_V_B2,SNR_V_B3,delta_R
_req,delta_R,delta_V_req,delta_V_X,delta_V_Y,delta_V_Z,t_estim,Se_Re_max_R,Se_Re_max_V,Input_motion,alph
a_beam_flag,T_meas_R_flag,PRF_R_flag,PRF_V_flag,P_T_R_flag,P_T_V_flag,Filter_flag)

%% % End Main Body

% Matlab Path list reset
rmpath('01_Input','02_Backscattering','03_SNR','04_Accuracy','05_Graphic')

```

```

% Script delegated to elaborate minimum theoretical accuracy

close all
clc

addpath('04_Accuracy','05_Graphic')

global teta_3_dB

% Null values setting
teta_B0 = 0 * teta_B0;

a_rad_B1 = 0 * a_rad_B1;
a_rad_B2 = 0 * a_rad_B2;
a_rad_B3 = 0 * a_rad_B3;

J_rad_B1 = 0 * J_rad_B1;
J_rad_B2 = 0 * J_rad_B2;
J_rad_B3 = 0 * J_rad_B3;

teta_rate_per_B1 = 0 * teta_rate_per_B1;
teta_rate_per_B2 = 0 * teta_rate_per_B2;
teta_rate_per_B3 = 0 * teta_rate_per_B3;

sigma_h = 0 * sigma_h;
slope = 0 * slope;

% Accuracy elaboration
[delta_R,delta_V_X,delta_V_Y,delta_V_Z] = ...
Measurement_Accuracy_Box(teta_B0,E_R,beta_2_R_old,SNR_V_B1,SNR_V_B2,SNR_V_B3,a_rad_B1,a_rad_B2,a_rad_B3,J_rad_B1,J_rad_B2,J_rad_B3,teta_rate_per_B1,teta_rate_per_B2,teta_rate_per_B3,PRF_V,T_meas_V,M_R,M_V,Br_R,N_R,fc,sigma_h,slope,c,H,lambda,teta_3_dB,alpha_beam,beta_beam);

% Figure output
Graphic_Output_Box(t,H,V_mod,a_mod,J_mod,teta_B0,teta_B1,teta_B2,teta_B3,teta_rate_mod,PRF_R,PRF_V,PRF_R_max,PRF_V_min,P_T_R,P_T_V,P_T_R_max,P_T_V_max,T_meas_R,T_meas_V,M_R,M_V,sigma_0_R,sigma_0_V_B1,sigma_0_V_B2,sigma_0_V_B3,Pr_R,Pr_V_B1,Pr_V_B2,Pr_V_B3,SNR_R,SNR_V_B1,SNR_V_B2,SNR_V_B3,delta_R_req,delta_R,delta_V_req,delta_V_X,delta_V_Y,delta_V_Z,t_estim,Se_Re_max_R,Se_Re_max_V,Input_motion,alpha_beam_flag,T_meas_R_flag,PRF_R_flag,PRF_V_flag,P_T_R_flag,P_T_V_flag,Filter_flag)

```

```

% Load workspace for comparison of performance between various engineering design.
% Also the excess of measurement accuracy respect to required measurement accuracy is considered.

close all
clc

% Altitude arrow
H = linspace(3000,10,100);

% Examination case
Choice = menu('Select Case:', 'Tmeas-Flat', 'Geometric-Tmeas', 'Geometric-Flat', '% Worst Exceed');

if Choice == 1

figure(1)
Var_Range = 1 - delta_R_2./delta_R;
Var_perc_Range = abs(Var_Range) * 100;
plot(H,Var_perc_Range)
title('Percent Range Accuracy Loss as function of Altitude')
xlabel('Altitude H [m]')
ylabel('Range Accuracy Loss (%)')

figure(2)
Var_Velocity_X = 1 - delta_V_X_2./delta_V_X;
Var_perc_Velocity_X = Var_Velocity_X * 100;
plot(H,Var_perc_Velocity_X)

```

```

title('Percent Velocity Accuracy Gain along X-axis as function of Altitude')
xlabel('Altitude H [m]')
ylabel('V_x Velocity Accuracy Gain (%)')

figure(3)
Var_Velocity_Y = 1 - delta_V_Y_2./delta_V_Y;
Var_perc_Velocity_Y = Var_Velocity_Y * 100;
plot(H,Var_perc_Velocity_Y)
title('Percent Velocity Accuracy Gain along Y&Z-axis as function of Altitude')
xlabel('Altitude H [m]')
ylabel('V_y & V_z Velocity Accuracy Gain (%)')

elseif Choice == 2

figure(1)
Var_Range = 1 - delta_R_2./delta_R;
Var_perc_Range = Var_Range * 100;
plot(H,Var_perc_Range)
title('Percent Range Accuracy Variation as function of Altitude')
xlabel('Altitude H [m]')
ylabel('Range Accuracy Variation (%)')

figure(2)
Var_Velocity_X = 1 - delta_V_X_2./delta_V_X;
Var_perc_Velocity_X = abs(Var_Velocity_X) * 100;
plot(H,Var_perc_Velocity_X)
title('Percent Velocity Accuracy Loss along X-axis as function of Altitude')
xlabel('Altitude H [m]')
ylabel('V_x Velocity Accuracy Loss (%)')

figure(3)
Var_Velocity_Y = 1 - delta_V_Y_2./delta_V_Y;
Var_perc_Velocity_Y = Var_Velocity_Y * 100;
plot(H,Var_perc_Velocity_Y)
title('Percent Velocity Accuracy Gain along Y&Z-axis as function of Altitude')
xlabel('Altitude H [m]')
ylabel('V_y & V_z Velocity Accuracy Gain (%)')

elseif Choice == 3

figure(1)
Var_Range = 1 - delta_R_2./delta_R;
Var_perc_Range = Var_Range * 100;
plot(H,Var_perc_Range)
title('Percent Range Accuracy Variation as function of Altitude')
xlabel('Altitude H [m]')
ylabel('Range Accuracy Variation (%)')

figure(2)
Var_Velocity_X = 1 - delta_V_X_2./delta_V_X;
Var_perc_Velocity_X = Var_Velocity_X * 100;
plot(H,Var_perc_Velocity_X)
title('Percent Velocity Accuracy Variation along X-axis as function of Altitude')
xlabel('Altitude H [m]')
ylabel('V_x Velocity Accuracy Variation (%)')

figure(3)
Var_Velocity_Y = 1 - delta_V_Y_2./delta_V_Y;
Var_perc_Velocity_Y = Var_Velocity_Y * 100;
plot(H,Var_perc_Velocity_Y)
title('Percent Velocity Accuracy Variation along Y&Z-axis as function of Altitude')
xlabel('Altitude H [m]')
ylabel('V_y & V_z Velocity Accuracy Variation (%)')

elseif Choice == 4

Excess_R = (delta_R - delta_R_req)./delta_R_req;

```

```

Excess_R_perc = Excess_R * 100;

figure(1)
plot(H,Excess_R_perc)
title('Range Accuracy Excess as function of Altitude')
xlabel('Altitude H [m]')
ylabel('Range Accuracy Excess (%)')

Excess_Vert = (delta_V_X - delta_V_req)./delta_V_req;
Excess_Vert_perc = Excess_Vert * 100;

figure(2)
plot(H,Excess_Vert_perc)
title('Velocity Accuracy Excess along X-axis as function of Altitude')
xlabel('Altitude H [m]')
ylabel('V_x Velocity Accuracy Excess (%)')

Excess_Hor = (delta_V_Y - delta_V_req)./delta_V_req;
Excess_Hor_perc = Excess_Hor * 100;

figure(3)
plot(H,Excess_Hor_perc)
title('Velocity Accuracy Excess along Y&Z-axis as function of Altitude')
xlabel('Altitude H [m]')
ylabel('V_y & V_z Velocity Accuracy Excess (%)')

end

```

```

function B = B_BRF(alpha, beta)

% Transformation matrix from BeRF to BRF
% Alpha and beta angles are expressed in radians

B(1) = cos(alpha);
B(2) = sin(alpha) * cos(beta);
B(3) = sin(alpha) * sin(beta);

```

```

function Import_XLS(XLS)

% Imports data from the specified file XLS to read
% Auto-generated by MATLAB on 05-Mar-2009 11:16:40

% Import the file
newData1 = importdata(XLS);

% For some XLS and other spreadsheet files, returned data are packed
% within an extra layer of structures. Unpack them.
fields = fieldnames(newData1.data);
newData1.data = newData1.data.(fields{1});
fields = fieldnames(newData1.textdata);
newData1.textdata = newData1.textdata.(fields{1});
fields = fieldnames(newData1.colheaders);
newData1.colheaders = newData1.colheaders.(fields{1});

% Break the data up into a new structure with one field per column.
colheaders = genvarname(newData1.colheaders);
for i = 1:length(colheaders)
    dataByColumn1.(colheaders{i}) = newData1.data(:, i);
end

% Create new variables in the base workspace from those fields.
vars = fieldnames(dataByColumn1);
for i = 1:length(vars)
    assignin('base', vars{i}, dataByColumn1.(vars{i}));
end

```

```

function
[alpha_beam,beta_beam,teta_att_worst,teta_rate_mod_worst,slope,t,H,V_mod,a_mod,J_mod,H_worst_req,V_m
od_worst_req,a_mod_worst_req,J_mod_worst_req,teta_rate_mod_worst_req,teta_B0,teta_B1,teta_B2,teta_B3,a
_rad_B1,a_rad_B2,a_rad_B3,J_rad_B1,J_rad_B2,J_rad_B3,teta_rate_mod,teta_rate_per_B1,teta_rate_per_B2,teta
_rate_per_B3,PRF_R,PRF_V,PRF_R_max,PRF_V_min,P_T_R,P_T_V,P_T_R_max,P_T_V_max,T_meas_R,T_meas_V,M
_R,M_V,Br_R,Br_V,N_R,N_V,lambda,teta_3_dB,n_over,delta_R_req,delta_V_req,Se_Re_max_R,Se_Re_max_V] = ...
Input_elaboration(position_z_up,position_z_down,H_P_T_flat,H_worst,V_xb_worst,V_yb_worst,V_zb_worst,a_xb
_worst,a_yb_worst,a_zb_worst,J_xb_worst,J_yb_worst,J_zb_worst,teta_att_worst_deg,teta_rate_mod_worst_deg
,H0,V0,H1,V1,H2,V2,H3,H4,V_xb_worst_non_amb,V_yb_worst_non_amb,V_zb_worst_non_amb,alpha_beam_deg
_vett,beta_beam_deg,c,K_Boltzman,Temp,f_update,f0,fc,P_T_down,P_T_up_R,P_T_up_V,D_ant,slope_deg,F,req_
perc,Input_motion,alpha_beam_flag,T_meas_R_flag,PRF_R_flag,PRF_V_flag,P_T_R_flag,P_T_V_flag)

% Raw data elaboration for RDA evaluations

global time position_z velocity_x velocity_y velocity_z yawAngle pitchAngle rollAngle acc_x acc_y acc_z yawRate
pitchRate rollRate

% Parameter setting after input selection
alpha_beam_deg = alpha_beam_deg_vett(alpha_beam_flag);
teta_worst_deg = teta_att_worst_deg + alpha_beam_deg;

% Degree to Radiant Conversion
alpha_beam = deg2rad(alpha_beam_deg);
beta_beam = deg2rad(beta_beam_deg);
teta_att_worst = deg2rad(teta_att_worst_deg);
teta_worst = deg2rad(teta_worst_deg);
teta_rate_mod_worst = deg2rad(teta_rate_mod_worst_deg);
slope = deg2rad(slope_deg);

% "Worst Case" module elaboration
V_mod_worst = sqrt(V_xb_worst.^2 + V_yb_worst.^2 + V_zb_worst.^2);
a_mod_worst = sqrt(a_xb_worst.^2 + a_yb_worst.^2 + a_zb_worst.^2);
J_mod_worst = sqrt(J_xb_worst.^2 + J_yb_worst.^2 + J_zb_worst.^2);

% Safe coefficients requirements values elaboration
H_worst_req = H_worst * req_perc;
V_mod_worst_req = V_mod_worst * req_perc;
a_mod_worst_req = a_mod_worst * req_perc;
J_mod_worst_req = J_mod_worst * req_perc;
teta_rate_mod_worst_req = teta_rate_mod_worst * req_perc;

% Two Simulated (1&2) or "Worst Case" (3) input analysis
if (Input_motion == 1) || (Input_motion == 2)

    if Input_motion == 1
        Import_XLS('Slow_Vert_Sim_Descent.xls')
    elseif Input_motion == 2
        Import_XLS('Fast_Vert_Sim_Descent.xls')
    end

    % Altitude arrow rimodulation
    ind_position_z_up = find(abs(position_z)<=abs(position_z_up),1);
    ind_position_z_down = find(abs(position_z)<=abs(position_z_down),1);
    if position_z(ind_position_z_down) > 0
        ind_position_z_down = ind_position_z_down - 1;
    end

    % Motion Input
    delta_ind = ind_position_z_up : ind_position_z_down;
    delta_t = time(delta_ind)' - time(delta_ind-1)';

    t = time(delta_ind)';
    H = abs(position_z(delta_ind))';
    V_x = velocity_x(delta_ind)';
    V_y = velocity_y(delta_ind)';
    V_z = velocity_z(delta_ind)';
    yaw = yawAngle(delta_ind)';

```

```

pitch = pitchAngle(delta_ind);
roll = rollAngle(delta_ind);
a_x = acc_x(delta_ind);
a_y = acc_y(delta_ind);
a_z = acc_z(delta_ind);
yaw_rate = yawRate(delta_ind);
pitch_rate = pitchRate(delta_ind);
roll_rate = rollRate(delta_ind);

J_x = (acc_x(delta_ind)' - acc_x(delta_ind-1)) ./ delta_t;
J_y = (acc_y(delta_ind)' - acc_y(delta_ind-1)) ./ delta_t;
J_z = (acc_z(delta_ind)' - acc_z(delta_ind-1)) ./ delta_t;

% Module elaboration
V_mod = sqrt(V_x.^2 + V_y.^2 + V_z.^2);
a_mod = sqrt(a_x.^2 + a_y.^2 + a_z.^2);
J_mod = sqrt(J_x.^2 + J_y.^2 + J_z.^2);

% Angles & Projections elaborations
vers_z_GRF = [0, 0, 1];
vers_xb_BRF = [1, 0, 0];
vers_yb_BRF = [0, 1, 0];

B1_BRF = B_BRF(alpha_beam,0*beta_beam);
B2_BRF = B_BRF(alpha_beam,1*beta_beam);
B3_BRF = B_BRF(alpha_beam,2*beta_beam);

teta_B0 = zeros(1,length(t));
teta_B1 = zeros(1,length(t));
teta_B2 = zeros(1,length(t));
teta_B3 = zeros(1,length(t));

a_rad_B1 = zeros(1,length(t));
a_rad_B2 = zeros(1,length(t));
a_rad_B3 = zeros(1,length(t));

J_rad_B1 = zeros(1,length(t));
J_rad_B2 = zeros(1,length(t));
J_rad_B3 = zeros(1,length(t));

teta_rate_mod = zeros(1,length(t));

teta_rate_per_B1 = zeros(1,length(t));
teta_rate_per_B2 = zeros(1,length(t));
teta_rate_per_B3 = zeros(1,length(t));

for ii = 1 : length(t)

    vers_xb_GRF = M_GRF2BRF(roll(ii),pitch(ii),yaw(ii))' * vers_xb_BRF';

    B1_GRF = M_GRF2BRF(roll(ii),pitch(ii),yaw(ii))' * B1_BRF';
    B2_GRF = M_GRF2BRF(roll(ii),pitch(ii),yaw(ii))' * B2_BRF';
    B3_GRF = M_GRF2BRF(roll(ii),pitch(ii),yaw(ii))' * B3_BRF';

    teta_B0(ii) = acos(dot(vers_z_GRF,vers_xb_GRF));
    teta_B1(ii) = acos(dot(vers_z_GRF,B1_GRF));
    teta_B2(ii) = acos(dot(vers_z_GRF,B2_GRF));
    teta_B3(ii) = acos(dot(vers_z_GRF,B3_GRF));

    a = [a_x(ii) a_y(ii) a_z(ii)];

    a_rad_B1(ii) = dot(a,B1_GRF);
    a_rad_B2(ii) = dot(a,B2_GRF);
    a_rad_B3(ii) = dot(a,B3_GRF);

    J = [J_x(ii) J_y(ii) J_z(ii)];

```

```

J_rad_B1(ii) = dot(J,B1_GRF);
J_rad_B2(ii) = dot(J,B2_GRF);
J_rad_B3(ii) = dot(J,B3_GRF);

vers_yb_GRF_gamma = M_GRF2BRF(0,0,yaw(ii))' * vers_yb_BRF';
vers_xb_GRF_gamma_beta = M_GRF2BRF(0,pitch(ii),yaw(ii))' * vers_xb_BRF';

teta_rate_vett = yaw_rate(ii) * vers_z_GRF' + pitch_rate(ii) * vers_yb_GRF_gamma + roll_rate(ii) *
vers_xb_GRF_gamma_beta; % Written in GRF
teta_rate_mod(ii) = sqrt(teta_rate_vett(1)^2 + teta_rate_vett(2)^2 + teta_rate_vett(3)^2);

teta_rate_rad_B1 = dot(teta_rate_vett,B1_GRF);
teta_rate_rad_B2 = dot(teta_rate_vett,B2_GRF);
teta_rate_rad_B3 = dot(teta_rate_vett,B3_GRF);

teta_rate_per_B1(ii) = sqrt(teta_rate_mod(ii)^2 - teta_rate_rad_B1^2);
teta_rate_per_B2(ii) = sqrt(teta_rate_mod(ii)^2 - teta_rate_rad_B2^2);
teta_rate_per_B3(ii) = sqrt(teta_rate_mod(ii)^2 - teta_rate_rad_B3^2);

end

elseif Input_motion == 3

% Time, Altitude and Attitude arrows definition
t = linspace(0,100,100);
H = linspace(H_worst,abs(position_z_down),length(t));
teta_B0 = teta_att_worst * ones(1,length(H));
teta_B1 = teta_worst * ones(1,length(H));
teta_B2 = teta_B1;
teta_B3 = teta_B1;

% Module elaboration
V_mod = V_mod_worst;
a_mod = a_mod_worst;
J_mod = J_mod_worst;
teta_rate_mod = teta_rate_mod_worst;

% Angles & Projections elaboration
a_rad_B1 = a_mod_worst;
a_rad_B2 = a_mod_worst;
a_rad_B3 = a_mod_worst;

J_rad_B1 = J_mod_worst;
J_rad_B2 = J_mod_worst;
J_rad_B3 = J_mod_worst;

teta_rate_per_B1 = teta_rate_mod_worst;
teta_rate_per_B2 = teta_rate_mod_worst;
teta_rate_per_B3 = teta_rate_mod_worst;

end

% Required & Non-Ambiguity Max Values
delta_R_req(1,:) = max(0.33/100 .* H + 0.8,0);

V_worst = sqrt(V_xb_worst^2 + V_yb_worst^2 + V_zb_worst^2);
V_worst_non_amb = sqrt(V_xb_worst_non_amb^2 + V_yb_worst_non_amb^2 + V_zb_worst_non_amb^2);

V3 = V_worst;
V4 = V_worst_non_amb;

ii = find(H<=H1);
V_max(ii) = ((V1 - V0)/(H1 - H0)) * (H(ii) - H0) + V0;
ii = find((H>H1) & (H<=H2));
V_max(ii) = ((V2 - V1)/(H2 - H1)) * (H(ii) - H1) + V1;
ii = find((H>H2) & (H<=H3));
V_max(ii) = ((V3 - V2)/(H3 - H2)) * (H(ii) - H2) + V2;

```

```

ii = find((H>H3) & (H<=H4));
V_max(ii) = ((V4 - V3)/(H4 - H3)) * (H(ii) - H3) + V3;

delta_V_req(1,:) = max(0.6/100 * V_max + 0.1,0);

% PRF laws
R_B0 = H/cos(teta_att_worst);

PRF_R_max = c/2./R_B0;

if PRF_R_flag == 1
    PRF_R = PRF_R_max;
elseif PRF_R_flag == 2
    PRF_R = ones(1,length(t)) * min(PRF_R_max);
elseif PRF_R_flag == 3
    ii = find(H<=1200);
    PRF_R(ii(1):ii(end)) = min(PRF_R_max(ii));
    ii = find((H>1200) & (H<=H3));
    PRF_R(ii(1):ii(end)) = min(PRF_R_max(ii));
    ii = find((H>H3) & (H<=H4));
    PRF_R(ii(1):ii(end)) = min(PRF_R_max(ii));
elseif PRF_R_flag == 4
    PRF_R_lim = 200e3;
    PRF_R = PRF_R_max;
    ii = find(PRF_R>PRF_R_lim);
    PRF_R(ii(1):ii(end)) = PRF_R_lim;
end

PRF_V_min = 4 * V_max/c * f0;

if PRF_V_flag == 1
    PRF_V = PRF_V_min;
elseif PRF_V_flag == 2
    PRF_V = ones(1,length(t)) * max(PRF_V_min);
elseif PRF_V_flag == 3
    ii = find((H<=H2));
    PRF_V(ii(1):ii(end)) = max(PRF_V_min(ii));
    ii = find((H>H2) & (H<=1200));
    PRF_V(ii(1):ii(end)) = max(PRF_V_min(ii));
    ii = find((H>1200) & (H<=H3));
    PRF_V(ii(1):ii(end)) = max(PRF_V_min(ii));
    ii = find((H>H3) & (H<=H4));
    PRF_V(ii(1):ii(end)) = max(PRF_V_min(ii));
elseif PRF_V_flag == 4
    PRF_V_opt = 2600;
    PRF_V = PRF_V_min;
    ii = find(PRF_V < PRF_V_opt);
    PRF_V(ii(1):ii(end)) = PRF_V_opt;
end

% Integrations Time Laws
TO_1 = fzero(@(x)V_mod_worst_req * x + a_mod_worst_req/2 * x^2 + J_mod_worst_req/3 * x^3 - c/8/fc,0);
TO_2 = acos(H_worst_req/(H_worst_req + c/8/fc))/teta_rate_mod_worst_req;

T_meas_R_worst = min(TO_1,TO_2);

if T_meas_R_flag == 1
    T_meas_R = ones(1,length(t)) * T_meas_R_worst;
elseif T_meas_R_flag == 2
    ii = find((H<=H2));
    T_meas_R(ii(1):ii(end)) = T_meas_R_worst * 0.2;
    ii = find((H>H2) & (H<=1200));
    T_meas_R(ii(1):ii(end)) = T_meas_R_worst * 0.4;
    ii = find((H>1200) & (H<=H3));
    T_meas_R(ii(1):ii(end)) = T_meas_R_worst * 0.6;
    ii = find((H>H3) & (H<=H4));
    T_meas_R(ii(1):ii(end)) = T_meas_R_worst * 0.8;
end

```

```

elseif T_meas_R_flag == 3
    ii = find((H<=H2));
    T_meas_R(ii(1):ii(end)) = T_meas_R_worst * 0.1;
    ii = find((H>H2) & (H<=1200));
    T_meas_R(ii(1):ii(end)) = T_meas_R_worst * 0.2;
    ii = find((H>1200) & (H<=H3));
    T_meas_R(ii(1):ii(end)) = T_meas_R_worst * 0.3;
    ii = find((H>H3) & (H<=H4));
    T_meas_R(ii(1):ii(end)) = T_meas_R_worst * 0.4;
elseif T_meas_R_flag == 4
    ii = find((H<=H2));
    T_meas_R(ii(1):ii(end)) = 1.01./PRF_R(ii(1));
    ii = find((H>H2) & (H<=1200));
    T_meas_R(ii(1):ii(end)) = 2.01./PRF_R(ii(1));
    ii = find((H>1200) & (H<=H3));
    T_meas_R(ii(1):ii(end)) = 2.01./PRF_R(ii(1));
    ii = find((H>H3) & (H<=H4));
    T_meas_R(ii(1):ii(end)) = 2.01./PRF_R(ii(1));
end

f_meas_R = 1./T_meas_R;
f_meas_V = 1./((1./f_update - 1./f_meas_R)/3);

T_meas_V = 1./f_meas_V;

% Pulse Duration Laws
PRI_R = 1./PRF_R;
PRI_V = 1./PRF_V;

P_T_R_max_1 = 2 * H / c;
P_T_R_max_2 = PRI_R;
P_T_R_max = min(P_T_R_max_1,P_T_R_max_2);

P_T_V_max_1 = 2 * H / c;
P_T_V_max_2 = PRI_V;
P_T_V_max = min(P_T_V_max_1,P_T_V_max_2);

if P_T_R_flag == 1
    P_T_R = P_T_R_max;
elseif P_T_R_flag == 2
    ind_H_P_T_flat = find(H<=H_P_T_flat,1);
    P_T_R = (P_T_up_R - P_T_down)/(H(1) - H(ind_H_P_T_flat)) .* (H(1:ind_H_P_T_flat) - H(ind_H_P_T_flat)) +
    P_T_down;
    P_T_R(ind_H_P_T_flat+1:length(t)) = P_T_down;
elseif P_T_R_flag == 3
    ii = find((H<=H2));
    P_T_R(ii(1):ii(end)) = min(P_T_R_max(ii));
    ii = find((H>H2) & (H<=1200));
    P_T_R(ii(1):ii(end)) = min(P_T_R_max(ii));
    ii = find((H>1200) & (H<=H3));
    P_T_R(ii(1):ii(end)) = min(P_T_R_max(ii));
    ii = find((H>H3) & (H<=H4));
    P_T_R(ii(1):ii(end)) = min(P_T_R_max(ii));
elseif P_T_R_flag == 4
    P_T_R = P_T_R_max;
end

if P_T_V_flag == 1
    P_T_V = P_T_V_max;
elseif P_T_V_flag == 2
    P_T_V = (P_T_up_V - P_T_down)/(H(1) - H(ind_H_P_T_flat)) .* (H(1:ind_H_P_T_flat) - H(ind_H_P_T_flat)) +
    P_T_down;
    P_T_V(ind_H_P_T_flat+1:length(t)) = P_T_down;
elseif P_T_V_flag == 3
    ii = find((H<=H2));
    P_T_V(ii(1):ii(end)) = min(P_T_V_max(ii));
    ii = find((H>H2) & (H<=1200));

```

```

P_T_V(ii(1):ii(end)) = min(P_T_V_max(ii));
ii = find((H>1200) & (H<=H3));
P_T_V(ii(1):ii(end)) = min(P_T_V_max(ii));
ii = find((H>H3) & (H<=H4));
P_T_V(ii(1):ii(end)) = min(P_T_V_max(ii));
elseif P_T_V_flag == 4
P_T_V = P_T_V_max;
if alpha_beam_deg == 15
ii = find(H > 400);
elseif alpha_beam_deg == 20
ii = find(H > 50);
end
P_T_V(ii) = min(P_T_V_max(ii));
end

% Pulses Number
M_R = floor(PRF_R .* T_meas_R);
M_V = floor(PRF_V .* T_meas_V);

% Range and Velocity Receiver Bandwidth
Br_R = 1./P_T_R;
Br_V = 1./P_T_V;

% Range and Velocity Received Noise
N_R = K_Boltzman * Temp * Br_R * F;
N_V = K_Boltzman * Temp * Br_V * F;

% Radar Parameters
lambda = c/f0;
teta_3_dB = 0.88 * lambda/D_ant;

n_over(H<=H_worst) = 30;
n_over(H<=H3) = 50;
n_over(H<=1200) = 100;
n_over(H<=H2) = 200;
n_over(H<=H2/3) = 300;

% Signal Trip Time & Send/Return Time
STT_max_R = 2 * H / c / cos(teta_att_worst); % Range Max Signal Travel Time along H
Se_Re_max_R = 0 * P_T_R + STT_max_R; % Range Max Front-End Signal Send-Return Time along H

STT_max_V = 2 * H / c / cos(teta_att_worst + alpha_beam); % Range Max Signal Travel Time along H
Se_Re_max_V = 1 * P_T_V + STT_max_V; % Range Max Signal Send-Return Time along H

% Input Conguence Control
ii = find(PRF_R > PRF_R_max,1);
if not(isempty(ii))
error('Range PRF over its max value: Decrease it') %#ok<ERTAG>
end

ii = find(PRF_V < PRF_V_min,1);
if not(isempty(ii))
error('Velocity PRF under its min value: Increase it') %#ok<ERTAG>
end

ii = find(T_meas_R > T_meas_R_worst,1);
if not(isempty(ii))
error('Range Integration Time over its worst case value: Decrease it') %#ok<ERTAG>
end

ii = find(T_meas_R >= 1/f_update,1);
if not(isempty(ii))
error('Range Integration Time over Total Time integration: Decrease it') %#ok<ERTAG>
end

ii = find(P_T_R > PRI_R,1);
if not(isempty(ii))

```

```

error('Range Pulse Width over PRI: Decrease it or Increase PRI') %#ok<ERTAG>
end

ii = find(P_T_V > PRI_V,1);
if not(isempty(ii))
    error('Velocity Pulse Width over PRI: Decrease it or Increase PRI') %#ok<ERTAG>
end

ii = find(P_T_R > P_T_R_max,1);
if not(isempty(ii))
    error('Range Pulse Width over its max value: Decrease it') %#ok<ERTAG>
end

ii = find(P_T_V > P_T_V_max,1);
if not(isempty(ii))
    error('Velocity Pulse Width over its max value: Decrease it') %#ok<ERTAG>
end

ii = find(M_R <= 0,1);
if not(isempty(ii))
    error('There are NO pulses for Range Estimation: Check Range PRF & Time Integration parameters')
    %#ok<ERTAG>
end

ii = find(M_V <= 0,1);
if not(isempty(ii))
    error('There are NO pulses for Velocity Estimation: Check Velocity PRF & Time Integration parameters')
    %#ok<ERTAG>
end

```

```

function
[position_z_up,position_z_down,H_P_T_flat,H_worst,V_xb_worst,V_yb_worst,V_zb_worst,a_xb_worst,a_yb_worst
,a_zb_worst,J_xb_worst,J_yb_worst,J_zb_worst,teta_att_worst_deg,teta_rate_mod_worst_deg,H0,V0,H1,V1,H2,V
2,H3,H4,V_xb_worst_non_amb,V_yb_worst_non_amb,V_zb_worst_non_amb,alpha_beam_deg_vett,beta_beam_d
eg,c,K_Boltzman,Temp,f_update,f0,f_IF,fc,Bt,Pt,P_T_down,P_T_up_R,P_T_up_V,D_ant,eta_ant,Epsilon,D,sigma_h,s
lope_deg,F,L_atm,L_sys,req_perc,Input_motion,alpha_beam_flag,T_meas_R_flag,PRF_R_flag,PRF_V_flag,P_T_R_f
lag,P_T_V_flag,Filter_flag] = ...
    Input_RDA

% Input function for RDA performance analysis.
% With this function are assigned trajectory, attitude, motion data, radar parameters, Mars surface
% parameters, boundary condidtion.
% All data are expressed in SI

% Simulation Altitude Interval
position_z_up = -3000;
position_z_down = -10;

H_P_T_flat = 100;

% Worst Case Values in BRf
H_worst = 3000;

V_xb_worst = 64;
V_yb_worst = 45;
V_zb_worst = 45;

a_xb_worst = 2.65;
a_yb_worst = 9.3;
a_zb_worst = 9.3;

J_xb_worst = 26.5;
J_yb_worst = 93;
J_zb_worst = 93;
teta_att_worst_deg = 35; % Degree

```

```

teta_rate_mod_worst_deg = 60; % Degree

% Required & Non-Ambiguity Max Values Input in BRF
H0 = 0; V0 = 0;
H1 = 12; V1 = 0.2;
H2 = 450; V2 = 55;
H3 = 2000;
H4 = 3000;

V_xb_worst_non_amb = 160;
V_yb_worst_non_amb = 45;
V_zb_worst_non_amb = 45;

% Beam Geometric Parameters
alpha_beam_deg_vett = [15 20]; % Degree
beta_beam_deg = 120; % Degree

% Radar Parameters
c = 3e8;
K_Boltzman = 1.38e-23;
f_update = 20;
f0 = 35e9;
f_IF = 50e6;
fc = 100e6;
Pt = 1; % Transmitted Peak Power
Bt = 200e6; % Peak Rise Time setted equal to 5 ns
P_T_down = 40e-9; % Pulse duration at low altitude
P_T_up_R = 10e-6; % Range Pulse duration at low altitude
P_T_up_V = 2e-6; % Range Pulse duration at low altitude
D_ant = 0.15;
eta_ant = 0.653;
Temp = 290;
F = 10^(5/10); % Receiver Noise Figure in W (= 5 dB)
L_sys = 10^(4/10); % System Losses in W (= 4 dB)
L_atm = 10^(4/10); % Atmospheric Losses in W (= 4 dB)

% Mars Parameters
Epsilon = 3;
D = 0.04;
sigma_h = 0.1;
slope_deg = 10;

% Elaboration Parameters
req_perc = 1;

% Input Selection
Input_motion = menu('Select Motion Data','Slow_Vert_Sim_Descent', 'Fast_Vert_Sim_Descent','Worst Case
Descent');
alpha_beam_flag = menu('Select Beam Angle','15 deg','20 deg');
T_meas_R_flag = menu('Select Range Time Measurement', 'Flat', '0.2 - 0.4 - 0.6 - 0.8', '0.1 - 0.2 - 0.3 - 0.4',
'Optimum');
PRF_R_flag = menu('Select Range PRF law:', 'Max', 'Flat', 'Step', 'Optimum (Flat / Max)');
PRF_V_flag = menu('Select Velocity PRF law:', 'Min', 'Flat', 'Step', 'Optimum (2.6 KHz / Min)');
P_T_R_flag = menu('Select Range P_T law:', 'Max', 'Ramp', 'Step', 'Optimum (Max)');
P_T_V_flag = menu('Select Velocity P_T law:', 'Max', 'Ramp', 'Step', 'Optimum (Max / Flat)');
Filter_flag = menu('Do you want to use a Chebyshev Type II filter during SNR evaluation?','Yes','No');

```

```

function M = M_GRF2BRF(alpha,beta,gamma)

% Flight Angle Matrix Rotation, with notation:
% Alpha = Roll angle
% Beta = Pitch angle
% Gamma = Yaw angle
% Rotation sequence used: 321 or Yaw-Pitch-Roll
% All Angles are expressed in radians

```

```

M(1,1) = cos(beta) * cos(gamma);
M(1,2) = cos(beta) * sin(gamma);
M(1,3) = -sin(beta);

M(2,1) = -cos(alpha) * sin(gamma) + sin(alpha) * sin(beta) * cos(gamma);
M(2,2) = cos(alpha) * cos(gamma) + sin(alpha) * sin(beta) * sin(gamma);
M(2,3) = sin(alpha) * cos(beta);

M(3,1) = sin(alpha) * sin(gamma) + cos(alpha) * sin(beta) * cos(gamma);
M(3,2) = -sin(alpha) * cos(gamma) + cos(alpha) * sin(beta) * sin(gamma);
M(3,3) = cos(alpha) * cos(beta);

```

```

function [sigma_0_R,sigma_0_V_B1,sigma_0_V_B2,sigma_0_V_B3] =
Backscattering_Box(teta_B0,teta_B1,teta_B2,teta_B3,Epsilon,D,lambda)

% Box delegated to four beams backscattering elaboration

sigma_0_R = Backscattering_Model(teta_B0,Epsilon,D,lambda);

sigma_0_V_B1 = Backscattering_Model(teta_B1,Epsilon,D,lambda);
sigma_0_V_B2 = Backscattering_Model(teta_B2,Epsilon,D,lambda);
sigma_0_V_B3 = Backscattering_Model(teta_B3,Epsilon,D,lambda);

```

```

function sigma_0 = Backscattering_Model(teta,Epsilon,D,lambda)

% Hagfors-Model for Mars Surface Backscattering (developed for the Lunar surface)

Gamma = ((1-sqrt(Epsilon))/(1+sqrt(Epsilon)))^2;
sigma_h = D/3;
ND = 5.61*exp(-12.05 * D);
l_c = sqrt(2/ND);
m_s = sigma_h/l_c;
C = (lambda/(4*pi*sigma_h)).^2*(1/m_s^2);

sigma_0 = (Gamma*C/2)*1./(cos(teta).^4+C*sin(teta).^2).^^(3/2);

```

```

function b=B(T,H,c,teta_off)

teta = acos(2*H/c./T);
b = 2^5 * pi * H.^6 / c^4 ./ T.^5 .* Gain_2(teta - teta_off);

```

```

function G = Gain(teta)

% Antenna Gain

global teta_3_dB

G = ones(size(teta));
ii = find(abs(teta)>1e-40);

G(ii) = abs(sin(pi/teta_3_dB * 0.88 .* sin(teta(ii)))/sin(teta(ii)) * teta_3_dB/pi/0.88).^2;

```

```

function G = Gain_2(teta)

G = Gain(teta).^2;

```

```

function [Pr,SNR,E,beta_2] = ...
SNR(teta,sigma_0,P_T,M,Br,N,H,Pt,Bt,teta_3_dB,c,lambda,D_ant,eta_ant,fc,n_over,L_atm,L_sys,Filter_flag)

% Signal to Noise Ratio elaboration for Range and Velocity Beams

```

```

% Waitbar Title Setting
Case = inputname(1);
if strcmp(Case, 'teta_BO')
    waitbar_handle = waitbar (0, 'Beam 0 (Range) SNR Evaluation...');
elseif strcmp(Case, 'teta_B1')
    waitbar_handle = waitbar (0, 'Beam 1 (Velocity) SNR Evaluation...');
elseif strcmp(Case, 'teta_B2')
    waitbar_handle = waitbar (0, 'Beam 2 (Velocity) SNR Evaluation...');
elseif strcmp(Case, 'teta_B3')
    waitbar_handle = waitbar (0, 'Beam 3 (Velocity) SNR Evaluation...');
elseif strcmp(Case, 'teta_BO_worst')
    waitbar_handle = waitbar (0, 'Worst Case Range Beam SNR Evaluation...');
elseif strcmp(Case, 'teta_B123_worst')
    waitbar_handle = waitbar (0, 'Worst Case Velocity Beam SNR Evaluation...');
else
    error('ERROR: Bad initialization of SNR Evaluation') %#ok<ERTAG>
end

% Pre-Allocations
E = zeros(1,length(H));
beta_2 = zeros(1,length(H));
A_eq = zeros(1,length(H));

% Elaboration
delta_tt = 1/fc./n_over;
A_ant = D_ant^2;
G0 = 4 * pi/lambda^2 * A_ant * eta_ant;

L_H = length(H);
for jj = 1 : L_H

    waitbar(jj / L_H);

    T_min = 2 * H(jj)/c;
    T_max = max(2 * H(jj)/cos(teta(jj) + teta_3_dB * 2)/c, T_min + P_T(jj));

    tt = 0 : delta_tt(jj) : T_min;
    i_tt = find(tt<=P_T(jj));
    pt(i_tt) = 1; %#ok<AGROW>
    pt(i_tt+1:length(tt)) = 0; % Transmitted Pulse

    if Filter_flag == 1
        [b_t_a_t] = cheby2(5,25,Bt./(fc * n_over(jj)));
        pt=filter(b_t,a_t,sqrt(pt)).^2;
    end

    tt_CC = T_min : delta_tt(jj) : T_max;
    CC = conv(pt,B(tt_CC,H(jj),c,teta(jj))) * delta_tt(jj);
    ii_CC = find(CC>0,1,'last');
    CC = CC(1:ii_CC);

    tt_conv = 0 : delta_tt(jj) : (length(CC) + length(pt)-1) * delta_tt(jj); % Convolution Time Starts
    Int_area_over(1:length(pt)) = 0; % Integration Area Oversampled
    Int_area_over(length(pt)+1:length(tt_conv)) = CC; % Integration Area Oversampled
    Int_area_over(length(tt_conv)+1:length(tt_conv)+1+n_over(jj)*2) = 0;

    if Filter_flag == 1
        [b_r_a_r] = cheby2(5,25,Br(jj)/(fc * n_over(jj)));
        Int_area_over = filter(b_r,a_r,sqrt(Int_area_over)).^2;
    end

    A_eq_max = max(Int_area_over);
    A_eq(jj) = mean(Int_area_over(Int_area_over > 0.5 * A_eq_max));

    if nargout == 4 % Only for Range SNR Estimation
        tt_sig = 0 : delta_tt(jj) : (length(CC)+length(pt)+n_over(jj)*2) * delta_tt(jj); % Convolution Time Starts
        sig_IF = sqrt(Int_area_over * Pt * lambda^2 * G0^2 * sigma_0(jj)/(4 * pi)^3./H(jj).^4/L_atm/L_sys);
    end
end

```

```

sig_IF_f = fftshift(fft(sig_IF));
ff = -fc/2 : fc/length(tt_sig) : fc/2-fc/length(tt_sig);
E(jj) = trapz(tt_sig,abs(sig_IF).^2);
beta_2(jj) = trapz(ff,ff.^2.*abs(sig_IF_f).^2)/fc^2*(2*pi)^2/E(jj);
end

clear tt_i tt_tt_CC CC tt_conv tt_sig sig_IF ff pt Int_area_over

end

Pr = Pt.* lambda^2 * G0^2 * sigma_0 .* A_eq/(4 * pi)^3./H.^4/L_atm/L_sys;
SNR = Pr./N .* M;

close(waitbar_handle)

```

```

function [Pr_R,Pr_V_B1,Pr_V_B2,Pr_V_B3,SNR_R,SNR_V_B1,SNR_V_B2,SNR_V_B3,E_R,beta_2_R_old] = ...
SNR_Box(teta_B0,teta_B1,teta_B2,teta_B3,sigma_0_R,sigma_0_V_B1,sigma_0_V_B2,sigma_0_V_B3,P_T_R,P_T_V,
M_R,M_V,Br_R,Br_V,N_R,N_V,H,Pt,Bt,teta_3_dB,c,lambda,D_ant,eta_ant,fc,n_over,L_atm,L_sys,Input_motion,Filter_flag)

% Box delegated to four beams Received Power and Signal to Noise Ratio elaboration
% In "Worst Case" analysis, only Range and one Velocity beam elaborations are done because of all
% three Velocity beams have the same Pr and SNR that leads to less elaboration time.

if (Input_motion == 1) || (Input_motion == 2)

    [Pr_R,SNR_R,E_R,beta_2_R_old] = ...
SNR(teta_B0,sigma_0_R,P_T_R,M_R,Br_R,N_R,H,Pt,Bt,teta_3_dB,c,lambda,D_ant,eta_ant,fc,n_over,L_atm,L_sys,Filter_flag);

    [Pr_V_B1,SNR_V_B1] = ...
SNR(teta_B1,sigma_0_V_B1,P_T_V,M_V,Br_V,N_V,H,Pt,Bt,teta_3_dB,c,lambda,D_ant,eta_ant,fc,n_over,L_atm,L_sys,Filter_flag);
    [Pr_V_B2,SNR_V_B2] = ...
SNR(teta_B2,sigma_0_V_B2,P_T_V,M_V,Br_V,N_V,H,Pt,Bt,teta_3_dB,c,lambda,D_ant,eta_ant,fc,n_over,L_atm,L_sys,Filter_flag);
    [Pr_V_B3,SNR_V_B3] = ...
SNR(teta_B3,sigma_0_V_B3,P_T_V,M_V,Br_V,N_V,H,Pt,Bt,teta_3_dB,c,lambda,D_ant,eta_ant,fc,n_over,L_atm,L_sys,Filter_flag);

elseif Input_motion == 3

    teta_B0_worst = teta_B0;
    teta_B123_worst = teta_B1;

    [Pr_R,SNR_R,E_R,beta_2_R_old] = ...
SNR(teta_B0_worst,sigma_0_R,P_T_R,M_R,Br_R,N_R,H,Pt,Bt,teta_3_dB,c,lambda,D_ant,eta_ant,fc,n_over,L_atm,L_sys,Filter_flag);

    [Pr_V_B1,SNR_V_B1] = ...
SNR(teta_B123_worst,sigma_0_V_B1,P_T_V,M_V,Br_V,N_V,H,Pt,Bt,teta_3_dB,c,lambda,D_ant,eta_ant,fc,n_over,L_atm,L_sys,Filter_flag);

    Pr_V_B2 = Pr_V_B1;
    Pr_V_B3 = Pr_V_B1;

    SNR_V_B2 = SNR_V_B1;
    SNR_V_B3 = SNR_V_B1;

end

```

```

function C = C_BeRF2BRF(alpha, beta)

% Transformation Matrix from BeRF to BRF
% All Angles are expressed in radians

```

```

C(1,1) = -cos(beta)/cos(alpha) * 1/ (1 - cos(beta));
C(1,2) = 1/4 * 1/sin(beta/2)^2 * 1/cos(alpha);
C(1,3) = 1/4 * 1/sin(beta/2)^2 * 1/cos(alpha);

C(2,1) = 1/sin(alpha) * 1/(1 - cos(beta));
C(2,2) = -1/2 * 1/sin(alpha) * 1/(1-cos(beta));
C(2,3) = -1/2 * 1/sin(alpha) * 1/(1-cos(beta));

C(3,1) = 0;
C(3,2) = 1/2 * 1/sin(alpha) * 1/sin(beta);
C(3,3) = -1/2 * 1/sin(alpha) * 1/sin(beta);

```

```

function [delta_R,delta_V_X,delta_V_Y,delta_V_Z] = ...

Measurement_Accuracy_Box(teta_B0,E_R,beta_2_R_old,SNR_V_B1,SNR_V_B2,SNR_V_B3,a_rad_B1,a_rad_B2,a_rad_B3,J_rad_B1,J_rad_B2,J_rad_B3,teta_rate_per_B1,teta_rate_per_B2,teta_rate_per_B3,PRF_V,T_meas_V,M_R,M_V,Br_R,N_R,fc,sigma_h,slope,c,H,lambda,teta_3_dB,alpha_beam,beta_beam)

% Box delegated to Range and 3D Velocity Measurement Accuracy elaboration

[delta_R] = Range_Accuracy(teta_B0,E_R,beta_2_R_old,M_R,Br_R,N_R,fc,sigma_h,slope,c,H,teta_3_dB);

[delta_V_X,delta_V_Y,delta_V_Z] = ...

Velocity_Accuracy(SNR_V_B1,SNR_V_B2,SNR_V_B3,a_rad_B1,a_rad_B2,a_rad_B3,J_rad_B1,J_rad_B2,J_rad_B3,teta_rate_per_B1,teta_rate_per_B2,teta_rate_per_B3,PRF_V,T_meas_V,M_V,lambda,teta_3_dB,alpha_beam,beta_beam);

```

```

function [delta_R] = Range_Accuracy(teta,E,beta_2_old,M,Br,N,fc,sigma_h,slope,c,H,teta_3_dB)

% Range Measurement Accuracy elaboration

N_0 = N ./ Br;

% Surface Roughness Effect
sigma_t_1 = 2 * sigma_h/c;

% Slope Terrain Effect
SW_teta = H .* (1./cos(teta + teta_3_dB/2) - 1./cos(teta - teta_3_dB/2));
SW_teta_s = H .* (1./cos(teta + slope + teta_3_dB/2) - 1./cos(teta + slope - teta_3_dB/2));
sigma_t_2 = 2 * (SW_teta_s - SW_teta)/c;

% Sigma_t without corrections
sigma_t_old = 1./2./pi./sqrt(beta_2_old);

% Sigma_t with corrections
sigma_t_new = sqrt(sigma_t_old.^2 + sigma_t_1.^2 + sigma_t_2.^2); % New sigma_t

beta_2_new = (1./2./pi./sigma_t_new).^2; % New beta_2

% Partial Delta_Rs
delta_T_R = 1./sqrt(beta_2_new * 2 .* M .* E ./ N_0);
delta_T_q = 1/fc/sqrt(12);

% Range Measurement Accuracy
delta_R = c/2 * sqrt(delta_T_R.^2 + delta_T_q.^2);

```

```

function [delta_V_X,delta_V_Y,delta_V_Z] = ...

Velocity_Accuracy(SNR_V_B1,SNR_V_B2,SNR_V_B3,a_rad_B1,a_rad_B2,a_rad_B3,J_rad_B1,J_rad_B2,J_rad_B3,teta_rate_per_B1,teta_rate_per_B2,teta_rate_per_B3,PRF_V,T_meas_V,M_V,lambda,teta_3_dB,alpha_beam,beta_beam)

% Velocity Measurement Accuracy elaboration

```

```

% Parameters Setting
C = C_BeRF2BRF(alpha_beam, beta_beam); % Transformation Matrix from BeRF to BRF
V_a = PRF_V .* lambda/2; % Unambiguous Velocity

% Evaluation of Doppler spectrum spread
sigma_V_1 = lambda/2./T_meas_V; % Finite observation time effect

sigma_V_2_B1 = a_rad_B1 .* T_meas_V + J_rad_B1/2 .* T_meas_V.^2; %
sigma_V_2_B2 = a_rad_B2 .* T_meas_V + J_rad_B2/2 .* T_meas_V.^2; % Acceleration and Jerk effect
sigma_V_2_B3 = a_rad_B3 .* T_meas_V + J_rad_B3/2 .* T_meas_V.^2; %

sigma_V_3 = lambda * PRF_V/4 * teta_3_dB; % Antenna aperture effect

sigma_V_4_B1 = lambda * PRF_V/2 .* teta_rate_per_B1 .* T_meas_V; %
sigma_V_4_B2 = lambda * PRF_V/2 .* teta_rate_per_B2 .* T_meas_V; % Antenna rotation effect
sigma_V_4_B3 = lambda * PRF_V/2 .* teta_rate_per_B3 .* T_meas_V; %

% Sigma_V for three Velocity Beams
sigma_V_B1 = sqrt(sigma_V_1.^2 + sigma_V_2_B1.^2 + sigma_V_3.^2 + sigma_V_4_B1.^2);
sigma_V_B2 = sqrt(sigma_V_1.^2 + sigma_V_2_B2.^2 + sigma_V_3.^2 + sigma_V_4_B2.^2);
sigma_V_B3 = sqrt(sigma_V_1.^2 + sigma_V_2_B3.^2 + sigma_V_3.^2 + sigma_V_4_B3.^2);

% Rho_2 for three Velocity Beams
rho_2_B1 = exp(- 4 * (pi .* sigma_V_B1./V_a).^2);
rho_2_B2 = exp(- 4 * (pi .* sigma_V_B2./V_a).^2);
rho_2_B3 = exp(- 4 * (pi .* sigma_V_B3./V_a).^2);

% delta_V_pp for three Velocity Beams
delta_V_pp_B1 = sqrt(V_a.^2/8/pi^2./M_V .* (1./rho_2_B1 .* (1 + 1./SNR_V_B1).^2 - 1));
delta_V_pp_B2 = sqrt(V_a.^2/8/pi^2./M_V .* (1./rho_2_B2 .* (1 + 1./SNR_V_B2).^2 - 1));
delta_V_pp_B3 = sqrt(V_a.^2/8/pi^2./M_V .* (1./rho_2_B3 .* (1 + 1./SNR_V_B3).^2 - 1));

% delta_V_pp for Velocity along BRF
delta_V_pp_X = sqrt((C(1,1) * delta_V_pp_B1).^2 + (C(1,2) * delta_V_pp_B2).^2 + (C(1,3) * delta_V_pp_B3).^2);
delta_V_pp_Y = sqrt((C(2,1) * delta_V_pp_B1).^2 + (C(2,2) * delta_V_pp_B2).^2 + (C(2,3) * delta_V_pp_B3).^2);
delta_V_pp_Z = sqrt((C(3,1) * delta_V_pp_B1).^2 + (C(3,2) * delta_V_pp_B2).^2 + (C(3,3) * delta_V_pp_B3).^2);

delta_V_q = V_a ./ M_V ./ sqrt(12);

% Velocity Measurement Accuracy along BRF
delta_V_X = sqrt(delta_V_pp_X.^2 + delta_V_q.^2);
delta_V_Y = sqrt(delta_V_pp_Y.^2 + delta_V_q.^2);
delta_V_Z = sqrt(delta_V_pp_Z.^2 + delta_V_q.^2);

```

```

function [] =
Graphic_Output_Box(t,H,V_mod,a_mod,J_mod,teta_B0,teta_B1,teta_B2,teta_B3,teta_rate_mod,PRF_R,PRF_V,PRF
_R_max,PRF_V_min,P_T_R,P_T_V,P_T_R_max,P_T_V_max,T_meas_R,T_meas_V,M_R,M_V,sigma_0_R,sigma_0_V
B1,sigma_0_V_B2,sigma_0_V_B3,Pr_R,Pr_V_B1,Pr_V_B2,Pr_V_B3,SNR_R,SNR_V_B1,SNR_V_B2,SNR_V_B3,delta_R
_req,delta_R,delta_V_req,delta_V_X,delta_V_Y,delta_V_Z,t_estim,Se_Re_max_R,Se_Re_max_V,Input_motion,alph
a_beam_flag,T_meas_R_flag,PRF_R_flag,PRF_V_flag,P_T_R_flag,P_T_V_flag,Filter_flag)

% Function delegated to show the results of elaborations

% Command Window Outputs
fprintf('\nElaboration data for')
if Input_motion == 1
    fprintf(' "Slow_Vert_Sim_Descent.xls" input.')
elseif Input_motion == 2
    fprintf(' "Fast_Vert_Sim_Descent.xls" input.')
elseif Input_motion == 3
    fprintf(' "Worst Case Descent" input.')
end

fprintf('\n\nSelected Beam Angle is')
if alpha_beam_flag == 1
    fprintf(' "15 deg";')

```

```

elseif alpha_beam_flag == 2
    fprintf(' "20 deg;')
end

fprintf('\n\nSelected Range Time Measurement is')
if T_meas_R_flag == 1
    fprintf(' "Flat;')
elseif T_meas_R_flag == 2
    fprintf(' "0.2 - 0.4 - 0.6 - 0.8;')
elseif T_meas_R_flag == 3
    fprintf(' "0.1 - 0.2 - 0.3 - 0.4;')
elseif T_meas_R_flag == 4
    fprintf(' "Optimum;')
end

fprintf('\n\nSelected Range PRF law is')
if PRF_R_flag == 1
    fprintf(' "Max;')
elseif PRF_R_flag == 2
    fprintf(' "Flat;')
elseif PRF_R_flag == 3
    fprintf(' "Step;')
elseif PRF_R_flag == 4
    fprintf(' "Optimum (Flat/Max);')
end

fprintf('\n\nSelected Velocity PRF law is')
if PRF_V_flag == 1
    fprintf(' "Min;')
elseif PRF_V_flag == 2
    fprintf(' "Flat;')
elseif PRF_V_flag == 3
    fprintf(' "Step;')
elseif PRF_V_flag == 4
    fprintf(' "Optimum (2.6 KHz/Min);')
end

fprintf('\n\nSelected Range P_T_R law is')
if P_T_R_flag == 1
    fprintf(' "Max;')
elseif P_T_R_flag == 2
    fprintf(' "Ramp;')
elseif P_T_R_flag == 3
    fprintf(' "Step;')
elseif P_T_R_flag == 4
    fprintf(' "Optimum (Max);')
end

fprintf('\n\nSelected Velocity P_T_V law is')
if P_T_V_flag == 1
    fprintf(' "Max;')
elseif P_T_V_flag == 2
    fprintf(' "Ramp;')
elseif P_T_V_flag == 3
    fprintf(' "Step;')
elseif P_T_V_flag == 4
    fprintf(' "Optimum (Max/Flat);')
end

fprintf('\n\nChebyshev Type II filter is')
if Filter_flag == 1
    fprintf(' used.')
elseif Filter_flag == 2
    fprintf(' not used.')
end

fprintf('\n\nTotal Estimation Time elapsed is %f, t_estim)

```

```

fprintf(' seconds.\n\n')

% Figure Outputs
figure(1)
plot(t,H)
title('Altitude as a function of Descending Time')
xlabel('time t [s]')
ylabel('H [m]')

figure(2)
plot(H,V_mod)
title('Velocity as a function of Altitude')
xlabel('Altitude H [m]')
ylabel('V [m/s]')

figure(3)
plot(H,a_mod)
title('Acceleration as a function of Altitude')
xlabel('Altitude H [m]')
ylabel('a [m/s^2]')

figure(4)
plot(H,J_mod)
title('Jerk as a function of Altitude')
xlabel('Altitude H [m]')
ylabel('J [m/s^3]')

figure(5)
plot(H,rad2deg(teta_B0))
title('Sideloop Beam 0 Angle as a function of Altitude')
xlabel('Altitude H [m]')
ylabel('\theta_0 [deg]')

figure(6)
plot(H,rad2deg(teta_B1),H,rad2deg(teta_B2),H,rad2deg(teta_B3))
title('Sideloop Beam 1,2,3 Angles as a function of Altitude')
xlabel('Altitude H [m]')
ylabel('\theta_i [deg]')
legend('\theta_1','\theta_2','\theta_3')

figure(7)
plot(H,rad2deg(teta_rate_mod))
title('Theta rate as a function of Altitude')
xlabel('Altitude H [m]')
ylabel('\theta_t [deg/s]')

figure(8)
hold on
plot(H,PRF_R/1000)
plot(H,PRF_R_max/1000,'-r','LineWidth',1.5)
axis([0 H(1) 0 1.5 * max(PRF_R/1000)])
title('Range PRF as a function of Altitude')
xlabel('Altitude H [m]')
ylabel('PRF [KHz]')
legend('PRF_R','PRF_R_m_a_x')
hold off

figure(9)
hold on
plot(H,PRF_V/1000)
plot(H,PRF_V_min/1000,'-r','LineWidth',1.5)
title('Velocity PRF as a function of Altitude')
xlabel('Altitude H [m]')
ylabel('PRF [KHz]')
legend('PRF_V','PRF_V_m_i_n')
hold off

```

```

figure(10)
hold on
plot(H,P_T_R*10^6)
plot(H,P_T_R_max*10^6,'--r','LineWidth',1.5)
title('Range Trasmitted Pulse Duration as a function of Altitude')
xlabel('Altitude H [m]')
ylabel('PT [\mus]')
legend('PT_R','PT_R_m_a_x')
hold off

figure(11)
hold on
plot(H,P_T_V*10^6)
plot(H,P_T_V_max*10^6,'--r','LineWidth',1.5)
title('Velocity Trasmitted Pulse Duration as a function of Altitude')
xlabel('Altitude H [m]')
ylabel('PT [\mus]')
legend('PT_V','PT_V_m_a_x')
hold off

figure(12)
PRI_R = 1./PRF_R;
plot(H,Se_Re_max_R*10^6,H,PRI_R*10^6)
title('Max Range Signal Send-Return Time & Pulse Repetition Interval as a function of Altitude')
xlabel('Altitude H [m]')
ylabel('SRT_m_a_x & PRI [\mus]')
legend('SRT_m_a_x','PRI')

figure(13)
PRI_V = 1./PRF_V;
plot(H,Se_Re_max_V*10^6,H,PRI_V*10^6)
title('Max Velocity Signal Send-Return Time & Pulse Repetition Interval as a function of Altitude')
axis([0 H(1) 0 1.5 * max(Se_Re_max_V* 10^6)])
xlabel('Altitude H [m]')
ylabel('SRT_m_a_x & PRI [\mus]')
legend('SRT_m_a_x','PRI')

figure(14)
plot(H,T_meas_R*1000,H,T_meas_V*1000)
title('Integration Time as a function of Altitude')
xlabel('Altitude H [m]')
ylabel('t [ms]')
legend('T_m_e_a_s_,_R','T_m_e_a_s_,_V')

figure(15)
plot(H,T_meas_R*1e6)
title('Range Integration Time as a function of Altitude')
xlabel('Altitude H [m]')
ylabel('t [\mus]')

figure(16)
plot(H,T_meas_V*1e3)
title('Velocity Integration Time as a function of Altitude')
xlabel('Altitude H [m]')
ylabel('t [ms]')

figure(17)
plot(H,M_R,H,M_V)
title('Pulse Numbers as a function of Altitude')
xlabel('Altitude H [m]')
ylabel('M')
legend('M_R','M_V')

figure(18)
plot(H,M_R)
title('Range Pulse Numbers as a function of Altitude')
xlabel('Altitude H [m]')

```

```

ylabel('M')

figure(19)
plot(H,M_V)
title('Velocity Pulse Numbers as a function of Altitude')
xlabel('Altitude H [m]')
ylabel('M')

figure(20)
plot(H,sigma_0_R)
title('Range Backscattering as a function of Altitude')
xlabel('Altitude H [m]')
ylabel('\sigma_0')

figure(21)
plot(H,sigma_0_V_B1,H,sigma_0_V_B2,H,sigma_0_V_B3)
title('Velocity Backscattering as a function of Altitude')
xlabel('Altitude H [m]')
ylabel('\sigma_0_i')
legend('\sigma_0_1','\sigma_0_2','\sigma_0_3')

figure(22)
plot(H,10*log10(Pr_R)+30)
title('Received Range Power as a function of Altitude')
xlabel('Altitude H [m]')
ylabel('Pr_R [dBm]')

figure(23)
plot(H,10*log10(Pr_V_B1)+30,H,10*log10(Pr_V_B2)+30,H,10*log10(Pr_V_B3)+30)
title('Received Velocity Power as a function of Altitude')
xlabel('Altitude H [m]')
ylabel('Pr_V_i [dBm]')
legend('Pr_V_1','Pr_V_2','Pr_V_3')

figure(24)
plot(H,10*log10(SNR_R))
title('Range Signal Noise Ratio as a function of Altitude')
xlabel('Altitude H [m]')
ylabel('SNR_R [dB]')

figure(25)
plot(H,10*log10(SNR_V_B1),H,10*log10(SNR_V_B2),H,10*log10(SNR_V_B3))
title('Velocity Signal Noise Ratio as a function of Altitude')
xlabel('Altitude H [m]')
ylabel('SNR_V_i [dB]')
legend('SNR_V_1','SNR_V_2','SNR_V_3')

figure(26)
hold on
plot(H,delta_R_req,'--r','LineWidth',1.5)
plot(H,delta_R)
title('Range Accuracy Estimation as a function of Altitude')
xlabel('Altitude H [m]')
ylabel('\deltaR [m]')
legend('\deltaR_req','\deltaR')
hold off

figure(27)
hold on
plot(H,delta_V_req,'--r','LineWidth',1.5)
plot(H,delta_V_X,H,delta_V_Y,H,delta_V_Z)
title('BRF Velocity Accuracy Estimation as a function of Altitude')
xlabel('Altitude H [m]')
ylabel('\deltaV_i [m/s]')
legend('\deltaV_req','\deltaV_X','\deltaV_Y','\deltaV_Z')
hold off

```

REFERENCES

- Ref. 1 ESA Press Release N° 74-2000: *ESA and the European Union adopt a common strategy for space.*
(http://www.esa.int/esaCP/Pr_74_2000_p_EN.html)
- Ref. 2 ESA web site: *Aurora's Origins.*
(http://www.esa.int/esaMI/Aurora/SEMZOS39ZAD_0.html)
- Ref. 3 ESA web site: *About the ExoMars Mission.*
(http://www.esa.int/SPECIALS/ExoMars/SEM10VLPQ5F_0.html)
- Ref. 4 M. I. Skolnik, *Introduction to Radar Systems*, McGraw-Hill Science Engineering.
- Ref. 5 K.S. Miller and M.M. Rochwarger, "A Covariance Approach to Spectral Moment Estimation," *IEEE Trans. on Information Theory*, vol. 18, no. 5, pp 588-596, 1972.
- Ref. 6 S. S. Abeysekera, "Performance of Pulse-Pair Method of Doppler Estimation," *IEEE Transactions on Aerospace And Electronic Systems*, vol. 34, NO. 2 April 1998.
- Ref. 7 F. T. Ulaby, R. K. Moore, and A. K. Fung, *Microwave Remote Sensing: Active and Passive, from Theory to Applications*, Artech House Remote Sensing Library.
- Ref. 8 R. A. Williams, "Optimum Choice of Pulse Pair Spacing," *Proceedings of the IEEE*, December 1973.

Web Sites

www.esa.int – *European Space Agency* home page.

www.esa.int/esaMI/Aurora – *Aurora Program* home page.

www.esa.int/SPECIALS/ExoMars – *ExoMars Mission* home page.

www.corista.unina.it – *Co.Ri.S.T.A. (Consortium for Research on Advanced Remote Sensing Systems)* home page.

ACKNOWLEDGEMENTS

I would like to express sincerest gratitude to my thesis advisor, Prof. Eng. Antonio Moccia of D.I.A.S. (Department of Aerospace Engineering), and to my thesis co-advisor, Head Researcher Radar Sector, Eng. Giovanni Alberti of Co.Ri.S.T.A. (Consortium for Research on Advanced Remote Sensing Systems), whose guidance was instrumental in helping me to complete this work.

Special thanks go to the Head Researcher Radar Sector, Eng. Leonardo Borgarelli of TAS-I Rome (Thales Alenia Italy in Rome) and to the Eng. Adriano Carbone and Eng. Marco Iorio for their contribute to preliminary TAS-I Proposal.

Special thanks also go to my Family, above all my mother Elisa and my father Carmine that have supported me during the academic years in every possible way, every day.

A Great thanks goes to my colleague Ernesto d'Aquino, Luigi Manzo, Pasquale Arpaia and Pasquale Cesarano to have shared with me the whole academic experience.

I wish to thank Antonio Vitiello, Donatella Telesca, Flavio Malacario, Laura Calascibetta, Lucia Fancello, Mariateresa Sorrentino and Mario Fontana for their constant affection, support and encouragement shown me in these years.

Finally, the warmest thanks go to Charlize, David, Saul and William for the inspiration that they have given me when the study was very binding.

Thanks a lot.